Czech Technical University
in Prague

Faculty of Mechanical
Engineering

Advanced coatings by thermal spray methods

Jan CIZEK

A habilitation thesis submitted to

FACULTY OF MECHANICAL ENGINEERING

FACULTY
OF MECHANICAL
ENGINEERING
CTU IN PRAGUE

CZECH TECHNICAL UNIVERSITY IN PRAGUE

CTU

CZECH TECHNICAL
UNIVERSITY
IN PRAGUE

Prague, January 2020

Preface

The surface is a crucial part of any material. In fact, the quality and durability of surfaces are usually the decisive factors for the overall performance and reliability of components, appliances and workpieces. Naturally, efforts to enhance the surface properties were realized throughout the history. For more than a century now, thermal spray technologies rank among cost-effective and reliable methods for doing so.

The presented thesis comprises two major parts: first, it introduces the thermal spray technologies. Briefly, their history is presented and the underlying fundamental principles are explained. To illustrate the versatility of these processes, selected key technologies are introduced along with their respective advantages. Owing to the professional interests of the candidate, two of these technologies are presented in more detail: atmospheric plasma spray and cold kinetic spray.

The former is an established and industrially well-proven technology that has been systematically upgraded for the past 50 years. Its versatility allows to modify surfaces of materials intended for applications such as aerospace, automotive, marine, mining and oil, chemical, power generation, paper production, or even electronics. Last but not least, the technology also assists in hard tissue bioapplications.

Research-based studies centered on cold kinetic spraying started to appear after 2003 only. Given its novelty, several physical aspects of the technology are still not perfectly understood at the moment. Nonetheless, the potential of this technology itself started to draw major attention of industrial companies and the technology is now readily applied in numerous sectors that engage with metals and cermets. Considering its rather unique, solid-state concept, the method technically does not directly compete with thermal spray processes. Still, it has a strong potential to replace its predecessors in several application fields.

Being actively involved in both technologies since 2004, the scientific and technological advances of both technologies are discussed and illustrated with the help of own publication record of the candidate. These include plasma sprayed thermal barrier coatings (aerospace applications) deposited from powders as well as from liquid feedstock, a rather novel concept in the field. Further, bioactive coatings applicable in hard tissue implants were studied, partially also using the liquid spraying concept (the importance of this contribution to the plasma spray community was recently recognized by industry as we were awarded the Werner von Siemens award for the Most significant accomplishment in basic research award in 2019). Another contribution of the candidate to the thermal spray community is based on his cold spray research and includes, among other, first interpretation of an interesting interface phenomenon not encountered in other thermal spray processes, work on architectured bi-metallic materials, or fundamental findings on mechanical response of the deposits in the elastic deformation range. Application-wise, the works include extension of lifetime of components by cold spraying, formation of oxide barriers for aerospace and automotive industry, or wear resistant diamond-based cermets for extreme environments. Importantly, a recent scientific breakthrough of the candidate's team includes the first ever successful deposition of thick tungsten coatings for nuclear fusion.

The second part of the thesis expands the information provided in the first part. Taking full advantage of the results obtained by the candidate and his colleagues, this part is provided in a form of eight selected papers published in recognized international journals, representing profile of the candidate's work and his R&D contribution since the beginnings in this field.

Keywords

Thermal spraying; atmospheric plasma spray; suspension spraying; thermal barrier coatings; bioactive implants; antibacterial silver nanoparticles; interface; cold gas kinetic spray; additive manufacturing; intertwining phenomenon; architectured metals; elastic isotropy; high cycle fatigue; CoNiCrAlY bond coats; advanced diamond cermets; tungsten coatings

Acknowledgments

I would like to express my utmost gratitude to all my science friends who have helped me on the battlefield of the mesmerizing Planet Science. This includes a whole range of support, from sharing the - countable - hooray moments upon making an important achievement or discovery, to moral support of a heartbroken scientist in the - rather uncountable - moments when our theory was swept away by an insidious experiment.

Given the long-term collaborations, which I humbly and deeply appreciate, the list of my science friends is rather long, making my fear of omitting any important name quite legitimate. With this concern expressed, my thanks go to all science friends and colleagues.

Aside from science, there is one more aspect of a life of every scientist, his/her personal life. Without a solid support in the background, it would be plain impossible to focus on research. That said, my thanks go to all my family members, including my wife Kata, my parents, or my brother and his girlfriend. Also, three more folks (A+F+w) whom I have the luck to call best friends deserve to be thanked.

Table of contents

List of Figures

List of Tables

Nomenclature

Symbols

T_m	Melting temperature
v_p	In-flight or impact velocity (of particles)

Abbreviations

AISI	American Iron and Steel Institute
APS	Atmospheric plasma spray
ASI	Adiabatic shear instability (in cold spray)
CAPS	Controlled atmosphere plasma spray
CGDS	Cold gas dynamic spraying, identical to CS
CS	Cold spray
CVD	Chemical vapor deposition method
DC	Direct current, type of plasma spray generation
FEM	Finite element method modeling
GSP	Gas-stabilized plasma generation
HA	Hydroxyapatite
HVAF	High velocity air-fuel spraying method
HVOF	High velocity oxy-fuel spraying method
PS	Plasma spray
PVD	Physical vapor deposition method
R&D	Research and development
RF-ICP	Radio frequency inductively-coupled plasma
SPS	Suspension plasma spray method
TBC	Thermal barrier coating
TS	Thermal spray (processes)
WSP-H	Hybrid water-stabilized plasma generation

Scope

The presented thesis comprises of four parts. In the first chapter, a brief introduction on surface engineering is made to present the readers with the motives and aims of the thesis.

The second chapter is devoted to thermal spray processes: here, a review of history is provided, along with the underlying physical principles influencing the final properties of the applied materials. Some general issues are addressed and a summary of advantages and possible problematic areas is discussed. The chapter then focuses on two methods that are the focal points of the candidate's research interests: atmospheric plasma spray and cold kinetic spraying. Plasma spray is a widespread, flexible and economical method. The process is described from the start of plasma generation to the end, i.e., final coating properties, including examples of applications. The last part of the chapter then refers to cold kinetic spray process, a young and novel member of the TS family. Here again, a brief historical background is provided along with the current-most development in this field. Given the rather unique concept of solid-state coatings formation (as opposed to the TS counterparts), the governing physical principles are explained in more detail. The chapter then provides examples of applications of the technology, stressing the potential of cold spray to be used as additive manufacturing technology for e.g. repairs.

The third chapter provides a summary, a brief debate on relative strength and weaknesses of the two methods.

The thesis then presents eight selected papers of the candidate and his colleagues (four for plasma spray, four for cold spray) to illustrate own contribution to the state-of-the-art know-how in both fields, including a short explanation on the novelty and importance of each of the papers.

Chapter 1

Introduction

Every solid material comprises of inner bulk and a surface. Due to the different physical forces the individual atoms are subjected to, the latter exhibits properties that may vary significantly from those of the bulk. Due to the geometry, the surface is generally also subjected to the highest levels of loading, be it of mechanical, thermal, or e.g. electrochemical origin. In most applications, the combination of these two factors often yields the surface as the most critical part of every component or product [1, 2].

Naturally, humans understood this concept centuries ago when the first efforts to improve the quality of surfaces were being made, signifying a birth of surface engineering. From the initial concept of simple case hardening of weapons millennia ago, the progress and understanding of the underlying fundamentals enabled the advent of myriad of methods that are available to us nowadays.

Despite the breadth of the choice, the surface technologies could basically be divided into two major groups: modification of an existing surface, or a deposition of an added material in a form of a coating [1, 2]. A simple way to distinguish between the two resides in a fact that while the former involves modification of the surface microstructure and/or composition without any dimensional change of the part or component, the latter essentially leads to increase in at least one of the dimensions (thickness).

Thermal hardening, mechanical hardening and thermochemical processes in general are prime examples of traditional surface modification technologies, having modern counterparts in technologies such as e.g. ion implantation [3] or laser or electron beam modification [4, 5, 6, 7, 8]. Likewise, the surface coatings methods range from simple painting, through plating (both electro-

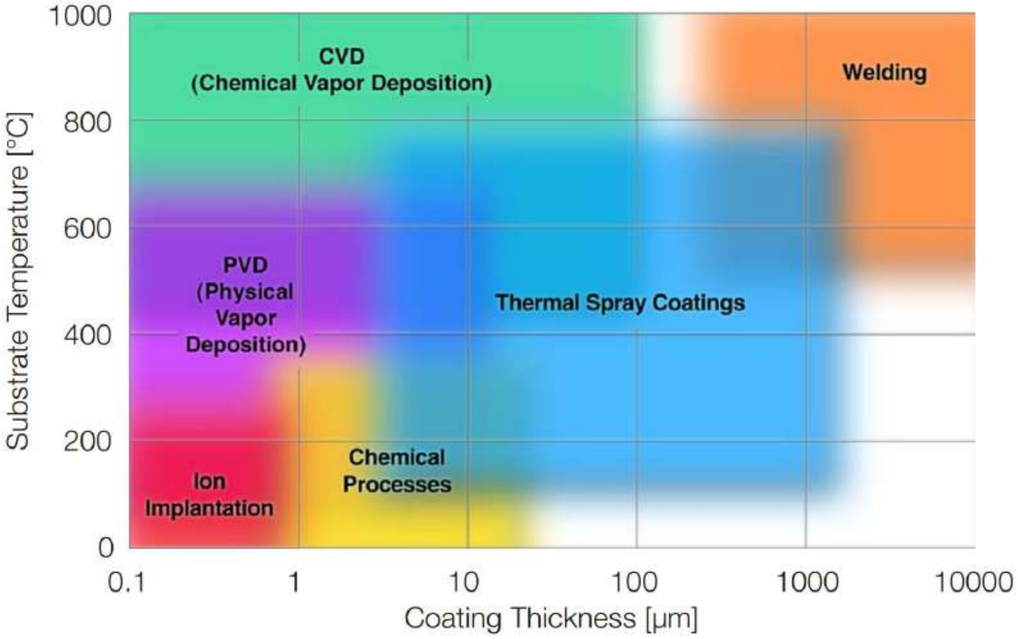

Figure 1.1: Overview of selected coating processes. Image courtesy of Sulzer Metco, Switzerland.

and electroless-), through important processes of physical or chemical vapor deposition (PVD, CVD) [9, 4], all the way to a family of thermal spray processes (TS, Fig. 1.1) [10].

Regardless of the choice of the method, the rapid growth of the entire surface engineering sector triggered an improved economy of the processes, thereby enabling routine fabrication of components with enhanced performance, extended lifetime or even e.g. improved appearance. Owing to these, surface engineering has established itself as a widespread set of technologies used in virtually all applications, including e.g. aerospace, automotive, power generation, mining, petrochemical, chemical, machine tooling or even biomedical.

As the surface technologies that are of primary research interest of the candidate, thermal spray methods will be further introduced in more detail in the next chapter.

Chapter 2

Thermal spray processes

In the late 19th century, Swiss inventor Max Schoop discovered that upon injecting metallic powder into a stream of hot gases (formed by a combustion of oxygen and a fuel gas such as propane or acetylene), the heat-softened powder would adhere to the surface of a substrate toward which the stream had been directed [10]. Ever since then, this new process (later known as metallizing, Fig. 2.1) became a standard method for applying metallic coatings for several decades. Importantly, it has also become a foundation stone of what is nowadays known as thermal spray technologies.

In the following years, novel methods and their respective modifications emerged, increasing the global versatility and applicability of these processes. Owing to this, the thermal spray industry underwent an unprecedented growth since 1960s. From 1997 to 2002, an annual increase of more than +6.1% was recorded; at the moment, the thermal spray market is valued at stunning US$8.70 billion (2017), with forecasts to reach US$15.10 billion by 2026 [11].

Importantly, the group of processes is still being actively developed, with new members of the TS family emerging as late as 2002 (cold kinetic spray [12]), 2006 (warm spray [13]) or even after 2010 (HVAF [14]).

2.1 Fundamental principles

The thermal spray is a group of processes in which metallic or non-metallic materials are deposited in a molten, semi-molten or even solid state onto a prepared substrate to form a spray deposit, so called coating [10]. In general, three distinct phases can be defined in every thermal deposition process:

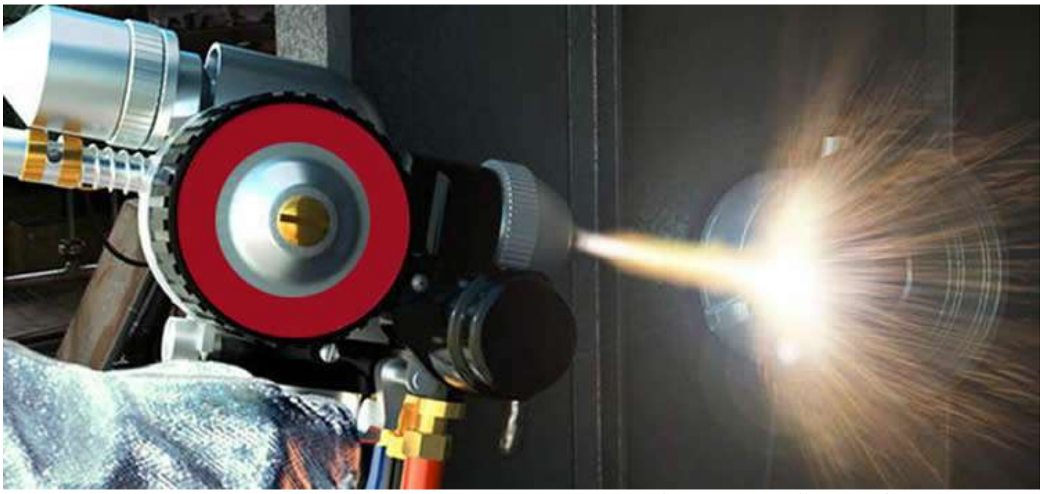

Figure 2.1: Metallizing process. Image courtesy of Thermal Spray Gun, India.

- injection of the material and its interaction with the surrounding atmosphere
- interaction of the material with the substrate surface and formation of the first layer
- coating build-up by stacking of layers

In the first phase, the material is inserted in front of or directly into the thermal spray torch. Owing to the versatility of the methods, the feedstock material can be used in various forms, such as wires, rods, or (the most frequent form in the last decades due to commercial availability) finely divided powders (Fig. 2.2). Since approximately 2002, the development introduced the feedstock materials in a form of liquid-based suspensions (SPS) [15, 16, 17, 18, 19].

Upon insertion, the energy of the material particles is increased by means of the chemical energy of gas combustion, energy stored in plasma jet, electrical energy and/or the energy of the acting gases and is then partially transferred into heat and velocity. While the former results into partial or full-scale melting of the particles [20], the latter propels the material toward the substrate. Depending on the technology, the high velocities of acting gases cause acceleration of the small particles of the material up to v_p=1400 m·s^{-1} [12].

In-flight, the jet of semi- or fully-molten particles is surrounded by air or controlled atmosphere (CAPS, more expensive solution [21]). The heat ab-

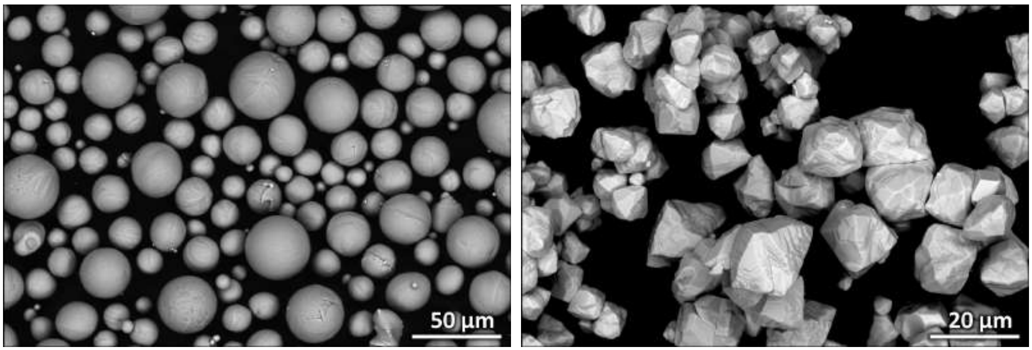

Figure 2.2: Examples of commercially sold powders: Ti (left) and W (right). Own research.

sorbed by a particle is influenced by a range of factors such as temperature spatial distribution (given by the selection of working gases or jet length) [22, 23, 24, 25, 26, 27].

In the second phase of the process, the sprayed particles impinge at the substrate surface. At that moment, they undergo rapid cooling (up to 10^6 K·s^{-1} [20]) and their kinetic energy and accumulated heat are transformed into deformation (resulting into particles flattening, spreading, shape deformation or conformation and adherence to surface irregularities), solidification (liquid to solid state transformation, phase changes related to cooling, inherent stresses buildup [28, 29, 30]), underlying substrate microscale melting and global composite heating. The solidified particles are called splats and due to common concurrence of acting temperature and velocity, their resulting shape is far from ideal spheres, with their shape best described as lamellar (pancake-like, Fig. 2.3). Generally, the size of these solidified platelets ranges from few micrometers to over 100 μm in diameter and about 1–50 μm in thickness [31, 32, 33]. Synchronous relative movement of the thermal spray torch against the substrate enables covering the substrate in individually deposited layers, each consisting of millions of such solidified splats.

Certain important characteristics of the final coatings (such as e.g. adhesion) are predominantly influenced by the quality of the first deposited layer of splats. This layer is in a direct contact with the substrate surface. To reflect this, adequate surface preparation is frequently implemented prior to the deposition process.

One of the methods employed for durable substrates is blasting or shot-

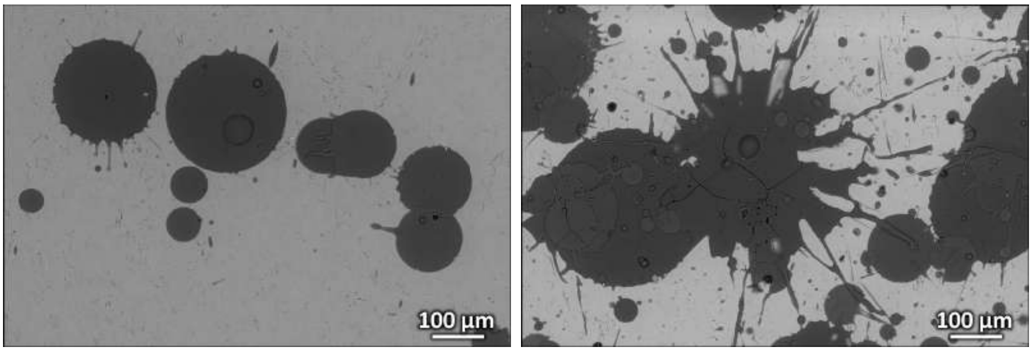

Figure 2.3: Morphology of splats can range from perfect pancake-like (left) to splashed (right) depending on the spray parameters and substrate conditions. Illustrated using hydroxyapatite (HA) splats on Ti6Al4V substrates. Own research.

peening [34]. This is usually done by using a stream of abrasive particles, but can also have a form of a pulsed water jet [35] or blasting by dry-ice cubes [36]. This way, the substrate roughness is enhanced, yielding a better bond strength of the coatings. On a micro-scale, a rough future contact area between substrate and impacting particle facilitates the mechanism of mechanical interlocking, thereby improving the bonding quality.

Other procedures to improve the first layer qualities are related to the chemical nature of the substrate surface, in particular its composition, purity, or its wettability. To modify such properties, chemical modifications are employed prior to thermal deposition, such as chemical cleaning or degreasing. Alternatively, application of grease or oil contaminant films or even deliberate surface oxidation may be used in special applications to e.g. introduce an inter-layer that ensures more coherent and continual transition of properties (such as good bonding to both the substrate and the coating) [37].

Lastly, preheating of the substrates is used to aid in the final quality. The substrate temperature highly influences the behavior of a particle upon impact and the changes of morphology and shape prior to its solidification [38, 39]. While for relatively cold substrates, non-uniform splats are formed with noticeable splashing, no splashing occurs and a regular disc-shaped splat formation is observed above certain temperature threshold of the substrate (Fig. 2.3). Consequently, microstructure integrity is improved and number of properties is significantly enhanced. Further, the practice of substrates preheating may also be exploited in fabrication of free-standing components, i.e., thicker coatings that self-detach (or are easy to detach) from the sub-

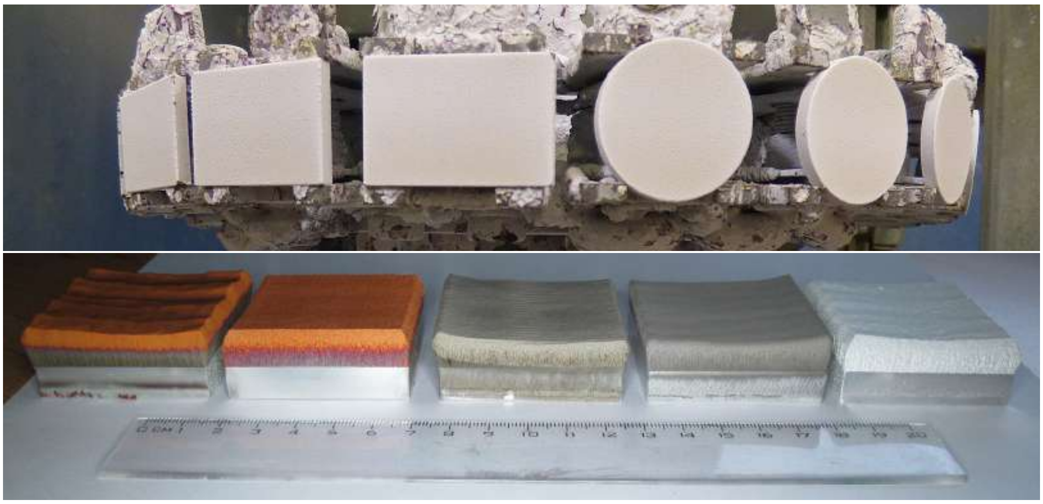

Figure 2.4: Macro overview of typical coatings produced by plasma spraying (top) and cold spraying (bottom). Illustrated using Al_2O_3 coatings on AISI 304 steel substrates and Cu (fine), Cu (coarse), Ni, Ti and Al coatings on Al substrates. Own research.

strates owing to differences in thermal expansion coefficients [40].

As the spray torch is moved over the surface in successive passes during the deposition process, a coating is created on the substrate material in the third phase. Its overall thickness is influenced by a number of spray gun passes, relative speed of the gun towards the surface, the efficiency of the deposition process and the material deposition rate [20]. Typically, thermally sprayed coatings thickness could vary from 5 μm (usually a single layer coating) up to 10 mm (usually a coating with graded or sandwich layer structure). In fact, some thermal spray processes (such as cold kinetic spraying) allow fabrication of coatings with virtually unlimited thickness, classifying them among additive manufacturing methods too (Fig. 2.4) [41].

2.2 Coating properties

Layer by layer, the coating is built up. Due to conditions to which the material is exposed to during its spraying (e.g. elevated temperatures, rapid solidification, plastic deformations), several phenomena are observed in TS [10]:

- presence of unmolten particles
- presence of impurities

- presence of porosity
- phase and structural changes
- oxidation
- chemical decompositions
- selective component evaporation
- internal stresses build up
- coatings cracking
- coatings poorer adhesion or even complete delamination

As much as some of these may not necessarily present a detrimental factor (e.g. porosity of a coating is a desired property in several major applications [16, 30, 37, 42, 43, 44]), all of these phenomena are directly reflected in the inimitable microstructure of the coatings. Consisting of solidified splats, unmolten or semi-molten particles, various impurities such as inclusions and/or oxidized particles, micro-cracks, gas filled voids and inherent porosity, the coatings are largely heterogeneous, anisotropic and consisting of both amorphous and recrystallized phases in various polymorphic forms (Fig. 2.5). Frequently, changes in stoichiometry of the original feedstock are observed, leading to multiphase coatings formation. Naturally, such microstructure significantly influences the overall coating properties.

2.3 Selected thermal spray technologies

Thermal spraying covers a range of techniques which differ in the process of heat generation and subsequent jet properties. A broad spectrum of applicable materials allows a production of coating of properties targeted for particular applications. The main thermal spray techniques and their relative properties are summarized in Table 1 [10]. The variations in resulting coating properties are predominantly caused by the differences in the respective temperatures of generated jets and the velocities the particles are accelerated to.

In the flame spray process (the oldest of the thermal spray processes), oxygen and fuel gas such as hydrogen, acetylene or propylene are fed into a torch and ignited to create a flame [10, 45]. The chemical energy released

Table 1: Overview of main thermal spray processes

Deposition technique	**Flame spraying**	**Electric arc spraying**	**Detonation gun**	**HVOF**	**Plasma spray**	**Cold spray**
Heat source	$O_2 + H_2$ $O_2 + C_2H_2$ $O_2 + C_3H_6$	arc between electrodes	oxygen C_2H_2	$O_2 + H_2$ $O_2 + C_2H_2$ $O_2 + C_3H_6$ $O_2 + C_3H_8$ O_2+kerosene	plasma arc	regular gas heating
Propellant	O_2	air	detonation shock waves	O_2	He, Ar	He, N_2, air
Material feed type	powder, wire, rod	wire	powder	powder	powder	powder
Flame or plasma exit temperature [K]	2800–3300	4300–6300	4800	3000–3400	3000–16000	20–700
Typical particle velocity [m·s^{-1}]	30–180	240	800–1000	800–1400	120–600	300–1200
Coating materials	metallic, ceramic	ductile materials	metallic, ceramic, plastic	metallic, ceramic	metallic, ceramic, plastic	metallic, ceramic, plastic
Bond strength [MPa]	20–28	40–60	>70	40–96	10–70	40–300
Porosity [%]	10–25	8–15	0.5–6	0.1–2	2–20	0.1–3
Oxide content [%]	4–6	0.5–3	0.1	0.2	< 1.0	< 0.1
Particle injection mode	axial, perpendicular	at angle to jet	axial	axial	perpendicular	perpendicular
Flame length [cm]	< 10	< 15	< 10	< 10	< 15	< 10
Relative cost [$]	3	1	10	5	5–10	7

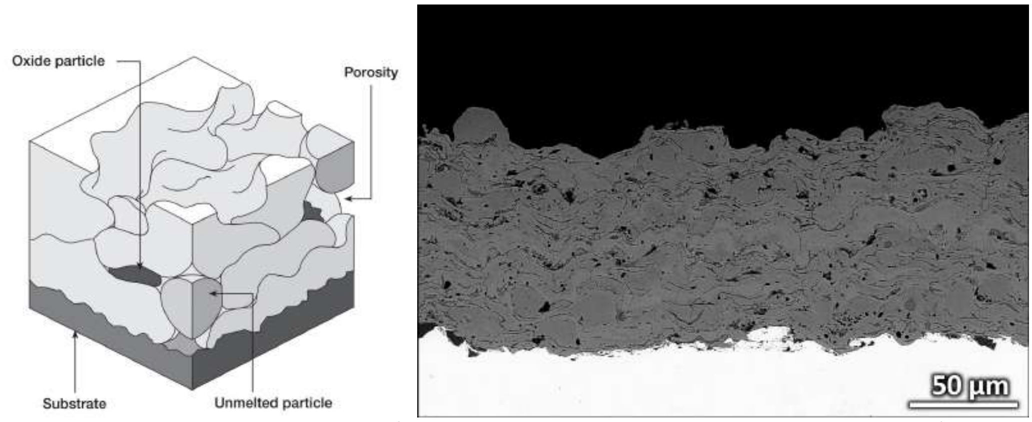

Figure 2.5: Microstructure of thermally sprayed coatings. Typical features include porosity, unmolten particles, inclusions, microcracks, etc. (left). Real coating microstructure (right) illustrated using hybrid coatings sprayed from suspension of hydroxyapatite (HA) and TiO_2 powder on AISI 304 steel. Schematics image courtesy of FST, Netherlands. Real coating from own research.

from the combustion is used to heat the powder, rod, wire or liquid suspension and blow the molten particles onto the substrate. The flame spray technique has generally a low cost, but achieves the lowest temperature and velocity of the processes. It is therefore not recommended for use with materials requiring high temperatures to melt (e.g. tungsten or ceramics). Due to lower spraying velocities, the resultant coating has relatively high porosity and low bond and cohesive strengths. Recently, a method of high velocity suspension flame spraying was introduced to the TS community [46].

In the electric arc spray process (also wire arc spray, Fig. 2.6), two wires are simultaneously brought into close contact with each other at the nozzle. A high-current potential difference is applied on the wires and initiates an arc that melts the tips of the wires. Atomizing gas (usually compressed air), is used to strip the molten material off the wires and transport it towards the substrate. Electric arc spray has the highest deposition rate of all thermal spray processes and can be used to spray large surface areas or employed in a flow production components spraying. The combination of relatively high temperature and slightly higher particle velocities gives wire arc sprayed coatings superior bond strengths and lower porosity levels as compared to flame sprayed coatings [10]. However, the use of compressed air for droplet atomization and propulsion gives rise to high oxide content in the coating.

Figure 2.6: Wire arc spray process. Image courtesy of Office of Technology Commercialization, University of Minnesota, USA.

Figure 2.7: Detonation gun spray process. Image courtesy of Praxair Surface Technologies, USA.

A detonation gun technology consists of a water-cooled barrel and a spark plug mechanism. A controlled mixture of gases, usually oxygen and acetylene, is fed to the barrel with portion of a powder. A spark is used to ignite the gas and the resulting detonation wave heats and accelerates the powder as it moves down the barrel. A pulse of nitrogen gas is used to purge the barrel after each detonation. The process is repeated up to 10× per second [47]. A combination of high temperature and supersonic velocity of particles gives rise to one of the smallest porosities among the thermal spray processes and high adhesion strengths between the coating and the substrate. The detonation gun spraying is a non-continuous technique, often resulting in unevenness in the coating thicknesses. Excessive noise is generated during the deposition process.

In high-velocity oxy-fule process (HVOF), a fuel gas such as hydrogen, acetylene, kerosene (a mixture of petroleum hydrocarbons C_9H_{20}–$C_{17}H_{36}$), propane or propylene are injected into the combustion chamber of the torch at high pressures and mixed with oxygen. The mixture is ignited and then exits through a small-diameter water-cooled barrel, generating a supersonic exhaust gas jet. The internal combustion considerably increases the kinetic energy of the particles. They achieve supersonic velocities, one of the highest among thermal spray processes, resulting in very dense coatings [6, 7, 37, 48, 49]. Also the uniformity of HVOF sprayed coatings is superior to the coatings prepared by other methods. Disadvantages of HVOF include low deposition rates, increased in-flight oxidation rates and limitations on applicable materials due to temperature constraints.

Figure 2.8: High velocity oxy-fuel spray process (HVOF). Hand-held torch (left) and illustration of Mach diamonds from the supersonic flow of gases (right). Images courtesy of Avweld, Australia.

2.3.1 Plasma spray

Plasma spraying (PS, APS for its most common atmospheric version) is generally regarded as the most versatile of all the thermal spray processes [10, 20]. Thermal plasmas are generated in inductively coupled discharges (radio frequency inductively coupled plasma, RF-ICP) or in direct electric arcs (direct current plasma, DC) that are stabilized by flow of gases (GSP) or water vortex (WSP-H).

During gas-stabilized plasma process (GSP) operation, gases or gas mixtures such as argon, helium, nitrogen and hydrogen are passed through a torch. An electric arc between co-axially aligned central cathode and water cooled anode gives the gas molecules enough energy to dissociate and ionize by atomic collisions during their passing through an anode orifice. Beyond the nozzle, the atomic components recombine, giving off a tremendous amount of heat. Powder is injected externally or internally into the jet, melted and accelerated towards the substrate (Fig. 2.9). The heat content, temperature and the velocity of the plasma jet are controlled by the torch geometry, the arc current, the gases flow rate and/or mixture ratio.

In the hybrid water-stabilized plasma process (WSP-H) developed at Institute of Plasma Physics (Prague, Czech Republic), the plasma is generated in the gas stabilized section first and then enters the water-stabilized plasma section (water vortex) where its enthalpy is substantially increased. Thereby, significantly superior heat input is transferred to the sprayed material, ensur-

Figure 2.9: Plasma spray spray processes. Standard DC gas-stabilized torch (illustrated using SG-100 torch, Praxair Surface Technologies, USA, left) and hybrid water-stabilized plasma (WSP-H500, Institute of Plasma Physics, The Czech Academy of Sciences, Czech Republic, right). Own research.

ing its proper deposition and generally allowing higher material throughput (Fig. 2.9) [17, 18, 42, 50]. As opposed to conventional gas-stabilized plasma torches, its lower plasma density allows easier penetration of the feedstock into the plasma jet core, even at the very high operating powers of up to 160 kW [19]. Secondly, its consumption of plasma forming gases (e.g. argon at 12 slpm) and water (at 20 ml$\cdot$min^{-1}) is very low compared to hundreds of slpm of plasma-forming gases needed for high-enthalpy gas-stabilized plasma torches. Therefore, significantly lower operating cost can be achieved along with short production times.

As seen from Table 1, the plasma core temperatures reach values up to 16000 K, well above the melting point of any solid material. Plasma spray can therefore be used for spraying of materials unsuitable for other techniques. The relatively low velocities of particles as compared to e.g. HVOF or detonation gun deposition generally result in coatings with higher porosity levels and lower bond strengths [10].

Plasma spray remains the most commonly used method off all the thermal spray processes. Its versatility provides a broad spectrum of usage, e.g. thermal barrier coatings (TBC) of turbine combustion chambers [17, 19, 50, 51], wear resistant Al_2O_3 and Cr_2O_3 coatings on printing rolls designed for subsequent laser and diamond engraving and etching, Mo-alloys coatings on diesel engine pistons, W-based coatings for fusion [52] or biomaterial coatings of hard tissue prostheses [16, 26, 53, 54, 55, 56].

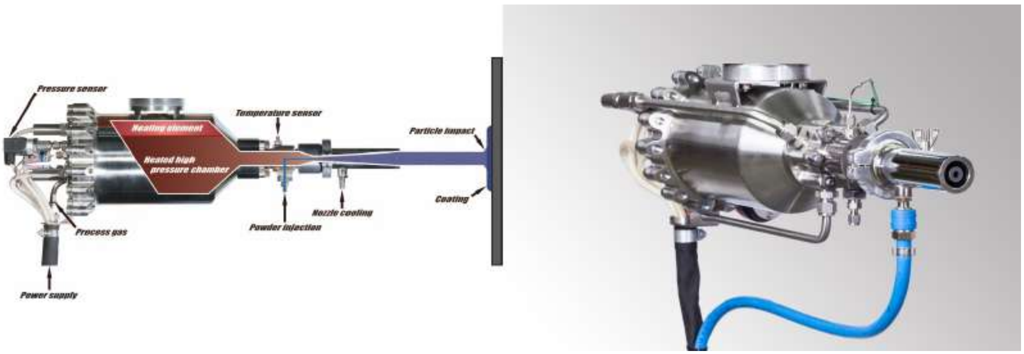

Figure 2.10: Cold kinetic spray process. Schematics of working principles (left) and commercially available torch (right). Both illustrated using 5/11 high pressure system. Images courtesy of Impact Innovations, Germany.

2.3.2 Cold kinetic spray

The innovative low-temperature cold kinetic spray process (cold gas dynamic spray, kinetic spray, CS, CGDS, Fig. 2.10) is regarded as a thermal spray technique [12, 57]. In cold spray, compressed gas such as helium, nitrogen or air is divided into pressure gas section and a powder feeder section. The pressure gas is moderately heated and exits the spray gun via a conical convergent-divergent de Laval nozzle accelerated to supersonic velocities. Feedstock powder is injected axially into the gas flow at the gun nozzle intake and accelerated to velocities of v_p=300–1200 m·s^{-1}.

Contrary to its high-temperature counterparts, cold sprayed coating is not built up by means of melting and solidifying of impinging particles. Solid-state plastic deformation and fusion of particles occurs instead [12, 57, 58]. The bonding of the particles occurs solely when the impact velocities of particles exceed a critical value. This critical velocity depends on the type of material, the powder quality, particle sizes and the particle impact temperature. Particles cold sprayed below the threshold do not deposit but rather rebound from the substrate surface. Too fast particles also do not deposit, they merely act as abrasives, a process similar to grit-blasting [59, 60].

Bonding upon impact in cold spray comprises three different phenomena: metallurgical bonding, mechanical interlocking, and interface intertwining.

- The well-documented metallurgical bonding [61] resulting from a nano-scale chemical reaction at the interface is known to be the dominant mechanism for both inter-particle and coating-substrate bonding. In

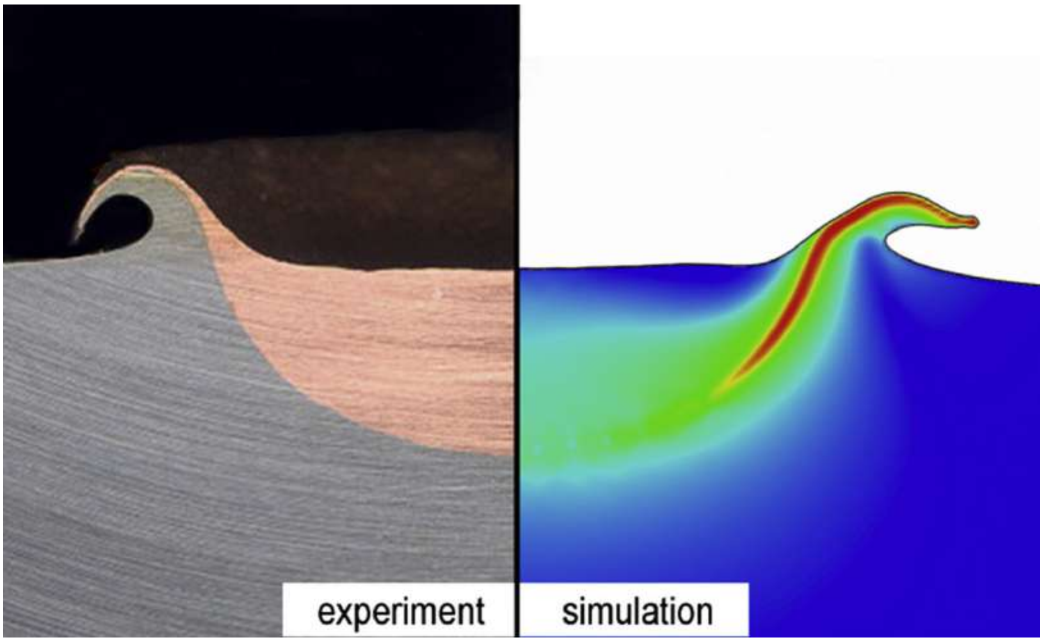

Figure 2.11: Metallurgical bonding in cold kinetic spray process. Illustrated on a macro-scale using for 20-mm Cu ball impacted onto a steel substrate at v_p=750 m·s^{-1} (left) and Eulerian-based FEM simulation of the same (right) [57].

this respect, adiabatic shear instability (ASI) caused by high strain deformation rate [58] and an intimate metal-to-metal contact [62] arising from the impact-induced oxides removal are the prerequisites for the occurrence of such chemical reaction (Fig. 2.11).

- Mechanical interlocking, another important mechanism contributing to the overall coating-substrate adherence is commonly present in cases when the substrate material is softer than the particle material. Non-chemical bonding in its nature, the interlocking is represented by hard particle material being embedded into and trapped by the soft substrate material (Fig. 2.12) [63].

- Apart from the two major mechanisms, another bonding phenomenon in the form of particle elongation, fracture and mutual intertwining at the coating-substrate interface was observed in cases when a large number of particles impact onto sufficiently thin coatings [64, 65]. These are conditions most likely to prevail during cold spraying at low deposition efficiencies. The repetitive impacts of the rebounding particles induce periodical shear stresses that accumulate damage at the coating-substrate interface, which can in turn result in the material fracture and

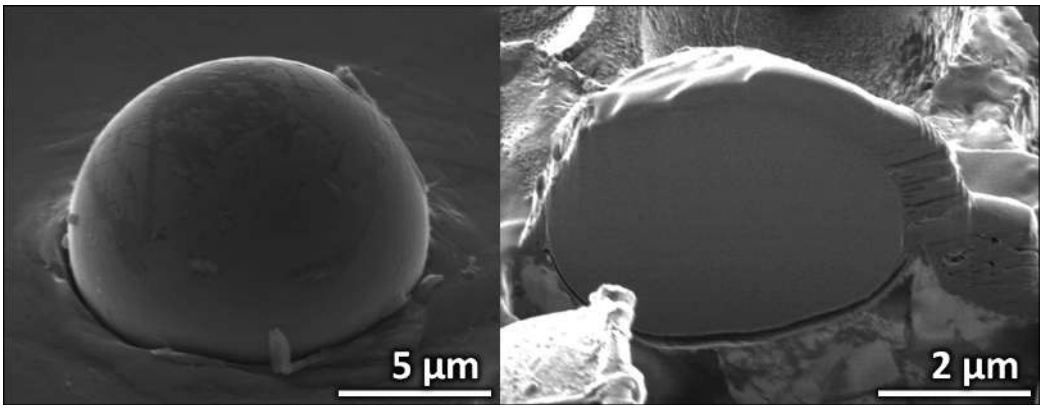

Figure 2.12: Mechanical bonding in cold kinetic spray process. Illustrated on a $Fe_{48}Mo_{14}Cr_{15}Y_2C_{15}B_6$ particle on AISI 4140 steel substrate (left) and its respective FIB cross-section cut (right). Modified from [63].

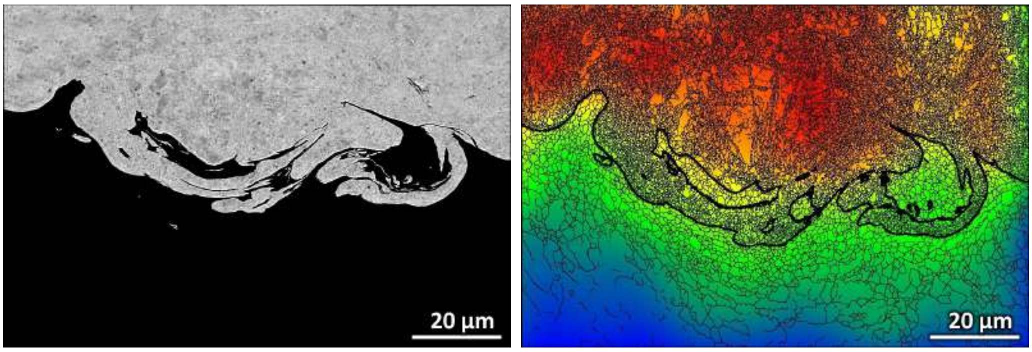

Figure 2.13: Interfacial intertwining phenomenon in cold kinetic spray process. Illustrated on Cu coatings deposited on Al substrates. SEM (left) and EBSD (right) imaging. Own research, in review now [65].

intertwining formation (Fig. 2.13).

The latest of all the processes in thermal spray family, cold spray is the next progressive step in the development of high kinetic energy coating processes. It follows the trend of increasing particle spray velocity and reducing particle temperature [13]. Due to its ambient-temperature character, cold spraying eliminates the detrimental effects of high processing temperatures experienced in other thermal spray techniques [61, 66, 67, 68]. Phase and composition changes as well as chemical decompositions of the original feedstock are negligible, yielding post-spray heat treatments unnecessary. Suppression of material oxidation results in a dramatic increase of thermal and electrical conductivities [61]. The absence of oxides further restrains coating delamination and decohesion and improves the intrinsic bonding strength, resulting in the highest adhesion among thermal spray processes (up to

300 MPa). Increase in amorphous content of original feedstock characteristic for all high-temperature processes is negligible in case of cold spray, as is the thermal load on the materials, thereby effecting eliminating the formation of tensile thermal stresses [68]. Coating hardness is also improved [69]. Other advantages of cold spray technique include reduced material loss by vaporization, low gas entrapment and insignificant grain growth and recrystallization.

A choice of coating materials is limited to ductile materials as hard and brittle materials like ceramics can not be sprayed in a pure form (except few special cases). Substrate materials are also limited to those that can withstand the aggressive action of the sprayed particles (soft or friable substrates will erode rather than being coated) [52]. On the other hand, cold spray allows spraying materials with low decomposition temperatures, unsuitable for high-temperature treatment, such as polymers [70].

High spray rates (up to 10 $\mathrm{kg \cdot hr^{-1}}$) and deposition efficiency (up to 70%) allow fast coating build-ups of about 250 μm per pass. Along with the compressive stresses present in the coatings, cold spray allows deposition of coatings with virtually unlimited thickness. Coupled together with superior machinability [69, 71, 72] and ease of surface finishing of these deposits (cf. frequent cracking and spallation in machining of coatings deposited by other thermal spray methods), cold spray can readily fabricate complex bulk components (Fig. 2.14) or even repair damaged or worn components (Fig. 2.15) at low production costs, ranking it also among additive manufacturing methods [41].

Typical applications of cold spray technology include coatings with increased thermal conductivity, wear [74] and fatigue resistant coatings [68, 75, 76] on biomedical implants, deposition of electrical conductors in electronics industry, corrosion protection coatings with enhanced performance due to low oxide content [69, 77, 78] and deposition onto glass or aluminum and other comparatively low-temperature melting substrate materials to locally increase hardness or wear resistance.

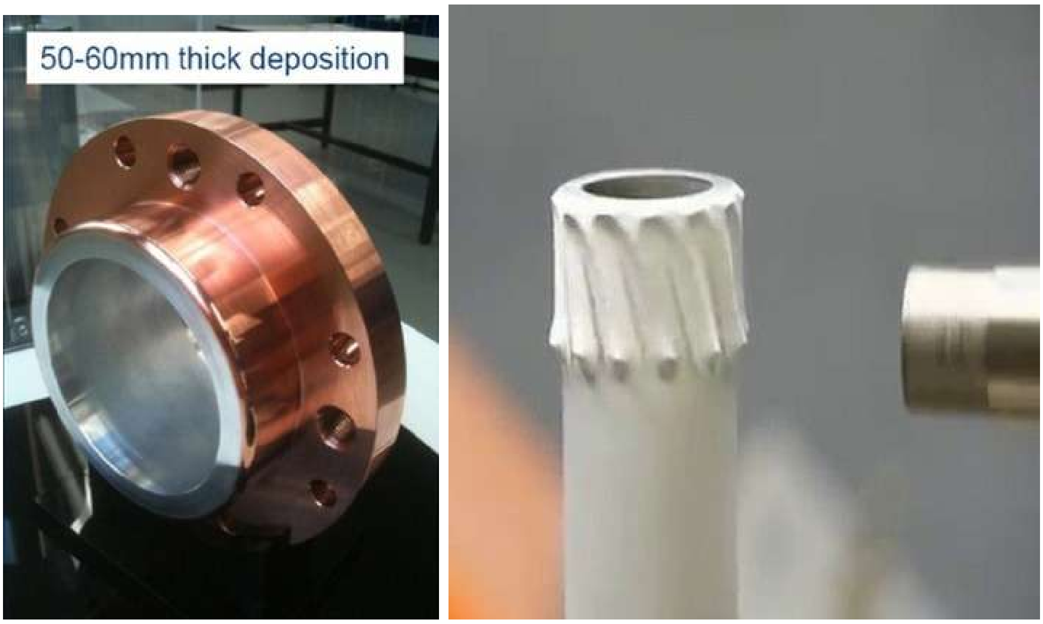

Figure 2.14: Complex 3D components fabricated by cold spraying and milling/tooling. Aluminum-copper composite flange (left) and gear (right). Images courtesy of Plasma Giken, Japan and General Electrics, USA.

Figure 2.15: Restoration of worn or damaged components by cold spray. The speed of cold sprayed coatings build-up and their ease of machining, mechanical strength, and superior adhesion offers significant economical advantage over other restoration processes [73].

Chapter 3

Summary

The properties of traditional (steels or ceramics) and even advanced (metal matrix composites, high-performance plastics, sintered ceramics, superalloys) materials became insufficient to the requirements of current materials engineering lately. Driven by the need for lighter, stronger, stiffer, tougher, fatigue or environment resistant or human tissue compatible materials, the market demands superior, high-performance materials of unique properties tailored for particular uses.

However, a production of materials able to withstand increased mechanical loading, high temperatures, chemical attacks or various degrading environmental factors still remains a challenging topic. The problem becomes even increasingly difficult in case of combination of several concurrent degrading factors (some of the most frequently referred materials degrading factors are summarized for illustration):

- abrasion, wear, erosion or material fatigue (mechanical loading)
- general, pitting, crevice, galvanic or high temperature corrosion, oxidation, de-alloying, aggressive chemical intrusion, stress corrosion cracking (chemical attacks)
- high temperature fatigue, thermal fatigue, creep or thermal shocks (thermal degradation)
- hydrogen embrittlement, radiation, body fluids and tissue activities, aging (environmental factors)

The most susceptible part of virtually any component from the failure point of view is its surface, where majority of the degrading processes are initiated [1, 2]. To suppress the impact of these degradation processes, tailored surface modifications and alterations are often employed, e.g. changing the composition, microstructure or properties of the outermost surface layers by chemical, thermal, mechanical or combined processes. Alternatively, forming a special protective or function-performing coating on the surface of the component can be used. A typical group of methods representing such practice are the thermal spray technologies [10].

As illustrated in this thesis, due to extensive development in the last century, there are around ten TS processes available nowadays, each having its own advantages and drawbacks. Two technologies were presented in more detail: plasma spraying and cold kinetic spraying.

The former method represents a well established technology that has been used for more than sixty years now. Plasma spraying is a versatile process capable of working with high T_m materials such as ceramics or carbides [10, 20]. It offers relatively cheap technological solution and can produce coatings of thicknesses up to several mm on large surface areas. However, it cannot operate with low T_m materials such as plastics and is, unless performed in a controlled atmosphere at increased costs [21], unable to prevent oxidation in case of metallic materials. Frequently, plasma deposition leads to changes in phase composition of the materials too.

The latter method represents a potential successor of plasma spraying in a number of applications. Cold kinetic spraying is a favorable technology when the materials in question are metals [12]. No oxidation, phase or chemical changes, negligible porosity and high adhesion strength of cold sprayed coatings are among its major advantages. Cold spray can also process cermet materials, such as hardmetals [79, 80, 81], and work with polymer deposits or even polymer substrates [70, 82]. Due to the compressive stress nature of the deposits [75, 76], the method allows (only one among the TS group) fabrication of thick coatings that can be turned into bulk 3D components, or restoration and repairs of damaged components, both with very high economical indicators [73]. The limitations of cold spray are materials than cannot readily plastically deform such as ceramics (in fact, there may be a way to overcome this limitation [83, 84, 85]) and spraying onto thin substrates (generally below 0.5 mm) that cannot withstand the aggressive impact of the particles.

References

The following literature sources were used for compilation of chapters 1–3. Journal articles arising from own research of the candidate and colleagues are denoted in red color font.

[1] C.M. Cotell and J.A. Sprague, editors. *ASM Handbook Volume 5: Surface Engineering*. ASM International, 2011.

[2] D.K. Dwivedi. *Surface Engineering*. Springer India, 2018.

[3] I. Tsyganov, M.F. Maitz, and E. Wieser. Blood compatibility of titanium-based coatings prepared by metal plasma immersion ion implantation and deposition. *Appl Surf Sci*, 235(1-2):156–163, 2004.

[4] R. Zenker, G. Sachera, A. Buchwalder, J. Liebich, A. Reiterd, and R. Hasslere. Hybrid technology hard coating electron beam surface hardening. *Surf Coat Technol*, 202(4-7):804–808, 2007.

[5] R. Zenker, A. Buchwalder, K. Ruthrich, W. Griesbach, and K. Nagel. First results of a new duplex surface treatment for cast iron: Electron beam remelting and plasma nitriding. *Surf Coat Technol*, 236:58 – 62, 2013.

[6] J. Cizek and M. Matejkova and J. Kouril and J. Cupera and I. Dlouhy. Potential of new-generation electron beam technology in interface modification of cold and HVOF sprayed MCrAlY bond coats. *Adv Mater Sci Eng*, 2016:1–6, 2016.

[7] P. Gavendova and J. Cizek and J. Cupera. and M. Hasegawa and I. Dlouhy. Microstructure modification of CGDS and HVOF sprayed CoNiCrAlY bond coat remelted by electron beam. *Procedia Mater Sci*, 12:89–94, 2016.

[8] P. Krajnakova and I. Dlouhy and J. Cizek and J. Cupera and R. Shvab. Effect of double electron beam remelting on microstructure of HVOF and CGDS bond coat. *Mater Sci Forum*, 891:574–578, 2017.

[9] D.M. Mattox. *Handbook of Physical Vapor Deposition (PVD) Processing*. Elsevier, 2010.

[10] R.C. Tucker, editor. *ASM Handbook: Thermal Spray Technology*. ASM International, 2013.

[11] Thermal spray coatings market. Technical report, Industry Research, 2019.

[12] A. Papyrin, V. Kosarev, S. Klinkov, A. Alkimov, and V. Fomin. *Cold Spray Technology*. Elsevier, 2007.

[13] S. Kuroda, J. Kawakita, M. Watanabe, and H. Katanoda. Warm spraying - a novel coating process based on high-velocity impact of solid particles. *Sci Technol Adv Mater*, 9:033002, 2008.

[14] S. Hashmi, C.J. van Tyne, G.F. Batalha, and B. Yilbas, editors. *Comprehensive Materials Processing*. Elsevier, 2014.

[15] P. Fauchais, M. Vardelle, S. Goutier, and A. Vardelle. Key challenges and opportunities in suspension and solution plasma spraying. *Plasma Chem. Plasma Process.*, 35(3):511–525, 2014.

[16] J. Cizek and V. Brozek and T. Chraska and F. Lukac and J. Medricky and R. Musalek and T. Tesar and F. Siska and Z. Antos and J. Cupera and M. Matejkova and Z. Spotz and S. Houdkova and M. Kverka. Silver-doped hydroxyapatite coatings deposited by suspension plasma spraying. *J Therm Spray Technol*, 27(8):1333–1343, 2018.

[17] T. Tesar and R. Musalek and F. Lukac and J. Medricky and J. Cizek and V. Rimal and S. Joshi and T. Chraska. Increasing alpha-phase content of alumina-chromia coatings deposited by suspension plasma spraying using hybrid and intermixed concepts. *Surf Coat Technol*, 371:298–311, 2019.

[18] T. Tesar and R. Musalek and J. Medricky and J. Cizek. On growth of suspension plasma-sprayed coatings deposited by high-enthalpy plasma torch. *Surf Coat Technol*, 371:333–343, 2019.

[19] T. Tesar and R. Musalek and F. Lukac and J. Medricky and J. Cizek and S. Csaki and O. Panak and M. Drzkova. Solution precursor plasma spraying of Cr-doped Al2O3 thermochromic coatings. *J Therm Spray Technol*, 29(1-2):199–211, 2020.

[20] P. Fauchais. Understanding plasma spraying. *J Phys D: Appl Phys*, 37(9):R86–R108, 2004.

[21] M.E. Pons. *Developing hydroxyapatite CAPS coatings on metallic implants for tissue replacement.* PhD thesis, Nanyang Technological University, 2004.

[22] J. Cizek and K.A. Khor and Z. Prochazka. Influence of spraying conditions on thermal and velocity properties of plasma sprayed hydroxyapatite. *Mat Sci Eng C - Bio S*, 27(2):340–344, 2007.

[23] J. Cizek and K.A. Khor. Role of in-flight temperature and velocity of powder particles on plasma sprayed hydroxyapatite coating characteristics. *Surf Coat Technol*, 206(8-9):2181–2191, 2012.

[24] J. Cizek and K.A. Khor and I. Dlouhy. In-Flight Temperature and Velocity of Powder Particles of Plasma-Sprayed TiO2. *J Therm Spray Technol*, 22(8):1320–1327, 2013.

[25] J. Cizek and I. Dlouhy and F. Siska and K.A. Khor. Modification of Plasma-sprayed TiO2 Coatings Characteristics via Controlling the In-flight Temperature and Velocity of the Powder Particles. *J Therm Spray Technol*, 23(8):1339–1349, 2014.

[26] J. Cizek and O. Kovarik and F. Siska and J. Bensch and J. Cupera and M. Matejkova and J. Siegl and T. Chraska and K. A. Khor. Increasing fatigue endurance of hydroxyapatite and rutile plasma sprayed biocomponents by controlling deposition in-flight properties. *ACS Biomater Sci Eng*, 5(4):1703–1714, 2019.

[27] N.W. Khun and Z. Li and K.A. Khor and J. Cizek. Higher in-flight particle velocities enhance in vitro tribological behavior of plasma sprayed hydroxyapatite coatings. *Tribol. Int.*, 103:496–503, 2016.

[28] J. Siegl and J. Bensch and J. Cizek and K.A. Khor. Influence of spraying conditions on fatigue behaviour of hydroxyapatite coatings. *Acta Technica CSAV*, 52(3):205–215, 2007.

[29] R. Ahmed and N.H. Faisal and S.M. Knupfer and A.M. Paradowska and M.E. Fitzpatrick and K.A. Khor and J. Cizek. Neutron diffraction residual strain measurements in plasma sprayed nanostructured hydroxyapatite coatings for orthopaedic implants. *Mater Sci Forum*, 652:309–314, 2010.

[30] H. Li, K.A. Khor, and P. Cheang. Thermal sprayed hydroxyapatite splats: nanostructures, pore formation mechanisms and TEM characterization. *Biomaterials*, 25(17):3463–3471, 2004.

[31] P. Fauchais, M. Fukumoto, A. Vardelle, and M. Vardelle. Knowledge concerning splay formation: an invited review. *J Therm Spray Technol*, 13(3):337–360, 2004.

[32] M. Vardelle, A. Vardelle, and P. Fauchais. Spray parameters and particle behavior relationships during plasma spraying. *J Therm Spray Technol*, 2(1):79–91, 1993.

[33] Z. Prochazka and K.A. Khor and J. Cizek. Influence of input parameters on splat formation and coating thermal diffusivity in plasma spraying. *Adv Eng Mater*, 8(7):645–650, 2006.

[34] R. Ghelichi, D. MacDonald, S. Bagherifard, H. Jahed, M. Guagliano, and B. Jodoin. Microstructure and fatigue behavior of cold spray coated Al5052. *Acta Mater*, 60(19):6555–6561, 2012.

[35] T. Samson, D. MacDonald, R. Fernandez, and B. Jodoin. Effect of pulsed waterjet surface preparation on the adhesion strength of cold gas dynamic sprayed aluminum coatings. *J Therm Spray Technol*, 24(6):984–993, 2015.

[36] B. Song, S. Dong, B. Hansz, H. Liao, and C. Coddet. Effect of dry-ice blasting on structure and magnetic properties of plasma-sprayed Fe-40Al coating from nanostructured powders. *J Therm Spray Technol*, 23(1-2):227–235, 2013.

[37] W.R. Chen, X. Wu, B.R. Marple, D.R. Nagy, and P.C. Patnaik. TGO growth behaviour in TBCs with APS and HVOF bond coats. *Surf Coat Technol*, 202(12):2677 – 2683, 2008.

[38] Y. Tanaka and M. Fukumoto. Investigation of dominating factors on flattening behavior of plasma sprayed ceramic particles. *Surf Coat Technol*, 120-121:124–130, 1999.

[39] M. Fukumoto, H. Nagai, and T. Yasui. Influence of surface character change of substrate due to heating on flattening behavior of thermal sprayed particles. *J Therm Spray Technol*, 15(4):759–764, 2006.

[40] K. Neufuss, P. Chraska, B. Kolman, S. Sampath, and Z. Travnicek. Properties of plasma-sprayed freestanding ceramic parts. *J Therm Spray Technol*, 6(4):434–438, 1997.

[41] S. Yin and J. Cizek and X. Yan and R. Lupoi. Annealing strategies for enhancing mechanical properties of additively manufactured 316L stainless steel deposited by cold spray. *Surf Coat Technol*, 370:353–361, 2019.

[42] P. Ctibor and B. Nevrla and J. Cizek and F. Lukac. Strontium zirconate TBC sprayed by a high feed-rate water-stabilized plasma torch. *J Therm Spray Technol*, 26(8):1804–1809, 2017.

[43] R. Musalek, O. Kovarik, J. Medricky, N. Curry, S. Bjorklund, and P. Nylen. Fatigue testing of TBC on structural steel by cyclic bending. *J Therm Spray Technol*, 24(1-2):168–174, 2015.

[44] Y. Huang, L. Song, X. Liu, Y. Xiao, Y. Wu, J. Chen, F. Wu, and Z. Gu. Hydroxyapatite coatings deposited by liquid precursor plasma spraying: controlled dense and porous microstructures and osteoblastic cell responses. *Biofabrication*, 2(4):045003, 2010.

[45] S.A. Bortz and E.J. Onesto. Flame and plasma sprayed ceramics for uses in biomedical applications. *Composites*, 5(4):151–156, 1974.

[46] L. Altomare, D. Bellucci, G. Bolelli, B. Bonferroni, V. Cannillo, L. De Nardo, R. Gadow, A. Killinger, L. Lusvarghi, A. Sola, and N. Stiegler. Microstructure and in vitro behaviour of 45S5 bioglass coatings deposited by high velocity suspension flame spraying (HVSFS). *J Mater Sci Mater Med*, 22(5):1303–1319, 2011.

[47] P.L. Ke, Y.N. Wu, Q.M. Wang, J. Gong, C. Sun, and L.S. Wen. Study on thermal barrier coatings deposited by detonation gun spraying. *Surf Coat Technol*, 200(7):2271–2276, 2005.

[48] R. S. Lima and B. R. Marple. Optimized HVOF titania coatings. *J Therm Spray Technol*, 12(3):360–369, 2003.

[49] P. Richer, M. Yandouzi, L. Beauvais, and B. Jodoin. Oxidation behaviour of CoNiCrAlY bond coats produced by plasma, HVOF and cold gas dynamic spraying. *Surf Coat Technol*, 204(24):3962 – 3974, 2010.

[50] J. Medricky and F. Lukac and S. Csaki and S. Houdkova and M. Barbosa and T. Tesar and J. Cizek and R. Musalek and O. Kovarik and T. Chraska. Improvement of mechanical properties of plasma sprayed Al2O3-ZrO2-SiO2 amorphous coatings by surface crystallization. *Materials*, 12(19):3232, 2019.

[51] O. Kovarik and A. Materna and J. Siegl and J. Cizek and J. Klecka. Fatigue crack growth in plasma-sprayed refractory materials. *J Therm Spray Technol*, 28(1-2):87–97, 2018.

[52] J. Cizek and J. Klecka. Harnessing fusion power: W and W-Cr armor coatings for plasma-facing components in tokamaks. *Adv Mater Process*, 177(5):46–49, 2019.

[53] J.L. Xu and D. Joguet and J. Cizek and K.A. Khor and H.L. Liao and C. Coddet and W.N. Chen. Synthesis and characterization on atomphospheric plasma sprayed amorphous silica doped hydrxoyapatite coatings. *Surf Coat Technol*, 206(22):4659–4665, 2012.

[54] J. Cizek and J. Matejicek. Medicine meets thermal spray technology: a review of patents. *J Therm Spray Technol*, 27(8):1251–1279, 2018.

[55] B. Zheng, Y. Luo, H. Liao, and C. Zhang. Investigation of the crystallinity of suspension plasma sprayed hydroxyapatite coatings. *J. Eur. Ceram. Soc.*, 37(15):5017–5021, 2017.

[56] X. Zhang, W. Chaimayo, C. Yang, J. Yao, B.L. Miller, and M.Z. Yates. Silver-hydroxyapatite composite coatings with enhanced antimicrobial activities through heat treatment. *Surf Coat Technol*, 325:39–45, 2017.

[57] H. Assadi, H. Kreye, F. Gartner, and T. Klassen. Cold spraying - a materials perspective. *Acta Mater*, 116:382–407, 2016.

[58] H. Assadi, F. Gartner, T. Stoltenhoff, and H. Kreye. Bonding mechanism in cold gas spraying. *Acta Mater*, 51(15):4379–4394, 2003.

[59] T. Klassen, F. Gartner, T. Schmidt, J.O. Kliemann, K. Onizawa, K.R. Donner, H. Gutzmann, K. Binder, and H. Kreye. Basic principles and application potentials of cold gas spraying. *Materialwiss Werkst*, 41(7):575–584, 2010.

[60] T. Schmidt, H. Assadi, F. Gartner, H. Richter, T. Stoltenhoff, H. Kreye, and T. Klassen. From particle acceleration to impact and bonding in cold spraying. *J Therm Spray Technol*, 18(5-6):794–808, 2009.

[61] S. Yin and J. Cizek and C. Chen and R. Jenkins and G. O'Donnell and R. Lupoi. Metallurgical bonding between metal matrix and core-shelled reinforcements in cold sprayed composite coating. *Scr Mater*, 177:49–53, 2020.

[62] Y. Ichikawa, R. Tokoro, M. Tanno, and K. Ogawa. Elucidation of cold-spray deposition mechanism by auger electron spectroscopic evaluation of bonding interface oxide film. *Acta Mater*, 164:39–49, 2019.

[63] C.W. Ziemian, W.J. Wright, and D.E. Cipoletti. Influence of impact conditions on feedstock deposition behavior of cold-sprayed fe-based metallic glass. *J Therm Spray Technol*, 27(5):843–856, 2018.

[64] Y. Xie and S. Yin and J. Cizek and J. Cupera and E. Guo and R. Lupoi. Formation mechanism and microstructure characterization of nickel-aluminum intertwining interface in cold spray. *Surf Coat Technol*, 337:447–452, 2018.

[65] S. Yin and J. Cizek and J. Cupera and M. Hassani and R. Jenkins and X. Luo and Y. Xie and W. Li and R. Lupoi. Formation mechanisms of intertwined cold spray coating-substrate interfaces. *Acta Mater*, 2020, in review process.

[66] H. Seiner and J. Cizek and P. Sedlak and R. Huang and J. Cupera and I. Dlouhy and M. Landa. Elastic moduli and elastic anisotropy of cold sprayed metallic coatings. *Surf Coat Technol*, 291:342–347, 2016.

[67] M. Janovska and H. Seiner and J. Cizek and P. Sedlak and M. Landa. Evolution of elastic properties of cold sprayed metal coatings at elevated temperatures. *Acta Phys Pol A*, 134(3):794–798, 2018.

[68] O. Kovarik and J. Siegl and J. Cizek and T. Chraska and J. Kondas. Fracture toughness of cold sprayed pure metals. *J Therm Spray Technol*, 29(1-2):147–157, 2020.

[69] J. Cizek and M. Vilemova and F. Lukac and M. Koller and J. Kondas and R. Singh. Cold sprayed tungsten armor for tokamak first wall. *Coatings*, 9(12):836, 2019.

[70] R. Lupoi and W. O'Neill. Deposition of metallic coatings on polymer surfaces using cold spray. *Surf Coat Technol*, 205(7):2167–2173, 2010.

[71] I. Dlouhy and L. Rehorek and H. Seiner and J. Cizek and F. Siska. Architectured multi-metallic structures prepared by cold dynamic spray deposition. *Key Eng Mater*, 810:107–112, 2019.

[72] F. Siska and J. Cizek and H. Seiner and I. Dlouhy. Numerical analysis of geometrically induced hardening in planar architectured materials. *Compos Struct*, 233:111633, 2020.

[73] S. Yin, P. Cavaliere, B. Aldwell, R. Jenkins, H. Liao, W. Li, and R. Lupoi. Cold spray additive manufacturing and repair: Fundamentals and applications. *Addit Manuf*, 21:628–650, 2018.

[74] S. Yin and Y. Xie and J. Cizek and E.J. Ekoi and T. Hussain and D.P. Dowling and R. Lupoi. Advanced diamond-reinforced metal matrix composites via cold spray: properties and deposition mechanism. *Compos Part B Eng*, 113:44–54, 2017.

[75] J. Cizek and O. Kovarik and J. Siegl and K.A. Khor and I. Dlouhy. Influence of plasma and cold spray deposited Ti Layers on high-cycle fatigue properties of Ti6Al4V substrates. *Surf Coat Technol*, 217:23–33, 2013.

[76] J. Cizek and M. Matejkova and I. Dlouhy and F. Siska and C.M. Kay and J. Karthikeyan and S. Kuroda and O. Kovarik and J. Siegl and K. Loke and K.A. Khor. Influence of Cold Sprayed, Warm Sprayed and Plasma Sprayed Layers Deposition on Fatigue Properties of Steel Specimens. *J Therm Spray Technol*, 24(5):758–768, 2015.

[77] J. Cizek and O. Man and P. Roupcova and K. Loke and I. Dlouhy. Oxidation performance of cold spray Ti-Al barrier coated gamma-TiAl intermetallic substrates. *Surf Coat Technol*, 268:85 – 89, 2015.

[78] J. Vit and J. Cupera and J. Cizek. On the search for producing intermetallics by diffusion reaction of cold spray bulk deposits. *Surf Coat Technol*, 268:216 – 223, 2015.

[79] S.M. Ang, C.C. Berndt, and P. Cheang. Deposition effects of WC particle size on cold sprayed WC-Co coatings. *Surf Coat Technol*, 205(10):3260–3267, 2011.

[80] S. Yin, E.J. Ekoi, T.L. Lupton, D.P. Dowling, and R. Lupoi. Cold spraying of WC-Co-Ni coatings using porous WC-17Co powders: Formation mechanism, microstructure characterization and tribological performance. *Mater Design*, 126:305–313, 2017.

[81] R.S Lima, J. Karthikeyan, C.M Kay, J. Lindemann, and C.C. Berndt. Microstructural characteristics of cold-sprayed nanostructured WC-Co coatings. *Thin Solid Films*, 416(1-2):129–135, 2002.

[82] K. Ravi, Y. Ichikawa, T. Deplancke, K. Ogawa, O. Lame, and J.Y. Cavaille. Development of ultra-high molecular weight polyethylene (UHMWPE) coating by cold spray technique. *J Therm Spray Technol*, 24(6):1015–1025, 2015.

[83] M. Yamada, H. Isago, K. Shima, H. Nakano, and M. Fukumoto. Deposition of TiO2 ceramic particles on cold spray process. In *Proc. International Thermal Spray Conference*, pages 187–191. DVS-ASM, 2010.

[84] T.N. Salim, M. Yamada, H. Nakano, K. Shima, H. Isago, and M. Fukumoto. The effect of post-treatments on the powder morphology of titanium dioxide (TiO2) powders synthesized for cold spray. *Surf Coat Technol*, 206(2-3):366–371, 2011.

[85] M.E. Dickinson and M. Yamada. A new method for measuring shear adhesion strength of ceramic cold spray splats. *NNL*, 2(4):348–351, 2010.

Chapter 4

Selected papers

Aside from frequent conference talks, the contribution of the candidate to the worldwide R&D in both plasma spraying and cold kinetic spraying covers 36 papers (out of 50 materials science-related) in recognized, international impacted journals. Of these, eight papers are selected and presented in this thesis (arranged by year of publication) to illustrate the advancement in the field contributed within the work of the candidate and his colleagues.

Four of these papers relate to plasma spraying and four to cold spraying. A short explanation on the reason for selection and the importance of each of the papers follows herein.

Plasma spraying:

1. **N.W. Khun, Z. Li, K.A. Khor, J. Cizek**
   Higher in-flight particle velocities enhance in vitro tribological behavior of plasma sprayed hydroxyapatite coatings
   Tribol Int, 2016, 103, 496–503

   The paper showed that under certain spray parameters, the bioactive coatings can be tailored to exhibit significantly improved in-vitro tribological performance, a property desirable especially in hard tissue implants such as joints.

2. **J. Cizek, J. Matejicek**
   Medicine meets thermal spray technology: a review of patents
   J Therm Spray Technol, 2018, 27 (8), 1251–1279

   Selected as article of the year 2018 by Journal of Thermal Spray Technology editors. An invited review paper presenting a comprehensive overview of patented components, ideas and technological procedures related to thermal spraying for bioapplications.

3. **J. Cizek, V. Brozek, T. Chraska, F. Lukac, J. Medricky, R. Musalek, T. Tesar, F. Siska, Z. Antos, M. Matejkova, Z. Spotz, S. Houdkova, M. Kverka**
   Silver-doped hydroxyapatite coatings deposited by suspension plasma spraying
   J Therm Spray Technol, 2018, 27 (8), 1333–1343

   For the first time in history, bioactive hydroxyapatite coatings with dispersion of antibacterial Ag nanoparticles were produced from liquid feedstock.

4. **J. Cizek, O. Kovarik, F. Siska, J. Bensch, J. Cupera, M. Matejkova, J. Siegl, T. Chraska, K.A. Khor**
   Increasing fatigue endurance of hydroxyapatite and rutile plasma sprayed biocomponents by controlling deposition in-flight properties
   ACS Biomater Sci Eng, 2019, 5 (4), 1703–1714

   The paper showed that fatigue properties of components with bioactive hydroxyapatite and TiO_2 coatings can be significantly improved (up to +46%) by controlling the in-flight properties. Importantly, this can be achieved without any compromise in either the coatings microstructure or phase composition.

Cold kinetic spraying:

1. **H. Seiner, J. Cizek, P. Sedlak, R. Huang, J. Cupera, I. Dlouhy, M. Landa**
   Elastic moduli and elastic anisotropy of cold sprayed metallic coatings
   Surf Coat Technol, 2016, 291, 342–347

   Contrary to general understanding of the cold spray community at that time, this paper showed that the cold sprayed coatings behave isotropically in the elastic deformation range.

2. **S. Yin, Y. Xie, J. Cizek, E. Ekoi, T. Hussain, D. Dowling, R. Lupoi**
   Advanced diamond-reinforced metal matrix composites via cold spray: properties and deposition mechanism
   Compos Part B-Eng, 2017, 113, 44–54

   The first successful deposition of thick (copper-clad) diamond coatings by cold spray. Their wear properties were shown to be excellent, superior even to the WC-Co pin counterpart that was used in the testing.

3. **Y. Xie, S. Yin, J. Cizek, J. Cupera, E. Guo, R. Lupoi**
   Formation mechanism and microstructure characterization of nickel-aluminum intertwining interface in cold spray
   Surf Coat Technol, 2018, 337, 447–452

   For the first time, the intertwining phenomenon occurring at the interface under certain conditions in cold spray was investigated and explained. This is a major finding for the CS community and an expanded and more detailed study was carried out and is now reviewed in Acta Mater journal.

4. **J. Cizek, M. Vilemova, F. Lukac, M. Koller, J. Kondas, R. Singh**
   Cold sprayed tungsten armor for tokamak first wall
   Coatings, 2019, 9 (12), 836

   For the first time in history, thick tungsten coatings (previously deemed unsprayable) were successfully deposited using cold spray. This breakthrough discovery may be very significant for nuclear fission industry.

Tribology International 103 (2016) 496–503

Contents lists available at ScienceDirect

Tribology International

journal homepage: www.elsevier.com/locate/triboint

Higher in-flight particle velocities enhance in vitro tribological behavior of plasma sprayed hydroxyapatite coatings

N.W. Khun [a], Z. Li [a], K.A. Khor [a], J. Cizek [b],*

[a] School of Mechanical and Aerospace Engineering, Nanyang Technological University, 50 Nanyang Avenue, 639798, Singapore
[b] Netme Centre, Institute of Materials Science and Engineering, Brno University of Technology, Technicka 2896/2, 61669 Brno, Czech Republic

ARTICLE INFO

Article history:
Received 8 March 2016
Received in revised form
27 July 2016
Accepted 5 August 2016
Available online 6 August 2016

Keywords:
HA coating
Thermal spraying
Bio-tribology
Hanks' solution
Friction
Wear

ABSTRACT

Hydroxyapatite (HA) coatings were deposited onto Ti6Al4V substrates via atmospheric plasma spraying under systematically varying spray parameters, leading to different in-flight particle velocities. Morphology, composition, and tribological properties of the coatings were then studied. The coatings deposited at higher in-flight particle velocities exhibited smoother surface topography, better inter-particle bonding and higher Young's modulus and hardness. Ball-on-disc tribological results showed that the friction and wear of the HA coatings significantly decreased with increased in-flight particle velocity under both dry and wet (Hanks' solution) conditions. All HA coatings exhibited lower friction and wear during the wet sliding due to the lubricating effect of the solution.

© 2016 Elsevier Ltd. All rights reserved.

1. Introduction

As one of the most widely used bioceramics, hydroxyapatite (HA) has been traditionally utilized in orthopedic applications due to its excellent biocompatibility and bioactivity [1]. However, mechanical properties of HA are insufficient for major load-bearing applications. Deposition of HA coatings onto metallic substrates such as Ti and Ti-alloys is therefore carried out to overcome such issues [2]. It was reported that bioactive HA coatings on metallic implants could (1) promote earlier stabilization of the implants in the surrounding bone, (2) support bone in-growth and improve the implant-bone bonding strength, (3) decrease the release of metallic ions from the implants, thereby reducing possible toxicity in the vascular system and subsequent health hazards, and (4) shield the prosthesis implants from environmental attacks to facilitate long-term performance, therefore lowering the risk of their failure and extend their functional life [3,4]. However, when implanted *in vivo*, the repetitive loading and rubbing contact with counter materials or surrounding tissue experienced by the coatings can result in easy removal of materials and release of debris, thereby jeopardizing the mechanical and biological performance, which in turn may lead to an early failure of the whole structure in service. Therefore, investigation into the tribological behavior of HA coatings has emerged as an important issue in both the research filed and clinical applications [5,6]. In order to improve the wear resistance and other properties of HA coatings, it is of special importance to optimize the fabrication process used for HA coating deposition [4].

Plasma spray processes have been widely used for various industrial applications due to their versatility, high deposition rates and a wide range of applicable materials [4]. Although the processes are presently used to deposit protective and biocompatible HA coatings on Ti and Ti-alloy substrates, numerous issues such as insufficient coating adhesion, coating fracture, and thermal shock to the substrate materials are still reported [4,7]. The issues have been addressed individually by focusing on various aspects of the plasma spray process [7]. One of such aspects is the in-flight properties (such as temperature and velocity) that the sprayed material particles attain within the plasma jet. It has been shown that such factors significantly influence the structure, density, and the coating-substrate bonding strength [4,8–10].

The previous studies of plasma sprayed HA coatings have aimed at physical, mechanical and chemical properties [4,8,11]. Tribological properties of such HA coatings deposited on metallic substrates have been less reported. Fu et al. [12] investigated fretting wear of thermally sprayed HA coatings under dry conditions and found that the HA coatings had poor resistance to wear. Dey and co-workers [5] developed microplasma sprayed HA coatings with poor scratch and wear resistance.

Hanks' solution has physiological pH and salt concentration and is thus widely used in cell culture as a buffer system. It can further be used to simulate body fluid conditions to study the bio-

---

* Corresponding author.
E-mail address: cizek@fme.vutbr.cz (J. Cizek).

http://dx.doi.org/10.1016/j.triboint.2016.08.006
0301-679X/© 2016 Elsevier Ltd. All rights reserved.

tribological properties of thermally sprayed coatings under physiological conditions. Although the morphological and structural changes associated with dissolution of plasma sprayed HA coating in Hanks' solution have been studied widely, the effect of Hanks' solution (or other physiological media) on the tribological behavior of HA coatings has been much less studied [13–16].

In this study, four different HA coatings were deposited onto commercially available Ti6Al4V substrates via plasma spray process by systematically varying the in-flight particle velocities. The coatings tribological properties with and without Hanks' solution were systematically investigated using ball-on-disc micro-tribological test.

2. Experimental details

2.1. Sample preparation

In-house fabricated spray-dried HA powders with diameters of 39.9 ± 10.6 μm were used as the feedstock. The details of the HA powder preparation were reported in our previous studies [4,8]. For the substrates, commercially available Ti6Al4V alloy (99.9% purity, Titan Engineering, Singapore) were cut to 10 mm × 10 mm × 2 mm coupons. An atmospheric plasma system (Praxair Inc., Danbury, USA) equipped with SG-100 gun was employed to deposit the HA coatings. Purified argon was used as the main arc forming gas and carrier gas, while helium was used as an auxiliary enthalpy gas. In total, four runs with different system parameters were carried out to produce coatings under different in-flight properties (from [8]). Annotation of the four samples (HA1 to HA4) is provided in Table 1 along with the corresponding values of the system parameters. The selection of the process parameters was based on prior work reported in [4,16]. During the spraying, the in-flight particle properties (temperature and velocity) were measured with a fast-shutter CCD laser-assisted camera (Oseir Ltd., Tampere, Finland). The measured values are further provided in Table 1.

2.2. Characterization

The surface morphology and topography of the coatings were studied using SEM (JEOL-JSM-5600LV, Japan) and surface profilometry (Talyscan 150 with 4 μm diameter diamond stylus, Taylor Hobson, UK). Three measurements per sample were carried out to obtain the average root-mean-squared surface roughness (R_q). To evaluate the coatings microstructure, sample cross-sections were ground using 800, 1200, 2400 and 4000 grit SiC papers and polished to 1 μm surface finish with diamond paste. The phase composition of the coatings was examined using an X-ray diffractometer (Philips MPD 1880, PANalytical, the Netherlands) with Cu K_α radiation at 40 kV and 30 mA and the chemical composition was studied using energy-dispersive X-ray spectroscopy (EDX, Model 6647, Oxford Instruments, UK).

Nanoindentation has been proved to be a powerful method to measure the mechanical properties of thermally sprayed ceramic coatings, and has the capability to probe individual splats inside the coating [17]. Young's modulus (E) and hardness (H) were measured by nanoindentation (Agilent G200, Keysight Technologies, USA) on the polished cross section of the coatings. The continuous stiffness measurement technique was used, with the strain rate target and depth limit being 0.05 s^{-1} and 2000 nm, respectively. In total 20 indentations were made on each sample to obtain the average E and H values. The tribological properties of the samples were investigated using ball-on-disc micro-tribological test (CSM High Temperature Tribometer, CSM Instruments SA, Switzerland). The samples were tested against 100Cr6 steel balls ($R_q = 0.032$ μm, $H = 7.5$ GPa) of 6 mm in diameter in a circular path of 1 mm in radius for 40,000 laps at a sliding speed of 2 cm/s under a normal load of 3 N at room temperature (22–24 °C). In order to eliminate the influence of the substrate during the tribological testing, the coatings were deposited so that the thickness exceeded 300 μm [18]. The samples were tested in both air and Hanks' solution (H9269, Sigma-Aldrich, Singapore). Three measurements per sample were carried out to obtain the average friction coefficient. Considering the difficulty in measuring the wear depth due to the relatively high surface roughness of the coatings, the wear width was used as the major index to assess the wear resistance of the different HA coatings in this study. The width of the wear tracks was measured by surface profilometry. Wear morphology of the steel balls rubbed against the HA coatings under dry conditions was observed by light microscopy (Zeiss Axioskop 2 with JVC Color Video Camera, Carl Zeiss, Germany). Due to extensive corrosion, the wear morphology of the steel balls tested under wet conditions is not included in the paper due to low information yield.

3. Results and discussion

3.1. Coating properties

As determined by Rietveld analysis of the obtained XRD patterns, the dominant phase in the produced powder is HA [4,19]. A 5% $CaCO_3$ content was detected; this could have originated from a reaction of the original $Ca(OH)_2$ with atmospheric CO_2 during the powder production [4]. After the plasma spray process, the produced coatings mainly consisted of HA, with varying content of metastable tri-calcium and tetra-calcium phosphate phases (α-TCP, β-TCP, TTCP), as reported earlier in [4].

The surface topography of the as-sprayed HA coatings is presented in Figs. 1 and 2. The R_q values of the as-sprayed coatings are summarized in Table 2. It was found that the HA1 coatings exhibited a relatively rough surface topography with a number of protruded particles above the surface, yielding the highest R_q value. The existence of such particles can probably be attributed to the small degree of deformation of the HA particles at a low in-flight velocity, as can be observed in Fig. 2. The HA2 coatings exhibited smaller R_q due to a significantly smaller number of the protruded particles (Fig. 1). Presumably, the decline in the protrusions' quantity was triggered by the higher impact energy of the HA particles via increasing the in-flight particle velocity (to ~204m/s). This was confirmed via SEM as increased HA particles

Table 1
Plasma spray process parameters used for deposition of different HA coatings.

Set annotation	Net power [kW]	Main gas [L/min]	Auxiliary gas [L/min]	Feed rate [rpm]	Carrier gas [L/min]	Spray distance [mm]	Temperature [K]	Velocity [m/s]
HA1	7	20	10	2	3	75	2540	175
HA2	7	34	24	3	5	100	2513	204
HA3	11	48	38	2	3	100	2500	243
HA4	11	34	24	4	7	75	2470	275

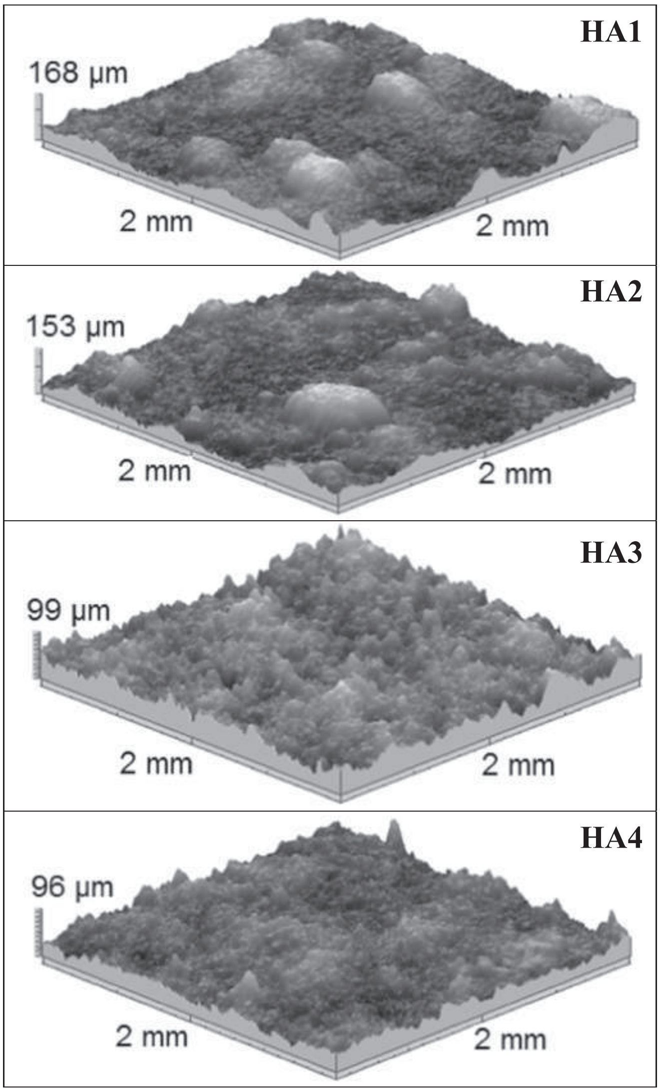

Fig. 1. Surface topography of as-sprayed HA coatings.

flattening was observed in the HA2 coatings (Fig. 2). No large protruded particles could be seen in the surface topography (Fig. 1) images of the HA3 and HA4 coatings, leading to a further decrease in the R_q values. The HA4 coating exhibited the smoothest surface topography and lowest R_q value probably due to the highest compaction of the surface via the highest in-flight particle velocity (275m/s).

Fig. 3 presents the cross-sectional morphology and microstructure of the HA coatings. The highest number of inter-particle gaps was found in the HA1 coating, probably due to the weak inter-particle bonding in the coating as it was deposited at the lowest in-flight particle velocity [5,12]. Additionally, compared with the other three coatings, HA1 coating showed the smallest amount of particle deformation, with some HA particles still retaining their spherical shape. As the in-flight particle velocity increased in HA2–4, the inter-particle gaps were significantly reduced (Fig. 3), implying stronger inter-particle bonding in those coatings. While large pores (~50µm or above) could be observed in the HA2 coating, they were absent on the cross-section of the HA3 and HA4 coatings. This further proves that higher in-flight particle velocity resulted in denser microstructure of the coatings. The results signify that the in-flight particle velocity is an important factor in controlling the microstructure, and thereby possibly influencing the wear resistance of the plasma sprayed HA coatings.

It can be seen in Fig. 4 that the *E* and *H* of the coatings generally increased with the in-flight particle velocity. The respective values

Table 2
Surface roughness (R_q) and wear properties of different HA coatings.

Sample	R_q [µm]	Friction coefficient		Wear width [µm]	
		Without Hanks' solution	With Hanks' solution	Without Hanks' solution	With Hanks' solution
HA1	18.7 ± 1.4	0.79 ± 0.03	0.61 ± 0.01	1267.5 ± 105.6	756.3 ± 42.7
HA2	12.6 ± 1.9	0.67 ± 0.02	0.51 ± 0.12	747.8 ± 106.6	576.7 ± 25.1
HA3	11.0 ± 0.1	0.63 ± 0.06	0.44 ± 0.06	583.5 ± 44.5	402.3 ± 29.7
HA4	8.8 ± 0.2	0.61 ± 0.08	0.32 ± 0.06	337.5 ± 44.0	260.7 ± 8.1

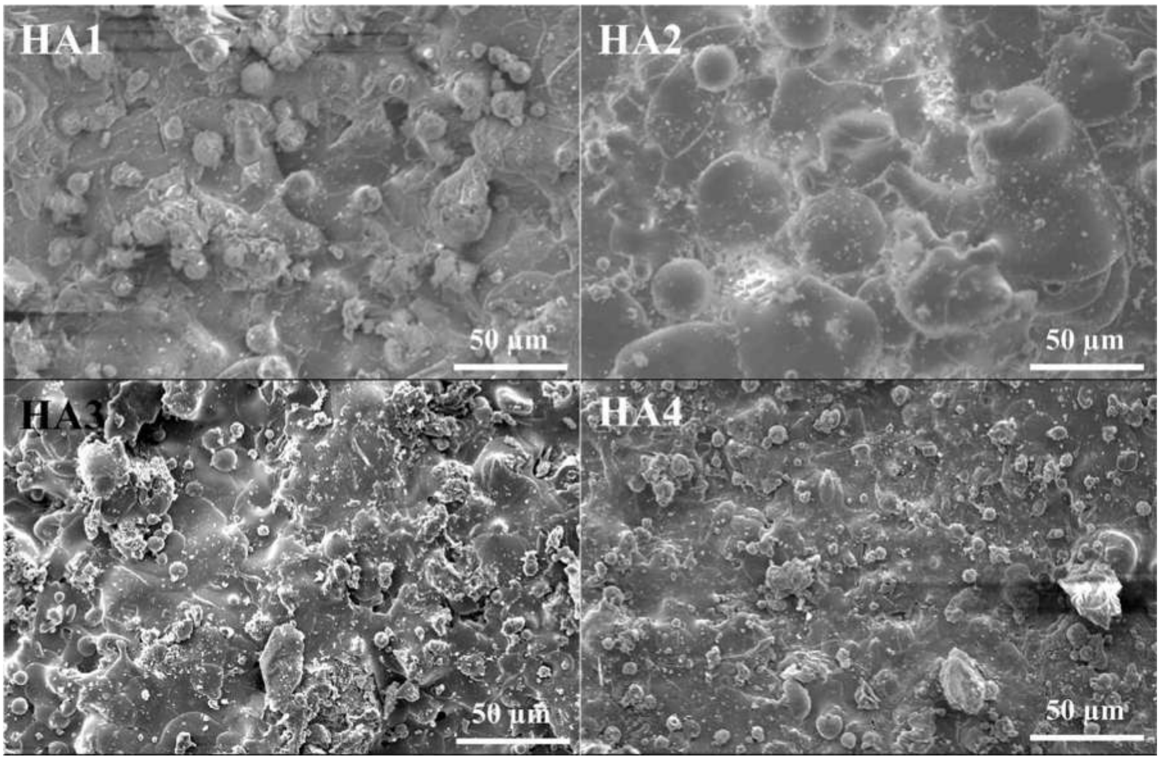

Fig. 2. Surface morphology of as-sprayed HA coatings.

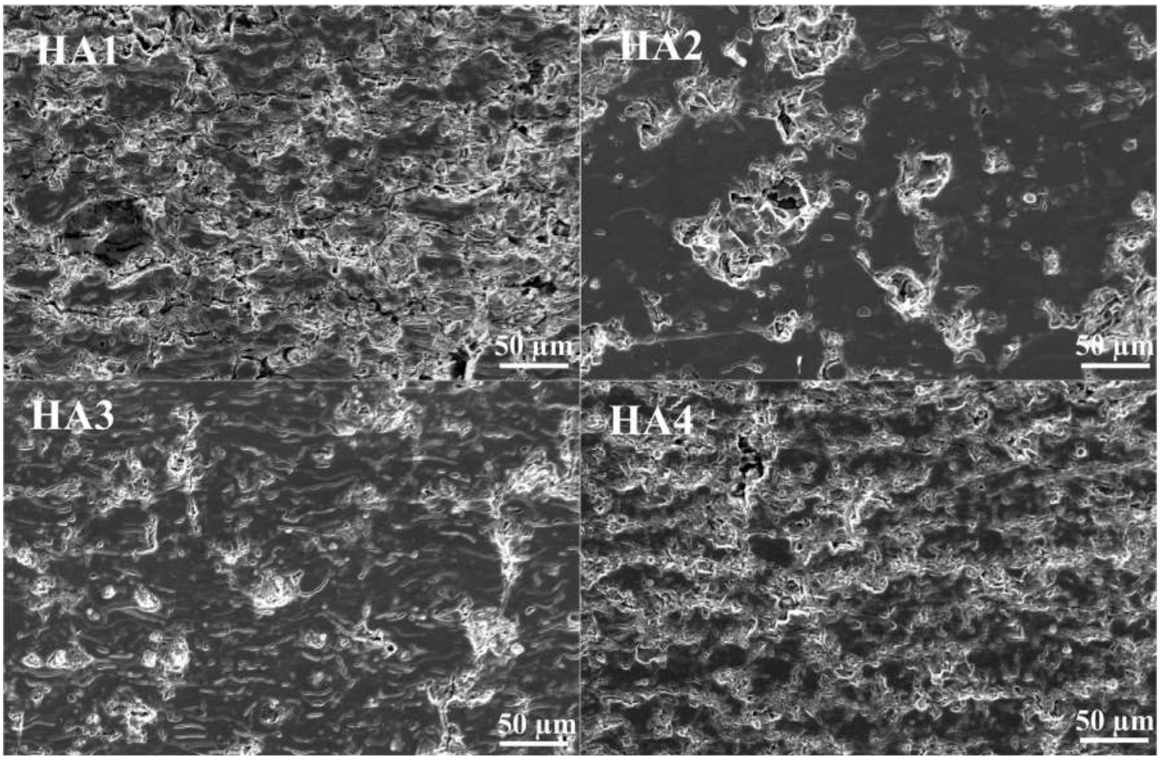

Fig. 3. Microstructure of as-sprayed HA coatings.

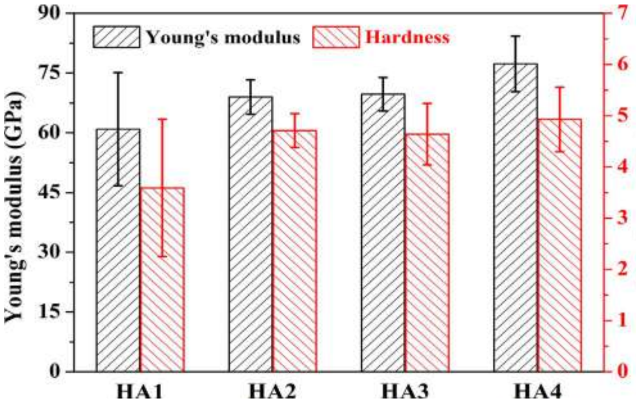

Fig. 4. Young's modulus and hardness of as-sprayed HA coatings.

of HA4 (E=77.3 GPa, H=4.9 GPa) are highest among the four coatings and represent a 26.9% and 37.3% improvement, respectively, as compared with HA1. Such increases are probably associated with the lowest porosity (i.e., the most compact structure) obtained under the highest in-flight particle velocity during the plasma spray process. In addition, the inter-particle bonding, which is believed to be strengthened at higher in-flight particle velocities, can affect the sample displacement during nanoindentation. This in turn would influence the obtained E and H values [20]. Nanoindentation has been extensively used to investigate the mechanical properties of HA coatings. Saber-Samandari et al. [17] reported that the E and H of flame sprayed HA coatings to be in the range of 114–121 GPa and 5.0–5.8 GPa, respectively. In the study of Surmeneva et al. [21], the E and H values of RF magnetron sputter-deposited HA coating were reported to be 112.0 GPa and 7.0 GPa, respectively. Both studies therefore obtained coatings with higher E and H than in the presented study. On the other hand, some other studies reported much lower E and H values. For instance, McManamon et al. [22] found that their plasma sprayed HA coatings possessed a E of 4.1 GPa and a H of 0.29 GPa; low E (6 GPa) and H (1 GPa) were also obtained by Sidane et al. [23] for their sol-gel HA coating, although they used the same indentation depth and strain rate as our study. These results suggest that the mechanical properties of HA coatings depend on various factors such as crystallinity, porosity, particle size and processing routes. It should be pointed out that overall the E and H values obtained here agree well with those reported in a number of previous studies on pure HA ceramics [24,25].

It is worth mentioning that HA1 showed significantly higher variation in E and H (error bar in Fig. 4) than the other coatings. Fabricated under the lowest in-flight particle velocity, HA1 possessed the least compact microstructure and its highest porosity and inhomogeneous pore distribution probably induced the measured data scatter.

3.2. Tribological properties

Fig. 5a presents the mean friction coefficients of the four different HA coatings tested against a 100Cr6 steel ball without and with Hanks' solution. The friction coefficients of the HA coatings presented in Fig. 5a were averaged from the global trends of friction coefficient versus laps presented in Fig. 5b. The measured friction coefficients well correlate to the respective in-flight velocities (Table 1): the increased in-flight particle velocity significantly decreased the friction of the HA coatings probably through the decreased roughness of the surfaces. At the same time, an improved wear resistance of the HA coatings was observed. In addition, all the HA coatings tested with Hanks' solution exhibited lower friction coefficients as compared to their counterparts tested under dry conditions. The reason is that the Hanks' solution lubricated the rubbing surfaces and prevented a direct solid–solid contact between them during the sliding [26–28].

Fig. 5b illustrates the development of the HA coatings friction coefficients tested without and with Hanks' solution as a function

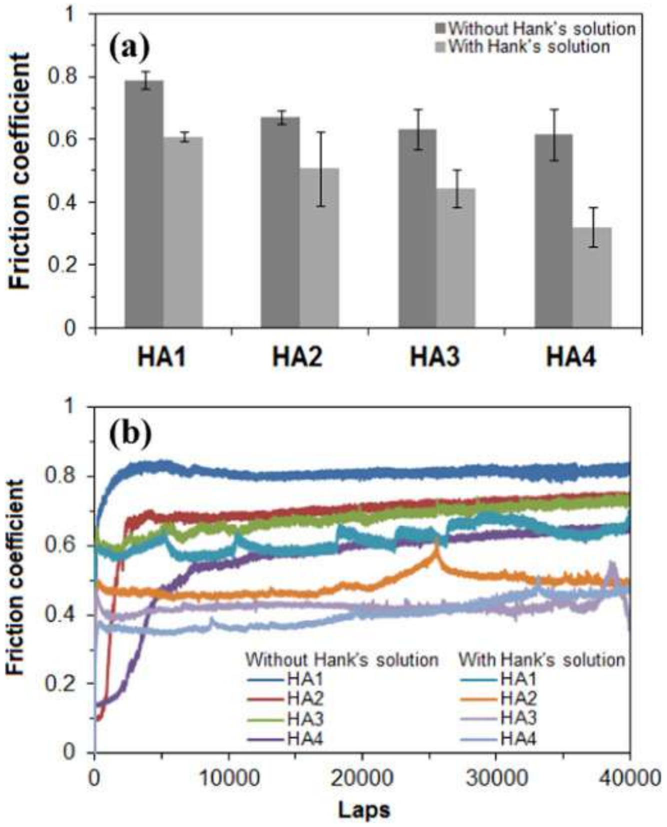

Fig. 5. (a) Friction coefficients of HA coatings tested with and without Hanks' solution; (b) friction coefficients of HA coatings as a function of the number of laps.

of the number of laps. The HA coatings deposited at the higher in-flight particle velocities exhibited lower friction during the entire sliding without and with Hanks' solution as a result of a lower wear of the coatings. Under the wet conditions, the HA coatings generally showed lower friction coefficients with respect to laps due to the lubricating effect of the solution [26].

The high surface roughness of the HA coatings lessened their contact areas with the counter steel balls under the dry condition, therefore the corresponding initial friction coefficients of the coatings were relatively low (Fig. 5b). Subsequently, the increased wear of the rubbing surfaces with increased laps in the running-in period increased the contact area between them, yielding the increased friction of the HA coatings. The HA coatings tested with Hanks' solution did not exhibit the relatively low friction in the beginning phase as the presence of the solution between two rubbing surfaces mitigated the influence of surface roughness on the initial friction of the coatings. During the prolonged sliding, the lower surface roughness of the HA coatings gave rise to their lower friction because of the reduced mechanical interaction between asperities of the two rubbing surfaces under both dry and wet conditions.

Fig. 6 shows the wear widths of the different HA coatings tested with and without Hanks' solution. It was found that the widths of the wear tracks of the HA coatings tested under both conditions significantly decreased at higher in-flight particle velocities through the enhanced inter-particle bonding, and increased *E* and *H* of the fabricated coatings. In addition, the HA coatings tested with Hanks' solution exhibited lower wear (i.e., narrower wear tracks) as opposed to their dry-tested counterparts, confirming the lubricating effect of the Hanks' solution. The similar trends between the friction (Fig. 5a) and wear (Fig. 6) of the HA coatings imply that the frictional behavior of the HA coatings is closely related to their wear behavior.

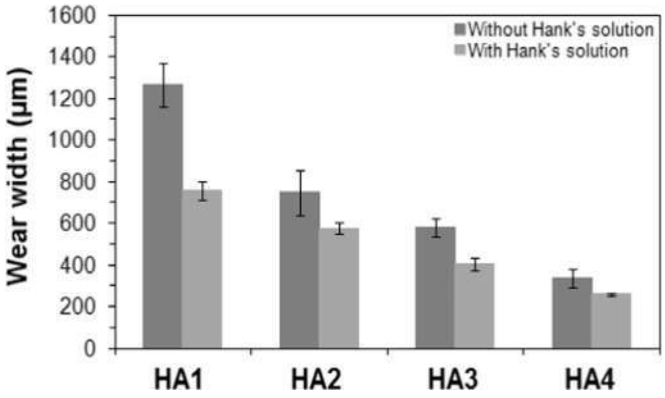

Fig. 6. Wear track widths of different HA coatings.

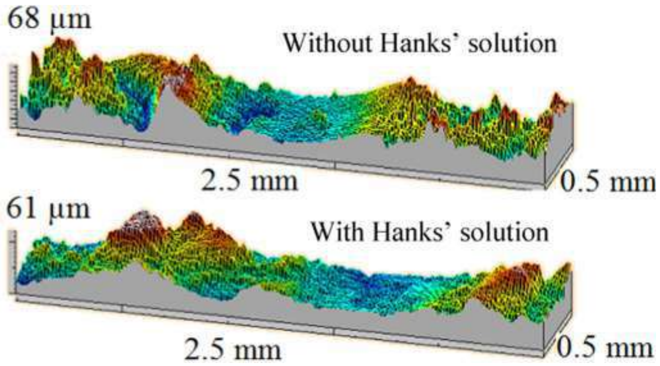

Fig. 7. Surface topography of HA1 coatings after tribological testing without and with Hanks' solution.

After the tribological tests, the wear topography and morphology of the HA coatings were examined. As shown in Fig. 7, the dry sliding of the steel ball against the HA1 coating removed the surface material up to a wear depth of 46 ± 5 μm. The introduction of the Hanks' solution during the sliding led to a decrease in the wear depth of the HA1 coating to 28 ± 3 μm (Fig. 7).

Fig. 8 shows the wear morphology of the HA coatings tested without Hanks' solution. It was consistently found that the HA1 coating exhibited significant material removal during the dry sliding against the steel ball. Such material removal was not observed for the other HA coatings tested under the dry conditions (Fig. 8) due to their higher abrasive wear resistance. The wear track width (indicated by arrows in Fig. 8) of the HA coatings significantly decreased with increased particle velocity. Following this trend, the HA4 coating tested under dry conditions did not exhibit a significant wear track on the surface. The results therefore confirmed the assumption that the increased in-flight particle velocity greatly improves the abrasive wear resistance of the HA coatings under the dry conditions.

Fig. 9 shows the wear morphology of the HA coatings tested with Hanks' solution. The introduction of Hanks' solution during the sliding against the steel ball significantly reduced the abrasive wear of the HA1 coating, as confirmed by its smaller wear width and depth (Fig. 7). In addition, the presence of Hanks' solution between two rubbing surfaces can lessen the adhesive wear of the HA coatings by serving as a spacer to prevent a direct contact between the rubbing surfaces. Similar to the dry condition, it was found that the wear track width (indicated by arrows in Fig. 9) of the HA coatings tested with Hanks' solution decreased according to the relation of HA1 > HA2 > HA3 > HA4 due to the increased abrasive wear resistance of the HA coatings associated with higher in-flight particle velocities. Overall, the SEM observation clearly

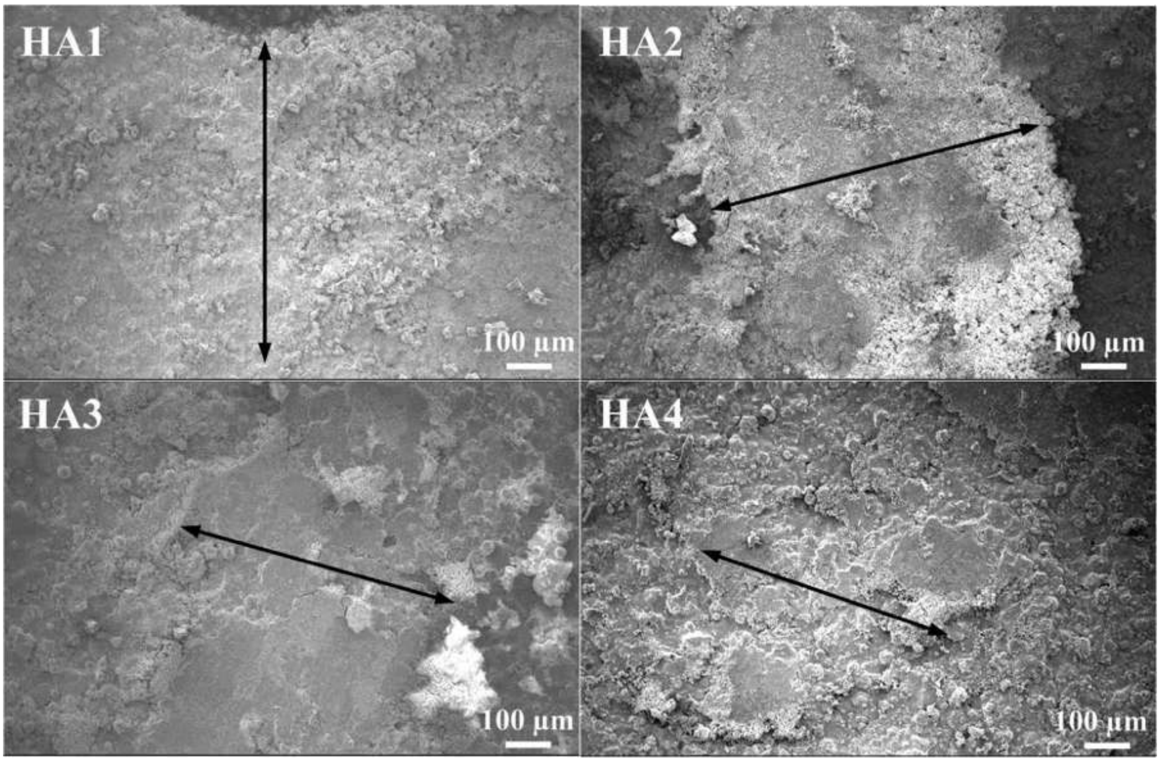

Fig. 8. Wear morphology of HA coatings observed after tribological testing without Hanks' solution. Arrows indicate wear widths.

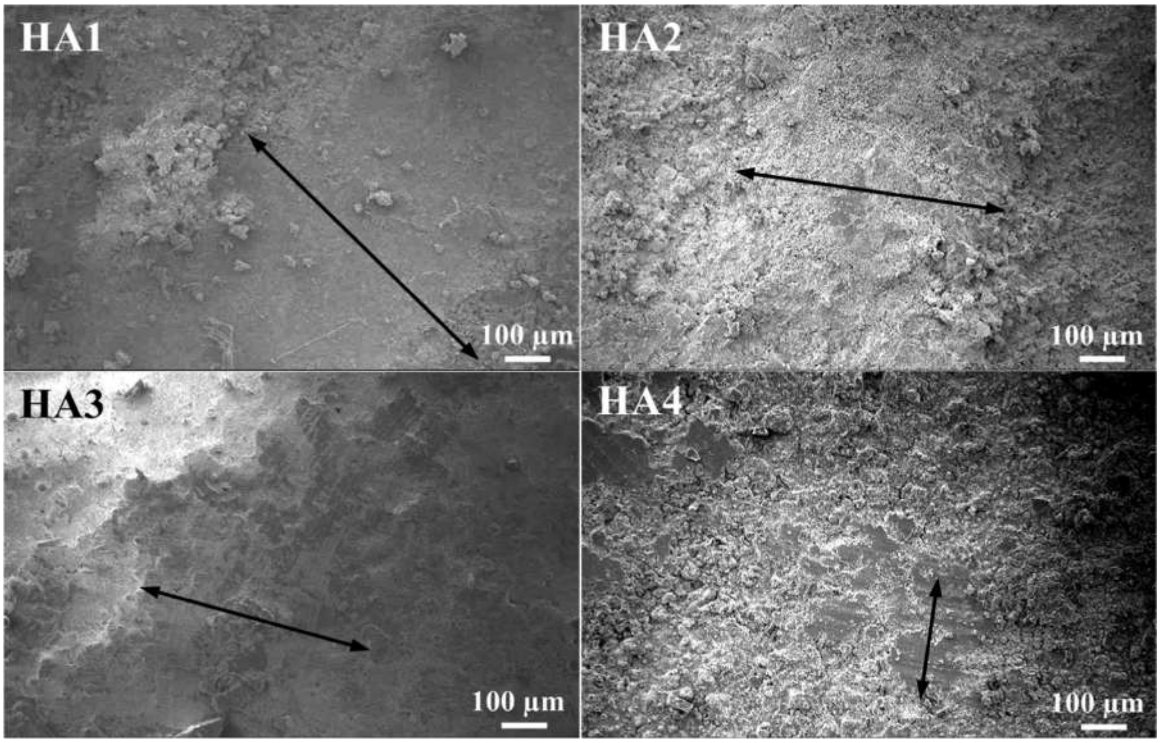

Fig. 9. Wear morphology of HA coatings observed after tribological testing with Hanks' solution. Arrows indicate wear widths.

showed that the HA coatings exhibited a decrease in their friction and wear with the increased in-flight particle velocity under both dry and wet sliding conditions and that the introduction of Hanks' solution during the sliding apparently lowered the friction and wear of all HA coatings most likely due to the lubricating effect of the Hanks' solution.

The EDX measurement within the wear track of the HA4 coating tested with Hanks' solution detected C, Ca, O, and P presence (data not shown). The Ca, O, and P peaks are associated with the HA matrix and the C peak could probably be attributed to surface carbon contamination. No Fe associated with the wear of the steel ball was detected in the spectra, suggesting that no

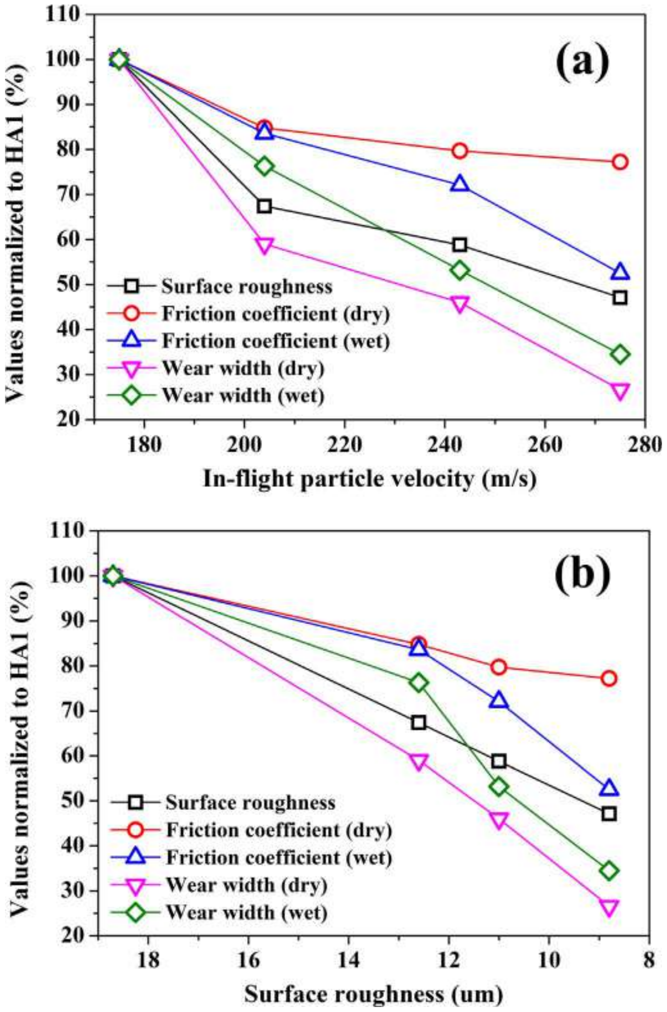

Fig. 10. Surface roughness, friction coefficient and wear width of HA coatings normalized to the corresponding values of HA1 vs. (a) in-flight particle velocity and (b) surface roughness.

significant (detectable) transfer of Fe into the HA coating occurred.

The effect of the surface roughness on the tribological properties of the HA coatings must be further taken into account. A rougher surface can lead to a higher friction and wear via increased mechanical interaction between the two rubbing surfaces [29–32]. As shown in Table 2, a strong correlation between the surface roughness and friction and wear properties of the HA coatings was observed, thereby clearly indicating that the surface roughness of the HA coatings has a significant influence on their friction in terms of mechanical interaction.

The surface roughness, friction coefficient and wear width values vs. in-flight particle velocity normalized to those of HA1 are presented in Fig. 10a. Marked decreasing trends were detected for all the parameters, indicating that a higher in-flight particle velocity resulted in smoother HA coatings with enhanced friction and wear resistance. Furthermore, when these parameters were normalized to the corresponding values of HA1 and plotted against the surface roughness (Fig. 10b), similar decreasing trends were observed, implying a strong correlation between the friction and wear properties and the surface roughness of the coatings. It is suggested here that the reduction of the wear widths by increasing in-flight particle velocity was realized through a smoother surface topography, i.e. less mechanical interaction between the rubbing surfaces. In addition, when smoother coating surfaces were obtained under higher in-flight particle velocities, Hanks' solution was able to prevent a direct solid-solid contact between two smooth surfaces more effectively, thereby further reducing the friction coefficient.

Fig. 11a and b shows the rubbing surface morphology of the 100Cr6 steel balls used for the HA1 and HA4 coatings after dry wear tests, respectively. The steel ball rubbed on the HA4 coating had a significantly larger wear width of 658 ± 86 μm than the one rubbed on the HA1 coating (wear width of 236 ± 54 μm). Such result further supported the conclusion that the HA4 coating deposited at the higher in-flight particle velocity possessed a higher wear resistance, giving rise to the higher wear of its counter steel ball during the prolonged sliding [26].

4. Conclusions

Hydroxyapatite coatings were deposited onto Ti6Al4V substrates via atmospheric plasma spray process by systematically varying the in-flight powder particle velocities. The tribological properties of the coatings without and with Hanks' solution were investigated using ball-on-disc micro-tribological test. The HA coatings deposited at higher in-flight particle velocities exhibited smoother surface topography and possessed improved Young's modulus and hardness. As a result, the corresponding HA coatings exhibited significantly lower friction coefficients and wear against the steel ball under both dry and lubricated (Hanks' solution) conditions. The HA coatings tested with Hanks' solution had lower friction and wear due to the boundary lubricant effect of the solution. It is therefore concluded that higher in-flight particle velocity enhances the tribological properties of the plasma sprayed HA coatings under both dry and wet conditions.

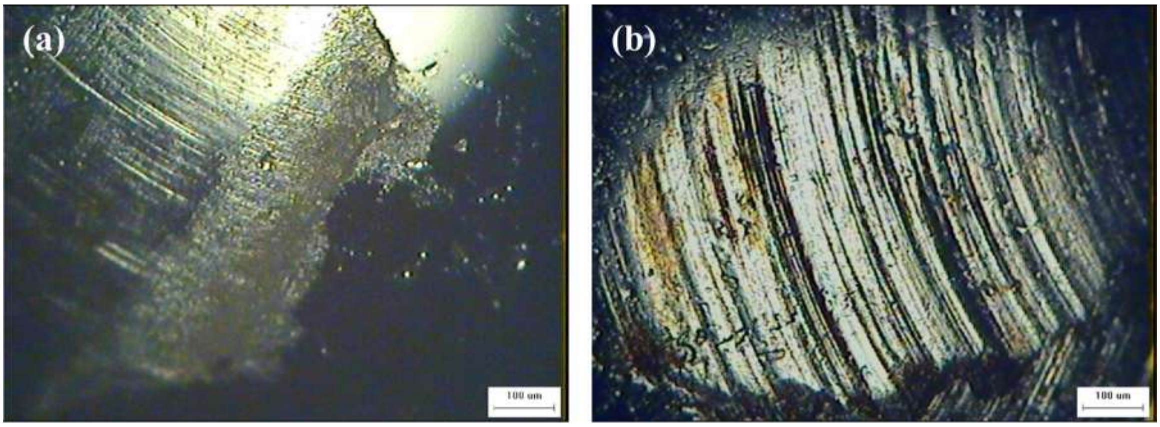

Fig. 11. Wear morphology of 100Cr6 steel balls rubbed on (a) HA1 and (b) HA4 coatings under dry sliding conditions.

Acknowledgments

The work of Jan Cizek has been supported by the project NETME Centre Plus (Lo1202), project of Ministry of Education, Youth and Sports under the “National Sustainability Programme”. Support of Czech Science Foundation project Nr. 13-35890S and FME BUT specific research project FSI-S-14–2427 is further acknowledged.

References

[1] Hench LL. Bioceramics: from concept to clinic. J AM Ceram Soc 1991:1487–510.
[2] Gross KA, Gross V, Berndt CC. Thermal analysis of amorphous phases in hydroxyapatite coatings. J Am Ceram Soc 1998:106–12.
[3] Lacefield WR. Hydroxyapatite coating, in an introduction to bioceramics. In: Hench LL, Wilson J, editors. Advanced Series in Ceramics. World Scientific Publishing CO. Pte. Ltd.; 1993. p. 223–38.
[4] Cizek J, Khor KA. Role of in-flight temperature and velocity of powder particles on plasma sprayed hydroxyapatite coating characteristics. Surf Coat Technol 2012:2181–91.
[5] Dey A, Sinha A, Banerjee K, Mukhopadhyay AK. Tribological studies of microplasma sprayed hydroxyapatite coating at low load. Mater Technol: Adv Biomater 2014:B35–40.
[6] Liu Y, Dang Z, Wang Y, Huang J, Li H. Hydroxyapatite/graphene-nanosheet composite coatings deposited by vacuum cold spraying for biomedical applications: Inherited nanostructures and enhanced properties. Carbon 2014:250–9.
[7] Khor KA, Gu YW, Quek CH, Cheang P. Plasma spraying of functionally graded Hydroxyapatite/Ti–6Al–4V Coatings. Surf Coat Technol 2003:195–201.
[8] Cizek J, Khor KA, Prochazka Z. Influence of spraying conditions on thermal and velocity properties of plasma sprayed hydroxyapatite. Mater Sci Eng: C 2007:340–4.
[9] Cizek J, Khor KA, Dlouhy I. In-flight temperature and velocity of powder particles of plasma-sprayed TiO_2. J Therm Spray Technol 2013:1320–7.
[10] Cizek J, Dlouhy I, Siska F, Khor KA. Modification of plasma-sprayed TiO_2 coatings characteristics via controlling the in-flight temperature and velocity of the powder particles. J Therm Spray Technol 2014:1339–49.
[11] Vahabzadeh S, Roy M, Bandyopadhyay A, Bose S. Phase stability and biological property evaluation of plasma sprayed hydroxyapatite coatings for orthopedic and dental applications. Acta Biomater 2015:47–55.
[12] Fu YQ, Batchelor AW, Wang Y, Khor KA. Fretting wear behaviors of thermal sprayed hydroxyapatite (HA) coating under unlubricated conditions. Wear 1998:132–9.
[13] Reis RL, Monteiro FJ. Crystallinity and structural changes in HA plasma-sprayed coatings induced by cyclic loading in physiological media. J Mater Sci: Mater Med 1996:407–11.
[14] Whitehead RY, Lucas LC, Lacefield WR. The effect of dissolution on plasma sprayed hydroxylapatite coatings on titanium. Clin Mater 1993:31–9.
[15] Lin JH, Liu ML, Ju CP. Morphologic variation in plasma-sprayed hydroxyapatite-bioactive glass composite coatings in Hank' s solution. J Biomed Mater Res 1994:723–30.
[16] Fu YQ, Batchelor AW, Khor KA. Fretting wear behavior of thermal sprayed hydroxyapatite coating lubricated with bovine albumin. Wear 1999:98–102.
[17] Saber-Samandari S, Gross KA. Nanoindentation on the surface of thermally sprayed coatings. Surf Coat Technol 2009:3516–20.
[18] Cizek J. Thermally sprayed bio-ceramic coatings: a study on process parameters influence on coating properties [PhD theis]. Singapore: Nanyang Technological University; 2010.
[19] Young RA. The Rietveld method. IUC monographs on crystallography 5. International Union of Crystallography, UK: Oxford University Press; 1993.
[20] Oliver WC, Pharr GM. Measurement of hardness and elastic modulus by instrumented indentation: Advances in understanding and refinements to methodology. J Mater Res 2004:3–20.
[21] Surmeneva MA, Mukhametkaliyev TM, Tyurin AI, Teresov AD, Koval NN, Pirozhkova TS, et al. Effect of silicate doping on the structure and mechanical properties of thin nanostructured RF magnetron sputter-deposited hydroxyapatite films. Surf Coat Technol 2015:176–84.
[22] McManamon C, de Silva JP, Power J, Ramirez-Garcia S, Morris MA, Cross GLW. Interfacial characteristics and determination of cohesive and adhesive strength of plasma-coated hydroxyapatite via nanoindentation and microscratch techniques. Langmuir 2014:11412–20.
[23] Sidane D, Chicot D, Yala S, Ziani S, Khireddine H, Iost A, et al. Study of the mechanical behavior and corrosion resistance of hydroxyapatite sol–gel thin coatings on 316 L stainless steel pre-coated with titania film. Thin Solid Films 2015:71–80.
[24] Gross KA, Saber-Samandari S. Revealing mechanical properties of a suspension plasma sprayed coating with nanoindentation. Surf Coat Technol 2009:2995–9.
[25] Song J, Liu Y, Zhang Y, Jiao L. Mechanical properties of hydroxyapatite ceramics sintered from powders with different morphologies. Mater Sci Eng: A 2011:5421–7.
[26] Khun NW, Frankel GS, Sumption M. Effects of normal load, sliding speed, and surface roughness on tribological properties of niobium under dry and wet conditions. Tribol Trans 2014:944–54.
[27] Wong HC, Umehara N, Kato K. Frictional characteristics of ceramics under water-lubricated conditions. Tribol Lett 1998:303–8.
[28] Khun NW, Liu E. Tribological behavior of polyurethane immersed in acidic solution. Tribol Trans 2012:401–8.
[29] Svahn F, Kassman-Rudolphi Å, Wallen E. The influence of surface roughness on friction and wear of machine element coatings. Wear 2003:1092–8.
[30] Menezes PL, Kailas SV. Influence of surface texture and roughness parameters on friction and transfer layer formation during sliding of aluminium pin on steel plate. Wear 2009:1534–49.
[31] Barrett TS, Stachowiak GW, Batchelor AW. Effect of roughness and sliding speed on the wear and friction of ultra-high molecular weight polyethylene. Wear 1992:331–50.
[32] Khun NW, Zhang H, Yang J, Liu E. Mechanical and tribological properties of epoxy matrix composites modified with microencapsulated mixture of wax lubricant and multi-walled carbon nanotubes. Friction 2013:341–9.

J Therm Spray Tech (2018) 27:1251–1279
https://doi.org/10.1007/s11666-018-0798-8

REVIEW

Medicine Meets Thermal Spray Technology: A Review of Patents

J. Cizek[1] · **J. Matejicek**[1]

Submitted: 12 July 2018 / in revised form: 10 October 2018 / Published online: 4 December 2018
© ASM International 2018

Abstract The patent literature concerning thermal spraying for biomedical applications is reviewed in this contribution. The patents were compiled from multiple databases search spanning the 2005-2018 period. For clarity and ease of reading, the results have been grouped into sections according to four individual material groups (apatites, titanium, oxide ceramics, other), with the secondary sorting criterion being related to the specific bioapplication areas (maxillofacial, orthopedic, methods). Lastly, the patents are grouped according to the selected thermal spray method within the individual subsections. In the paper, recent R&D trends in this field are further identified and briefly commented.

Keywords applications · atmospheric plasma spray (APS) · biomaterials · cold spray · feedstock · HVOF · hydroxyapatite · processing · titanium · wire arc spray

1 Introduction

1.1 Biomaterials

Factors such as diseases, traumas, acute injuries, hereditary and genetic disorders, lifelong collection of toxicants and, most of all, aging, reduce the ability of a human body to replace defective or necrotic cells and repair damaged tissues. The history of medical sciences, the means of suppressing the impact of these negative factors, can be traced back to the beginnings of ancient civilizations. With the evolution of these sciences, aiding healing, correcting deformities or restoration of lost functions of various parts of human body have become progressively successful.

A special part of medical sciences is endeavors to partially or fully repair or replace defective tissues or body organs. The pioneering attempts in this area often resulted in unwanted consequences such as infections, embolism or tissue inflammation or necrosis that generally caused additional difficulties such as worsening of patient hardship, contiguous systems malfunctions, or, in the worst case, death.

The intensified public demands to develop this section of medical sciences evoked a rapid progress. It was not until 1860s when the advent of aseptic surgical techniques allowed an unprecedented boom in this area. After overcoming the primary problems with surgical methodology, the focus of research turned to a second milestone: the (bio)materials.

Initially, the empirical methodology of surgery allowed use of only a limited range of materials that were affordable and easy to acquire, process and manufacture. Wood, a natural high strength-to-weight-ratio composite, was used for limb prostheses and artificial teeth (Ref 1). Gold, a malleable and inert metal, was used in dentistry. Iron and brass were used to rejoin fractured bones, as well as original bone structures from other mammals (e.g., ivory). Glass was used as an eye replacement due to its cosmetic appearance. However, success in application of such traditional materials happened more by accident than by design, and these materials have become obsolete. The need to find suitable materials applicable to the needs of the human body became critical during the 1960s (Ref 2).

It was clear that the materials stood for the major hindrance in the area of human surgical operations. The

---

✉ J. Matejicek
jmatejic@ipp.cas.cz

[1] Institute of Plasma Physics, The Czech Academy of Sciences, Prague, Czech Republic

approach of usage of traditional materials in surgery was reassessed, and novel types of materials were introduced. Surpassing the benefits and performance of the traditional materials, this new group of materials remains the source of intense research until today. Generally known as biomaterials, they provide the solution to many problems encountered in the area of medical sciences.

High biocompatibility (the ability of a material to perform with an appropriate host response in a specific application) is the first and most important condition required for present-day materials. Materials not meeting this criterion (materials with undesirable effects, secondary side effects) are no longer acceptable for medical and/or surgical purposes. Required levels of biocompatibility depend, among other factors, on the contact time between biomaterial and biological tissue, ranging from few seconds where the requirements need not to be strict (e.g., syringe needle, tongue depressor) to several decades where ultimate biocompatibility is an imperative (e.g., bone screws, total hip replacement).

The biocompatibility indicates the response of the host tissues when in contact with biomaterial. Furthermore, there is also a varying degree of interaction between the biomaterial and the tissue (Ref 2, 3):

- Bioinert materials are non-toxic and remain chemically stable even in long-term applications (years). Usually, a thin fibrous tissue surrounding the bioinert implant is formed as a tissue reaction. There are currently attempts to replace these first generation materials with proactive functioning materials. Stems of orthopedic implants or dental replacements are made of bioinert materials.
- Bioresorbable (biodegradable) materials are gradually resorbed by the body. Sometimes, the decay of a biomaterial is followed by a replacement with new tissues. The process usually ends when the biomaterial fully vanishes or is fully replaced by biological tissues. Controlled drug-delivery systems or vascular grafts and nerve guidance channels are made of bioresorbable materials.
- Bioactive materials actively elicit a specific biological response at the interface, usually resulting in a formation of a bond between the biomaterial and surrounding tissues. Bioactive materials are intermediate between bioresorbable and bioinert as they can retain both designs. Surface coatings of hard tissue implants or skin tissue implants are made of bioactive materials.

Bioactive and bioresorbable materials are referred to as second generation biomaterials. Third generation materials are bioactive materials with external activation of surrounding tissue cells and genes by adsorbed bone growth-stimulating proteins such as bone morphogenetic proteins (BMPs) or non-collagenous proteins such as osteocalcin. The activation is based on stimulation of specific cellular responses at a molecular level.

Assistance applications, i.e., aiding the biological system in performing its function, include dental repairs, caps, cavity fillers; cardiac pacemakers, cardiac assistive devices; contact lenses; scoliosis spine device; lung oxygenator machine; kidney dialysis machine; cosmetic surgery materials, augmentation mammoplasty, chin augmentation.

Common examples of repair applications (aiding the biological system as it physiologically restores its function) are fracture fixation devices; bone cement, bone plates; sutures; catheters, drains, shunts; burn dressings; artificial skin.

Removing the original diseased or damaged organ and substituting it with artificial biomaterials (replacement applications) are performed in case of artificial heart, heart valve (Ref 4); heart–lung machine; blood vessel replacement; cochlear replacement; eye lens replacement, glass eye; dentures, bridges; ligaments and tendons; intervertebral disks; artificial joints: hips, knees, shoulders, ankles, wrists, elbows. Some examples on the usage of materials for human bioapplications are illustrated in Fig. 1.

1.2 Thermal Spraying

Thermal spraying belongs to a group of processes in which metal or nonmetal materials are deposited in a molten or semi-molten state onto a prepared substrate to form a spray deposit (Ref 5). The material is inserted in various forms such as powders, suspensions, rods or wires, heated in a plasma jet or combustion flame and propelled toward the substrate surface (Ref 6). Depending on the technology, the high velocities of acting gases cause acceleration of the small particles of the material up to 1400 m/s (Ref 7). Eventual heating can cause further increase in the particles kinetic energy and likely cause partial or full-scale melting of the particles (Ref 8). The immense kinetic energies stored in the particles account for the large amount of elastic and plastic deformation of the molten or semi-molten particles during the process of its solidification at the surface. The solidified particles are called splats, and their size ranges from few micrometers to over 100 micrometers in diameter and about 1-20 µm in thickness. Synchronous movement of the thermal spray source relative to the substrate enables covering the substrate in individually deposited layers, each consisting of millions of the solidified splats. Thermally sprayed coatings often consist of several layers, and their typical thickness could vary from 5 µm (usually a single layer coating) to 10 mm.

The flexibility and versatility of thermal spray methods allowed them to enter a whole range of applications in the biomedical sector. Differing by the used technique, used

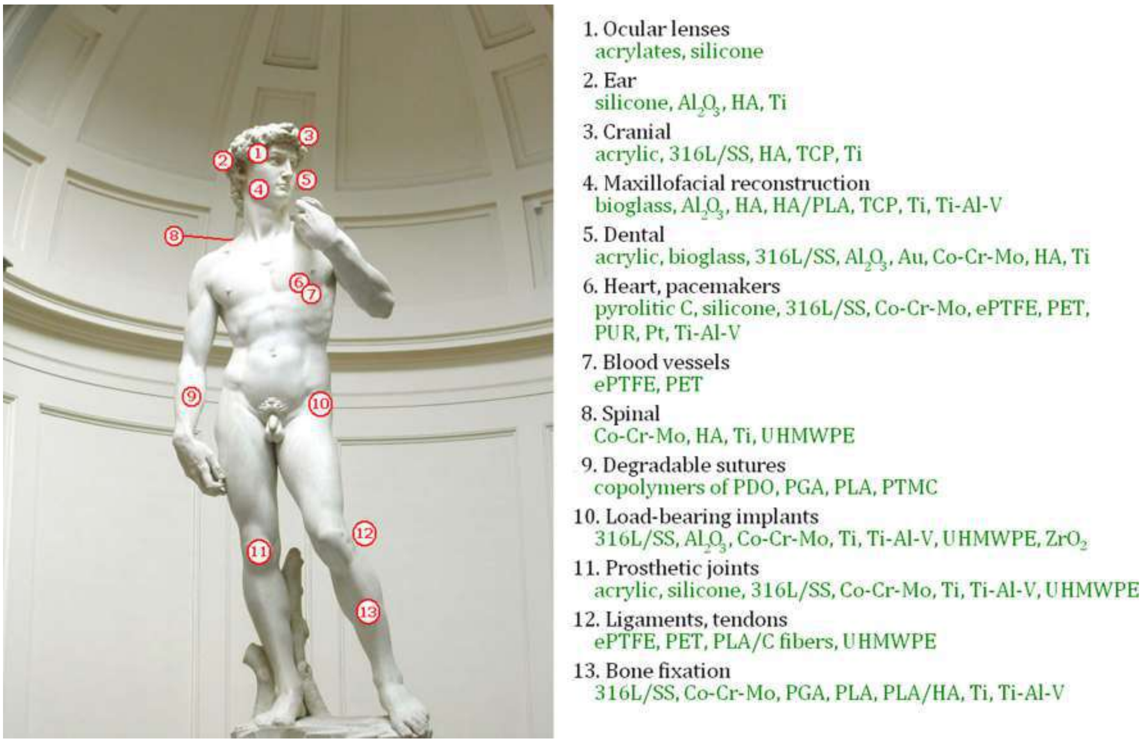

Fig. 1 Illustration of the materials commonly used in human bioapplications. (Statue of David by Michelangelo Buonarroti from the collections of Galleria dell'Accademia di Firenze, Florence, Italy. Photographed by David Gaya, license: Wikimedia Commons)

materials for both substrates and coatings, they currently span the entire spectrum from assistance to repair to replacement applications.

2 Patent Search

Given the advantages of using thermal spray technologies in the biomedical sector, many patents in this area are filed annually. In this contribution, we present a digest of the patent literature (both granted patents and patent applications) going back to 2005. The literature search was done primarily through Web of Science—Derwent Innovation Index (Ref 9), with the help of European Patent Office—Espacenet (Ref 10) and US Patent and Trademark Office databases (Ref 11), using keywords related to known thermal spray methods, materials, and applications in the biomedical sector. The sources included world patents (WIPO—World Intellectual Property Organization), as well as patents filed in the USA, European Union, China, Japan, Germany and the Czech Republic. No limitations were imposed on the country of origin. Some (relevant) patents may not have been included into this paper due to the non-uniform nature of the individual patent databases, and hence, the above search criteria used for data mining are stated herein.

The search focused on three topical groups—materials, application areas and methods. The patent claims varied from material preparation to novel processing methods (spraying, as well as pre- and post-treatment) to complete components (e.g., dental or hip implants). The role of thermal spraying ranged from a key part of the patent to one of possible alternatives.

Typical examples of the search terms according to the selected criteria included, e.g.,

- [(thermal or plasma or HVOF or cold) and spray*] and (hydroxyapatite or apatite or implant)
- [(thermal or plasma or HVOF or cold) and spray*] and (gahnite or baghdadite or calcium phosphate) and (implant or biomed*)
- [(thermal or plasma or HVOF or cold or flame or arc) and spray*] and (TiNb or Ti or Ti-Nb or TiNbTaZr or CoNiCr*) and (implant or biomed*)

The primary search according to these criteria returned 103 patents. Some of these documents were written in a way that the main patent claim was somewhat difficult to identify. Further, some of the patents were difficult to comprehend since the abstract was ambiguous when translated into English. In the following text (Sects. 3.1–3.4), the authors have tried to summarize the main patent claims and ideas in their own words for the benefit of the readers.

Figure 2 shows the distribution of the patent documents by the year of application and by the first inventor/assignee country. The time distribution shows a slight decrease in the years 2015-2017. This may be caused by some of the (pending) patents still being in the revision process by the respective offices. Considering the countries, the largest number of patents originated in the USA, followed by China, while all other countries had significantly lower numbers. This, again, has to be understood against the individual databases that were searched within the compilation of this document.

3 Patents List

There are several criteria for organizing the patents. In the text, the patents will first be sorted according to the materials used, with each materials group (apatites, titanium, oxides) dedicated to a separate Sub-sects. 3.1–3.3. Those patents, in which the sprayed material was not disclosed or was not important to the novelty idea, will be grouped in the last, separate Sect. 3.4. Each of these four sections is further sorted according to the criteria of applications (maxillofacial, orthopedic, innovative procedures). Finally, the last division of each section is done according to the used thermal spray methods, including post-processing of the coatings. A schematics of the paper distribution into the individual sections using the three criteria is shown in Fig. 3.

The innovative procedures enlisted in the applications (alongside maxillofacial and orthopedic) are those patents where the novelty is not directly related to a targeted application field, but rather the spraying procedure itself. Since the innovations concerning spraying methods/procedures are likely of higher interest to JTST readership, these are pinpointed with brief summary in Table 1. More detailed description is then provided in the corresponding sections of the main text. The methods/procedures generally involve spraying method modifications, special feedstock preparation, as well as pre- and post-treatments. Note that only novel approaches are presented in Table 1, omitting those documents that patented "general spraying" only.

3.1 Calcium Phosphates, Hydroxyapatite

3.1.1 Maxillofacial

Plasma Spraying Mandibular bone plate design improvement was patented in Ref 60, whereby two extension portions for defining bone facing surface were added. The portions are rotated along their length to better conform to the mandible bone. The extension portions are plasma-sprayed to obtain hydroxyapatite, titanium or antibacterial coatings so as to improve physical or chemical properties to provide medications (Fig. 4).

A method providing an active growth of bone tissue into dental implants is covered in Ref 61. The invention refers to making an intraosseous dental implant in several steps involving sand-blasting by Al_2O_3 particles and plasma spray-based deposition of a system of biocompatible coatings containing mixed titanium/titanium hydride or hydroxyapatite powders. The sequence actually comprises two 50-100 µm layers of titanium or titanium hydride of

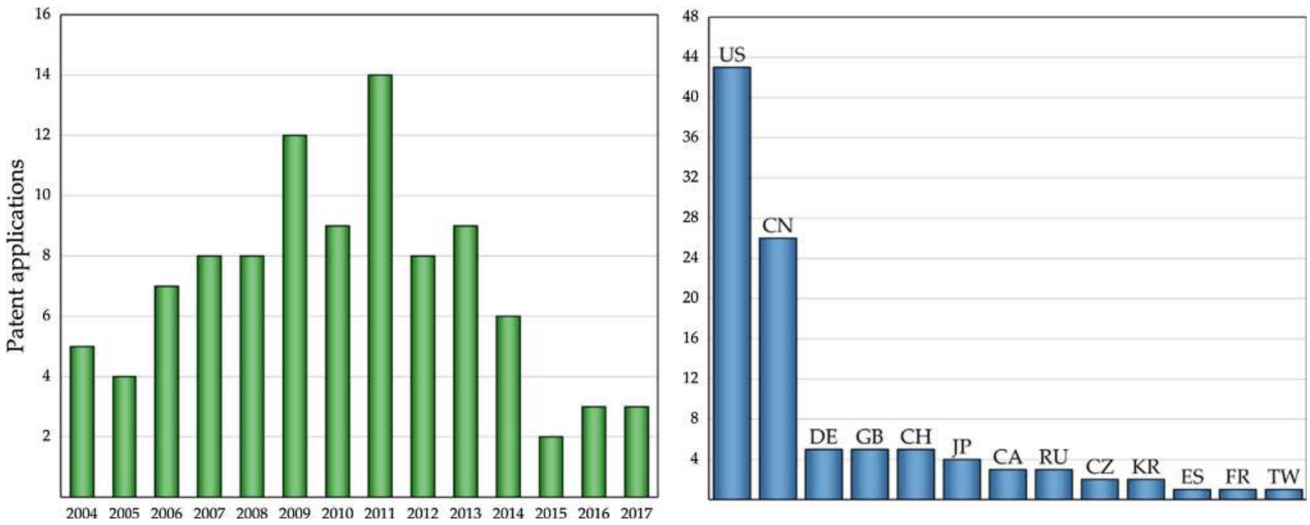

Fig. 2 Number of patent applications in individual years within 2004-2017 period (left), number of patent documents per the country of origin of the first inventor/assignee (right)

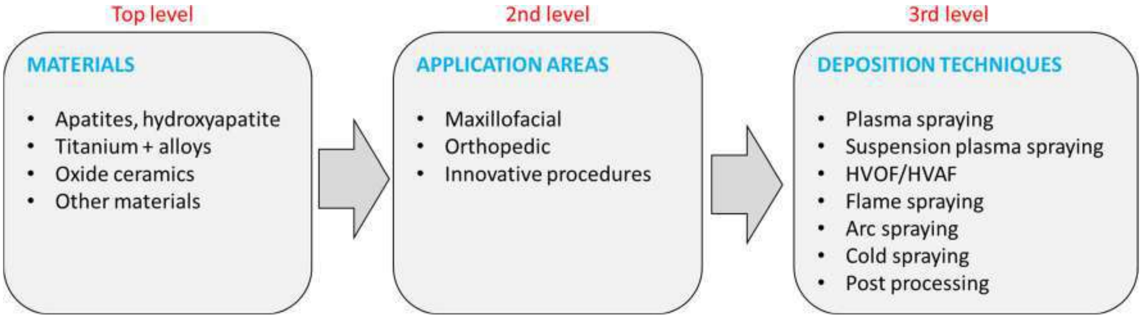

Fig. 3 Schematics of the paper organization into sections. Top-level subdivision is based on the materials groups. In the second-level subdivision, the third area contains patents focused on processing innovations. Third-level subdivision is made according to the specific deposition techniques. Cases where a generic term "thermal spraying" was used in the patent are assigned to plasma spraying sections in this paper

different porosities, followed by a 150-200-μm layer of mixed titanium or titanium hydride and hydroxyapatite (20-40 wt.%), and, finally, another 200-300 μm layer of pure hydroxyapatite. The whole system is covered by a metal film consisting of a ferric triad (iron, cobalt or nickel) of thickness 20-35 nm deposited by magnetron sputtering and a carbon 10 μm nanocoating comprised of carbon nanotubes and carbon nanofibres of diameters 50-200 nm (Fig. 5).

A dental root implant useful in surgery process was patented in Ref 62. The component has a cylindrical core and a threaded part for fixation. The central part of the base is covered by a recrystallized, plasma-sprayed layer of a mixture of at least two different calcium phosphate materials. These have to have different melting temperatures. The economically manufactured dental implant supposedly has excellent attachment and quick gingival bonding, high durability and excellent stability and masticatory power for long periods of time.

3.1.2 Orthopedic

Plasma Spraying A component for installing artificial hip joints in a recess cover of the pelvis bone is presented in Ref 63. The component is fabricated using surface treatments such as thermal spraying and subsequent roughening. The component (acetabular cup, actually) has an extra liner layer fitted in its inner side. An outer surface of the liner is provided with a taper-shaped surface. This is to make the two opposing surfaces to mutually contact reliably in a desired position, further suppressing any position shift of the liner, thereby suppressing damage rate of the liner in an effective manner (Fig. 6).

Novel implants with an open frame structure (apex, oblique and transverse support struts) retaining enough strength to prevent bending or failure are presented in Ref 64. The elongated implant body is made of metal and ceramic and is plasma spray-coated (from the outside) with hydroxyapatite or titanium. It could be used, e.g., for fusion of a joint or joining two bone segments. The bony ingrowth into the scaffold is promoted and, by the openings, introduction of bone graft material is allowed through the implant. A curved variant of the implant is held by a pivoting arm and inserted without the aid of a guide pin by rotating the curved arm. The curved implant variant could be used, e.g., for fixation or fusion of sacroiliac joint for treatment of degenerative sacroiliitis, inflammatory sacroiliitis, iatrogenic instability of sacroiliac joint or traumatic fracture dislocation of pelvis (Fig. 7).

Authors of Ref 64 also filed a similar patent (Ref 65). In the document, a modular straight implant for fixation or fusion of two bone segments such as, e.g., sacroiliac joint is presented. The implant has an elongated open frame structure body comprising a set of apex struts aligned along the longitudinal axis. A set of support struts forms the matrix structure. The open frame structure allows to be packed with a bone graft material while providing enough strength to facilitate fusion of the joint or two bone segments without implant bending or failure. The main body is plasma spray-coated with hydroxyapatite or titanium.

Shorter variant of the femoral prosthesis (femoral neck, in fact) is presented in Ref 66. In the patent, the prosthesis is installed or fixed at the proximal end of the femoral bone in a total hip replacement procedure. The prosthesis loads the proximal end of the femur so as to prevent bone resorption, where a small portion of bone is only resected in the implantation process, thus ensuring that the prosthesis is bone sparing and allows an easy insertion procedure. The prosthesis has a fixation surface selected from a group of porous surface, porous layer, sintered beads, metallic foam or plasma-sprayed porous coating such as hydroxyapatite.

A four-component artificial intervertebral disk is presented in Ref 67. Its geometry allows six degrees of movement (flexion, extension, lateral bending, axial

Table 1 Overview of patents focusing on the spraying methods/procedures. Abbreviations are explained in Sect. 5 at the end of the paper

Section	Ref	Core of the patent
3.1	Ref 12	PS sandwich coating (TiO_2/ZrO_2 + HA + Ti) for improved adhesion in implants
	Ref 13	Composite feedstock (HA core + Ti shell) and TS coatings
	Ref 14	FGM Ti + HA coating
	Ref 15	FGM Ti + HA coating
	Ref 16	HA feedstock with antimicrobial metal agent (Ag/Zn/Cu)
	Ref 17	HA feedstock with antimicrobial Ag additive
	Ref 18	HA + povidone-iodine mixture for antibacterial properties
	Ref 19	HA + silver salt SPS coating
	Ref 20	Modified Ca-P feedstock - some Ca replaced by Ag/Cu/Zn by ion exchange
	Ref 21	SPS HA coating with enhanced porosity by pore-creating agent
	Ref 22	Co-spraying of HA and Ti by HVOF
	Ref 23	Multilayer PS coating with porous outer layer (HA + Ti) and electrochemical integration layer of Ti alloy nanotubes
	Ref 24	Annealing of HA coating to improve crystallinity
	Ref 25	Electrolyte solution impregnation of HA coating to improve crystallinity
	Ref 26	Hydrothermal treatment of HA coating for nanostructure formation
	Ref 27	Micro-beam PS of HA
	Ref 28	CS of HA
	Ref 29 and 30	HA suspension feeding system
	Ref 31	SPS HA coating
	Ref 32	Surface nanocrystallization of PS HA
	Ref 33	Nanoscale HA powder
	Ref 34	SPS HA with collagen addition for improved bone formation
3.2	Ref 35	TS Ti + Ta coating on non-metallic substrates
	Ref 36	Porous VPS Ti coating for bone ingrowth
	Ref 37	Diffusion bonding of CS Ti on Cr
	Ref 38	CS Ti + Mg coating, vacuum annealing for controlled porosity
	Ref 39	Surface patterning before PS Ti coating
	Ref 40	PS Ti + micro-arc oxidation + PS $CaTiSiO_5$
	Ref 41	Co-spraying of Ti with another powder for porosity control
	Ref 42	Multilayer of silicate glass, PS Ti and PS Ca-P
3.3	Ref 43 and 44	PS Al_2O_3 + Ti + TiO_2 FGM on orthopedic implants
	Ref 45	PS nano-TiO_2 coating + UV radiation for bioactivation
	Ref 46	TS nanostructured ZrO_2, TiO_2, Al_2O_3, HA
	Ref 47	PS TiO_2 + Nb_2O_5 coating + surface activation
	Ref 48	Baghdadite feedstock synthesis
	Ref 49	PS MgO-SiO_2 coatings
	Ref 50	Production of refined Cr_2O_3 powder
3.4	Ref 51	TS W coating for radio-opacity of medical devices + biocompatible coating
	Ref 52	CS spraying + EDM cutting of bioresorbable stents etc.
	Ref 53	TS porous Ti or Ta coatings + grit blasting of oxidized outer layers
	Ref 54	Fixture for concurrent coating of multiple implant components
	Ref 55	Open-pore biocompatible coating filled with resorbable material
	Ref 56 and 57	Pre-oxidation of Zr substrate + PS ZrO_2 coating
	Ref 58	PS or HVOF ceramic coating + diffusion bonding
	Ref 59	CS composite bonding layer between thermoplastic substrates and ceramic or metallic coatings

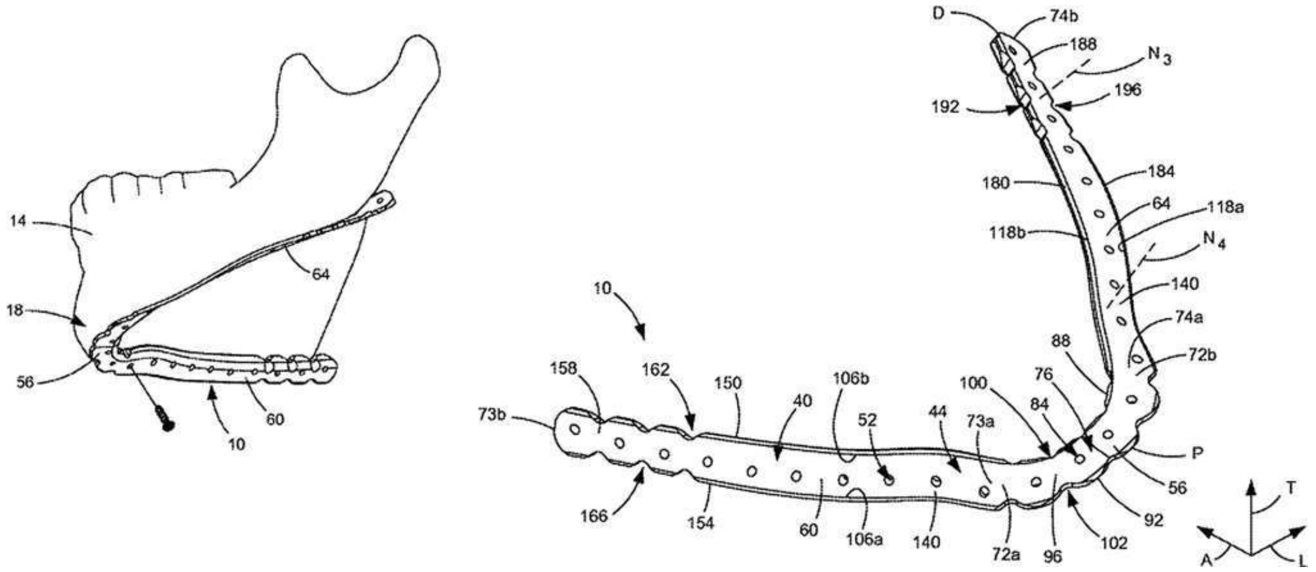

Fig. 4 An illustrative schematics compiled from the images provided in patent (Ref 60)

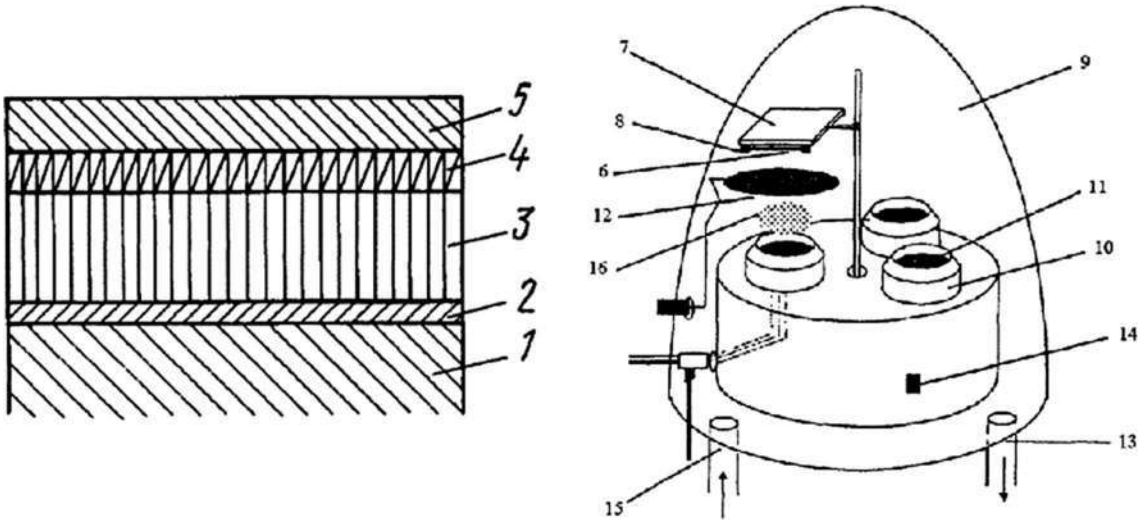

Fig. 5 An illustrative schematics compiled from the images provided in patent (Ref 61)

rotation, axial deflection and anterior/posterior translation), thus resulting in a more natural range of movement of the patient. The disk comprises a superior end plate and core, a flexible inferior core connected to its superior counterpart, an inferior end plate, and two PEEK inserts. The end plates comprise biconvex surfaces to provide an anatomical fit to the vertebral body and are covered by plasma-sprayed hydroxyapatite or titanium coatings. The disk is useful for replacing a diseased or damaged intervertebral disk during the spinal fusion procedure.

Two years later, the authors of Ref 67 filed a patent on a similar topic, artificial disk (Ref 68) for repairing and replacing intervertebral disks of a patient injured or damaged as a result of aging, trauma, fractures, degenerative disk disorder or a herniated disk. Designed for anterior or posterior procedures or minimally invasive surgeries, the disk also enables or restricts six degrees of movement and is compatible with a non-anterior surgical procedure. This time, shape memory alloys such as nitinol are used for the disk materials, providing increased durability. The superior and inferior end plates of the disk are treated with hydroxyapatite or titanium plasma-sprayed coating to encourage bony on-growth, thus improving strength and stability of connection to the underlying bone such as vertebral body. The rectangular-shaped prosthetic disk further provides a slim profile allowing easier insertion into the intervertebral space (Fig. 8).

Another orthopedic spine implant used, e.g., for the treatment of (lumbar) spinal stenosis is a device comprising of a couple of vertebral attachments, into which magnets

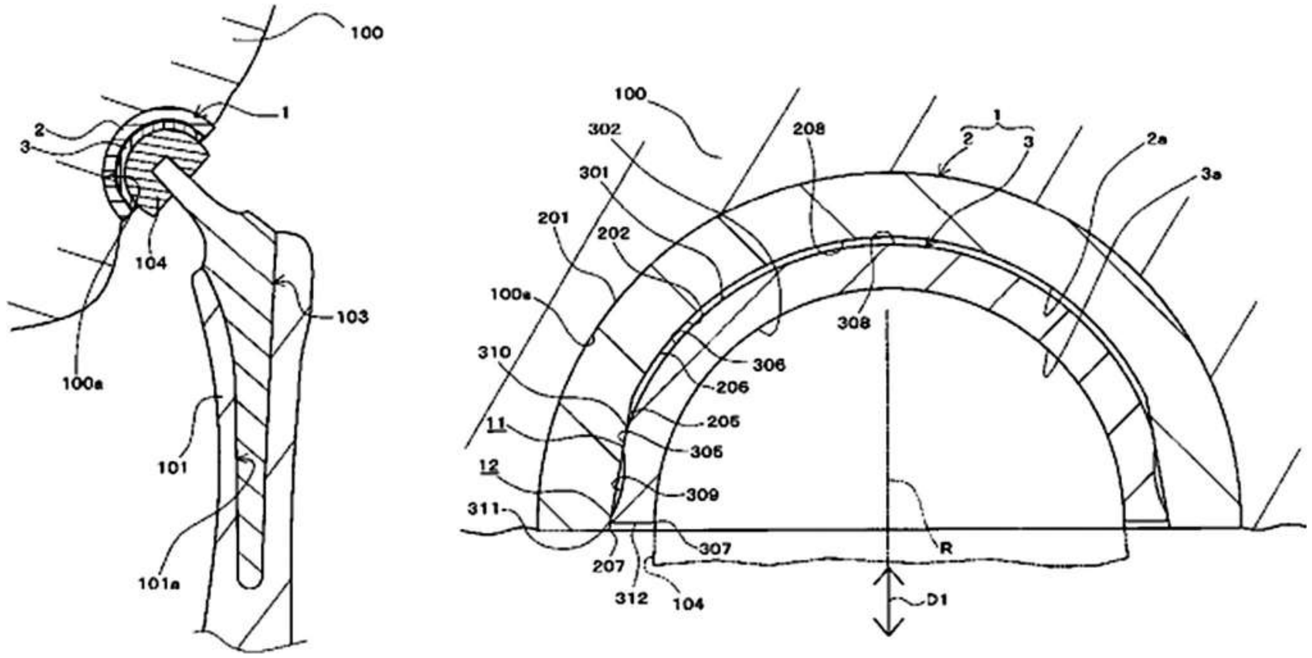

Fig. 6 An illustrative schematics compiled from the images provided in patent (Ref 63)

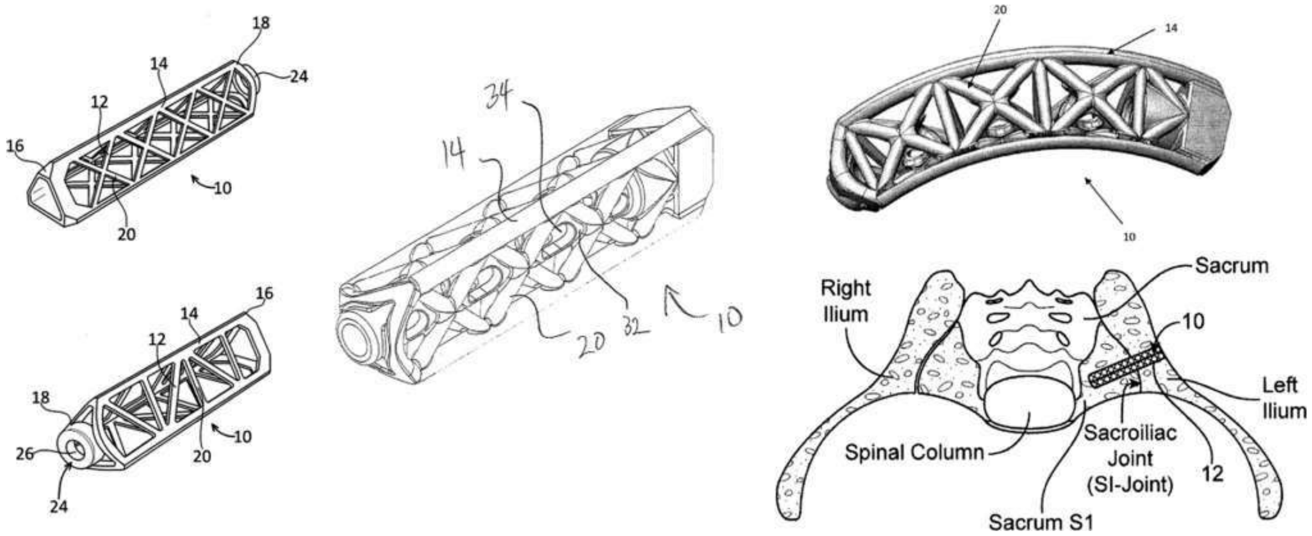

Fig. 7 An illustrative schematics compiled from the images provided in patent (Ref 64)

were incorporated (Ref 69). The attachments are either surface roughened or plasma-sprayed with hydroxyapatite or porous metallic coating to enhance their fixation to the spine. The magnets are made of nickel-plated, gold-coated neodymium grade N52. The device utilizes the magnets to balance in-plane and out-of-plane forces to provide an appropriate separation of the vertebral attachments during physiologic loading, thus reducing or eliminating the spinal stenosis and providing a constant relief on a nerve.

Another spinal plate for joining adjacent vertebrae to treat spinal deformities has a ridge connected to its bottom part that aids in attaching the plate to bone (Ref 70). The plate is applied over multiple vertebrae so as to prevent the vertebrae from relative movement. The whole ridge is treated with a plasma-sprayed coating such as hydroxyapatite and titanium to encourage bony on-growth, thus stabilizing or strengthening the interface. The spinal plate's intended uses include treatment of a herniated disk, rheumatoid arthritis, infection and tumor.

A concept of a flexible acetabulum cup is presented in Ref 71. The plasma-sprayed hydroxyapatite-covered cup has an inner bearing surface with a partly spherical portion and also two independent, outwardly bowed arms spaced to define an opening in the cup rim. Through the cup

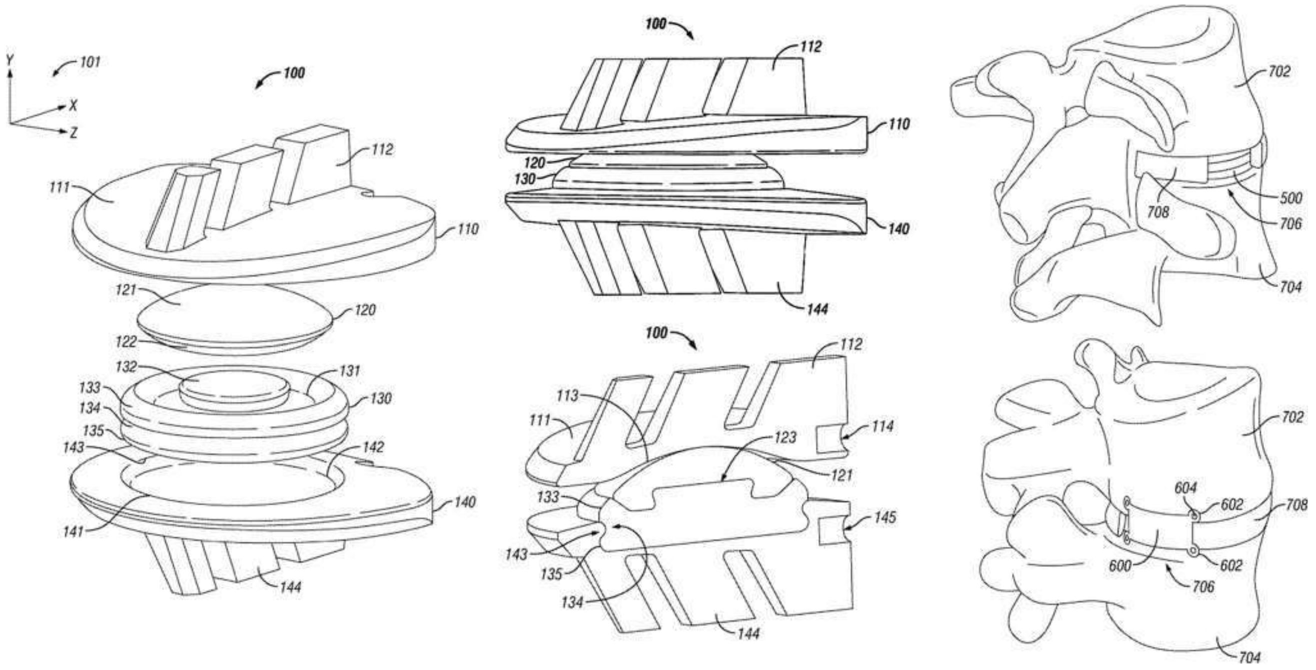

Fig. 8 An illustrative schematics compiled from the images provided in patent (Ref 68). Used with the permission of Globus Medical

geometry, the arms are prestressed toward each other upon insertion into the prepared acetabular socket. This arrangement prevents the polar area of contact from degenerating into a ring-type contact (Fig. 9).

A cost-effective artificial bone with high strength, excellent hardness, toughness and corrosion resistance is presented in patent (Ref 72). The bone comprises several layers of dissimilar properties: Its middle layer is made of a high-strength carbon fiber composite prepared by pre-soaking phenolic resin in unidirectional continuous fibers, while its outer layers comprise carbonized silicon layer, epoxy resin layer with silicon carbide, epoxy resin layer with plasma-sprayed hydroxyapatite, and, finally, hydroxyapatite layer provided with protein layer. The artificial bone is supposed to possess high bearing capacity, good tissue compatibility and good shaping performance. It is firm, durable, non-toxic, non-irritant and cost-effective.

A concept of hydroxyapatite-coated implant is filed in Ref 73. The hydroxyapatite coating is deposited from powder feedstock and has a rough surface, thereby enhancing the bone ingrowth. Importantly, it contains incorporated biocidal metal cations such as gold, platinum, palladium or silver. Through ion exchange, the implant then provides a controlled release of biocidal metal cations, thus preventing infection for extended time periods without causing toxic effects on body cells. The metallic implant is designated for surgical procedures such as, e.g., hip replacement or a prosthetic surgery such as, e.g., tibial prosthesis.

In 2013, the concept of the titanium implant from Ref 73) was further improved (Ref 74). In the updated version, anodizing was incorporated prior to the plasma deposition of hydroxyapatite coatings. Through the anodizing, hard oxide surface is created, containing numerous pits. Into the pits, biocidal silver ions are incorporated through immersion and a rough hydroxyapatite coating is then formed over the silver-containing oxide structure. After implantation, the silver ions can gradually leach through the ceramic coating into body fluids, effectively suppressing collagenous ingrowth without inhibiting the bone ingrowth. The implant is dedicated for surgical procedures such as replacement of a cancerous bone during prosthetic surgery or as a proximal tibia prosthesis.

A concept of titanium alloy-based orthopedic screw is patented in Ref 75. The surface of the screw is covered by hydroxyapatite, titanium or silicon-hydroxyapatite coating. Using the method, the screw exhibits better anti-pulling force and rotary torque, thereby preventing bolt loosening. The screw is embedded into a bone to provide better early stability and ensure a growth of microporous bone tissue structure, widening the application range and better clinical application value.

An implantable, hydroxyapatite plasma spray-coated device that provides structural support for the skeletal system such as the spine is patented in Ref 12. The device, made of PEEK, is dedicated for implantation to weight-bearing joints as a bone support. It has a deployable securing mechanism connected to an implant body. The 45-100-μm hydroxyapatite coating exhibited Ca/P ratio from 1.65 to 1.76 and $> 45\%$ crystallinity, with $< 5\%$ other phases present. Its adhesion exceeded 15 MPa. The

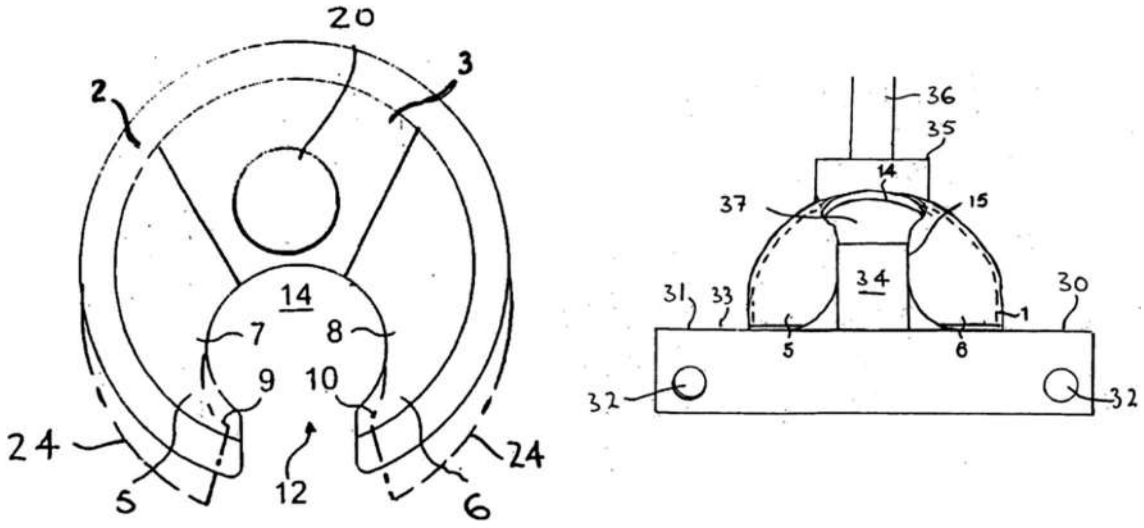

Fig. 9 An illustrative schematics compiled from the images provided in patent (Ref 71)

device is not fully specified in the document, and it is assumed that the patented novelty is the PEEK/HA combination, i.e., the device provides a bioactive coating of hydroxyapatite (HA) without altering the biocompatibility profile of the PEEK substrate. The device maintains the integrity of the hydroxyapatite (HA) coating and maximizes the strength of the implant.

3.1.3 Innovative Procedures

Plasma Spraying The method presented in patent (Ref 13) comprises plasma spraying of sandwich coatings: first, titanium dioxide or zirconium dioxide powder is deposited onto ceramic or polymer substrates to form an initial coating, followed by a further coating of hydroxyapatite (or metal). Within less than 10 min, plasma spraying or electrodeposition of pure titanium onto the initial coating is further applied. The time interval between the depositions is critical to prevent formation of cracks or even spallation of the first oxide layer. The initial titania or zirconia layer is claimed to avoid problems associated with poor adhesion and is useful for implants in prosthetic or orthopedic applications (dental, spinal, craniofacial or maxillofacial).

Thermally sprayed implants (surgical, dental) using special powder feedstock with two-component particles are presented in Ref 14. In this method, PVD, CVD, electroplating or the dipping method are suggested for the production of powder particles comprised of a core material (hydroxyapatite) and an outer shell (titanium). Such feedstock can then be deposited using a range of methods, spanning vacuum plasma spraying, gas plasma spraying, combustion spraying or even cold spraying. Using these, a composite coating is formed on the implant surface, exhibiting negligible porosity and good bonding with no signs of cracks.

Similar in principle to patents (Ref 14, 15), titanium-hydroxyapatite gradient coatings for titanium alloy implant surface are described in Ref 16. The sandwiched material fabricated via low-pressure plasma spray technique consists of a titanium layer, two titanium and hydroxylapatite mixed layers (ratios of 40/60 and 60/40) and finally a hydroxylapatite layer, arranged from inside to outside. As a result, a high stability and better bioactivity are reported. Such coating further exhibited reduced void content and an improved adhesion strength.

A method for multilayer plasma spraying of biologically active coatings onto a metal substrate of implants is patented in Ref 15. The coatings in this patent are graded, starting with 1-2 layers of titanium, followed by a layer comprised of a mixture of titanium and hydroxyapatite, while the fourth layer is solely formed of hydroxyapatite only. The implants are subsequently placed into a container with silver nitrate solution (a concentration of 0.04% $AgNO_3$) and exposed to 22 kHz ultrasound for 35 s at an ultrasound intensity of 9.6 W/cm^2. Such invention should promote fast and reliable osseointegration of the implant that also possesses bactericidal effect.

Thermally sprayed implants using modified hydroxyapatite feedstock are presented in Ref 17. The HA powder contains antimicrobial metal agent such as silver, copper or zinc, prepared by ion exchange or solgel methods. The powder is then plasma-sprayed onto selected parts of the medical implants. The presented method eliminates the need for post-process heat treatment to further consolidate the coating or bond it to the substrate and eliminates the need to blend the HA powder with silver-containing powders to incorporate silver into the coating. Such coated implant reduces the risk of postoperative infection at the site of the implant.

Similar to the concept of Ref 17, antimicrobial type of hydroxyapatite composite coating vacuum plasma-sprayed (10-30 kPa) on Ti6Al4V alloy is patented in Ref 18. The feedstock includes 1-5% metallic silver powder particles of 20-100 µm diameter as an antimicrobial additive ingredient, which is ball-milled into the original hydroxyapatite feedstock. Interestingly, the original hydroxyapatite particle diameter was smaller, 10-100 µm. The final composite coating exhibited excellent antimicrobial effect of more than 95% to Escherichia Coli, Pseudomonas aeruginosa and Staphylococcus aureus. The exosomatic cytotoxicity grade of such composite coating was zero, and the coating showed no cytotoxicity.

Another method of improving hydroxyapatite antibacterial properties is patented in Ref 19. By mixing of a hydroxyapatite powder and povidone iodine particles, the resulting vacuum plasma-sprayed coatings deposited on titanium and titanium alloy substrates retained 1-3% iodine content. Such composite coating exhibited good antibacterial performance and antibacterial kill rate for Escherichia coli, Bacillus pyocyaneus and Staphylococcus aureus higher than 95%. The composite coating retained good osseoconductivity, biocompatibility and showed no cytotoxicity.

Yet another bioactive coating doped with antibacterial content is patented in Ref 20. Specifically, the patent deals with hydroxyapatite coating containing silver ions (silver salt, in fact) on a surface of the substrate deposited by suspension plasma spraying. Misleading information on “the substrate material containing silver is added into the hydroxyapatite suspension” is provided in the text. The substrate materials from the patent involve titanium alloys, stainless steels, cobalt alloys, ceramic materials such as aluminum or cobalt oxides, and biomedical composites containing metal or ceramic. On these, an even coating is formed while avoiding releasing of the antibacterial ingredient.

Another antibacterial agent-containing coating was patented in Ref 21. The central part of the cementless implant (e.g., hip prosthesis for traumatology or orthopedics) has a plasma-sprayed calcium phosphate (e.g., hydroxylapatite) layer formed from powder feedstock and also 0.5-20 µm antibacterial-active ingredients (silver, copper, zinc). In detail, the method suggests replacement of calcium ions in the crystal lattice of the calcium phosphate by the metal ions through ion exchange. This is supposedly achieved in the hydroxyapatite precipitation phase by addition of the respective metal salts. It is suggested that the utilization of hydroxylapatite and Ag enables a rapid growth of bone tissues and achieves reduction of operative and postoperative infection risks without affecting the process of bone growth.

In Ref 22, plasma-sprayed total replacement of femoral and acetabular components is presented. The cementless hip implant has a transition portion whose outer surface is provided with a protective porous surface layer (hydroxyapatite, titanium) aimed at collecting the potential debris from the acetabulum. The main body of the prosthesis is further equipped with an integrative layer of (5-200 nm long) nanotubes directly formed at its surface via electrochemical methods. The nanotubes are chemically identical to the implant material (titanium alloys such as Ti6Al4V, TiNbTa and TiNbZr) and fix the anchoring shaft in the bone tissue. The porous layer should further prevent debris, potentially originating in the acetabulum part, from contact with the surrounding tissues.

Suspension Plasma Spraying Porosity and pore size are critical in terms of osseointegration. In Ref 23, a simple and inexpensive method for preparation of plasma-sprayed hydroxyapatite coating with enhanced porosity on biomedical material such as titanium is presented. The principle of the preparation is usage of hydroxyapatite suspension, into which a pore-creating agent is added, stirred and subsequently plasma deposited. Specifically, ethanol, ammonium carbonate, ammonium bicarbonate, hydrogen peroxide or deionized water could be used as the agents, provided the suggested content of 16-45% is used. As a result, the porous hydroxyapatite coating should be helpful for oxygen and nutrient substance transfer, discharge of metabolism waste and biological activity elevation, thus providing a suitable microenvironment for cells and tissue regeneration.

In Ref 24, a system for feeding hydroxyapatite suspensions is patented. The system comprises a plasma spray torch, a suspension feed system, metal substrate and a substrate fixing rack. The novelty of the patent relies in using a simple, clamp-on system of the small-diameter feed nozzle (injection pipe) mounted to a fixing holder. The holder is easily attachable to the torch and, using that, the suspension could be injected directly into the high-temperature area of the plasma flame. This patent was filed in August 2011. Interestingly, an identical patent with a difference in only a few phrases was filed by the same authors in 2008 (Ref 25).

The same group of authors also filed a Chinese patent on preparation of hydroxyapatite coatings by suspension plasma spraying. The method involves fabrication of the hydroxyapatite suspension, its transfer into the jet and a formation of the hydroxyapatite biological activity coatings (Ref 26). The suspension fabrication was described in the text as a slow, drop-wise controlled reaction of diammonium phosphate and calcium nitrate. In the reaction, the pH was controlled to be 9-12 at 30-90 °C. After the reaction, "stewing for 5-15 min" is claimed, followed by aging for 24-48 h. The suspension feeding is provided either by using a compressed air flow, or a peristaltic pumping drain from a container with high-energy ultrasound wave vibration function. Injection into the plasma jet is done either using a small-angle atomizing nozzle in a radial direction or a small-diameter duct in a straight line jetting manner. As opposed to traditional powder spraying, the method claims to simplify the spraying process, save the sprayed material and energy, and produce coatings with uniform structure.

Preparation of nanoscale hydroxyapatite particles useful, e.g., as granular fill for direct incorporation into the hard tissues, as bone implantable materials, as tooth filling compounds, or as bone cements and dentifrices is patented in Ref 27. The method involves combining an amount of calcium ion source (calcium acetate) with phosphate ion source under essentially ambient conditions. The particles have the BET surface of 200-3000 m^2/g. Importantly, by reducing the aging time, Ostwald ripening of the particles is suppressed and their size distribution is maintained at 1-9 nm. They are thus effective in drug delivery because they are more capable of penetrating the cellular wall (actually, also more readily processable by cells and tissues for regeneration and resorption) and carry a much higher surface area for adsorption of drug molecules. The range also allows the particles to be used intravenously as a drug therapy or for transdermal drug delivery. The particles can be either grown directly onto the metal surfaces without the need for any high-temperature processing, or can further be used in conventional processes such as solid-state sintering for polycrystalline ceramics, polymer-melt processing for polymer-ceramic composites or suspension plasma spraying for hydroxyapatite-coated titanium implants.

Calcium phosphate-based coatings fabricated by suspension phase plasma spraying were enhanced by the addition of collagen in Ref 28. The addition of collagen into the porous Ca-P coating (hydroxyapatite, tricalcium phosphate) structure is advantageous for the bone formation, as the phosphate-collagen composite coating could be loaded with growth factors or functional polypeptides for accelerating bone formation. The exact mechanism of collagen addition is not known from the patent. As a substrate, biomedical-grade titanium- or cobalt-based alloys or ceramics such as aluminum or zirconium oxides are suggested. Reportedly, the material is simple to prepare and has a low production cost, has better mechanical properties and significantly increases the success rate of implantable device, speeds up healing process, improves osteogenic activities of calcium phosphate bioactive coating, effectively accelerates cell adhesion, proliferation and differentiation, accelerates bone formation and early fixation of implants, improves performance for induction of the bone formation and accelerates early bone ingrowth.

HVOF Another innovation in two-component feedstock use for treatment of bone or joint implants is patented in Ref 29. Such treatment involves joint co-spraying of hydroxyapatite (5-97 wt.%) and titanium (3-95 wt.%) feedstock powders in at least one cycle by high-velocity oxy-fuel method or high-velocity flame spray method, thereby giving rise to 50-500 µm coatings containing 0.01-5 wt.% $CaTiO_3$ formed by an in situ reaction.

Cold Spraying Based on two different methods, simple patents on fabrication of hydroxyapatite coatings using cold spraying (Ref 30) and microbeam plasma spraying (Ref 31) were filed in China. The former method is claimed to be used for tooth root and artificial joints by using "baked" 28-53 µm hydroxyapatite powder (note that there is some uncertainty in the English translation) and its helium-argon deposition at rates of 0.05-0.50 g/min. Despite the feeding, high deposition efficiency is mentioned. The latter method involves spraying of dried hydroxyapatite powders onto a matrix of biomedical metal. The average powder diameters are also provided as 28-53 µm, while the transversal speed of the robot arm ("the speed of the gun pendulum" is mentioned in the original English translation) is given as 180-250 mm/s. Other parameters provided for the patent are standoff distance of 10-20 mm and 500-600 °C temperature and 2.5-3.0 MPa pressure of the nitrogen working gas. The method claims to be able to obtain hydroxyapatite coatings with high degree of crystallinity and good biological stability, while avoiding pyrolysis of HA and reducing loss of the hydroxyl groups. The final coating thickness is not provided in the text.

Post-Processing In Ref 32, a post-processing method for improving crystallinity of plasma spray-deposited hydroxyapatite coatings is introduced. The crystallization involves enclosing the hydroxyapatite-coated product in a sealed container, exhausting the container to a vacuum of 1×10^{-1} to 1×10^{-5} Pa and introducing saturated steam under 0.5-2 MPa pressure (1-50 kg/h feed), followed by container hydrothermal recrystallization at 500-900 °C for 2-6 h and, finally, cooling. The efficient and stable method can be used for improving crystallinity of plasma-sprayed hydroxyapatite coating used for surgical implants.

Another post-treatment method of increasing the plasma-sprayed hydroxyapatite coatings crystallinity is patented in Ref 33. The procedure involves impregnation of the coatings in an 0.1-10 mol/L electrolyte solution where all anions are hydroxide ions only. Anodic galvanostatic treatment follows, transforming any non-crystalline hydroxyapatite content due to the localized high temperature originating from the electrochemical reaction around the anode; the non-crystalline calcium phosphate in the coating electrochemically reacts with the hydroxide ions around the anode and converts into hydroxyapatite, leading to an increase in the coating stability. As an added benefit, the anodic treatment polarizes the coating and generates a large amount of negative charge, thereby increasing its biological activity. The method is claimed to have a short treatment time.

An efficient and economical method of post-processing plasma-sprayed HA coatings to obtain nanostructured material is patented in Ref 76. The method comprises vacuum plasma spray deposition of the coatings, followed by their hydrothermal treatment at 150-300 °C, rinsing the treated hydroxyapatite coating and, finally, its drying. Thereby, nanostructured hydroxyapatite coating with improved biocompatibility, bioapplicability and bioactivity, superior osteoacusis effect, excellent protein and heavy metal adhesion, enhanced antibacterial performance and high density and crystallinity, prospectively useful as a bone replacement in orthopedics or dental field is obtained.

Surface nanocrystallization method for hydroxyapatite coating is presented in Ref 34. In the method, a double hydroxyapatite coating is presented; the first layer of 30-60 μm deposited via plasma spray process and the second layer of 20-40 μm deposited by "bi-technology process," i.e., plasma spraying and a crystallizing treatment (unfortunately, no more details could be retrieved from the source). The coating reportedly exhibits excellent biological compatibility, comparatively quick osteogenesis speed, firm interface adhesion and a favorable long-term stability.

3.2 Titanium

3.2.1 Orthopedic

Plasma Spraying A modified hip implant with enhanced flexural capability and load-bearing qualities was patented in Ref 77. While the titanium plasma-sprayed (or sintered titanium wire) proximal end of the implant resembles that of the classical hip prosthesis, the distal portion was modified substantially to allow additional flexing: It has a cylindrical, constant diameter central aperture, where the wall thickness decreases progressively toward its end, including machined lateral cuts or slots on the outer surface, forming a continuous helix (Fig. 10). The selection of the slot geometry was made to prevent metal-to-metal contact on the adjacent surfaces during flexure that would eventually lead to formation of wear debris. The added flexibility should prevent bone tissue loss due to a lack of bone load-bearing capacity and reduce the stresses at the stem tip, thus preventing the postoperative thigh pain. Reportedly, such concept could be used for hip femoral head replacement, but also knee femoral and tibial component, humeral component for shoulder, elbow humeral component and bone plates as well as interlocking nails.

A concept of dual-taper lock modular prosthetic hip system for performing minimally invasive arthroplasty in hip (or shoulder) is presented in Ref 78. The system has a femoral neck implant component attached to a head, which is fitted within an acetabulum, allowing rotary movement. The outer acetabulum cup surface is designed to have a porous surface through plasma-sprayed titanium to grip the acetabulum, thus preventing slippage of the system during the insertion process. The system is further provided with a support sleeve made from cobalt-chromium, ceramic and stainless steel to achieve sufficient strength (Fig. 11).

A dedicated orthopedic device assembly for concurrent placing of implantable spacers between superior and inferior vertebral bones was patented in Ref 79. The device has a non-implantable placement instrument holding the implantable spacers and a cavity that is configured to contain a bone-forming material (Fig. 12). The assembly is manufactured with a porous ingrowth surface, such as titanium wire mesh or plasma-sprayed titanium and tantalum, and provided with a bioactive coating made of tantalum and/or carbon nanotubes in order to promote bone ingrowth or establish a mineralized connection between the bone and the implant, thus reducing the chance for the implant loosening.

An orthopedic intervertebral implant to be used as an intervertebral disk space, e.g., in the lumbar, thoracic, cervical, sacral, coccygeal region, is provided in Ref 80. It contains a fixation assembly rotated about its transverse axis covered by plasma-sprayed titanium coating to improve growth of bone (Fig. 13). The vertebral fixation members are carried by the assembly and moved in the superior and inferior channels to extend the fixation members. The implant is then inserted into the intervertebral space to achieve restoration of height and fusion of fractured bone segments and to locate the intervertebral space anywhere along the spine as desired.

A ball-shaped component for prosthetic joint such as spine joint fabricated from sintered titanium carbide substrate, a sintered polycrystalline diamond surface formed on the substrate and bone attachment surface plasma-sprayed from titanium is presented in patent (Ref 81). The substrate then comprises of 87.5 wt.% TiC and 12.5 wt.% Ti. The component exhibits sufficient abrasion resistance and improved strength, toughness and compatibility without stress or cracking between the substrate and the diamond layer.

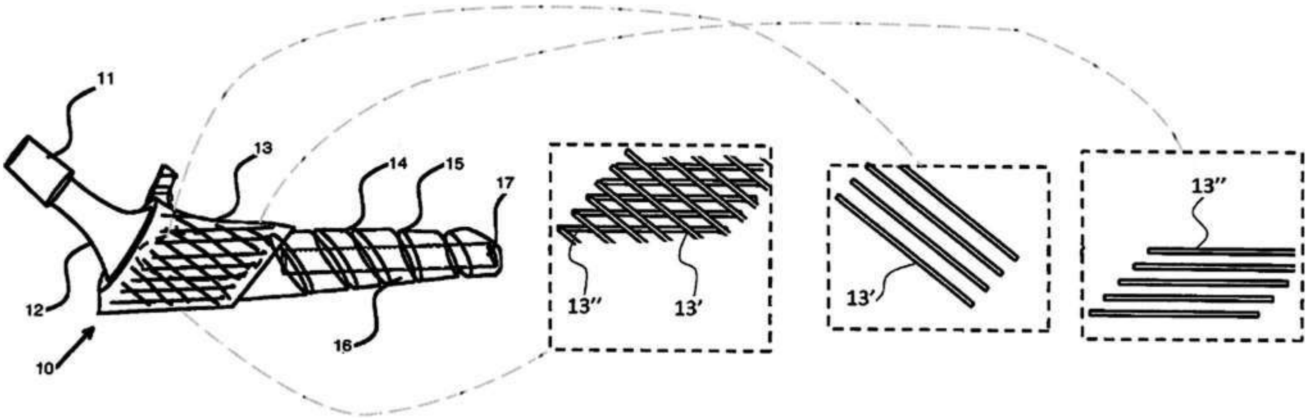

Fig. 10 An illustrative schematics compiled from the images provided in patent (Ref 77)

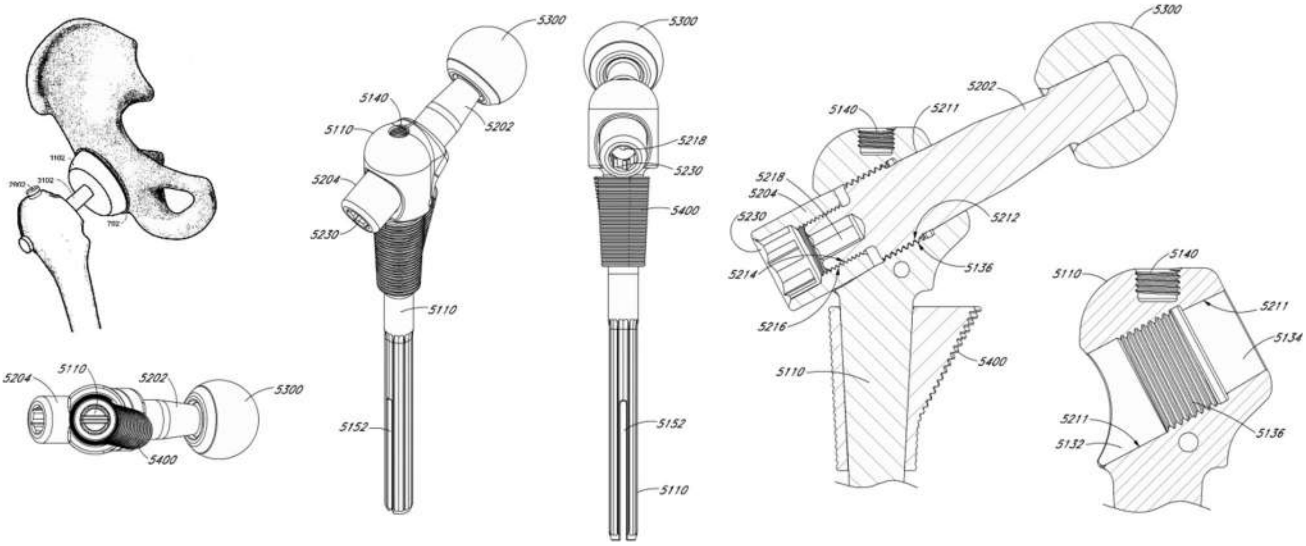

Fig. 11 An illustrative schematics compiled from the images provided in patent (Ref 78)

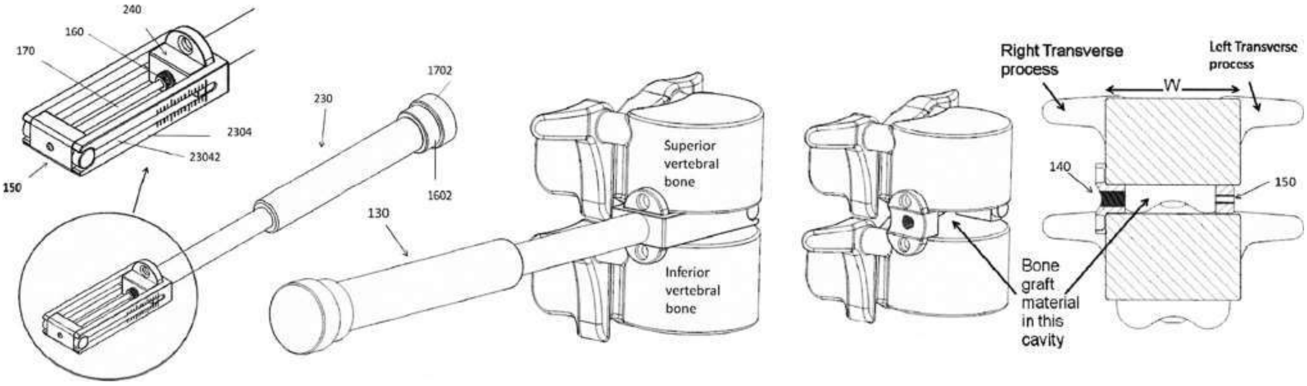

Fig. 12 An illustrative schematics compiled from the images provided in patent (Ref 79)

A combination of additive manufacturing, high-resolution computer tomography scanning and thermal spraying was presented in Ref 82. In the document, various stemless orthopedic implants to replace joint of shoulder are provided, starting with compaction of metallic powder into a component whose porous surface is replicated from a high-resolution scan of human bones. This is to promote ingrowth of tissue, along with a further, porous biological

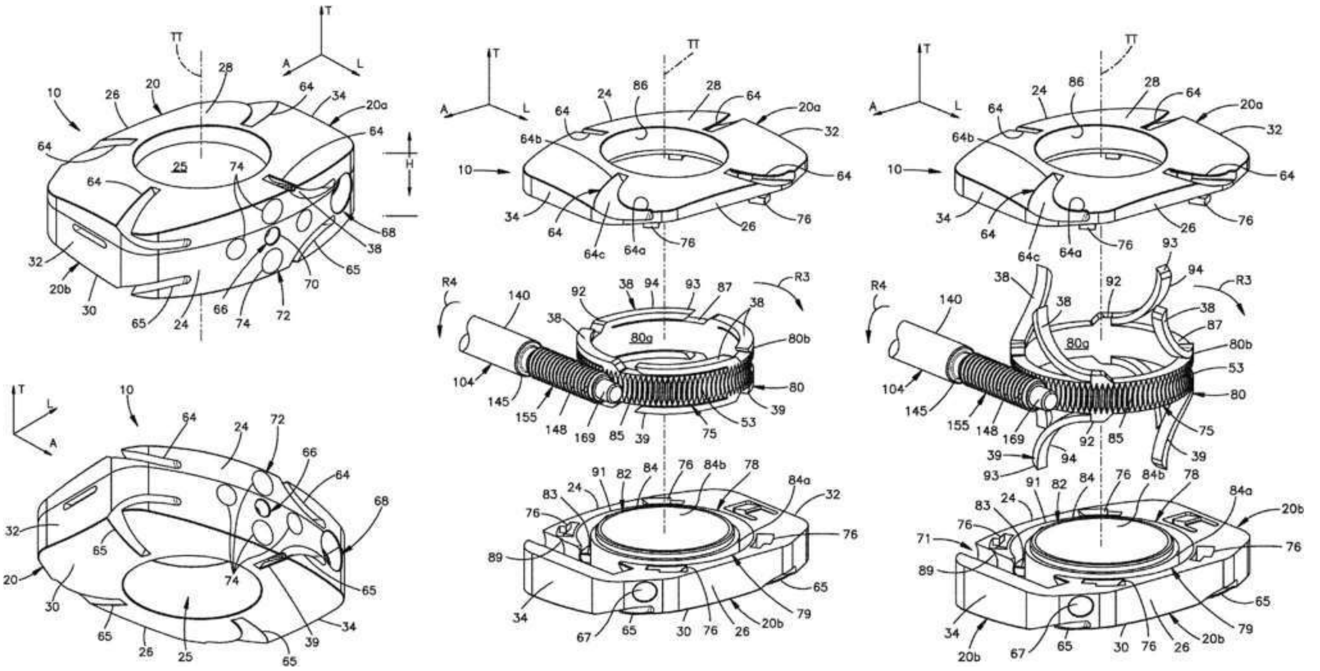

Fig. 13 An illustrative schematics compiled from the images provided in patent (Ref 80)

titanium surface coating created through plasma spraying. The implant uses a porous metal structure to mimic the trabecular architecture of the bone at a specific anatomical site where the implant is fixed. Generated by additive manufacturing technique, the time and cost of fabricating the implant should be reduced.

An important patent (Ref 83) was issued as late as 2008, in which a technique of covering a surgical implant for bone repair applications by layers of titanium of two granularities (20-50, 60-160 μm) and 15-55 μm hydroxyapatite is presented. The method for deposition was vacuum plasma spraying, and the obtained coatings thicknesses were 20-50, 70-150 and 30-100 μm, respectively. The coatings are claimed to have high adhesion.

An osteotomy implant used for internal fixation or fusion of a bone fracture is patented in Ref 84. The (e.g., PEEK) wedge of the implant helps to stabilize and orient the bone and can be produced in various sizes and shapes to fit the surrounding bone without any portion of the wedge protruding externally. The component surfaces can be roughened to provide an early stability and to ensure intimate osseointegration between the bone and the wedge. The osteoconductive structure comprises a plasma-sprayed titanium coating thin enough (2-500 μm) so that the component surface is transparent to imaging. Interestingly, the wedge core is deemed to have the same Young's modulus as bone (i.e., 3.6 GPa), thus preventing stress shielding of the bone.

A subcutaneous intramuscular mounting for a rigid transcutaneous implant is provided in Ref 35. The device uses polyurethane material in the bone stump that comprises a distance spacer, a socket and a shoulder part (Fig. 14). The adaptable and replaceable polyurethane pipe is fitted to the socket and has an antibacterial outer wall, i.e., a thermally sprayed titanium-based coating containing silver and, optionally, calcium phosphate. This provides the polyurethane pipe with a high germ barrier and antibacterial effects. The method is deemed cost-effective. However, no details on the deposition of the coatings onto the plastic substrate are provided in the document.

3.2.2 *Innovative Procedures*

Plasma Spraying Initially claimed as an orthopedic implant, the patent (Ref 36) could be considered as a general concept for deposition of thermally sprayed titanium onto nonmetallic substrates of various implants such as the shoulder, elbow, spine, hip, knee or finger. Furthermore, the titanium deposits are doped (0.01-20 at.%) with an x-ray-sensitive biocompatible metals such as tantalum. The atomic weight of such indicator metals is deliberately larger than that of titanium. The thermal-sprayed surface layer can be economically manufactured with an increased spatial resolution and excellent biocompatible properties and ensures desired acceleration of the healing process.

The patent (Ref 37) uses vacuum plasma spraying to deposit porous titanium (or titanium + additives) coatings onto implant surfaces for ingrowth of vascularized bone tissue. The open-pore biocompatible surface coating

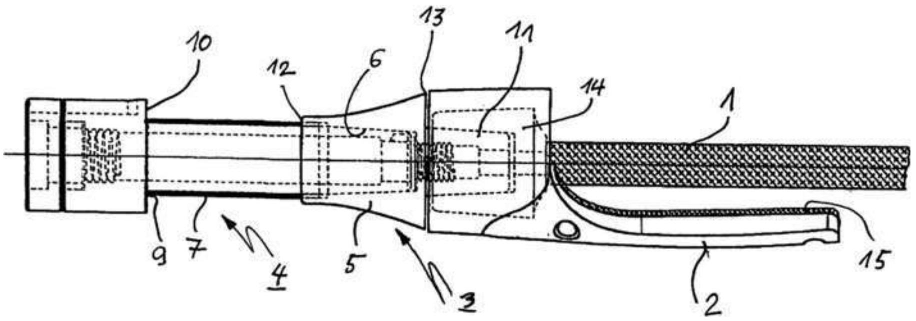

Fig. 14 An illustrative schematics compiled from the images provided in patent (Ref 35)

comprises a coherent pore network and has a defined surface area of at least 0.06 $\mu m/\mu m^2$ (edge length per unit area). These could be used in, for example, hip joint shafts or sockets, the femur or tibial components of a knee joint replacement, a component of a shoulder, elbow, toe or finger joint replacement, a lumbar vertebral fusion component, a component of an intervertebral disk replacement or a transgingival and orthodontic or dental implants.

Arc plasma spray method was patented for production of titanium coatings onto implant surfaces in Ref 38. The surface of the implant is further patterned through usage of template (“stencil”) prior to arc spraying of ~ 20-50 µm titanium powder. Thereby, the patterned hard tissue replacement material is manufactured efficiently with rapid early response and long-term stability.

A graded coating consisting of porous titanium, sphene (titanite, $CaTiSiO_5$) and titanosilicate ceramic deposited onto titanium-based implants surfaces was patented in Ref 39. Both coatings are deposited via plasma spraying. Before deposition of the sphene, micro-arc oxidation of the underlying surface is carried out. No further details could be derived from the document.

A somewhat broad patent was filed in Ref 40. The idea of the patent is concurrent (plasma) spraying of titanium powder and another powder without the need for their mutual milling or pre-sintering. The patent does not provide detailed information, aside from the remark that “the second material at least partially melts in the plasma and binds to the first material.” As substrate material for cementless fixation implants, titanium, zirconium, magnesium, tantalum or their alloys and cobalt-chromium alloys are mentioned, as well as a broad range of applications ranging from hip, knee, shoulder, spine, foot, toe, ankle or dental implants. The coating is presented as an open-porous structure providing micro-roughness for bone tissue stimulation, as well as macro-roughness for tissue/implant interlocking and an appropriate thickness for an integration zone. Reportedly, “an important advantage of the present method is a significant cost reduction for the production of an open-porous coating compared to the prior art.”

A method for producing a structured coating on the surface of a femoral knee joint implant involves application of a thin hardening layer, abrasive processing and deposition of titanium via plasma spraying (Ref 41). The implant is made of oxide ceramics, onto which a thin layer of silicate glass is applied and hardened by firing (silicate ceramic solder containing finely dispersed leucite, $K[AlSi_2O_6]$). Then, the layer of titanium is applied onto the surface structure by plasma spray technology (or CVD). A calcium phosphate layer is then applied as the last layer. The method provides a durable connection between the implant and the surrounding tissue or bone cement, increases the speed of bone integration and allows quick replacement by newly formed bone tissue after the implantation.

Cold Spraying A concept of producing cast or forged CoCr-based medical implants (ASTM F-75) covered by 5-3000 µm of titanium via cold spraying (gas pressures 2.5-6.5 MPa, gas temperatures up to 700 °C) is presented in Ref 42. The interface of the two materials is further strengthened via diffusion bonding occurring during a subsequent hot isostatic pressing of the coated component (480-1000 °C, 69-172 MPa, 1-5 h). The Ti-coated CoCr alloy medical implant has excellent resistance to corrosion and wear, as well as excellent fatigue life and biocompatibility.

A method of using two-powder feedstocks to produce thermally sprayed ~ 500 µm coatings of a given porosity (“aperture” in the original document) is presented in Ref 85. In the invention, titanium feedstock powder is mixed with magnesium and these are then sprayed onto Ti-based substrates via cold spray. As a key, subsequent step, high-temperature vacuum sintering takes place to obtain porosity of a given size range (30-200 µm) and content (30-65%). Importantly, the porosity is uniform and easily adjustable, thereby changing the modulus of the coating from 30 to 50 GPa. The adhesion of the coating reaches 60 MPa and can be used for production of artificial bone or tooth root.

3.3 Oxide Ceramics

3.3.1 Maxillofacial

Plasma Spraying Patent (Ref 86) provides information on the use of glasses and glass-based ceramics in dental and orthodontic applications. Manufacturing of such appliances (brackets, restoratives, replacements, inlays, onlays, veneers, crowns, bridges, implants, implant abutments, copings, anterior fillings, posterior fillings, cavity liners, sealants, dentures, posts and bridge frameworks) is achieved by thermal spraying of metal oxides onto substrates and, optionally, separating the coating from the substrates. The oxides provided in the patent comprise $>$ 35 wt.% aluminum oxide and a selection of metal oxides, such as boron oxide (B_2O_3), germanium dioxide (GeO_2), phosphorus (III) oxide (P_2O_3), silicon dioxide (SiO_2), tellurium dioxide (TeO_2), or vanadium oxide (V_2O_5) and rare earth oxides such as yttrium oxide (Y_2O_3), zirconium oxide (ZrO_2) and hafnium dioxide (HfO_2).

A patent on the use of nanostructured zirconia (ZrO_2) on the gingival part of a dental implant is provided in Ref 87. The gingival shoulder part of the implant is tapered and threaded. Plasma spraying is employed for the uniform coating deposition, while titanium or titanium alloys are used as base materials. The preparation process of the substrate involves soaking in an alkaline environment at 60-80 °C for 5-8 min, washing using acetone, rinsing with distilled water, surface treating and spraying with ethylene oxide. Such plasma spray-coated nano zirconia implants reportedly exhibit an excellent external appearance, biocompatibility and mechanical strength. No further information covering the deposition of nano-ZrO_2 could be derived from the patent.

Another design of a dental (tooth) implant is covered by patent (Ref 88). Made from ceramic materials such as zirconium or aluminum ceramics, or metal such as titanium or stainless steel, the implant body is inserted into a human jawbone, where the critical area is provided with a coating made from ceramic material. The rough surface coating is fabricated by using a plasma spray method, and the materials include zirconium oxide and, as a binder, silicon dioxide. That way, the implant possesses improved stability, while preventing damage and irritation of gum.

Thermal spray deposition to 6-50 μm thickness using a combination of aluminum oxide and zirconia is the core of patent (Ref 89). The coating is deposited on a metal (titanium, nickel titanium, Co30Cr5Mo vitalium or chrome cobalt) surface of, e.g., orthodontic arch-wire, partial denture clasp, dental implant, connector and abutment, whose surface is roughened and cleaned or etched before the deposition. The thermal spray process provides high bond strength and uniform thickness of the coating. The white ceramic surface coating itself further reduces and prevents growth of a biofilm.

Flame Spraying Antimicrobial dental implant such as artificial dental root, artificial tooth or artificial joint comprising of thermally sprayed brookite (TiO_2 polymorph) film on metal, ceramic or plastic substrates is provided in Ref 90. The coating is deposited via high-velocity flame spraying and exhibits superior antimicrobial activity in vivo as compared to the conventional antimicrobial products prepared using anatase-type titanium oxide as the active ingredient. Interestingly, the patent further suggests that the method can be applied for household products such as kitchen utensils, toilet products or even industrial products.

3.3.2 Innovative Procedures

Plasma Spraying A method of fabrication of acetabular shell cup through plasma spraying is detailed in two almost identical patents (Ref 43, 44). The method starts with a metallic mandrel that is sprayed with aluminum oxide first. After a suitable thickness is reached, the spray composition is gradually changed through a mixture of aluminum oxide, titanium and titanium oxide. The relative content of the aluminum oxide is decreased to the point where only a mixture of titanium and titanium oxide is sprayed. After the spraying process, the acetabular shell is extracted from the mandrel to form a freestanding coating part. Advantageously, the mandrel (fabricated via casting of slurry) is reusable due to its thermal stability. The methodology could be applied to obtain femoral, tibial or glenoid implants as well as tibial trays.

Another general method patent (Ref 45) covers the preparation of nanostructured titanium oxide coating layers with improved bioactivity. Preparing the bioactive layer includes deposition by atmospheric plasma spray method, washing and UV radiating for at least 12 h for biological activation. When in contact with body fluids, bone-like apatite is formed on the surface of the layer.

A method patented in 2006 (Ref 46) involves making of nanostructured biocompatible 1-550 μm coating for promoting osteoblast growth on implants such as artificial hip joints under controlled spray parameters. The nanostructured coating is produced having enhanced mechanical properties and biocompatibility. Nanostructured agglomerated zirconia, titania, alumina or hydroxyapatite of the sizes from 0.1 to 200 μm are covered in the document as the coating materials. As the methods, atmospheric plasma spray, HVOF, VPS, HVAF, low-pressure plasma spray (LPPS) and even high-frequency pulse detonation (HFPD) plus suspension variants of these are mentioned.

Preparing of titanium-niobium oxides composite coating provided with biological activity for surface activation treatment is patented in Ref 47. Prior to their 30-50 kW atmospheric plasma spray deposition, the two powders (TiO_2, Nb_2O_5) are wet-mixed in alcohol bonding agent (5-40 wt.%), ball-milled, dried, ground and sieved to a 25-105-μm fraction. After the coating formation, soaking in "energy body fluid" (no details provided, presumably SBF) to induce bone-like apatite on the surface is used. The raw materials are easy to obtain, and the process is easy to control.

As a material prospectively competing with hydroxyapatite, plasma spraying of baghdadite ($Ca_3Zr[/Si_2O_7/O_9]$) onto titanium alloys is patented in Ref 48. Such coating has an adhesion exceeding 28 MPa, good bioactivity, low degradation rate in tri-hydrochloride buffer solution (possibly TRIS buffer), long-term stability and induces a formation of bone-like apatite (in simulated body fluid). The patent also includes a method of baghdadite powder synthesis via a high-temperature solid-phase reaction, its mixing with polyvinyl alcohol aqueous solution (5-10 wt.%), drying the mixture and sieving the powder to 45-170 µm.

Another method related patent involving use of oxide ceramics was filed in Ref 49. This time, titanium or titanium alloy hard tissue replacements are covered with magnesium silicate coatings ($MgSiO_3$ or $Mg_2Si_2O_4$) mixed with "a little glass phase" (undisclosed). Air plasma spraying technology is used for the deposition, with argon and hydrogen as arc plasma gases at 35-45 L/min and 7-15 L/min flows, respectively, standoff distance 80-120 mm, spray current 500-700 A and powder feed rate of 12-18 g/min. Such coating should enable the implant to resist damage from physiological body fluids for a long time and facilitate its long-term stabilization.

The patent (Ref 50) describes a method for production of a refined chromium oxide powder. The method comprises spray drying of a raw chromium oxide feedstock, its fusing and crushing, followed by its acid and reduction washing. This results in a reduced amount of hexavalent chromium in the product (< 2 ppm), thereby achieving biocompatible threshold levels that can be used in thermal spraying of a Cr_2O_3 coating onto a medical implant. Packaging the refined chromium oxide powder to limit oxidation and absorption of moisture is also part of the patent.

3.4 Other/Non-disclosed Materials

3.4.1 Maxillofacial

Plasma Spraying Fabrication of dental components via several methods is patented in Ref 91. As the base material, beta-phase TiZrNbTa alloy with improved compressive strength, fatigue resistance, low modulus of elasticity and biocompatibility is manufactured from 50 to 250 µm powder feedstock. The bulk material can be produced from the feedstock by several methods, all included in the patent document: thermal spraying of the powders onto a bed, selective laser melting, electron beam melting, three-dimensional printing, vacuum induction melting, vacuum arc reflow, melting plasma arc fusion, hot isostatic pressing or metal injection molding.

A method combining plasma spray deposition and sintering to produce dental implants is presented in Ref 92. Using metal such as Ni, Cr, Ti, Pt, Pd, Cu, Zn, Au and Ag as a substrate, a non-specified bioactive bond coat material is plasma-sprayed using argon, helium, nitrogen and hydrogen as plasma-forming gases first. Subsequently, a second ceramic layer (dental porcelain made of SiO_2 quartz, feldspar and other oxides such as ZrO_2, Al_2O_3 or even hydroxyapatite) is sintered from powders onto the surface of the plasma-deposited coating. Thereby, the adhesion strength between the metal cap and the dental porcelain layer is increased, and the metal caps are protected from the influence of metal ions in the human body, further reducing its oxidation. The dental implant can be precisely positioned on the gums, and the gum wear can be reduced to improve the patient comfort.

A tooth (or bone) implant plasma spray-coated with strontium-doped calcium polyphosphate (no further information) layer onto titanium substrate is patented in Ref 93. With such coating, the implant exhibits enhanced biological activity and bone cell ingrowth and vascularization. It can further improve the implant and tissues interface compatibility and facilitate synostosis. For the deposition, 50-100 µm powders are used and nitrogen as plasma-forming gas is suggested in the patent. The substrates are annealed at 700-800 °C prior to deposition.

3.4.2 Orthopedic

Plasma Spraying An expandable orthopedic implant for replacing hip joint is presented in Ref 94. The acetabular implant comprises two independent segments separated by a slit (Fig. 15). An expansion member placed between the segments can be adjusted to displace the portions relatively to each other, thus expanding the implant size. A screw passes through the implant to connect the implant to the acetabulum. The implant allows controlling the amount of torque applied to the expansion member, so that a proper press fit and interference with the surrounding bone is achieved. The implant is plasma-sprayed with a porous ingrowth material to improve strength and flexibility. Aside from the hip prosthesis, the concept could also be used for spine arthroplasty surgery, cranio-maxillofacial procedures, knee or shoulder arthroplasty, foot, ankle or hand extremity procedure.

A hollow, tubular threaded bone implant for fixation of sacroiliac joint is patented in Ref 95. The titanium implant body has a set of openings ("pores" in the original text) that do not extend through its entire thickness and a set of threads machined onto its exterior surface (Fig. 16). The former encourage tissue ingrowth into the implant, while the latter help inhibit loosening of the component in the bone. The implant includes a safety feature for preventing being driven too far into the bone. Importantly, the implant eliminates the need for autologous grafts, bone graft material, additional screws or rods, hollow modular anchorage screws, cannulated compression screws, cages, or other fixation screws, allowing less invasive surgical techniques. A porous plasma-sprayed coating with irregular surface supports a stable bone fixation/fusion.

Similar in concept to the patents (Ref 64, 65), a bone fixation implant for fusion of sacral-iliac joint is provided in Ref 96. The idea involves inserting the implant laterally through ilium, sacral-iliac joint and sacrum, stabilizing the adjacent bone segments (Fig. 17). Since the bony ingrowth region has a porous plasma-sprayed coating on its surface, a biomechanically rigorous fixation system is created to support a reliable fixation and acute weight-bearing capacity, and the pain generated from sacral-iliac joint is relieved in a minimally invasive manner.

A cementless implant with a patterned surface used, e.g., in knee replacement or tibial or femoral repairs is described in Ref 97. On the surface, tapered protrusions in a form of trapezoidal blades extending from the base are to mate with human bone. Additionally, each of the protrusions has a textured or porous surface to increase the area for bone growth provided by a thermally sprayed coating.

A multiple-step procedure for production of implants used for repair of the ends of bones at orthopedic joints is covered in patent (Ref 98). To match the Young's modulus of the human cortical bone, the implant is created from structurally strong isotropic graphite. It is then coated with hard, isotropic > 100 μm pyrolytic carbon layer of a density 1.7-2.1 g/cm^3, hardness of at least 200 HV and surface roughness of $R_a > 2$ μm, formed from aggregated 0.15-0.5 μm carbon particles. Porosity of the layer is provided as 2-10% with the pore sizes suggested at 0.05-0.1 μm. This layer is then polished and serves as a receiving surface for a 2-10-μm metal coating deposited via PVD process. During the PVD, the metal penetrates into the pores to create a secure bond and smoothen the pyrocarbon surface. Lastly, plasma spraying of a > 25-μm biocompatible metal layer onto a designated portion of the implant is carried out. The implant produced through this method should promote attachment to bones without the need for ancillary cement and exhibit high strength, wear resistance, resistance to cyclic fatigue, biocompatibility, and a modulus of elasticity similar to cortical bone.

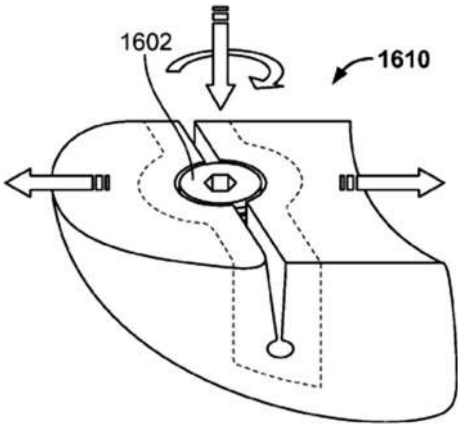

Fig. 15 An illustrative schematics compiled from the images provided in patent (Ref 94)

A concept of an apparatus to provide coupling pads for an implant is presented in Ref 99. These are made of porous metal with suture accepting holes that help attaching the surrounding soft tissue to the implant. The area defined by the notched surface of the soft tissue coupling mechanism is filled with porous plasma-sprayed layer allowing vascularization/angiogenesis and nutrient delivery important for soft tissue ingrowth. Mechanically, the pads are attached to the implant through a locking mechanism such as threaded fastener, which prevents unwanted movement (Fig. 18). The complete implant is then implanted into a bone with the soft tissue attachment pads. The concept could be used for, e.g., shoulder arthroplasty.

3.4.3 Innovative Procedures

Plasma Spraying A unique solution for sensitive medical devices such as pacemakers, defibrillators, nerve stimulators, hearing aids or drug pumps with incorporated radio-opaque and biocompatible coatings is patented in Ref 51. In the method, a radiation shield made of tungsten is integrated with an implantable medical device by thermal spraying, partially surrounding its electronic circuitry (Fig. 19). Subsequently, the device is provided with a biocompatible coating defining at least a portion of its outside surface (bioglass, hydroxyapatite, titanium, titanium alloys, alpha-alumina, stabilized zirconia, or apatite ceramics). In an example where the device is a nuclide source for destroying malignant cells, such arrangement allows prospective radiation to be directed only to the tissue to be treated.

A rather universal patent filed in 2017 (Ref 100) deals with the method of thermal spraying (atmospheric plasma and vacuum plasma) deposition of ceramic layers onto surfaces of components for functionalization of medical devices, preferably prostheses and implants. The patent lists the following materials: Al_2O_3, ZrO_2, SiO_2, bioglass, TCP and hydroxyapatite. However, no further details could be acquired from the documentation.

A method of deposition of non-oxidized metallic (e.g., titanium, tantalum) coatings onto medical devices such as

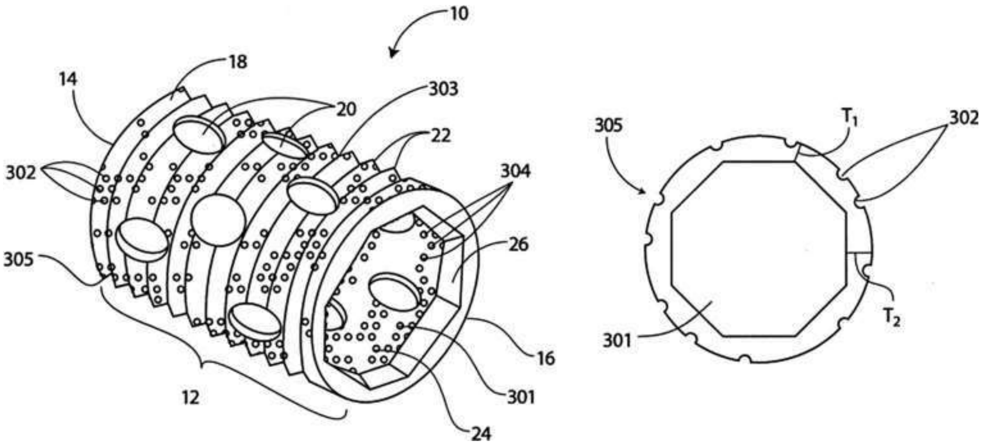

Fig. 16 An illustrative schematics compiled from the images provided in patent (Ref 95)

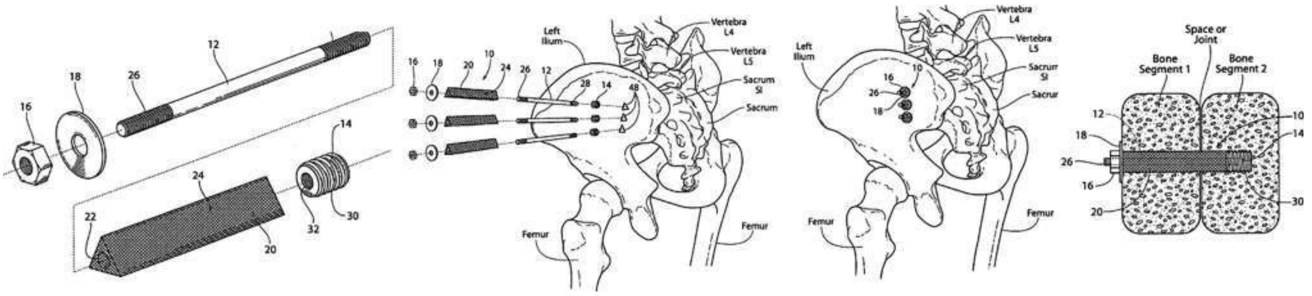

Fig. 17 An illustrative schematics compiled from the images provided in patent (Ref 96)

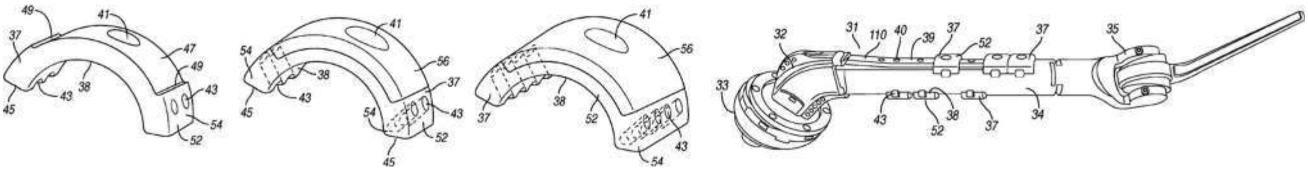

Fig. 18 An illustrative schematics compiled from the images provided in patent (Ref 99)

implants via atmospheric plasma spraying is patented in Ref 52. The core of the idea is spraying of rather big metallic powder particles (180 μm) to form a thicker (0.25-5 mm), porous (> 35%) coating and subsequently removing the upper parts that may have been oxidized or formed nitrides, hydrides, carbides in the process. The removal process involved grit blasting with abrasive media that is soluble in a passivation solution. A part of the document is concerned with a potential use of inert gas shrouding to minimize the oxidation levels. The method should allow safe, effective and economical formation of the porous metal coating with high purity and desirable material properties such as high tensile strength, fatigue strength, strength-to-weight-ratio, flexibility, toughness, wear resistance and biocompatibility. The patent also covers arc wire and HVOF spray processes for achieving the same.

Also connected to biomedical use, a complex system for concurrent application of coatings onto multiple implant components is designed in Ref 53. The basis of the system is a holding fixture having multitude of mounting stations for installing of the implants such as femur balls or hip joint cups. Each of the mounting stations revolves individually, allowing the implants to be coated from all sides. Temperature of each of the implants is monitored independently. The system ensures economical and rapid application of the coating on the medical implant component with less residual stress, high quality, enhanced deposition efficiency and longevity, minimizing overheating of the coating layer.

A method for production of open-pore biocompatible surface layer filled with resorbable material is patented in Ref 54. The layer is deposited onto a surface of an implant with a thickness of 0.5-1.5 mm, thereby allowing ingrowth of osteoblast cells. The viable methods for deposition include vacuum plasma spraying, physical vapor deposition (PVD), chemical vapor deposition (CVD), solgel process or sintering. At least 30% of the pores should be filled with the bioresorbable material of particle sizes from

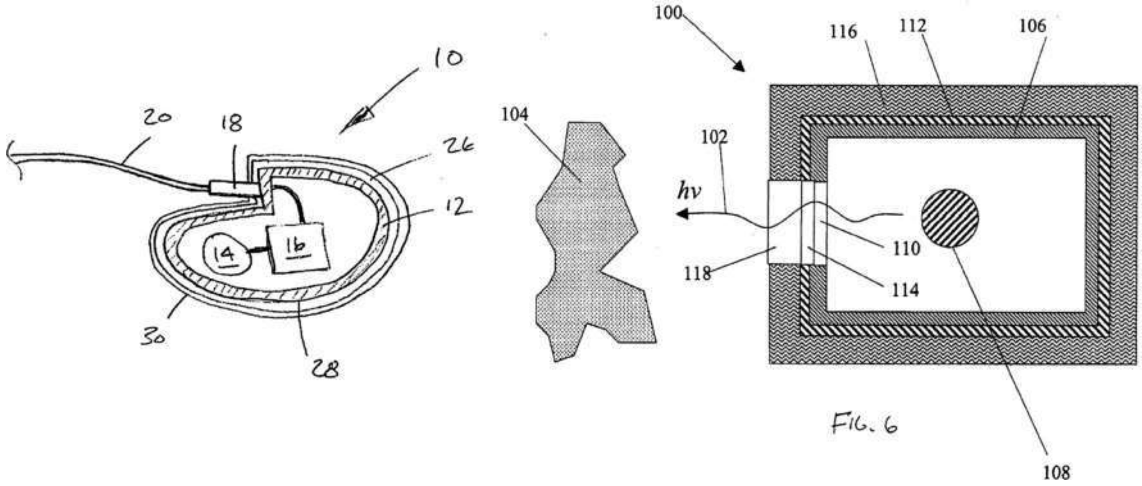

Fig. 19 An illustrative schematics compiled from the images provided in patent (Ref 51)

0.005-50 µm. The document specifies these as calcium phosphates (HA, TCP), SiO_2, TiO_2, gelatin, collagen, hydrogels. The method could be applied to a variety of implants such as hip shaft, acetabular cups, femur components for knee joint replacement, or shinbone components for knee joint replacement, components for shoulder joints replacement, elbow joints replacement, toe joint replacement, finger joint replacement, for a component for fusion of vertebral body of lumbar spinal column and intervertebral disk replacement, and for transgingival implant systems, orthodontic implant systems, tooth implants and bone implants.

A method for increasing the lifetime of zirconium (Zircadyne 702 or 705, Zircalloy) orthopedic implants is provided in patent (Ref 55). Using examples such as hip implant or knee implant, the surface of the metal stem comprises an oxidized 1-20-µm zirconium layer and an additional plasma-sprayed porous coating. The oxidation is made using air, steam, water or salt bath process conditions at temperatures of 540 °C. The method is capable of effectively manufacturing non-toxic and biocompatible implants that resist articulative and fixation failures. Similar concept was filed by the same authors three years earlier (Ref 101), where a hip joint stem fitting into a femur using the oxidized zirconium concept was presented.

A method of fabricating medical implant with thermally sprayed surface layers comprising added carbides is given in Ref 102. Fabrication of the implant involves producing a sacrificial substrate (to be removed later) and plasma or HVOF spraying of cobalt-chrome particles, i.e., not highly brittle, biocompatible material with relatively good fatigue properties. Into the feedstock, at least 6.17% of carbide source material such as 10-200 nm graphite is added through an atomization process. Using the method, medical components that exhibit increased wear properties are produced.

Another combined process is used for fabricating medical implant components (Ref 56). These include femoral ball head, femoral knee, patella femoral bearing, modular tibial baseplate/tray and spinal implant, cardiovascular devices, stent and medical implant components for joints such as shoulder, ankle, elbow and finger. Technologically, the two-step process involves plasma or HVOF spraying of 100-500 µm ceramic coatings onto the component and subjecting the coated portion to hot isostatic pressing or vacuum/controlled atmosphere sintering. The latter processes enable a chemical or diffusion bond among the substrate and the coating, yielding a bond strength of 48-62 MPa, reduced porosity of the coating, increased hardness and further provide a hardness gradient between the substrate and the coating. In addition, the metal ion release is reduced due to improvement in corrosion resistance. The coatings also exhibit improved scratch resistance and wear resistance. Almost identical patent was filed as (Ref 57).

Arc Spraying A rather general method of fabricating dense > 25 µm ceramic coatings on medical implants through high-velocity thermal spray method is given in Ref 103. The (undisclosed, potentially high-velocity arc spraying) method is described as atmospheric and the in-flight velocity of the particles should reach at least 200 m/s, but remain below sonic speed. The deposited material is, according to the document, “any oxide, carbide, nitride or nitro-carbide of any of the following elements: Si, Ti, Ta, W, Zr, Nb, Cr, Al,” i.e., the patent covers almost all known bioceramics. The target density of the coating is $> 99\%$ and, upon spraying, the grain size remains virtually unchanged (maximum 25% difference). Importantly, this is done without any post-treatment. The implants covered in this patent include femoral knee component, a tibial tray, a patella button, a femoral stem, and femoral head.

Cold Spraying A method of spraying of bioresorbable stents, markers, anchors, clips, sutures and orthopedic support devices is covered in patent (Ref 104). Specifically, the document deals with cold spray deposition of mixed coatings onto planar substrates, from which the stents are machined via EDM. The bioresorbable coatings are a mixture of "cathodic and anodic particles" bound together, creating a galvanic couple. The cathodic particles are either cobalt-chromium alloys, stainless steel, tantalum, or titanium, and the anodic particles are iron, iron alloys, or vanadium. All particles are preferably 1-10 µm, and their specific weight and hardness should not differ by more than 50% (preferably 20%). The material porosity is provided as 0.2% or less, a consequence of the cold spray deposition method. Surprisingly, the coating is "annealed after deposition to increase hardness" (probably by precipitation, undisclosed). Reportedly, it is possible to predetermine the bioresorption rate (i.e., the galvanic corrosion) in the coating production process.

Drug-delivery components prepared via thermal spraying method are provided in Ref 105. Under a controlled release rate, the therapeutic agents and drugs used in the components (antiplatelets, anticoagulants, antithrombins, anti-inflammatories and antiproliferatives) are useful to treat/reduce/prevent thrombosis or restenosis. Preparing of such medical device comprises forming a near-net shape porous component and its machining, followed by a coating deposition through cold spray, combustion spray process, arc wire spray, high-velocity oxygen fuel or detonation spray process (Fig. 20). The method is also useful for preparing stents, anastomosis clips, embolic protection filters, graft attachment systems, ring markers, guide wires, mitral valve repair devices, tubular or wire based implants, defibrillator or pacemaker lead tips and catheters or other delivery system devices. Another patent filed by the same authors (Ref 58) covers almost identical topic, focusing solely on cold spray technology this time.

A rather general idea was patented in 2006, a cold spray deposition of tissue-friendly materials onto (polyethylene) medical implant for joints, covered in Ref 106. Ideally, the (titanium) powder is supposed to reach 1-50 µm and the final coating porosity in the 20-40% range.

In Ref 59, fabrication of a bond layer for attachment of ceramic or metallic coatings to thermoplastic substrates is presented, which could be used for implantable prosthetic bones. The bond layer contains 2-70% ceramic or metallic filler particles (HA, stainless steel, WC-Co, ZrO_2, Al_2O_3, SiO_2, TiO_2) in a thermoplastic matrix that is compatible with the substrate. The bond layer deposited preferentially via cold spraying reduces chipping or wear of the ceramic or metallic coating and prevents damage to the thermoplastic (e.g., PET, PA, PBT, PS, PES, PPS, PA, PP, PEEK) substrate during the subsequent thermal spray deposition. The model top coating presented in the document is hydroxyapatite deposited via thermal spraying.

4 Trends

It is difficult to predict trends and future perspectives solely from the list of patented ideas. Upon compilation of this paper, it rather seems that there are several isolated areas that the individual submissions tend to wrap around (such as small differences in the designs of hip prosthesis).

Nevertheless, comparison with recent non-patent literature sources (such as the compilations of Heimann (Ref 107, 108) and Driver (Ref 109)) provides a clearer insight into what the future trends might be—although some of the areas are yet waiting for their first patent claims at the moment.

Aside from the coating materials, this paper covered also the substrate materials. In these, titanium and its alloys represent a long-term top-notch entry from the list. For decades now, the main alpha + beta alloy Ti6Al4V is slowly being replaced by alloys not containing cytotoxic vanadium. This said, the attention seems to shift to Nb-containing alloys (Ti_xAl_yNb) and also, lately, Ti5Al2.5Fe and TiZrNbTa. The patent claims contained in this paper suggest that attempts at further lowering the modulus of the substrates to match that of cortical human bone (10-30 GPa) are still ongoing. This could open up the application potential also to beta-type Zr-containing titanium alloys (such as Ti13Nb13Zr) with moduli below 50 GPa (Ref 107). Aside from titanium, certain well-proven alloys such as CoCrMo continue to be used. Recent journal papers on application of mechanical surface modifications (drilling, milling) of CrCrMo-based alloys (Ref 110) allow to anticipate patent claims in the near future. Tantalum exhibited several promising results so far and is already included in the latest patents (from 2012), too. Frequently covered in recent journal papers, magnesium and its alloys with their high specific strength, low stiffness and low density advantages have been used in bioapplications already (e.g., biodegradable osteosynthetic devices, cardiovascular stents). The application of Mg for orthopedic applications is currently hindered by its high corrosion rates in contact with extracellular fluids (associated with evolution of hydrogen gas that tends to counteract the osseointegration). Once this limitation is resolved, magnesium alloys could open up a whole new area of biomaterials applicable to endoprosthetic applications.

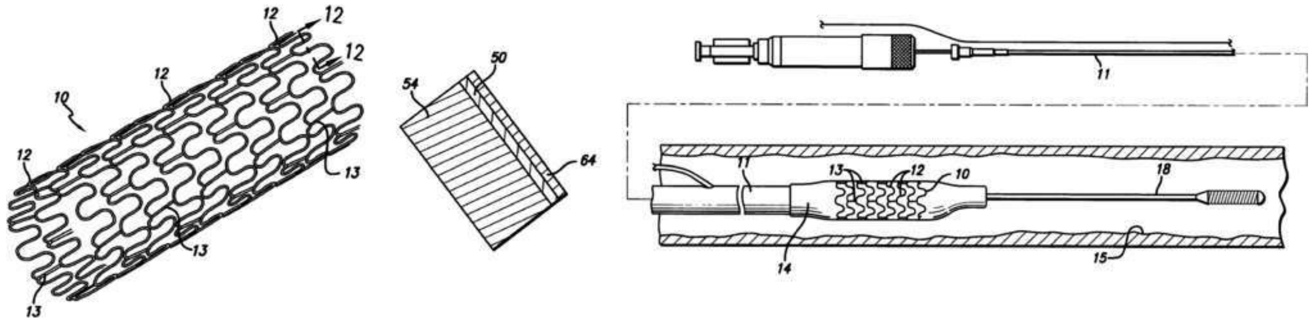

Fig. 20 An illustrative schematics compiled from the images provided in patent (Ref 105)

Concerning the materials used for coatings, the situation is very clear. Considering their natural resemblance to human bone tissues, calcium phosphates (dominantly HA, TCP) are the prime choice, as also reflected in the number of patents and research works filed in the last decades. A group of patents are devoted to improving the antibacterial properties of Ca-P coatings via addition of, e.g., silver (as also reported in the literature, (Ref 111). Very recently, a group of three materials with a promising potential appeared: gahnite ($ZnAl_2O_4$ spinel, melting temperature indicated as 1950 °C), baghdadite ($Ca_3(Zr,Ti)[(Si_2O_7/O_2)]$) and strontium hardystonite ($Sr_2ZnSi_2O_7$) showed a very promising potential for bioapplications. In fact, some studies suggested these may even be a sensible replacement for hydroxyapatite. Few patents on these materials reported in this paper may indicate the future trend for this group of materials.

A second group of materials considered for deposition via thermal spray method are oxide ceramics. For years, several non-resolved issues influenced the journal and patent literature (such as, e.g., the dispute on the three TiO_2 polymorphs, anatase versus rutile versus brookite (Ref 7, 112)). These days, however, the Gordian knot seems to have been resolved: A clear trend to develop nanoscaled microstructure features could be observed. Despite their more complex fabrication as opposed to "traditional" microscaled coatings, the nanostructured oxide ceramics are more suitable for application and have already surpassed their predecessors in several areas. Importantly, the use of nanostructured powder feedstock allows the cold kinetic spray technology to enter the game, too, with its advantage of preserving the phase composition. A number of patents related to the deposition of nanostructured ceramics (oxides) could surely be expected in the forthcoming years.

Using other ceramics, the trend in using advanced bioceramic-polymer composites and bioglass for various applications is reflected in the patent literature. Frequently being associated with scaffolds, not many sources actually report these two material groups being treated via thermal deposition methods. Once the initial problems with, e.g., the thermal decomposition of these are overcome, it can be expected that a number of patents corresponding to bone augmentation (maxillofacial) will be filed, too. Another group of intensively developed materials are self-healing ceramics. However, no such patent sources could be located in our databases search (as of July 2018), and it is difficult to understand what is the major hindrance at the moment.

Among the metallic coatings reported in the patent literature, titanium and tantalum are of prime importance. With the development of non-oxidizing processes such as low-temperature HVOF and cold spraying, the application of metals for coatings is now wide open. In this paper, several such instances are summarized already. It could be expected that other metals such as alloyed (milled) or mixed feedstock will now be covered in patents on a regular basis.

Last group of materials yet waiting for its application via thermal spraying are polymers and engineering plastics. Supramolecular hydrogels, UHMWPE, PEEK and other polymer-based materials are currently being used in bioapplications. However, these are not processed through high-temperature thermal spray processes for obvious reasons. With the advent of cold spraying and first successful attempts to deposit these materials (UHMWPE, for instance, (Ref 113)), it could only be expected that the trend in this area will grow by an order of magnitude in terms of related journal and patent sources in the next decade.

Finally, a little prospect into the future: the era of third-generation biomaterials is at its strongest at the moment. However, the pioneering research attempts to initiate and instigate R&D efforts for the fourth-generation biomaterials that are on the way already (e.g., Ref 114). The fourth-generation biomaterials are based on integrating electronic systems with the human body to provide powerful diagnostic as well as therapeutic tools for basic research and clinical use. The functionalities of such biomaterial systems are thought to include manipulating cellular bioelectric responses for tissue regeneration as well as monitoring cellular responses with the aim to communicate with host tissues via bioelectric signals (Ref 107). This would surely open up a whole range of possibilities for the thermal spray method. This is probably the field where the majority of patents are going to be filed in the new decade.

5 Glossary

The following text contains numerous terms associated primarily with the biological sector. Secondly, a whole set of abbreviations used for the biomaterials appears throughout the paper. The following list is provided to familiarize the thermal spray researchers with the less commonly encountered terms. To complete the list of all abbreviations used throughout this paper, abbreviations pertaining to the thermal spray methods are provided in the table, too.

Acetabulum	Concave cavity in pelvis, femur bone contact region
Anastomosis	Connection between veins or nerves
Angiogenesis	Process of formation of new blood vessels, encountered in healing
Anticoagulants	Chemical substances that prevent blood coagulation, often employed to prevent thrombosis
Anti-inflammatories	Substances used for treatment of inflammation
Antimicrobial	Substances used for killing microorganisms or preventing their growth
Antiplatelets	Substances used for preventing blood platelets coagulation, preventing, e.g., thrombosis
Antiproliferatives	Substances inhibiting cell multiplication and growth
Antithrombins	Proteins produced in liver that inactivate coagulation enzymes
Articulation, articulative	Joint, connection of two bones such as knee or hip
Autologous	Derived from the same individual
Bacillus pyocyaneus	Equally Pseudomonas aeruginosa, bacterium partially resistant to antibiotics
Bactericidal	Substance killing bacteria, often antibiotics
Biocidal	Substance killing of any harmful organisms
BMP	Bone morphogenetic proteins, inducing formation of bones and cartilage
Catheters	Medical devices inserted into body to treat diseases, often hollow tubes
Cervical	Pertaining to neck, part of spine
Coccygeal	Pertaining to tailbone, part of spine
Cochlear	Pertaining to inner ear
Collagenous	Producing or containing collagen
Cranial	Pertaining to skull
Craniofacial	Pertaining to facial structures of a head
CS	Cold spraying
Cytotoxicity	Toxicity toward cells
Distal	Farther from the point of attachment, often distal end of bone
EDM	Electrical discharge machining
Embolism, embolic	Pertaining to blockage of blood vessel
ePTFE	Expanded polytetrafluoroethylene, for instance GoreTex
Escherichia Coli	Bacterium commonly found in lower intestine
Exosomatic	From outside of the body
FGM	Functionally graded materials
Gelatin	Colorless ingredient, often used as a binder
Gingival	Pertaining to gums
HA	Hydroxyapatite (hydroxylapatite)
HVOF	High-velocity oxy-fuel spraying
Iatrogenic	Induced inadvertently by a surgeon or medical treatment
Intraosseous	Situated, performed, or occurring within or entering by way of bone
Intravenous	Situated, performed, or occurring within or entering by way of vein
Lumbar	Pertaining to abdominal part, part of spine
Mammoplasty	Surgical procedure pertaining to breasts
Mandible bone, mandibular	Jawbone, the strongest of bones in face
Masticatory power	Related to chewing
Maxillofacial	Pertaining to jaws and face
Mitral valve	Valve in the heart between left atrium and left ventricle
Orthodontic	Dentistry focusing on prevention and correction of malpositioned teeth and jaws
Osseoconductivity	Property of material that promotes process of bone growth
Osseointegration	Process of bone adherence to the implant
Osteoacusis	Conducting of sound via bones, the ability of bone to conduct sound
Osteoblast	Single nucleus cells that synthetize bone
Osteocalcin	Bone-building protein produced by osteoblast cells
Osteoconductivity	See osseoconductivity
Osteogenesis	Formation of new bone tissue
Osteosynthetic	Pertaining to fixation of bone fracture using implants
Osteotomy	Surgical procedure pertaining to cutting of bones
PA	Polyamide
PBT	Polybutylene terephthalate
PDO	Polydioxanone, crystalline polymer
PEEK	Polyether ether ketone
PES	Polyether sulfone
PET	Polyethylene terephthalate
PGA	Polyglycolide, polyglycolic acid, thermoplastic polymer
PLA	

	Polylactide, polylactic acid, thermoplastic polymer
PLLA	L-chiral form of PLA
Povidone iodine	Antiseptic used for skin disinfection
PP	Polypropylene
PPS	Polyphenylene sulfide
Proximal	Closer to the point of attachment, often proximal end of bone
PS	Polystyrene, alternatively plasma spraying
Pseudomonas aeruginosa	See Bacillus pyocyaneus
PTMC	Polytrimethylene carbonate
PUR	Polyurethane
Restenosis	Recurrence of stenosis, a narrowing of a blood vessel
Sacral	Pertaining to sacrum bone, part of spine
Sacroiliac joint	Joint between the sacrum and the ilium bones of pelvis
Sacroiliitis	Inflammation of sacroiliac joint
SBF	Simulated body fluid, a solution simulating human blood plasma
Scoliosis	Sideways distortion of a spine
Spinal stenosis	Narrowing of the spinal canal causing pressure on spinal cord and nerves
SPS	Suspension plasma spraying
Staphylococcus aureus	Biochemically active bacterium found in human body, causes infections and intoxications
Subcutaneous	Pertaining to hypodermis, lowermost layer of skin tissue
Synostosis	Fusion of two bones
TCP	Tricalcium phosphate, $Ca_3(PO4)_2$
Thoracic	Pertaining to chest, part of spine
Thrombosis	Obstruction of blood flow through formation of blood clot
Tibia	Shinbone, the larger of the two leg bones below knee
Transcutaneous	Penetrating the skin
Transgingival	Penetrating the gums
TS	Thermal spraying
UHMWPE	Ultra-high molecular weight polyethylene, thermoplastics
Vascularization	Formation of blood vessels and capillaries in living tissue
Veneers	Layer of material placed over a tooth for protection and aesthetics
Vertebrae, vertebral	Bony or cartilaginous segments composing the spinal column

Acknowledgment Compilation of the paper was supported through Czech Science Foundation grant GB14-36566G "Multidisciplinary research centre for advanced materials."

References

1. K.A. Gross and E. Ezerietis, Juniper Wood as a Possible Implant Material, *J. Biomed. Mater. Res.*, 2003, **64A**, p 672-683
2. M.E. Pons, Developing Hydroxyapatite CAPS Coatings on Metallic Implants for Tissue Replacement, Ph.D. Thesis, Nanyang Technological University, Singapore 2004
3. R.E. Ant and I. Wang, Physical and Chemical Aspects of Biomaterials Used in Humans, in *Implantation Biology: The Host Response and Biomedical Devices*. CRC Press, Boca Raton, 1994, p. 13-38
4. R.C. Eberhart, H. Huo, and K. Nelson, Cardiovascular Materials, *MRS Bull.*, 1991, **16**, p 50-54
5. P. Chagnon and P. Fauchais, Thermal Spraying of Ceramics, *Ceram. Int.*, 1984, **10**(4), p 119-131
6. S. Sampath, X.Y. Jiang, J. Matejicek, L. Prchlik, A. Kulkarni, and A. Vaidya, Role of Thermal Spray Processing Method on the Microstructure, Residual Stress and Properties of Coatings: An Integrated Study for Ni-5 wt.%Al Bond Coats, *Mater. Sci. Eng. Struct. Mater. Prop. Microstruct. Process.*, 2004, **364**(1–2), p 216-231
7. J. Cizek, K.A. Khor, and I. Dlouhy, In-Flight Temperature and Velocity of Powder Particles of Plasma-Sprayed TiO_2, *J. Therm. Spray Technol.*, 2013, **22**(8), p 1320-1327
8. V. Palka, E. Postrkova, and H.K. Koerten, Some Characteristics of Hydroxylapatite Powder Particles after Plasma Spraying, *Biomaterials*, 1998, **19**(19), p 1763-1772
9. Clarivate Analytics, Web of Knowledge—Derwent Innovation Index. http://www.webofknowledge.com
10. European Patent Office, Espacenet. https://worldwide.espacenet.com
11. United States Patent and Trademark Office, Patent Full-Text Databases. http://patft.uspto.gov/netahtml/PTO/index.html
12. Q. Bao and T. Brown, Implantable device i.e. Weight-Bearing Implant, for Being Implanted into Weight-Bearing Joint, has Camming Surface Connected to Implant Body, Where Mechanical Bond Strength Between Implant Body and Coating About Specific MEGA PASCAL, US2009276053-A1, 2009
13. T.C. Prentice and A.R. McCabe, Applying a Coating to a Substrate Material, Comprises Plasma Spraying Powder of Titanium Dioxide onto a Substrate Material to Form an Initial Coating, and Applying A Further Coating of Metal and/or Hydroxyapatite onto the Initial Coating, WO2012110816-A1, 2012
14. R. Ahmed and G.H. Markx, Coating an Article, e.g. Implant for Surgical or Dental Use Involves Spray Coating the Powder Comprising Coated Particles onto Surface of Article to Form Composite Coating, US9421151-B2, 2016
15. O.A. Dudareva, I.P. Grishina, V.N. Lyasnikov, and A.V. Lyasnikova, Method for Making Implants Involves Multilayer Plasma Spraying of Biologically Active Coating onto Metallic Substrate of Implants, RU2529262-C1, 2014
16. L. Jiang, S. Lin, and L. Wang, Titanium-Hydroxylapatite Gradient Coating for Titanium Alloy Implant Surface, has Titanium Powder Layer, Two Titanium Powder and Hydroxylapatite Mixed Layers and Hydroxylapatite Layer that are Arranged from Inside to Outside, CN101612418-A, 2009
17. L. Gan, S.C. Jani, M.L Scott, Marcus, and S.C. Giani, Coating for Medical Implant, Comprises Osseointegration Agent and Antimicrobial Metal Agent Comprising Silver, Copper and/or Zinc, US9839720-B2, 2017
18. Y. Chen, X. Zheng, H. Ji, C. Ding, and Y. Xiang, Antimicrobial Type Hydroxyapatite Composite Coating Includes Metal Silver Powder as Antimicrobial Additive Ingredient and Hydroxyapatite Powder, CN100549109-C, 2009

19. J. Zhou, Iodine Antibacterial Hydroxyapatite Composite Coating Used for Coating Titanium and Titanium Alloy Based Substrate Used as Prosthetic Implant, Comprises Hydroxyapatite and Povidone Iodine Particles, CN102417741-A, 2012
20. L. Song, Y. Huang, L. Gan, Y. Wu, X. Liu, F. Wu, Y. Xiao, and Z. Tian, BIOMEDICAL MATERIAL i.e. Hydroxyapatite Coating Containing Silver ion Biomaterial, Contains Hydroxyapatite Coating that Contains Silver ion Which is Sprayed on Substrate Material by Plasma, CN101797399-A, 2010
21. H. Gruner, P. Gruner, and F. Tourenne, Implant i.e. Cement-Less Implanted Prosthesis, for e.g. Traumatology, has Cover Layer Formed of Powder by Application of Thermal Spray Method, Where Powder has Calcium Phosphate e.g. Hydroxylapatite, and Antibacterial Active Ingredients, EP2224970-B1, 2018
22. J. Fencl, J. Fojt, and L. Joska, Revision joint Implant Device for Performing Total Replacement of Femoral and Acetabular Components, has Transition Portion Whose Outer Surface is Provided with Protective Porous Surface Layer that is Matched with Integral Surface Layer, CZ306816-B6, 2017
23. J. Chen, J. Feng, Y. Huang, X. Liu, L. Song, F. Wu, Y. Xiao, and J. Cheng, Preparation of Multiple Pore Hydroxyapatite Coating on Biomedical Material, e.g. Titanium, by Spraying Plasma of Hydroxyapatite Suspending Liquid, Adding Pore-Creating Agent, e.g. Ethanol, Injecting to Plasma Flame Kernel, and Sedimenting, US8877283-B2, 2014
24. F. Wu, L. Song, Y. Xiao, X. Liu, Y. Huang, Y. Wu, and J. Chen, Suspension Injection Type Plasma Spray Coating Device For Preparing Biologically Active Hydroxyapatite Coating, Comprises Plasma Spray Gun, Metal Substrate, Substrate Fixed Beam, Storage Container, Suspension Conveying and Injection Systems, CN101250682-B, 2011
25. J. Chen, Y. Huang, X. Liu, L. Song, F. Wu, Y. Wu, and Y. Xiao, Suspending Liquid Injection Plasma Spraying Device Useful for Preparing Biological Active Coating Of Hydroxyapatite, Comprises a Plasma Spray Gun, a Metal Substrate, a Substrate Fixing Rack, and a Suspending Liquid Conveying System, CN201195743-Y, 2008
26. F. Wu, Y. Huang, X. Liu, Y. Wu, Y. Xiao, L. Song, and J. Chen, Preparation of Hydroxyapatite Biological Activity Coat by Spray Coating Suspension Plasma for Medical Consumption Comprises Preparing Hydroxyapatite Suspension, Transferring, Pouring and Generating Hydroxyapatite Biological Activity Coat, CN101250681-B, 2010
27. R.E. Riman and C. Sever, Preparation of Nanoscale Hydroxyapatite Particles Useful e.g. as Granular Fill Compounds, Bone Implant Materials Involves Combining Calcium Ion Source Having Calcium Acetate and Phosphate Ion Source Under Ambient Conditions, US8287914-B2, 2012
28. T. Huang, J. He, L. Gan, Y. Wu, F. Wu, and Z. Tian, Biomedical Material for Bone Formation, has Substrate Material Whose Surface is Compounded with Porous Calcium Phosphate Coating that is Compounded with Collagen so as to Build Porous Calcium Phosphate-Collagen Composite Coating, CN102145194-A, 2011
29. J. Fencl and J. Simek, Surface Treatment of Implants, that is Bone Preferably Joint Implants, Comprises Thermal Application of a Mixture of a Powdered Material Containing Hydroxyapatite Powder, and Titanium Powder on Surface, CZ201500934-A3; CZ306822-B6, 2017
30. S. Ban, L. Cui, D. He, J. Jiang, X. Li, Z. Wang, L. Zhao, Q. Zhao, and Z. Zhou, Preparation method for Making Hydroxyl Apatite Coating Through Cold Spraying, Involves Spraying Dried Hydroxyl Apatite Powders onto Matrix of Biomedical Implanted Metal Material Using Cold Spraying Device, CN101591777-B, 2011
31. S. Ban, L. Cui, D. He, J. Jiang, X. Li, Z. Wang, L. Zhao, Q. Zhao, and Z. Zhou, Preparation Method of Hydroxyl Apatite Coating by Micro-beam Plasma Spraying for Medical Implant Pieces of Tooth Root and Artificial Joint Involves Providing Powder Conveying Gas with Predetermined Flow Rate and Conveying Rate, CN101591759-B, 2011
32. B. Hou, Y. Huang, T. Li, Z. Liu, Z. Qiao, Z. Xiong, G. An, and G. Qin, Crystallization of Plasma-Sprayed Hydroxyapatite Coating Used for Surgical Implant, Involves Providing Hydroxyapatite Coating Product into Closed Container, Introducing Vacuum and Saturated Steam, Heating Container, and Cooling, CN104164644-A, 2014
33. B. Yang, Y. Huang, J. Feng, J. Chen, and X. Zhang, Method for Post Treatment of Plasma Spraying Hydroxyapatite Coating, CN100357485-C, 2007
34. Y. Lu, J. Wang, and M. Li, Surface Nanocrystallization Method For Hydroxyapatite Coating, CN100348276-C, 2007
35. H. Grundei, Subcutaneous Intramuscular Camp for Rigid Transcutaneous Implant in Bone Stump, Comprises Distance Piece Having Rigid Socket Surface with Intracorporal Coupling Element and is Placed Between Implant and Extracorporal Coupling Device, EP1827317-B1, 2006
36. H. Zimmermann, Thermal Sprayed Surface Layer Made of Titanium on a non-metallic Substrate of an Orthopedic Implant, Comprises an x-Ray-Sensitive Mixture Made of Biocompatible Indicator Metal in Relation to Titanium, EP2199423-B1, 2013
37. R. Lerf, H. Schmotzer, and S. Siegmann, Open-Pore Biocompatible Surface Layer for Application to an Implant Comprises a Coherent Pore Network and has a Defined Surface Area, EP1942961-B1, 2013
38. Y. Xie and J. Zeng, Manufacture of Patterned Titanium-Coated Hard Tissue Replacement Material Involves Sand-Blasting Metal Implant, Cleaning, Spraying Titanium Powder on Metal Implant by Arc Plasma Method, and Forming Titanium Surface Layer, CN103805987-B, 2016
39. S. Cheng and X. Lu, Human Body Bone Substitute Connecting Piece for Use as Biological Medical Material, has Human Body Bone Substitute Connecting Piece Base Provided with Porous Titanium Surface Layer that is Coated with Titanite Layer, CN202982311-U, 2012
40. V.M. Frauchiger, S. Jaggi, and T. Wippich, Plasma Spray Process for Modifying Substrate Used in e.g. Hip Implants Involves Introducing two Materials into Plasma Source to Produce a Plasma Spray, Where Second Material at Least Partially Melts in the Plasma and Binds to First Material, WO2010037562-A2, 2010
41. M. Mitrovic, Method for Producing Structured Coating on Part of Surface of Artificial Femoral Knee Joint Implant to be Placed in Femur for Joint Replacement, Involves Hardening thin Layer, and Abrasively Processing and Functionalizing Produced Layer, WO2012126448-A1, 2012
42. J. Schleicher, J.K. Barrett, and J. Ault, Coating Cobalt-Chromium Alloy Medical Implant, by Applying Coating of Pure Titanium to Surface of Medical Implant by Cold Spray Process, and Diffusion Bonding Coating and CoCr Alloy Medical Implant Using Hot Isostatic Pressing, WO2014137316-A1; CA2903188-A1; EP2964802-A1; US2016030632-A1; EP2964802-A4, 2014
43. M. Kumar, Making Implant for Replacing Joint of Patients Involves Coating Textured Dies Surface with Powdered Metal, Injecting Slurry into Die Cavity, Casting Slurry Material, Removing Ceramic Shell, Plasma Spraying Layer onto Surface of Stable Dome, US2010136214-A1, 2010
44. M. Kumar, Formation of Acetabular Cup by Providing Working Surface, Spraying First Layer of Material Having First Composition onto Working Surface Defining Acetabular Shell, and

Removing Acetabular Shell from Working Surface, US7655162-B2, 2010
45. X. Liu, X. Zhao, and C. Ding, Preparing Nano-Titanium Oxide Coating Layer Having Bioactivity, CN100346001-C, 2007
46. R.S. Lima, B.R. Marple, H. Li, and K.A. Khor, Making of Biocompatible Coating for an Implant, e.g. Component of Artificial Hip Joint, Involves Thermally Spraying the Particles onto Substrate to Form Coating, and Controlling the Spray Parameters, US2006199024-A1, 2006
47. H. Zheng and X. Zaho, Preparing Titanium-Niobium Oxide Composite Coating for Surface Activation Treatment Comprises Preparing Coating Powders, Material Cleaning and Sand Blasting, Plasma Spraying, and Soaking in Energy Body Fluid, CN102816988-B, 2014
48. L. Huang, H. Ji, Y. Liang, Y. Xie, and X. Zheng, Bone Replacing Material of Baghdadite Coating-Titanium Alloy, Useful for Inducing Formation of Bone-Like Apatite in Simulated Body Fluid, Comprises Titanium and Its Alloy as Matrix and Coating is Deposited on Matrix by Plasma Spray Coating, CN102049065-A, 2011
49. J. Chang, C. Ding, Y. Xie, W. Zhai, and X. Zheng, Hard Tissue Substitute Comprises Magnesium Silicate Coating Layer Which is Coated on Substrate such as Titanium or Titanium Alloy, CN101658693-B, 2008
50. D.E. Lawrynowicz, H. Zeng, and Z. Zhang, Producing Refined Chromium Oxide Powder, Useful in Thermal Spraying a Coating on an Implant (which is medical implant), Comprises Acid and Reduction Washing of Chromium Oxide Powder, and PACKAGING the Chromium Oxide Powder, US2009162273-A1, 2009
51. W.J. Dalzell and K.H. Heffner, Integration of Radiation Shield, e.g. Tungsten, with Implantable Medical Device with Biocompatible Coating, e.g. Pacemaker, Involves Thermally Spraying Radio-Opaque Composition Particularly Around Electronic Circuitry of Medical Device, US2007055147-A1, 2007
52. E. Garofalo, M. Meehan, R. Montalbano, J. Wang, J. Whalen, and E. Garafalo, Forming Porous Metal Coating Over Substrate, by Thermally Spraying Metal Coating Material Over Surface of Substrate to form Applied coating Including Impurity-Rich Portion, and Removing The Portion of Applied Coating to Form the Coating, US9023419-B2, 2015
53. D.E. Lawrynowicz, A. Wang, Z. Zhang, and J. Krajewski, System for Applying Coating of Desired Material onto Medical Implant Component, Comprises Thermal Sprayers, Rotatable Holding Fixture Having Mounting Stations, Feeders for Supplying the Desired Material to the Sprayers, and Control Device, US7981479-B2, 2011
54. S. Koenig and H. Schmotzer, Open-pore Biocompatible Surface Layer for Use as Implant for Hip Shaft, Bowls for Hip Joints, Femur Components for Knee Joint Replacement, Shinbone Components for Knee Joint Replacement, is Disposed on Raw Surface of Implant, WO2009097968-A3, 2009
55. R.E. Brosnahan, R. Fesmire, H. Gupta, D.A. Heuer, G. Hunter, and V. Pawar, Manufacturing Medical Implant e.g. Hip Implant Having Oxidized Zirconium Surface and Porous Coating, by Forming Implant, Oxidizing Implant to Form Surface of Oxidized Zirconium, and Applying Coating to Portion of Implant by Plasma Spray, US2009012611-A1, 2009
56. D.E. Lawrynowicz and A. Wang, Fabricating Medical Implant Component such as Femoral Ball Head Component, Useful in e.g. Hip Replacement Surgery Involves Spraying Particles on Bearing Portion of Substrate; and Subjecting Coated Bearing Portion to Vacuum Sintering Process, EP1806155-B1, 2010
57. A. Wang, D.E. Lawrynowicz, Z. Zhang, and D. Lawrynowicz, Medical Implant Component e.g. Femoral Ball Head Component, Fabrication for e.g. Hip Replacement Surgery, Involves Spraying Particles of Ceramic Material onto Bearing Portion of Substrate by Thermal Type Spraying Process, EP1808186-B1, 2010
58. P.A. Kramer, Manufacturing Medical Device e.g. Drug Eluting Stent, Guide Wires, Lead Tips, Catheters, Markers Involves Forming Porous Substrate from Biocompatible Material Using Spray Process and Processing Porous Substrate INTO Medical Device, US7514122-B2, 2009
59. M.N. Bureau, J. Legoux, S. Belanger, and J.G. Legoux, Tie layer for Bonding Ceramic or Metallic Coating to Thermoplastic Substrate such as Implantable Prosthetic Bone, Contains Filler Particles such as Ceramic and/or Metallic Particles in Thermoplastic Matrix that is Compatible with Substrate, CA2593781-C, 2011
60. C.P. Cornelius, R. Schoutens, R. Gheorghe, and A. Mootien, Mandibular Bone Plate for Use With Mandible, has Extension Portion for Defining Bone Facing Surface, Where Extension Portion is Oriented such that line Tangential to Inferior End and Superior End of Bone Facing Surface is Rotated, WO2014158740-A1, 2014
61. V.N. Lyasnikov, O.D. Muktarov, and V.V. Perinskii, Method for Making Intraosseous Carbon-Nanocoated Dental Implant Involves Sand-Blast Finish of an Implant Surface by Aluminium Oxide Particles, RU2490032-C1, 2013
62. N. Urakabe and S. Urakabe, Dental Implant Useful in Surgery Process, has Cylindrical Core Material and Recrystallized Apatite-Based Ceramic Coating Layer Having Two or More Calcium-Phosphate-Type Compounds Which Differs in Melting Points, JP5891150-B2, 2016
63. F. Nakada, Component for Installing Artificial Hip Joints in Recess Cover of Pelvis, has Liner Whose Outer Surface is Provided with Opposing Surface Facing Another Surface, Where Opposing Surfaces are Made to Contact with Sides of Recessed Part, JP2013063103-A, 2013
64. B.W. Schneider, R. Simon, D. Lindsey, and S.A. Yerby, Modular Implant for Fixation/Fusion of Sacroiliac Joint, has Transverse Support Struts Arranged in Rectilinear Configuration at Proximal and Distal Ends of Repeating Internal Portion which is Positioned Between Distal and Proximal Portions, US2017296244-A1, 2017
65. B.W. Schneider, R. Simon, D. Lindsey, and S.A. Yerby, Modular Straight Implant for Performing Fixation or Fusion of Sacroiliac Joint of Patient for e.g. Degenerative Sacroiliitis, has First Guide Pin Receptacle Located Along Longitudinal Axis of Solid Elongate Body, US9662157-B2, 2017
66. B. Walter, D. Brazil, and T. McTighe, Femoral Prosthesis e.g. Hip Prosthesis, for Installing or Fixing at Proximal End of Proximal Femur of Human Patient in Total Hip Replacement Procedure, has Thinner Connecting Body Placed Between Columns, Where Columns are Spaced Apart, US8470049-B2, 2013
67. N. Hansell, E. Dwyer, and J. Bennett, Artificial Disc, Useful for Replacing Damaged Intervertebral Disc, Comprises Superior Core with Superior Surface Provided to Contact Inferior Surface of Superior Endplate, Inferior core to Connect to Superior Core, and Inferior Endplate, US9017410-B2, 2015
68. A. Balasubramanian, J. Bennett, N. Hansell, and J.B. Bennett, Artificial Disk for e.g. Replacing Intervertebral Disks, of Patient Injured or Damaged as Degenerative Disk Disorder Result, has Support Assembly Placed on Outer Surfaces of Endplates and for Coupling Superior Endplate to Inferior Endplate, US9937051-B2, 2018
69. S.D. Cook and S.L. Salkeld, Implant Device for Treating Lumbar Spinal Stenosis of Patient, has Vertebral Attachments Comprising Connecting Components that Affix Magnets to Superior or Inferior Vertebrae, Where Connecting Components Comprise Extension, US2014025122-A1, 2014

70. S. Petersheim and R. Agard, Bone Plate i.e. Spinal Plate, for Joining Adjacent Vertebrae to Treat Spinal Deformities, has Ridge Connected to Bottom Part and Inserted into Bone, and Hole Receiving Bone Screw for Attaching Plate to Bone, EP2753256-A1, 2014
71. P. Raugel and E. Jones, Flexible Acetabular Cup makes External Choral Dimensions of Cup, Which Runs Across Separation or Opening Between Arms, Greater than External Diameter of Partly Spherical Portion, EP1884220-B1, 2011
72. Y. Hai, Q. Luan, and Z. Zhou, Cost-Effective Artificial Bone with High Strength, Excellent Hardness, Toughness, and Corrosion Resistance, Comprises Middle Layer Comprising high Strength Carbon Fiber, CN202355616-U, 2012
73. T.C. Prentice, R.L. David, M.E.L. Pickford, and A.D. Turner, Implant Useful in Surgical Procedure e.g. Hip Replacement, Contains Metal Structure Coated with Biocompatible Metal by Plasma Spraying, and Biocidal Metal Cations Incorporated in Coating, EP2101835-B1, 2010
74. T.C Prentice, M.E.L. Pickford, D.R Lewis, and A.D. Turner, Implant for Contacting with a Bone During e.g. Prosthetic Surgery, Comprises Metal Structure Having a Surface with a Ceramic Coating Containing Hydroxyapatite and Silver Ions that Gradually Leach out in Body Fluids After Implantation, EP2316499-B1, 2013
75. H. Ao, Y. Liu, Y. Chen, H. Chen, C. Wang, W. Yuan, X. Wu, X. Wang, and X. Zheng, Plasma Spray Coating Orthopedics Screw, has Screw Main Body Whose Surface is Coated with Plasma Spray Coating, Where Screw Main Body is Made of Titanium Alloy, CN202288439-U, 2012
76. B.D. Hahn and D.S. Park, Preparation of Nano-structured Hydroxyapatite Coating Layer, Comprises Putting Hydroxyapatite Powder in Powder Chamber, Placing Metal Substrate in Deposition Chamber, and Keeping Deposition Chamber in Vacuum State Using Vacuum Pump, US2011281127-A1, 2011
77. C.G. Sidebotham, Load Bearing Implant, Useful for Medical Applications Including e.g. Femoral Head Replacement for Hip, Comprises Femoral Implant Stem Having Male Locking Tapered Fitting for Attachment to Internal Female Taper of Head, and Neck-Collar Area, US8778030-B2, 2014
78. A. Podolsky and Y. Garbuzov, Dual-Taper Lock Modular Prosthetic Hip System for Performing Minimally Invasive Total- or Hemi Hip Arthroplasty in Hip of Patient, has Prosthetic Femoral Head Implant Rotatably Fitted Within Acetabulum, US8579985-B2, 2013
79. S. Abdou, Orthopedic Device Assembly for Concurrently Placing Implantable Spacers into Intervertebral Disc Space Between Superior and Inferior Vertebral Bones, has non-Implantable Placement Instrument with Cavity Containing Bone Forming Material, US8845728-B1, 2014
80. P. Brun, S. Chegini, and P. Lindenmann, Intervertebral Implant i.e. Orthopedic Implant, for Implant Assembly to Implant in Intervertebral Disk Space in e.g. Spine Region, has Fixation Assembly Rotated Within Implant Body About Transverse Axis from Retracted to Extended Position, US8545563-B2, 2013
81. D.C. Blackburn, V. Carvajal, R.H. Dixon, C.F. Gardinier, D.P. Harding, T. Medford, B.J. Pope, J.K. Taylor, Component for Prosthetic joint e.g. Artificial Hip Joint, Comprises Sintered Carbide Substrate Comprising Titanium Carbide and Titanium Sintering Metal, Sintered Diamond Articulation Surface Formed on Substrate, and Bone Attachment Surface, US8603181-B2, 2013
82. T. Vanasse, G. Gupta, and J. Meridew, Medical Implant for e.g. Replacing Joint of Shoulder of Human Body During Shoulder Procedure, has Metallic Body Whose Surface is Replicated from High Resolution Scan of Bone and Promoting Bony On-Growth or In-Growth of Tissue, US2014371863-A1, 2014
83. M. Dai, Implantation Material for Surgery in Use for Repairing Bone, CN100364618-C, 2008
84. J. Tyber and C. Faresich, Osteotomy Implant of Osteotomy Implant System Used for Internal Fixation of Bone Fracture, in which Surfaces Extend in Respective Planes, US2018008419-A1, 2018
85. J. Sun, Y. Han, and K. Cui, Compound Technique for Preparing Multiaperture Titanium Coating by Cold Spray and Vacuum Sintering, CN100560143-C, 2009
86. A.Z. Rosenflanz, R.P. Rusin, and J.E. Swanson, Manufacture of Dental Article or Orthodontic Appliance, e.g. Brackets, by Plasma or Thermally Spraying Particles Comprising Metal Oxide Sources on a Substrate Such that the Particles Coalesce to Form Shaped Article Comprising Aluminum Oxide, US2005136176-A1, 2005
87. C. Li, Z. Wang, L. Zhu, N. Gao, D. Hao, H. Wang, J. La, M. Guo, and H. Li, Plasma-Spray-Coated Nano Zirconia Implant has Implant Component Containing Titanium or Titanium Alloy Material Having Monolithic Structure, and Base Having Transgingival Shoulder Portion Having Uniform Coating of Nano-Zirconia, CN104042350-A, 2014
88. G.A. Walther, Implant e.g. Tooth Implant, for Implanting in Bone i.e. Jawbone, has Implant Body Inserted into Human Jawbone, and Implant Support Inserted into Body, where Area Engaged into Jawbone is Provided with Coating Made from Ceramic Material, EP2361586-A1, 2011
89. P. Jensen, Dental Device e.g. Orthodontic Archwire, has Metallic Substrate Made Of Titanium, Titanium Oxide, Nickel Titanium, Vitalium or Chrome Cobalt, Where Device is Coated with Combination of Aluminum Oxide and Zirconia, US2011183281-A1, 2011
90. T. Hotokebuchi and I. Noda, Antimicrobial Product Useful in Biological Implant e.g. Artificial Dental Root, Comprises Thermal Spraying Film Formed by High-Speed Flame Spraying Powder Having Brookite-Type Titanium Oxide on Metal, Ceramic or Plastic Substrate, JP5308754-B2, 2013
91. A. Djemai, J.J. Fouchet and J. Fouchet, Formation of Beta Phase-Titanium-Zirconium Alloy for Manufacturing e.g. Dental Implant, Involves Stacking Layers Of Metal Powders, and Selectively Fusing Powders by Concentrating Laser-Beam or Using Sintering Modular Energy Source on Layers, FR3047489-A1; WO2017137671-A1, 2017
92. J. Cheng, Highly Connected Dental Structure for Dental Prostheses, has Ceramic Layer Which is Applied on the Inner and Outer Surfaces of Metal Cap Using a Plasma Spray Process, DE102011051594-A1, 2013
93. D. Wu, C. Zhining, C. Wan, and Q. Wang, IMPLANT For Bone Repair and Tooth Implant Comprises Strontium-Doped Calcium Polyphosphate Layer Coated on Surface of Matrix and Titanium Matrix, CN101927034-A, 2010
94. J.A. Sharp, Orthopedic Implant for Replacing Hip Joint with Prosthetic Joint During Replacement/Revision Hip Surgery of Patient, has Expansion Member Placed Between Portions and Adjusted by Tightening Tool to Displace Portions Relative to Each Other, WO2011156511-A3, 2011
95. R.G. Mauldin and R. Mauldin, Tubular Threaded Bone Implant for Fixation of Sacroiliac Joint e.g. for Degenerative Sacroiliitis, Has Set of Pores Defined on Body Such That Each Pore Does not Extend Through Entire Thickness of Wall of Body Between Surfaces of Body, WO2013134678-A1, 2013
96. M.A. Reiley, J. Lerman, and R.G. Mauldin, Method for Fusion of Sacral-Iliac Joint Between Iliac and Sacrum, Involves Inserting Bone Fixation Implant into Lateral Insertion Path Created Laterally Through Ilium, Sacral-Iliac Joint and Sacrum, US8986348-B2, 2015

97. T.D. Ferro, J.R. Phillips, and A.T. Ferro, Implant Device e.g. Cementless Unicompartmental Knee Replacement Implant Device, has Tapered Protrusions Extending from Surface of Base That Mates with Bone, Where Surface of Each Protrusion Includes Surface to Increase Area for Bone Growth, US2017312084-A1, 2017
98. J.P. Ritz and C. Scott, Making Bone Implant Used for Repair of the Ends of Bones at Orthopedic Joints Involves Creating Substrate of Structurally Strong Isotropic Graphite of the Shape Desired for Bone Implant, and coating with Microporous Isotropic Pyrocarbon, US8932663-B2, 2015
99. J.R. Porter, N.A. Winslow, J. Kneisl, and J.W. Sperling, Orthopedic Implant for use in Orthopedic Surgery e.g. Shoulder Arthroplasty, has Locking Mechanism that Prevents Movement of Soft Tissue Attachment Pad with Respect to Implant, US8715356-B2, 2014
100. H. Wecker and A. Rempp, Ceramic Layer Applied to the Surface of Component by Means of a Thermal Spraying Process, Useful for Functionalization of Medical Devices, Preferably Prostheses and Implants, WO2017055270-A1, 2017
101. R.E. Brosnahan, R. Fesmire, H. Gupta, D.A. Heuer, G. Hunter, and V. Pawar, Medical Implant for e.g. hip Joint, Has Surface of Oxidized Zirconium Adapted on Portion of Femoral and Tibial Components, and Plasma Sprayed Porous Coating Applied on Portion of Surface of Oxidized Zirconium, US2006052880-A1, 2006
102. D.E. Lawrynowicz, A. Wang, and Z. Zhang, Fabrication of Medical Implant Component Involves Producing Substrate Having Bearing Surface that Articulates with Bone or Another Medical Implant, and Spraying Particles of Same or Different Material Using Thermal Type Spraying Process, US7771775-B2, 2010
103. D.E. Lawrynowicz, A. Wang, and E. Jones, Providing Reactive Material on a Portion of Surface of Substrate of Medical Implant Component e.g. Femoral Stem Involves Placing Component in Holding Fixture at Atmospheric Pressure; and Spraying Material Particles at Predetermined Velocity, EP1806154-A1, 2007
104. R. Mongrain, O.F. Bertrand, S. Yue, and O. Bertrand, Intermixed Particulate Material Used in Bioresorbable stent comprises cathodic Particles Made of Cathodic Material and Anodic Particles Made of Anodic Material Bound to Each Other, where the Materials Form a Galvanic Couple, WO2013163747-A1, 2013
105. P.A. Kramer, Preparing Medical Device e.g. Stent, Useful e.g. to Treat/Prevent Restenosis, Comprises Forming Porous Component Comprising Near Net-Shaped Device by e.g. Arc Wire Spray Process, US7854958-B2, 2010
106. J. Garcia-Forgas, P. Heinrich, H. Kreye, W. Kroemmer, A. Salito, and F.J. Garcia, Production of a Medical Implant for Joints Comprises Coating the Implant with a Particulate Material by Cold Gas Spraying, EP1864686-A1, 2007
107. R.B. Heimann, Plasma-Sprayed Hydroxylapatite-Based Coatings: Chemical, Mechanical, Microstructural, and Biomedical Properties, *J. Therm. Spray Technol.*, 2016, **25**(5), p 827-850
108. R.B. Heimann and H.D. Lehmann, *Bioceramic Coatings for Medical Implants*, Wiley, New Yrok, 2015
109. M. Driver, *Coatings for Biomedical Applications*, Woodhead Publishing Ltd, Sawston, 2012
110. Y. Dong, P. Svoboda, M. Vrbka, D. Kostal, F. Urban, J. Cizek, P. Roupcova, H. Dong, I. Krupka, and M. Hartl, Towards Near-Permanent CoCrMo Prosthesis Surface by Combining Micro-Texturing and Low Temperature Plasma Carburising, *J. Mech. Behav. Biomed. Mater.*, 2015, **55**, p 215-227
111. J. Cizek, V. Brozek, T. Chraska, F. Lukac, J. Medricky, R. Musalek, T. Tesar, F. Siska, Z. Antos, J. Cupera, M. Matejkova, Z. Spotz, S. Houdkova, and M. Kverka, Silver-Doped Hydroxyapatite Coatings Deposited by Suspension Plasma Spraying, *J. Therm. Spray Technol.*, 2018. https://doi.org/10.1007/s11666-018-0767-2
112. J. Cizek, I. Dlouhy, F. Siska, and K.A. Khor, Modification of Plasma-sprayed TiO_2 Coatings Characteristics via Controlling the In-flight Temperature and Velocity of the Powder Particles, *J. Therm. Spray Technol.*, 2014, **23**(8), p 1339-1349
113. K. Ravi, T. Deplancke, K. Ogawa, J.-Y. Cavaillé, and O. Lame, Understanding Deposition Mechanism in Cold Sprayed Ultra High Molecular Weight Polyethylene Coatings on Metals by Isolated Particle Deposition Method, *Addit Manuf*, 2018, **21**, p 191-200
114. C. Ning, L. Zhou, and G. Tan, Fourth-Generation Biomedical Materials, *Mater. Today*, 2016, **19**(1), p 2-3

J Therm Spray Tech (2018) 27:1333–1343
https://doi.org/10.1007/s11666-018-0767-2

PEER REVIEWED

Silver-Doped Hydroxyapatite Coatings Deposited by Suspension Plasma Spraying

J. Cizek[1] · V. Brozek[1] · T. Chraska[1] · F. Lukac[1] · J. Medricky[1] · R. Musalek[1] ·
T. Tesar[1] · F. Siska[2] · Z. Antos[3] · J. Cupera[3] · M. Matejkova[3] · Z. Spotz[3] ·
S. Houdkova[4] · M. Kverka[5]

Submitted: 26 June 2018 / in revised form: 30 August 2018 / Published online: 12 October 2018
© ASM International 2018

Abstract Pure hydroxyapatite suspension was produced by wet chemical synthesis. Using a hybrid water-stabilized torch, a series of HA coatings were produced on SS304 and Ti6Al4V substrates and their properties were characterized by SEM, EDX and XRD techniques. After deposition, the amorphous phase content reached 6-10% and the coatings retained 75-82% of crystalline HA phase. Their thickness reached 145 μm. To understand the wear behavior of the coatings, pin-on-disc tribology evaluation was performed. Additionally, a set of HA coatings was prepared with pure metallic Ag content. This formed by in situ chemical decomposition of $AgNO_3$ added into the HA suspension. The Ag was dispersed evenly within the coatings in the form of submicron-sized particles situated predominantly along the HA splats boundaries with a total Ag content of 8 wt.%. Given the antibacterial properties of Ag, such result presents a promising step forward in the hard tissue replacement research.

✉ J. Cizek
cizek@ipp.cas.cz

[1] Institute of Plasma Physics, The Czech Academy of Sciences, Prague, Czech Republic

[2] Institute of Physics of Materials, The Czech Academy of Sciences, Brno, Czech Republic

[3] Institute of Materials Science and Engineering, Brno University of Technology, Brno, Czech Republic

[4] New Technologies Research Centre, University of West Bohemia, Pilsen, Czech Republic

[5] Institute of Microbiology, The Czech Academy of Sciences, Prague, Czech Republic

Keywords antibacterial property · HA · hybrid water-stabilized plasma · liquid feedstock · suspension plasma spraying

Introduction

The functionality and reliability are two factors predetermining the selection of materials used for hard tissue implants. In order to meet the stringent requirements for components in interaction with human tissues, the metallic implants are often subjected to additional technological processing, such as modifications of their surfaces. Traditionally, the metallic hard tissue replacements such as artificial joints are shielded by layers of bioceramic materials. Among them, the prominent position is reserved for calcium phosphates (Ref 1-7), owing to, e.g., their resemblance to natural bone tissue, outstanding bioactivity and osseoconductive properties. In particular, hydroxyapatite (HA) gained popularity due to its outstanding qualities (Ref 7-17). Bioactive HA layers on hard tissue implants have been reported to promote earlier stabilization of the implant within the surrounding bone, support bone in-growth, shield the implant from environmental attacks (such as corrosion by biofluid) and also prevent release of metallic ions to the body, reducing the possibility of intoxication (Ref 1).

Given their advantages, thermal spray processes are routinely used for deposition of bioactive coatings material. Prominent among other thermal spray technologies, plasma spraying has been readily applied for this task during the last decades (Ref 1, 18). The versatility of plasma deposition technology allows fabrication of coatings of thicknesses required for biological applications (Ref 1, 18).

Recently, introduction of suspensions into plasma spraying (Ref 19-21) provided a unique opportunity to produce coatings of novel, unparalleled microstructures with ultra-fine splats and high porosity. As opposed to their counterparts sprayed from powder precursor materials, the coatings often exhibit enhanced properties [e.g., lower thermal diffusivity, higher toughness and hardness (Ref 22, 23)]. Furthermore, through change in the suspension formulation (unparallelled in powder spraying), additional control of the coating microstructure is enabled, allowing, e.g., production of fully dense or, conversely, high porosity coatings or coatings with columnar surface protrusions. Another advantage is the potential of new phases formation through in situ pyrolysis of multiple suspensions (Ref 24) as well as two-phase materials production with homogeneous and fine distribution of both phases within the coating prepared from suspension–solution mixtures.

To obtain the ready-to-spray HA powder, rather arduous processes of atomization of the primary suspensions/solutions, furnace calcination and sieving are frequently involved (Ref 25). These are time- and cost-consuming and, inherently, include the potential risk of, e.g., additional impurities integration or deviations from the original phase composition. Naturally, the process yield is not 100%, further lowering the efficiency of the process. On the contrary, the potential usage of HA solutions or suspensions for direct feeding into the plasma torches presents a significantly simpler procedure with the further benefit to create novel microstructures.

Such alluring prospect has already received, albeit still limited at the moment, attention in the literature. In their initial attempts, Jaworski et al. (Ref 26, 27) and Kozerski et al. (Ref 28) synthesized HA suspension from 6 moles $(NH_4)_2HPO_4$, 10 moles $Ca(NO_3)_2$ and 8 moles NH_4OH. The resulting coatings were, however, too thin (10-33 µm) for practical application. Candidato, Mejias and colleagues (Ref 29, 30) produced HA coatings from solutions via in situ reaction of $Ca(OH)_2$ and 6 moles $(NH_4)_2HPO_4$. Using various plasma spray settings, the coatings thicknesses ranged 49-66 µm with low porosities of 1.3-5.1%. Cattini et al. (Ref 31, 32) achieved ~ 80 µm graded HA/bioglass coatings with individual HA layers thicknesses of 15-20 µm. Huang et al. (Ref 33) managed to form suspension-sprayed 100 µm HA coatings with enhanced porosity using a diluted liquid precursor. A direct comparison between solution and suspension-sprayed HA was made by Aruna et al. (Ref 34). In their study, the SPS HA contained CaO; nevertheless, it still exhibited superior corrosion and wear properties, and, importantly, in vitro bioactivity.

Biofilm-producing bacteria are the principal causes of infections associated with arthroplasty (Ref 35). Given its unique antibacterial properties (Ref 36), silver is an attractive element considered in the area of thermally sprayed layers. In the literature, very few attempts to add silver content into HA coatings could be found. At the time of writing, all of them were related to plasma spraying from (solid) powder feedstock (Ref 35, 37) or different coating deposition methods (Ref 38-44).

In our study, thick HA coatings were deposited directly from pure in-house produced suspensions using a hybrid water-stabilized plasma torch. Two different substrates were used and the coatings were sprayed under different spray parameters. Pin-on-disc wear performance of the coatings was evaluated. First time reported in the available literature, a novel approach is suggested in our paper: pure Ag content was formed within the coatings structure by in situ decomposition reaction, thereby significantly simplifying the entire process as opposed to the previous Ag-HA studies from (solid) powder feedstock.

Materials and Methods

Feedstock Preparation

The HA suspension was produced by wet chemical synthesis. In this neutralization reaction, $Ca(OH)_2$ as a source of calcium atoms was drop-wise added into H_3PO_4 at 36.8 °C. The suspension was stirred during the process and the reaction stopped upon reaching pH ~ 9 [more details can be found in the previous works (Ref 3, 4)]:

$$10Ca(OH)_2 + 6H_3PO_4 \rightarrow Ca_{10}(PO_4)_6(OH)_2 + 18H_2O.$$

The produced aqueous suspension was saturated with HA, but could also contain metastable phases such as TCP (tricalcium phosphate, $Ca_3(PO_4)_2$, Ca/P ratio 1.5) or TTCP (tetracalcium phosphate, $Ca_4O(PO_4)_2$, Ca/P ratio 2.00). As compared to the more stable HA phase, these phases are susceptible to continuous dissolution in a non-saturated aqueous solution. In such dissolution process, precipitation of additional HA is likely to occur (Ref 2, 4). This principle was used to obtain pure, non-contaminated HA: first, the suspension was left to settle for 48 h, leading to separation of excess water and the HA precipitate. The excess water was then removed, and new deionized water was mixed into the suspension again.

To determine the efficiency of the purification process, a sample of the suspension was dried in a vacuum furnace (60 °C, 10 h) and the obtained material was subjected to XRD analysis using Rietveld refinement (Ref 45). The collected spectrum corresponded to 100% pure HA phase (Fig. 1) with no or negligible amorphous content. The produced suspension exhibited a rather viscous behavior at 20 °C, measured as $\eta = 23\,\mathrm{mPa\,s}$ [DV2TLV, Brookfield, USA; cf., e.g., ethanol and water $\eta = 1.082\,\mathrm{mPa\,s}$ and

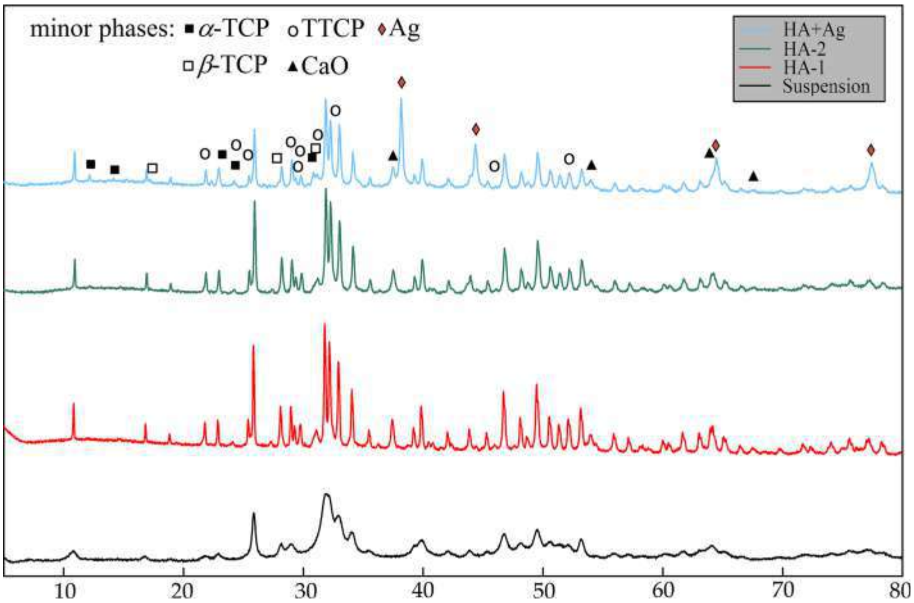

Fig. 1 XRD spectra of the (dried) HA suspension and the produced SPPS coatings. For clarity, only the peaks pertaining to the minor phases formed upon spraying were indexed. All the non-indexed peaks pertain to pure HA phase

$\eta = 0.890\,\text{mPa s}$, respectively (Ref 46)]. This viscosity is significantly higher than that of commonly sprayed suspensions (Ref 23). For the second set of coatings (HA-2, see "Coating Deposition" section), the viscosity of the suspension was therefore reduced to approximately 50% of the original through dilution by adding deionized water.

In the second part of this study, an attempt was made to precipitate pure metallic Ag content in the coatings through in situ chemical reaction. For that, 40% aqueous solution of $AgNO_3$ was added into the HA suspension (24.2 g of $AgNO_3$ solution per 1 L of HA suspension).

During spraying, both suspensions (pure HA, HA + $AgNO_3$) were thoroughly stirred to prevent sedimentation. A sample of each suspension was analyzed to determine the average size of the HA coagulates (Mastersizer 3000, Malvern, UK). There were no detectable differences between the suspensions and the average particle diameter reached $d_{50} = 0.89\,\mu\text{m}$.

As an alloy commonly used for hard tissue implants applications, 4-mm-thick Ti6Al4V (Grade 5 ELI) substrates were used in this study. In addition, 2.5-mm stainless steel AISI304 substrates were used. The use of such dissimilar materials (e.g., in terms of their heat conduction or thermal expansion properties) should aid in our understanding of the influence of the substrate material on the interface development and coating formation. All substrates were cut into 30 × 20 mm^2 coupons and grit-blasted prior to deposition (α-Al_2O_3 grit, 200-350 μm, perpendicular blasting from 150 mm distance), followed by ultrasonic cleaning (10 min) in isopropanol to remove grease and minimize potential residual grit. The substrates were then dried using hot air and immediately sprayed.

Coating Deposition

The prepared substrates were mounted into a carousel holder (revolving at 55 r.p.m., equivalent to $0.65\,\text{m}\,\text{s}^{-1}$), and their temperature in the spray process was measured using a thermo-camera as well as a thermocouple attached to the rear side of one of the substrates. To prevent excessive material heating, two air blades were mounted from side and rear of the carousel and run perpetually throughout the spraying. Prior to the first deposition cycle, the substrates were preheated to 200-220 °C by the plasma torch without material feeding. During spraying, the samples temperature increased to about 350-420 °C after each spray cycle. The torch was then moved into a distant position, and the substrates were left to cool to inter-cycle temperature of 200 °C (Fig. 2).

In this study, a high enthalpy hybrid water-stabilized plasma torch (WSP-H500) developed at the Institute of Plasma Physics (Prague, Czech Republic) was employed for coatings deposition. As opposed to gas-stabilized torches, the plasma in WSP-H500 is generated in the gas-stabilized section first (consumption of Ar 15-20 slpm in this experiment, Table 1) and then enters the water-stabilized plasma section (water vortex) where its enthalpy is substantially increased. Thereby, significantly superior heat input was transferred to the HA and HA + $AgNO_3$ suspensions, ensuring their proper deposition. The torch was operated at a current of 500 A, which corresponds to a net power of approximately 150 kW. More details on the torch specification could be find in our previous studies (Ref 23).

The suspensions were fed radially into the plasma jet. The demand for an accurate suspension penetration into the jet and, therefore, proper evaporation of the liquid carrier

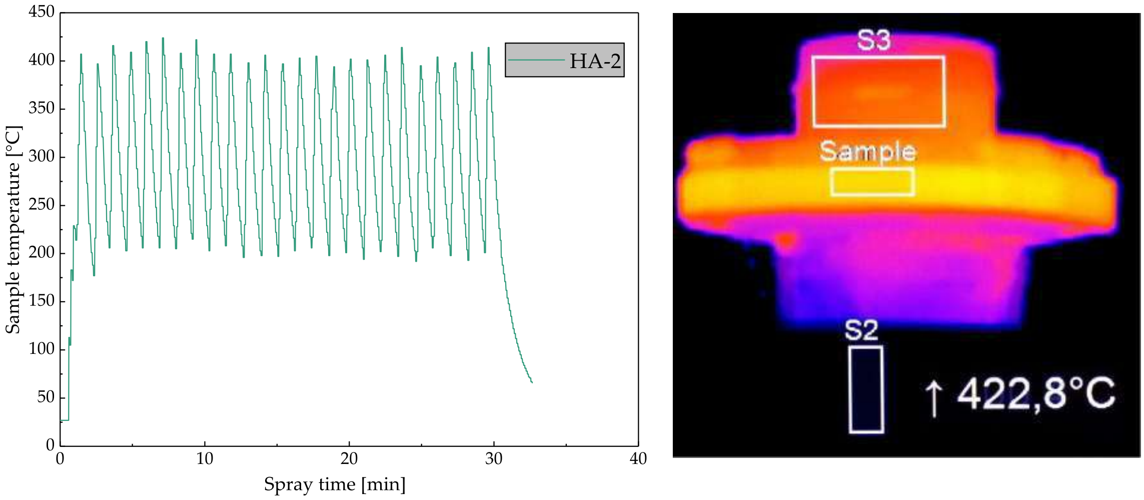

Fig. 2 Left: temporal development of the sample temperatures during coating deposition (illustrated for HA-2 sample) as measured by a thermocouple attached to the rear side of the substrates. Note that one peak (i.e., 1 cycle) in the curve corresponds to six passes of the torch. Right: temperature of the samples mounted into the revolving carousel measured by thermo-camera. Pre-heating to 200-220 °C was carried out for all coatings

Table 1 Hybrid plasma system settings for fabrication of the coating sets

Set	Torch current, A	Ar flow, slpm	Feed distance, mm	Feed pressure, bar	Feed angle, degrees	Feed rate, g min^{-1}	Torch passes	Standoff distance, mm
HA-1	500	15	20	3.0	20	97	240	100
HA-2	500	15	30	3.0	25	98	150	100
HA + Ag	500	20	30	3.0	25	99	136	150

and even melting of the deposited material requires usage of small diameter feeding nozzles with small suspension divergence. However, too small nozzle diameters could lead to clogging, in particular during runs with increased number of torch passes, such as is the case in this study. As a compromise, a 0.35-mm-diameter sapphire nozzle was used for the feeding. Prior to spraying, shadowgraphy imaging (SprayCam, Control Vision Inc., USA; Fig. 3) was used to optimize the injection pressure and the positioning of the feeder (feed angle and feed distance, i.e., the distance of the suspension entrance point from the plasma torch nozzle). After optimization, the torch was moved into a position in front of the substrates and the coatings were deposited.

To understand the development of the coating microstructures and outline the potential of the WSP-H plasma torch for modification of the sprayed materials properties, three different coating sets were fabricated. Two sets of pure HA (HA-1, HA-2) suspensions were sprayed under conditions leading to different heat transfer from the plasma jet (Table 1). Notably, two different feeding distances of 20 and 30 mm (cf. the relatively short total standoff distance of 100 mm) and different feeding angles were used, leading to a significant difference in the particles' dwell times. Additionally, one set of HA + $AgNO_3$ (denoted as HA + Ag in the text) coating was produced to demonstrate the feasibility of this simple method for readily incorporating this antibacterial element.

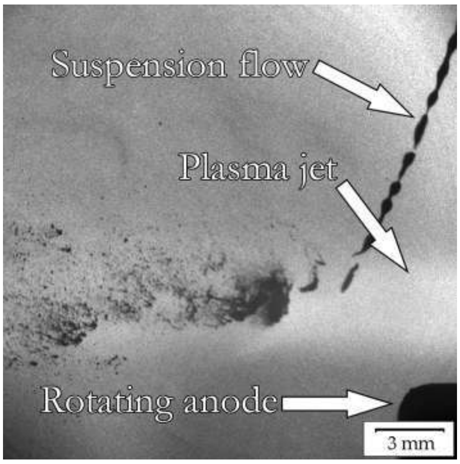

Fig. 3 Illustration of shadowgraphy optimization of suspension feedstock injection into the plasma jet. Spraying of suspension HA-1 is portrayed

For the HA + Ag samples, the argon flow was increased by 33% (Table 1) to promote suspension stream fragmentation via increased plasma density. Further to that, different standoff distance of 150 mm was used for the HA + Ag set. This was implemented to prolong the particles' dwell time within the plasma jet, thereby providing enhanced thermal input into HA suspension with added $AgNO_3$ content. From the bio-application point of view, the minimum coating thickness should reach $> 30\,\mu m$ (Ref 7). Given the inferior per-pass-thickness deposition of suspensions as compared to standard spraying of powders, the total number of torch cycles employed in the study exceeded 45 in all cases.

Coatings Characterization

The cross-sectional microstructure of the produced coatings was assessed using SEM (Zeiss MA 15 and Zeiss Ultra Plus). The samples were prepared using standard metallographic procedures, involving the final polishing steps using 1-µm diamond paste followed by 0.06-µm OPS colloidal silica. Assessment of the coatings chemical composition was performed using both point and area EDX analyses (XFlash 5010, Bruker, Germany). For visualization of Ag content, long-term EDX mapping was carried out. Complementary confirmation of the Ag presence was realized using XRF spectrometry (Axios, PANanalytical, Netherlands) with Rh source. Phase composition of the produced coatings was analyzed using Rietveld refinement of the measured XRD spectra (Smart lab 3kW, Rigaku, Japan and D8 Discover, Bruker, Germany). Given the nature of the coatings, Cu-K_α radiation in Bragg–Brentano geometry setup was used. Quantitative Rietveld analysis (Ref 45) was performed by TOPAS v5 (Bruker, Germany), and preferential orientation correction of the peak intensities was treated by the March–Dollase approach (Ref 47). The analysis also aided in determination of the amorphization of the originally crystalline HA content after spraying.

Surface roughness of the produced samples was measured using Taylor–Hobson Surtronic 3P. Ten measurements were taken for each sample with the track length of 4.5 mm. Given the dimensions of the inter-protrusion gaps with respect to the typical surface asperity sizes, R_a was selected as the proper roughness indicator as the values of R_z would be influenced by the protrusions existence, yielding the values difficult to compare with HA coatings deposited from solid powders in other studies.

Mechanical integrity of the deposits and their tendency toward material removal were studied using tribological evaluation of the three coatings (upon repetitive loading of the implants, the HA coating is brought into contact with surrounding tissues). For that, pin-on-disc testing was carried out (High-temperature tribometer, CSEM, Switzerland) using Al_2O_3 5-mm ball counterpart at ambient temperature. After trial runs, a 1 N load was selected as optimal and was used for evaluation of all samples to maintain mutual comparability. The relative speed of the counterparts was kept at $10\ cm\,s^{-1}$, and the tests were performed at ambient temperature (20 °C) in air. For each sample, four tests were made at 3000 cycles with 2.5-mm wear track diameter each and the average wear track depth was taken as the representative value characterizing the tribological performance. In these tests, the coatings deposited on the AISI304 substrates were used.

Results

Coatings Microstructure

Morphology of the fabricated coatings is shown in Fig. 4. The coatings exhibited the splat-like structure typical for plasma deposited materials as well as columnar protrusions, a feature characteristic of spraying from liquid feedstock (Ref 19, 23, 24). Partially owing to the inter-protrusion gaps (typically 30-50 µm wide), the roughness of the three coatings surfaces ($R_a = 10.5{-}15.9 \mu m$) exceeded that of the typical powder deposits (Ref 19). The samples HA-2 and HA + Ag contained a significantly lower number of the columnar protrusions (as compared to HA-1), thereby exhibiting lower surface roughness. The splats appeared well molten, with their respective diameters suggesting a pronounced in-flight agglomeration of the primary particles. At the same time, unmolten feedstock appeared within the structure. Also, no apparent through-thickness pores were detected in the coatings, effectively shielding the underlying substrates.

The total coatings thicknesses are listed in Table 2, as well as the values related to deposition rate (equivalent to 1 pass thickness increase). The coatings reached thicknesses ranging from 30-145 µm, the major difference being the existence of protrusions in coating HA-1. The values of 1 pass thickness increase were approximately two orders of magnitude lower than those typically encountered in spraying from powders [Table 2, (Ref 48)].

Within the coatings structure, a significant proportion of micro-porosity could be found (Table 2). The pore sizes were lower than those of their powder-sprayed counterparts (Ref 3, 4, 11), with typical (equivalent) diameter reaching 0.7-3.2 µm. There appeared to be no change in the inter-splat pore size or content along the coating thickness in the main coating. This contrasted with the markedly decreased porosity within the protrusions which appeared much denser. From the point of view of osteoblast cells attachment, the major contribution to the overall porosity was

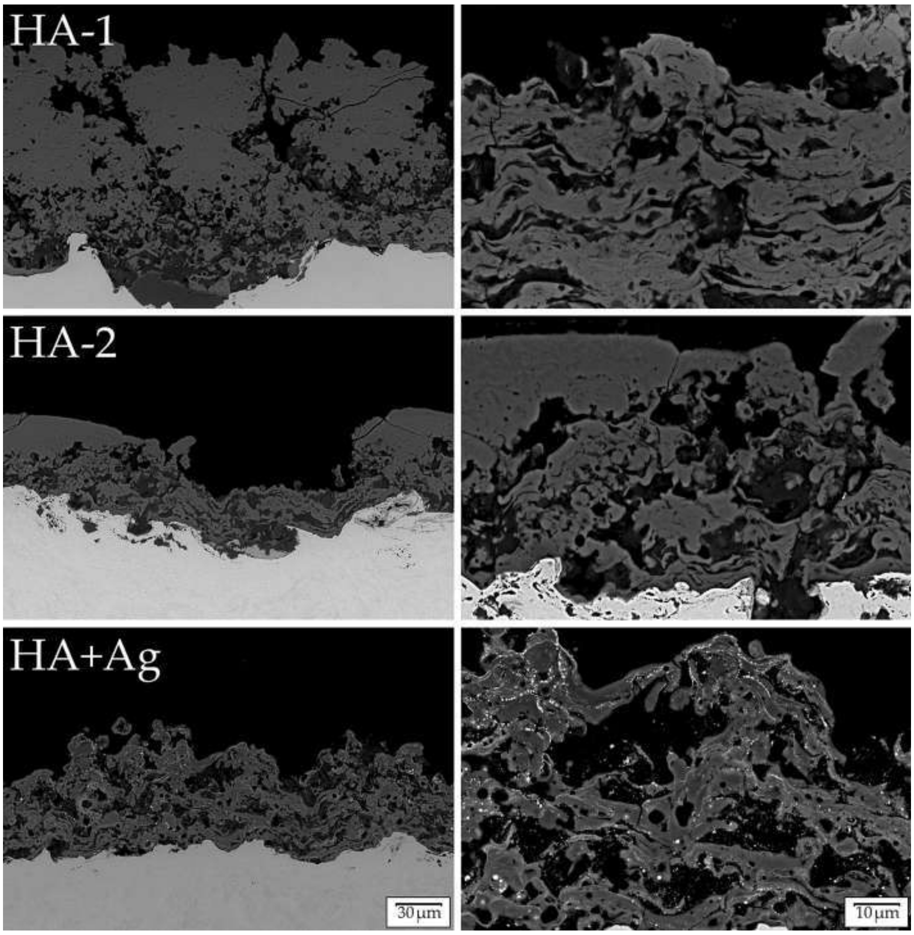

Fig. 4 Microstructure of the HA and HA + Ag coatings produced from suspensions on Ti6Al4V substrates. The white contrast sub-micron particles evenly dispersed in the HA + Ag coating are pure Ag

Table 2 Properties of the produced coatings

Set	Thickness, μm	Thickness per cycle, μm	Wear depth, μm	COF, –	Porosity, %
HA-1	145 ± 14	1.81 ± 0.18	63.10 ± 13.96	0.915 ± 0.239	6.2 ± 2.9
HA-2	30 ± 6	0.60 ± 0.12	10.80 ± 3.57	0.844 ± 0.265	3.9 ± 1.6
HA + Ag	50 ± 6	1.10 ± 0.12	67.05 ± 16.20	1.029 ± 0.288	4.5 ± 1.2

therefore represented by the inter-protrusion gaps at the very surface. The coatings further infrequently contained micro-cracks spanning several splats in the denser, columnar part. The cracks orientation was mostly vertical, i.e., parallel to spraying direction.

The coating and substrate materials were well connected at their mutual interface, and the conformity of the impacting molten material to the previously grit-blasted metal was good as no empty asperities were found along the entire interfaces. As compared to the AISI304 steel, the coatings produced on the Ti6Al4V substrates exhibited slightly better interface quality and a tendency to form smaller pores. However, these differences were not pronounced significantly and the morphology of the coatings deposited on the two different substrates could be considered comparable.

Coatings Composition

The Rietveld analysis allowed determination of the phase composition of the coatings (Fig. 1 and Table 3). As compared to the 100% crystalline suspension feedstock, 7-10 wt.% ACP content developed within the coatings, with slightly higher values recorded for sample HA-1. The retained crystalline HA levels in the coatings reached 76-78 wt.%, a value comparable to the counterparts sprayed from powder feedstock using conventional gas-stabilized torches (Ref 1, 3-5, 7). Thermal decomposition phases formed upon deposition included TTCP, α- and β-TCP, and lime (CaO), in total amounts ranging from 22-23 wt.% in the coatings. There were no major differences in the phase composition of the coatings deposited onto AISI304 steel or Ti6Al4V substrates, as shown in Table 3.

According to EDX analyses, the major HA elements (Ca, P) were distributed homogeneously within the fabricated coatings. Elemental maps obtained by EDX are shown in Fig. 5 for HA + Ag coating on an AISI304 substrate. The mutual ratio of Ca/P was noticeably increased in all coatings (2.03, 2.18, 2.08 for HA-1, HA-2 and HA + Ag, respectively) as opposed to the value of Ca/P = 1.67 of the initial HA suspension (matching the theoretical one). No diffusion of substrate elements into the coating material was observed.

The silver content in the sprayed coating HA + Ag reached as much as 8 wt.%. The presence of Ag was also confirmed by XRF analysis results (amount indicated as 12.1 wt.%). Owing to the limitations and different measurement principles of the two methods, the values can be considered to be in agreement. Importantly, the Ag content was detected as pure metal, with no residual $AgNO_3$ content. An even distribution of Ag within the sprayed coating was observed (Fig. 5) in the form of sub-micron-sized spherical particles. Those could be found both within the HA splats and at their surfaces (i.e., inter-splat boundaries), where a slightly increased Ag content could be observed.

Table 3 Phase composition of the produced coatings (wt.%)

Set	ACP	HA	TTCP	α-TCP	β-TCP	CaO	Ag
HA-1	10	77	15	1	2	5	–
	9	78	14	1	2	5	–
HA-2	9	79	14	2	0	5	–
	7	78	14	3	0	5	–
HA + Ag	8	70	8	7	3	4	8
	6	71	7	6	3	5	8

For each coating type, the first row shows the composition for AISI304 substrates, while the second row relates to Ti6Al4V substrates. ACP denotes amorphous calcium phosphate

Tribological Performance

The performance of the coatings in contact with an external solid body was assessed using pin-on-disc testing (Table 2). While the wear depth of the coating HA-2 reached values as low as ~ 11 µm, the other two tested coatings (HA-1, HA + Ag) exhibited similar wear tracks depths of 63 and 67 µm, respectively. Given the total thickness of the three coatings, the testing of sample HA + Ag most likely ended with the Al_2O_3 ball counterpart being in contact with the underlying AISI304 substrate material. However, the debris collected from the wear tracks contained HA particles only and no significant differences in terms of particles size distribution were found when comparing the three samples. At the same time, no metallic Ag was detected in the debris. The coefficients of friction of the samples HA-1, HA-2 and HA + Ag reached 0.915 ± 0.195, 0.844 ± 0.172 and 1.029 ± 0.025, respectively (Table 2).

Discussion

The results obtained from SEM, EDX, XRD and XRF analyses provided an overall characterization of the fabricated coatings. Within the coatings microstructure, the majority of the particles were fully molten, confirming that the enthalpy of the used WSP-H500 plasma torch effectively evaporated the liquid carrier and melted the hydroxyapatite particles in the suspension. The microstructure was much finer compared to the HA coatings sprayed from traditional powders, which is a

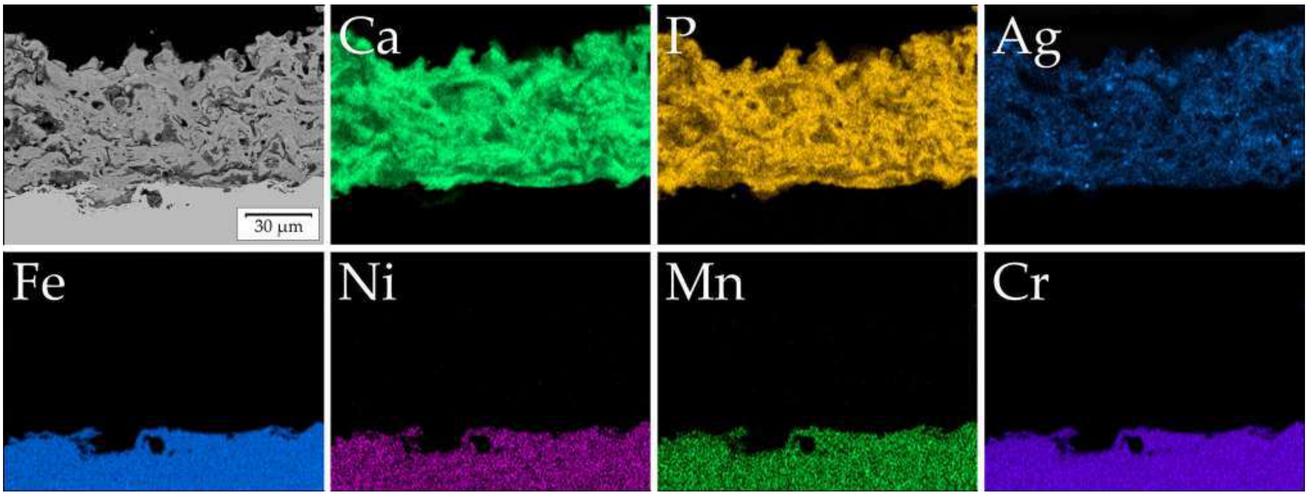

Fig. 5 EDX maps of HA + Ag coating on AISI304 substrate. The Ca, P and Ag contents are evenly distributed

consequence of the sub-micron size of the HA particles in the suspension (Ref 19, 23). This actually presents a significant advantage of the suspension route (save for the pore sizes, see below) that may be exploited in the future attempts and biological testing.

The thickness of the coatings differed due to both different number of spray passes and higher feed distance, but also due to the fact that the HA-2 coating was produced from a 50% diluted suspension in contrast to the original HA-1. This explains the measured reduction of ~ 66% in the per-pass thickness. Similar decrease of ~ 38% was measured for the HA + Ag coating. In this case, the reason being the addition of 40% aqueous solution of $AgNO_3$ and the longer standoff distance. The thicknesses presented in our study were comparable (HA-2, HA + Ag) or higher (HA-1) compared to those reported elsewhere (Ref 26, 29, 49).

Microcracking was observed in the coatings, likely a consequence of internal stress relaxation during cooling to room temperature due to shrinkage of both coating and substrate materials. As compared to the underlying coating part, increased occurrence of cracks appeared inside the columnar protrusions. This could have been caused by the relatively higher density of this region as well as its slower cooling rate due to a presence of underlying, low thermal conductivity HA layer.

The ~ 4 to 6% porosity contained within all three studied coatings was presumably formed as a consequence of insufficient local conformation of the impinging particles on the underlying asperities (e.g., solidification of the molten particle before filling the micro-asperities or effects associated with surface tension of the molten material), formation of micro-cracks, as well as a minor presence of unmolten feedstock due to delayed, post-deposition evaporation of the liquid carrier. Given the increased number of passes, there is, naturally, no trend in the porosity along the coating thickness (except for the columnar protrusions). The 0.7-3.2-µm pores are smaller than those of the powder-produced coatings [as also observed in (Ref 29) with the total low porosity of 1-5%]. In fact, their dimensions are unsuitable for in-growth of osteoblast cells at present and a targeted optimization will be required in the future [cf. Huang et al. (Ref 33) who achieved ~ 48% porosity with the pore sizes exceeding 10 µm]. Also, the average pore diameters are interesting when considering the average diameter of the original HA particles in the suspensions, 0.89 µm. The denser microstructure of the HA deposit within the protrusions (see, e.g., HA-1 in Fig. 4) could be a consequence of an improved mutual splats bonding facilitated through enhanced heat input. This, in turn, is a consequence of the existence of low thermal conductivity HA layer below the protrusions, resulting in the splats remaining at elevated temperatures for extended times.

Bearing in mind the typical splat sizes, the proportional surface roughness of the coatings surpassed substantially that of the powder-fabricated HA coatings, mostly due to the presence of the relatively big inter-protrusion gaps. Again, this presents a promising scaffold for subsequent attachment and proliferation of osteoblast cells upon implantation.

No significant differences were found in the coating structure or interface features for the coatings deposited onto either AISI304 stainless steel or Ti6Al4V alloy substrates. That said, the differences in the properties of the two metals such as thermal conductivity or thermal expansion did not seem to play a significant role in the suspension spray process. This, however, needs to be considered against the fact that intensive cooling of the substrates was used during the spray process, thereby effectively reducing the potential substrate influence.

The phase composition of the produced suspension was measured as 100% HA, with no amorphous content. This is a consequence of the used production route and the applied purification process. Upon spraying, the composition and respective HA crystallite size changed due to the plasma heat intake and melting of the HA particles, as it generally happens when spraying HA using thermal spray methods (Ref 2-4, 7). A clear difference in HA XRD peaks broadening is shown in Fig. 1 between the suspension and the three produced coatings. While the suspension consisted of small, 14 ± 1-nm HA crystallites within the individual precipitates, the coatings exhibited larger crystallite sizes of 325 ± 8, 182 ± 5 and 173 ± 9 nm for HA-1, HA-2 and HA + Ag coatings, respectively. Further to that, a small microstrain in the order of 10^{-4} resulting from the high-temperature thermal treatment and subsequent cooling was detected.

An amorphous content of 6-10% was formed [cf., e.g., 23-31% in a targeted HA crystallinity study (Ref 50) or even 0% in (Ref 51)]. According to the literature, a partial amorphous content is advantageous for hard tissue implant applications as compared to fully crystalline HA (Ref 10). The amorphous HA content was slightly higher for the coating HA-1. Even though such difference is negligible, this is in accordance with its spray parameters, where shorter feeding distance (by 10% relatively to the total standoff distance) and lower feeding angle were used as compared to the HA-2 coating. Both parameters would result in longer dwell times of the HA suspension in the plasma jet, thereby, in turn, forming the discussed increased amorphous content.

The levels of retained HA in the microstructure (76-78%) are superior to those obtained in the majority of other studies [e.g., 37-62% in (Ref 26) or 57-71% in (Ref 29)], but lower than 95-98% achieved from solution spraying in (Ref 52). A content of 4-5% of CaO was detected in the coatings (also, e.g., in Ref 34, cf. the extremely low content of 0.4-0.8% achieved by Latka et al. in Ref 53). This phase commonly forms upon spraying of HA (Ref 26) and was reported to negatively influence the acceptance of the implants inside the body owing to its inherent cytotoxicity. Reduction in CaO content will, too, be targeted in the future. There was no significant difference in the phase content of the samples HA-1 and HA-2. The sample HA + Ag contained exhibited decreased amounts of TTCP, in exchange for increased content of $\alpha + \beta$-TCP. Such change could have been triggered by the lower heat transfer to the particles in-flight due to enthalpy used for the $AgNO_3$ decomposition.

The elemental composition of the coatings indicated markedly increased values of the Ca/P ratio (cf. the theoretical value of 1.67 to the average value of 2.10 of the three coatings). This, again, is a consequence of the selected deposition process and the increase in Ca/P ratio was reported earlier for the powder HA depositions (Ref 4), presumably through selective evaporation of phosphorus. Partially, this may have triggered a formation of the ~ 14-15% content of TTCP with its 2.00 Ca/P ratio and the 4-5% presence of CaO phase. The seemingly lower content of HA phase in the HA + Ag coating (70% and 71% for AISI304 and Ti6Al4V substrates, respectively) is a consequence of the Ag content. Should the Ag be omitted from the calculations, the HA content in the two coatings would be marked as 75 and 77%, i.e., values comparable to 76-79% of the HA-1 and HA-2 coatings.

The desirable in situ decomposition of $AgNO_3$ into Ag was fully completed as no residual silver nitrate was detected in the coatings. Importantly, the silver does not form either chemical compounds or intemetallics with any of the other present elements. On the contrary, the entire silver content was detected as pure metallic Ag, i.e., the method suggested herein was proved as suitable. Further to that, the silver content is distributed evenly within the entire coatings, which could partially be attributed to the inferior per-pass thickness increase compared to the powder routes. That said, the Ag content must have been incorporated into the splats during the molten state of the HA phase. Lastly, the total Ag content exceeded the desirable target value of 5 wt.%., with its actual content being as high as 8%. This is significantly higher than the values reported by Ueno et al. (Ref 35) or Zhao et al. (Ref 37) (0.5-3.0% and 0.3-0.6%, respectively). According to the literature, all these properties combined should ensure antibacterial properties (Ref 44) and therefore aid in the reduction in any implant-associated infections, i.e., improving the chances of a successful implants surgery.

The increased wear resistance of HA-2 coating could be caused by its markedly denser microstructure. The layers' mutual coherence could be enhanced by this, thereby effectively decreasing the particles release upon contact with a solid body. Also, the HA-2 contained a lower number of the columnar protrusions that got detached preferentially from the HA-1 coating. The wear rates of the HA + Ag coating were comparable to those of HA-1. This result was rather surprising, owing to the fact that the HA + Ag coating was formed from a diluted suspension (analogous to HA-2). To some extent, the result could be attributed to the longer standoff distance and the resulting less compact structure. Nevertheless, this still needs to be studied in more detail in the near future. In any case, the wear track depth of this coating exceeded the average thickness of the produced coating (cf. ~ 67 and ~ 50 µm). No metallic content (including Ag) was found in the collected debris, though. Such results would indicate that the coating was either deformed deeper into the substrate below the moving alumina counterpart or the substrate itself deformed upon contact through its plasticity, with no material removal. The measured coefficients of friction suggest small differences between the three coatings. Despite the apparent difference of ~ 8% (Table 2, COF HA-1 versus COF HA-2), the relatively high noise/scatter of the values within the individual runs does not allow to make any secure conclusions. The scatter could most likely be attributed to the columnar protrusion structure of the coatings free surfaces and the heterogeneous microstructure resulting from the selected suspension plasma spraying route.

Conclusion

Thick hydroxyapatite coatings were suspension plasma sprayed, effectively avoiding the tedious procedure of powder fabrication. For the first time in the literature, silver-doped hydroxyapatite coatings were fabricated using chemical decomposition of $AgNO_3$ solution added into the HA suspension. From the obtained results, it could be concluded that:

- Pure, 100% hydroxyapatite suspension can be produced by wet chemical synthesis.
- Suspension spraying is a viable method to deposit thick ($> 140\,\mu m$) coatings with surface roughness suitable for osteoblast cells proliferation and osseointegration. Further optimization of the per-pass thickness increase will still be necessary, though, as it currently lacks behind deposition from solid powder feedstock.
- The selection of substrate material does not appear to have any significant influence on coating properties at the used spray distances of 100-150 mm since the

suspension-produced coating microstructures are fully comparable on AISI 304 steel and Ti6Al4V alloy.

- Phase changes (in particular, transformation of HA into other Ca-P phases) as well as amorphization are inherent to suspension spraying, too, with the values comparable to those of powder spraying methods.
- Mechanical integrity of the coatings is strongly dependable on the microstructure. The columnar protrusions distinctive for spraying from liquid feedstock are highly susceptible to wear damage.
- Silver can be readily dispersed within the HA coatings using in situ decomposition of $AgNO_3$ solution. Such methodology is considerably simpler than in the case of spraying from powders (e.g., no milling or co-precipitation needed) and leads to a homogeneous distribution of sub-micron Ag particles.
- The total Ag content can be simply controlled and could exceed that of the powder-sprayed coatings, effectively decreasing the risk of implant-associated infections upon surgery.

Acknowledgments The experimental study was supported through Czech Science Foundation grant GB14-36566G “Multidisciplinary research centre for advanced materials”.

References

1. L.L. Hench, Bioceramics-From Concept to Clinic, *J. Am. Ceram. Soc.*, 1991, **74**(7), p 1487-1510
2. L.L. Hench, Bioceramics, *J. Am. Ceram. Soc.*, 2005, **81**(7), p 1705-1728
3. J. Cizek, K.A. Khor, and Z. Prochazka, Influence of Spraying Conditions on Thermal and Velocity Properties of Plasma Sprayed Hydroxyapatite, *Mater. Sci. Eng. C*, 2007, **27**(2), p 340-344
4. J. Cizek and K.A. Khor, Role of In-Flight Temperature and Velocity of Powder Particles on Plasma Sprayed Hydroxyapatite Coating Characteristics, *Surf. Coat. Technol.*, 2012, **206**(8-9), p 2181-2191
5. J.L. Xu, D. Joguet, J. Cizek, K.A. Khor, H.L. Liao, C. Coddet, and W.N. Chen, Synthesis and Characterization on Atomphospheric Plasma Sprayed Amorphous Silica Doped Hydrxoyapatite Coatings, *Surf. Coat. Technol.*, 2012, **206**(22), p 4659-4665
6. R.B. Heimann, Materials Science of Crystalline Bioceramics: A Review of Basic Properties and Applications, *Chiang Mai Univ. J. Nat. Sci.*, 2002, **1**(1), p 23-45
7. R.B. Heimann, Plasma-Sprayed Hydroxylapatite-Based Coatings: Chemical, Mechanical, Microstructural, and Biomedical Properties, *J. Therm. Spray Technol.*, 2016, **25**(5), p 827-850
8. T.J. Levingstone, M. Ardhaoui, K. Benyounis, L. Looney, and J. Stokes, Plasma Sprayed Hydroxyapatite Coatings: Understanding Process Relationships Using Design of Experiment Analysis, *Surf. Coat. Technol.*, 2015, **283**, p 29-36
9. T.J. Levingstone, N. Barron, M. Ardhaoui, K. Benyounis, L. Looney, and J. Stokes, Application of Response Surface Methodology in the Design of Functionally Graded Plasma Sprayed Hydroxyapatite Coatings, *Surf. Coat. Technol.*, 2017, **313**, p 307-318
10. K.A. Gross, C.C. Berndt, and H. Herman, Amorphous Phase Formation in Plasma-Sprayed Hydroxyapatite Coatings, *J. Biomed. Mater. Res.*, 1998, **39**(3), p 407-414
11. M.F. Hasan, J. Wang, and C.C. Berndt, Effect of Power and Stand-Off Distance on Plasma Sprayed Hydroxyapatite Coatings, *Mater. Manuf. Process.*, 2013, **28**(12), p 1279-1285
12. S. Dyshlovenko, L. Pawlowski, P. Roussel, D. Murano, and A. le Maguer, Relationship Between Plasma Spray Operational Parameters and Microstructure of Hydroxyapatite Coatings and Powder Particles Sprayed Into Water, *Surf. Coat. Technol.*, 2006, **200**(12-13), p 3845-3855
13. V. Guipont, M. Espanol, F. Borit, N. Llorca-Isern, M. Jeandin, K.A. Khor, and P. Cheang, High-Pressure Plasma Spraying of Hydroxyapatite Powders, *Mater. Sci. Eng. A*, 2002, **325**(1-2), p 9-18
14. K.A. Khor, Y.W. Gu, C.H. Quek, and P. Cheang, Plasma Spraying of Functionally Graded Hydroxyapatite/Ti-6Al-4V Coatings, *Surf. Coat. Technol.*, 2003, **168**(2-3), p 195-201
15. K.A. Khor, C.S. Yip, and P. Cheang, Ti-6Al-4V/Hydroxyapatite Composite Coatings Prepared by Thermal Spray Techniques, *J. Therm. Spray Technol.*, 1997, **6**(1), p 109-115
16. R. Ahmed, N.H. Faisal, S.M. Knupfer, A.M. Paradowska, M.E. Fitzpatrick, K.A. Khor, and J. Cizek, Neutron Diffraction Residual Strain Measurements in Plasma Sprayed Nanostructured Hydroxyapatite Coatings for Orthopaedic Implants, *Mater. Sci. Forum*, 2010, **652**, p 309-314
17. N.W. Khun, Z. Li, K.A. Khor, and J. Cizek. Higher in-Flight Particle Velocities Enhance In Vitro Tribological Behavior of Plasma Sprayed Hydroxyapatite Coatings, *Tribol. Int.*, 2016, **103**, p 496-503
18. P. Fauchais, Understanding Plasma Spraying, *J. Phys. D: Appl. Phys.*, 2004, **37**(9), p R86-R108
19. L. Pawlowski, Suspension and Solution Thermal Spray Coatings, *Surf. Coat. Technol.*, 2009, **203**(19), p 2807-2829.
20. F.L. Toma, A. Potthoff, L.M. Berger, and C. Leyens, Demands, Potentials, and Economic Aspects of Thermal Spraying with Suspensions: A Critical Review, *J. Therm. Spray Technol.*, 2015, **24**(7), p 1143-1152.
21. P. Fauchais, M. Vardelle, S. Goutier, and A. Vardelle, Key Challenges and Opportunities in Suspension and Solution Plasma Spraying, *Plasma Chem. Plasma Process.*, 2014, **35**(3), p 511-525
22. R. Musalek, J. Medricky, T. Tesar, J. Kotlan, Z. Pala, F. Lukac, T. Chraska, and N. Curry, Suspensions Plasma Spraying of Ceramics with Hybrid Water-Stabilized Plasma Technology, *J. Therm. Spray Technol.*, 2016, **26**(1-2), p 37-46
23. T. Tesar, R. Musalek, J. Medricky, J. Kotlan, F. Lukac, Z. Pala, P. Ctibor, T. Chraska, S. Houdkova, V. Rimal, and N. Curry, Development of Suspension Plasma Sprayed Alumina Coatings With High Enthalpy Plasma Torch, *Surf. Coat. Technol.*, 2017, **325**, p 277-288
24. J. Kotlan, Z. Pala, R. Musalek, and P. Ctibor, On Reactive Suspension Plasma Spraying of Calcium Titanate, *Ceram. Int.*, 2016, **42**(3), p 4607-4615
25. S.S.A. Abidi and Q. Murtaza, Synthesis and Characterization of Nano-Hydroxyapatite Powder Using Wet Chemical Precipitation Reaction, *J. Mater. Sci. Technol.*, 2014, **30**(4), p 307-310
26. R. Jaworski, C. Pierlot, L. Pawlowski, M. Bigan, and M. Quivrin, Synthesis and Preliminary Tests of Suspension Plasma Spraying of Fine Hydroxyapatite Powder, *J. Therm. Spray Technol.*, 2008, **17**(5-6), p 679-684
27. R. Jaworski, L. Pawlowski, C. Pierlot, F. Roudet, S. Kozerski, and F. Petit, Recent Developments in Suspension Plasma Sprayed Titanium Oxide and Hydroxyapatite Coatings, *J. Therm. Spray Technol.*, 2010, **19**(1-2), p 240-247

28. S. Kozerski, L. Pawlowski, R. Jaworski, F. Roudet, and F. Petit, Two Zones Microstructure of Suspension Plasma Sprayed Hydroxyapatite Coatings, *Surf. Coat. Technol.*, 2010, **204**(9-10), p 1380-1387
29. R.T. Candidato, P. Sokolowski, L. Pawlowski, and A. Denoirjean, Preliminary Study of Hydroxyapatite Coatings Synthesis Using Solution Precursor Plasma Spraying, *Surf. Coat. Technol.*, 2015, **277**, p 242-250
30. A. Mejias, R.T. Candidato, L. Pawlowski, and D. Chicot, Mechanical Properties by Instrumented Indentation of Solution Precursor Plasma Sprayed Hydroxyapatite Coatings: Analysis of Microstructural Effect, *Surf. Coat. Technol.*, 2016, **298**, p 93-102
31. A. Cattini, D. Bellucci, A. Sola, L. Pawlowski, and V. Cannillo, Suspension Plasma Spraying of Optimised Functionally Graded Coatings of Bioactive Glass/Hydroxyapatite, *Surf. Coat. Technol.*, 2013, **236**, p 118-126
32. A. Cattini, D. Bellucci, A. Sola, L. Pawlowski, and V. Cannillo, Microstructural Design of Functionally Graded Coatings Composed of Suspension Plasma Sprayed Hydroxyapatite and Bioactive Glass, *J. Biomed. Mater. Res. B: Appl. Biomater.*, 2013, **102**(3), p 551-560
33. Y. Huang, L. Song, X. Liu, Y. Xiao, Y. Wu, J. Chen, F. Wu, and Z. Gu, Hydroxyapatite Coatings Deposited By Liquid Precursor Plasma Spraying: Controlled Dense and Porous Microstructures and Osteoblastic Cell Responses, *Biofabrication*, 2010, **2**(4), p 045003.
34. S.T. Aruna, S. Kulkarni, M. Chakraborty, S.S. Kumar, N. Balaji, and C. Mandal, A Comparative Study on the Synthesis and Properties of Suspension and Solution Precursor Plasma Sprayed Hydroxyapatite Coatings, *Ceram. Int.*, 2017, **43**(13), p 9715-9722
35. M. Ueno, H. Miyamoto, M. Tsukamoto, S. Eto, I. Noda, T. Shobuike, T. Kobatake, M. Sonohata, and M. Mawatari, Silver-Containing Hydroxyapatite Coating Reduces Biofilm Formation By Methicillin-Resistant Staphylococcus Aureus In Vitro and In Vivo, *BioMed. Res. Int.*, 2016, **2016**, p 1-7
36. J.L. Clement and P.S. Jarrett, Antibacterial Silver, *Met. Based Drugs*, 1994, **1**(5-6), p 467-482
37. L. Zhao and M.A. Ashraf, Influence of ag/HA Nanocomposite Coating on Biofilm Formation of Joint Prosthesis and Its Mechanism. *West Indian Med. J.*, 2015, **64**(5), p 506-513. https://doi.org/10.7727/wimj.2016.179
38. Y. Ghani, M.J. Coathup, K.A. Hing, and G.W. Blunn, Development of a Hydroxyapatite Coating Containing Silver for the Prevention of Peri-Prosthetic Infection, *J. Orthop. Res.*, 2011, **30**(3), p 356-363
39. M. Miranda, A. Fernandez, M. Diaz, L. Esteban-Tejeda, S. Lopez-Esteban, F. Malpartida, R. Torrecillas, and J.S. Moya, Silver-Hydroxyapatite Nanocomposites As Bactericidal and Fungicidal Materials, *Int. J. Mater. Res.*, 2010, **101**(1), p 122-127.
40. F.A.C. Andrade, L.C.O. Vercik, F.J. Monteiro, and E.C.S. Rigo, Preparation, Characterization and Antibacterial Properties of Silver Nanoparticles-Hydroxyapatite Composites By a Simple and Eco-Friendly Method, *Ceram. Int.*, 2016, **42**(2), p 2271-2280
41. X. Zhang, W. Chaimayo, C. Yang, J. Yao, B.L. Miller, and M.Z. Yates, Silver-Hydroxyapatite Composite Coatings with Enhanced Antimicrobial Activities Through Heat Treatment, *Surf. Coat. Technol.*, 2017, **325**, p 39-45
42. W. Chen, S. Oh, A.P. Ong, N. Oh, Y. Liu, H.S. Courtney, M. Appleford, and J.L. Ong, Antibacterial and Osteogenic Properties of Silver-Containing Hydroxyapatite Coatings Produced Using a Sol Gel Process, *J. Biomed. Mater. Res. A*, 2007, **82A**(4), p 899-906
43. C. Fu, X. Zhang, K. Savino, P. Gabrys, Y. Gao, W. Chaimayo, B.L. Miller, and M.Z. Yates, Antimicrobial Silver-Hydroxyapatite Composite Coatings Through Two-Stage Electrochemical Synthesis, *Surf. Coat. Technol.*, 2016, **301**, p 13-19
44. N. Sanpo, M.L. Tan, P. Cheang, and K.A. Khor, Antibacterial Property of Cold-Sprayed HA–Ag/PEEK Coating, *J. Therm. Spray Technol.*, 2008, **18**(1), p 10-15
45. H.M. Rietveld, Line Profiles of Neutron Powder-Diffraction Peaks for Structure Refinement, *Acta Cryst.*, 1967, **22**, p 151-152
46. B. Gonzalez, N. Calvar, E. Gomez, and A. Dominguez, Density, Dynamic Viscosity, and Derived Properties of Binary Mixtures of Methanol or Ethanol With Water, Ethyl Acetate, and Methyl Acetate at T = (293.15, 298.15, and 303.15)K, *J. Chem. Thermodyn.*, 2007, **39**(12), p 1578-1588
47. W.A. Dollase, Correction of Intensities for Preferred Orientation in Powder Diffractometry: Application of the March Model, *J. Appl. Crystallogr.*, 1986, **19**(4), p 267-272
48. L. Sun, C.C. Berndt, K.A. Gross, and A. Kucuk, Material Fundamentals and Clinical Performance of Plasma-Sprayed Hydroxyapatite Coatings: A Review, *J. Biomed. Mater. Res.*, 2001, **58**(5), p 570-592
49. G. Bolelli, D. Bellucci, V. Cannillo, L. Lusvarghi, A. Sola, N. Stiegler, P. Muller, A. Killinger, R. Gadow, L. Altomare, and L. de Nardo, Suspension Thermal Spraying of Hydroxyapatite: Microstructure and In Vitro Behaviour, *Mater. Sci. Eng. C*, **34**, 2014, p 287-303
50. B. Zheng, Y. Luo, H. Liao, and C. Zhang, Investigation of the Crystallinity of Suspension Plasma Sprayed Hydroxyapatite Coatings, *J. Eur. Ceram. Soc.*, 2017, **37**(15), p 5017-5021
51. H. Xu, X. Geng, G. Liu, J. Xiao, D. Li, Y. Zhang, P. Zhu, and C. Zhang, Deposition, Nanostructure and Phase Composition of Suspension Plasma-Sprayed Hydroxyapatite Coatings, *Ceram. Int.*, 2016, **42**(7), p 8684-8690
52. R.T. Candidato, P. Sokolowski, L. Pawlowski, G. Lecomte-Nana, C. Constantinescu, and A. Denoirjean, Development of Hydroxyapatite Coatings by Solution Precursor Plasma Spray Process and Their Microstructural Characterization, *Surf. Coat. Technol.*, 2017, **318**, 39-49
53. L. Latka, L. Pawlowski, D. Chicot, C. Pierlot, and F. Petit, Mechanical Properties of Suspension Plasma Sprayed Hydroxyapatite Coatings Submitted to Simulated Body Fluid, *Surf. Coat. Technol.*, 2010, **205**(4), p 954-960

ACS Biomaterials SCIENCE & ENGINEERING

Article

Cite This: *ACS Biomater. Sci. Eng.* 2019, 5, 1703−1714

pubs.acs.org/journal/abseba

Downloaded via Jan Cizek on April 8, 2019 at 15:52:32 (UTC).
See https://pubs.acs.org/sharingguidelines for options on how to legitimately share published articles.

Increasing Fatigue Endurance of Hydroxyapatite and Rutile Plasma Sprayed Biocomponents by Controlling Deposition In-Flight Properties

J. Cizek,*,† O. Kovarik,‡ F. Siska,§ J. Bensch,∥ J. Cupera,⊥ M. Matejkova,⊥ J. Siegl,‡ T. Chraska,† and K. A. Khor#

†Institute of Plasma Physics, The Czech Academy of Sciences, Za Slovankou 1782/3, 182 00 Prague, Czech Republic
‡Czech Technical University, Faculty of Nuclear Sciences and Physical Engineering, Trojanova 13, 120 00 Prague, Czech Republic
§Institute of Physics of Materials, The Czech Academy of Sciences, Zizkova 513/22, 616 62 Brno, Czech Republic
∥Glass Service Corporation, Rokytnice 60, 755 01 Vsetin, Czech Republic
⊥Institute of Materials Science and Engineering, Brno University of Technology, Technicka 2896/3, 616 69 Brno, Czech Republic
#Nanyang Technological University, School of Mechanical and Aerospace Engineering, 50 Nanyang Avenue, 639 798 Singapore

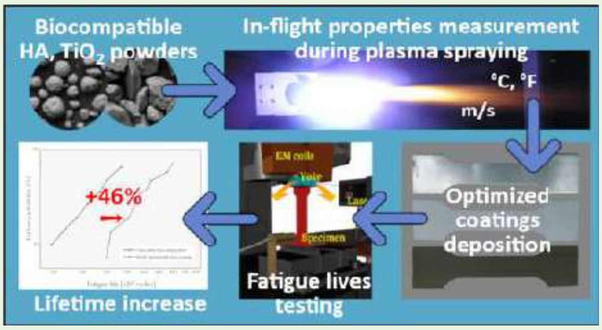

ABSTRACT: Three sets of hydroxyapatite and rutile-TiO_2 coatings were plasma sprayed onto metallic substrates. The spray parameters of the sets were modified so as to obtain different in-flight temperatures and velocities of the powder particles within the plasma jet (ranging from 1778 to 2385 K and 128 to 199 m s^{-1}, respectively). Fatigue endurance of the coated specimens was then tested. The samples were subjected to a symmetric cyclical bend loading, and the crack propagation was monitored until it reached a predefined cross-section damage. The influence of the coating deposition was evaluated with respect to a noncoated reference set and the in-flight characteristics. Attributed to favorable residual stress development in the sprayed samples, it was found that the deposition of the coatings generally led to a prolongation of the fatigue lives. The highest lifetime increase (up to 46% as compared to the noncoated set) was recorded for the coatings deposited under high in-flight temperature and velocity. Importantly, this was achieved without significantly compromising the microstructure or phase composition of the deposited HA and TiO_2 layers.

KEYWORDS: *atmospheric plasma spray, in situ PIV, fatigue testing, HA, titania*

1. INTRODUCTION

The increasing demand for the quality, functionality, and reliability of hard tissue replacements is a driving force for the ongoing research and development of new methods and materials applicable for such tasks. Attempts to replace the implant materials commonly used just a decade ago (such as the 316L steel or (α+β)-Ti6Al4V alloy) are carried out; the wave of new materials now includes either niobium- or iron-containing, as well as Zr-containing, β-type titanium alloys, such as Ti13Nb13Zr, Ti5Al2.5Fe, or TiNbTaZr. While the former group aims to replace the cytotoxic vanadium, the latter alloys aim at reduction of elastic moduli below 50 GPa,[1] nearing that of the human cortical bone (10−30 GPa). Aside from titanium, the CoCrMo-based alloys are further perfected[2], along with tantalum that has already exhibited several promising results.

Despite the achieved progress, the standalone alloys are not able to meet the stringent requirements for components in interaction with human tissues. Therefore, the metallic implants are often subjected to additional technological processing, such as modifications of their surfaces. One of the established routes for improving the functionality is a deposition of bioactive coatings onto the implant surfaces.[3] For the deposition, a whole range of techniques are readily available, differing in the material build-up mechanisms, which in turn influence the final coating properties (such as thickness, porosity, composition). Within the group of thermal spray deposition methods, two technologies are successfully employed: high velocity oxygen fuel (HVOF) and plasma spraying.[4] In the latter process, the material feedstock (frequently in the form of micrometer-grained powder) is introduced into a hot plasma jet generated by ionization and subsequent recombination of a mixture of gases, whereby it undergoes a full or partial melting and is propelled toward the substrate for a subsequent solidification, forming the final coating. A typical coating generally consists of a number of

Received: December 6, 2018
Accepted: March 12, 2019
Published: March 12, 2019

© 2019 American Chemical Society

DOI: 10.1021/acsbiomaterials.8b01545

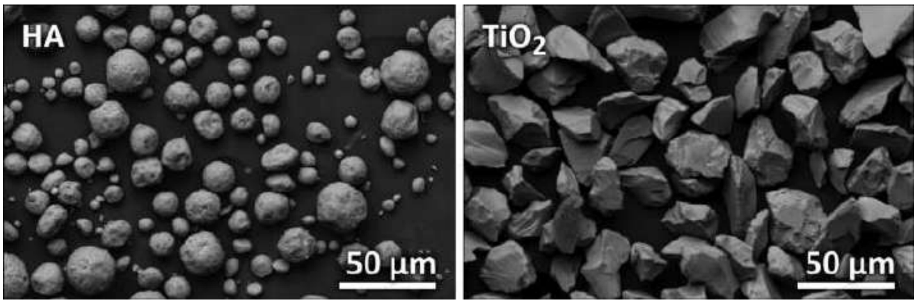

Figure 1. Feedstock powders used for coatings deposition: hydroxyapatite and TiO_2.

mutually interconnected splats (resolidified flattened powder particles), as well as other morphological attributes, such as pores or microcracks originating due to imperfect splat-to-splat bonds and residual stresses development.[5]

The so-called bioceramics have been traditionally used for the coatings,[3,6−8] with calcium phosphates as the preferred materials due to their resemblance to natural bone tissue, outstanding bioactivity, and osseoconductive properties. In particular, water-environment stable hydroxyapatite ("HA") gained popularity due to its outstanding qualities.[9,10] Bioactive HA layers on hard tissue implants have been reported to promote earlier stabilization in the surrounding bone, support the bone in-growth, shield the implant from environmental attacks, and also prevent release of metallic ions into the body, reducing the possibility of intoxication.[3]

Yet the usage of CaP-based ceramics is inherently associated with several negative factors stemming from their inferior mechanical properties such as strength or fracture toughness.[8] In order to address the issues, attempts were made to examine the performance of materials with superior mechanical properties for the surface shielding applications. Titanium dioxide ("titania") was shown to exhibit enhanced biocompatible properties at nanometric feedstock scales[11−16] and support osteoblast cells growth without negative effect on the cells viability.[17−19] The material also meets the mechanical criteria as the TiO_2 coatings generally exhibit superior adhesion, elastic modulus, and hardness as compared to the calcium phosphates.[20,21]

The versatility of plasma deposition technology allows fabrication of coatings of thicknesses required by the biological applications,[3,4] and due to its inherent high temperatures, the process facilitates deposition of a wide spectrum of materials including both HA and TiO_2 ceramics. However, significant thermally induced changes in the sprayed material may arise as a consequence of the heat (particle melting, thermal shocks from the plasma gun passes, solid-state cooling from the elevated temperatures, etc.), triggering a range of negative phenomena. For instance, the chemical/phase composition of the coatings may be compromised, yielding inferior bioactive properties of the coatings.

Additionally, internal stresses frequently develop, potentially jeopardizing the reliability of the components in bioapplications. In more detail, this phenomenon is generally associated with differences in thermal expansion coefficients of the coatings and the substrates ("secondary stresses").[4,22,23] In addition, primary stresses arising from the fast thermal contraction of the solidifying splats ("quenching stresses") are generally present, too. In combination with external loading to which the hard tissue implants are subjected during their service lives, the presence of the residual stresses may result in modification of the key mechanical properties (such as fatigue durability, reported to be enhanced in ref 24 for TBC or ref 25 for titanium or reduced for intermetallic coatings in ref 26), or changes of the adhesive strength at the coating−substrate interfaces (e.g., HA coatings on Ti substrates[27,28]).

To address this phenomenon, we have carried out an experimental work using two dissimilar bioactive materials, HA and rutile TiO_2 polymorph. Three coating sets were deposited under different conditions, resulting in different coating structures and different magnitude of the internal stress levels. Using a laser-assisted cyclic bending setup, the respective sets influence on the fatigue durability of steel samples was then determined.

2. EXPERIMENTAL SETUP

2.1. Materials. The HA powder used in the study was in-house produced using a pH-controlled wet chemical synthesis method with $Ca(OH)_2$ as a source of calcium atoms:

$$10Ca(OH)_2 + 6H_3PO_4 \rightarrow Ca_{10}(PO_4)_6(OH)_2 + 18H_2O$$

The produced slurry was spray dried under previously optimized conditions,[7,29] and the collected powder was then calcined at 1220 K to transform nonequilibrium phases that could have originated within the production process (tricalcium phosphate (TCP), tetracalcium phosphate (TTCP), CaO) and to improve the mutual bonding of the HA nanocrystallites into micrometric spherical agglomerates suitable for plasma spraying (Figure 1a). The heat treatment further improved the Ca/P ratio from the original 2.25 to 1.68 (determined by EDX; theoretical value 1.67). A 5% $CaCO_3$ phase content with no traces of TCP and TTCP phases was detected in the powder via Rietveld XRD analysis[30] (Cu Kα, Philips PW1710; Figure 2, Table 5). The detected $CaCO_3$ could have originated in the material by a reaction of the original $Ca(OH)_2$ with atmospheric CO_2 during the long-running synthesis.[31] The powder was thoroughly sieved into 29−50 μm range as measured by particle size analysis (NanoTec Analysette 22, Fritsch, Germany). Using helium pycnometry method (Accupyc 1330, Micromeritics Corp, USA; 99.995% purity helium used) at room temperature, the internal porosity of the produced powder particles was determined as 8%.

Commercially available angular TiO_2 powder (Amperit 782.1, HC Starck, Germany; Figure 1b) was sieved into 32−45 μm range. XRD investigation revealed the presence of both major (tetragonal) polymorphs in the powder: anatase and rutile. In the literature, a discussion pertaining to the mutual comparison of the biocompatible properties of the two polymorphs is not unanimous at the moment.[17−19,32−35] Rutile phase was selected for our study. Therefore, the powder was heat treated at 1150 K in order to induce anatase → rutile (nonreversible) phase transformation. The powder was then determined as 100% rutile TiO_2 (with traces of Fe_2O_3 hematite and quartz SiO_2, see the two minor peaks at 26.602° and 28.298° in Figure 2) after the treatment and contained 6% internal

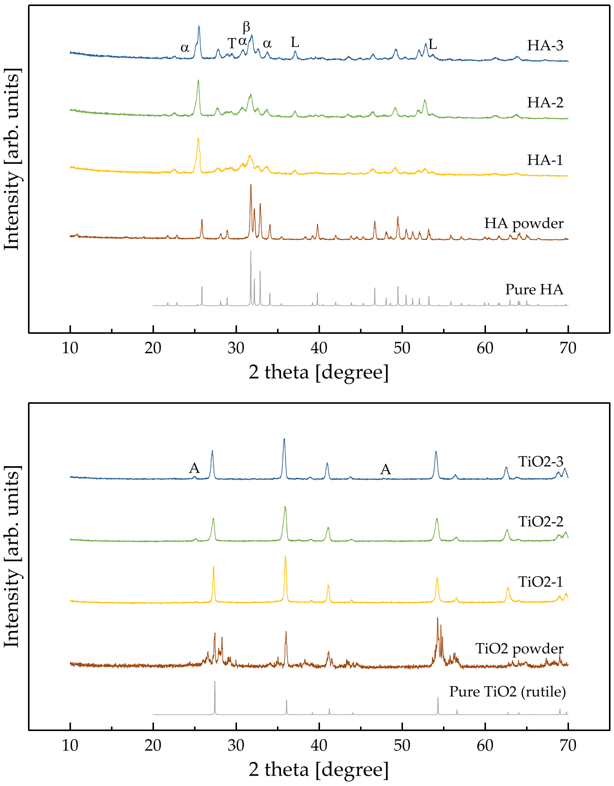

Figure 2. X-ray diffraction spectra of the feedstock powders and fabricated coatings. Theoretical prediction of pure phases (HA/rutile) is provided for reference. The major peaks pertaining to phases other than HA/rutile are denoted as (L)ime CaO, (T)TCP $Ca_4O(PO_4)_2$, (α)-TCP $Ca_3(PO_4)_2$, (β)-TCP $Ca_3(PO_4)_2$ and (A)natase TiO_2.

porosity (cf. the almost nonexistent porosity of other powders fabricated via the crushing method).

The substrate material was low-carbon steel 1.0038. The samples were cut from cold-rolled 4 mm sheets into a shape required by the fatigue testing device (Figure 3). The details on the geometry of the specimens and their respective preparation procedure can be found in our previous work.[22] To increase the statistical reliability of the results, five samples were used for each set, with their symmetrical design allowing two results per sample to be obtained. The fatigue values provided herein are therefore an average of ten measurements each.

2.2. Coatings Deposition and Characterization.

Prior to deposition, the substrates were grit-blasted to increase the surface roughness (R_a = 5.07 μm) and improve the coating adhesion. The residual grit was removed in an ultrasonic bath (ethyl alcohol, 60 min). Praxair atmospheric 4600 system equipped with an SG-100 gun was then used for the plasma spray deposition. Argon and helium were used as the main and auxiliary gases, respectively. In order to obtain different in-flight temperatures and velocities of particles of both powders, six selected plasma system parameters (net power, main and auxiliary gas flows, two parameters associated with powder feeding, (i.e., carrier gas flow and revolutions of the feeder system), and stand-off distance) were modified according to the results of the previous extensive Taguchi design studies (refs 7 and 29 for HA and refs 36 and 37 for TiO_2). In total, three sets were produced for each of the two materials, leading to three different in-flight conditions, ranging from high-temperature high-velocity to low-temperature low-velocity. The corresponding parameters are provided in Table 1.

The coatings were deposited onto both major faces of the samples at a target thickness of 400 μm. Such coatings were thicker than the 50−250 μm range typical for thermally sprayed materials. The thickness was selected to accentuate the prospective changes in the sample fatigue performance after the deposition. Due to anticipated different deposition efficiency of both powders, the total number of robot arm passes and its transversal velocity were adjusted for each of the two powder types (15 passes at 40 mm s^{-1} for HA and 10 passes at 100 mm s^{-1} for TiO_2; within each of the three sets, these robot parameters were held constant). To maintain mutual comparability

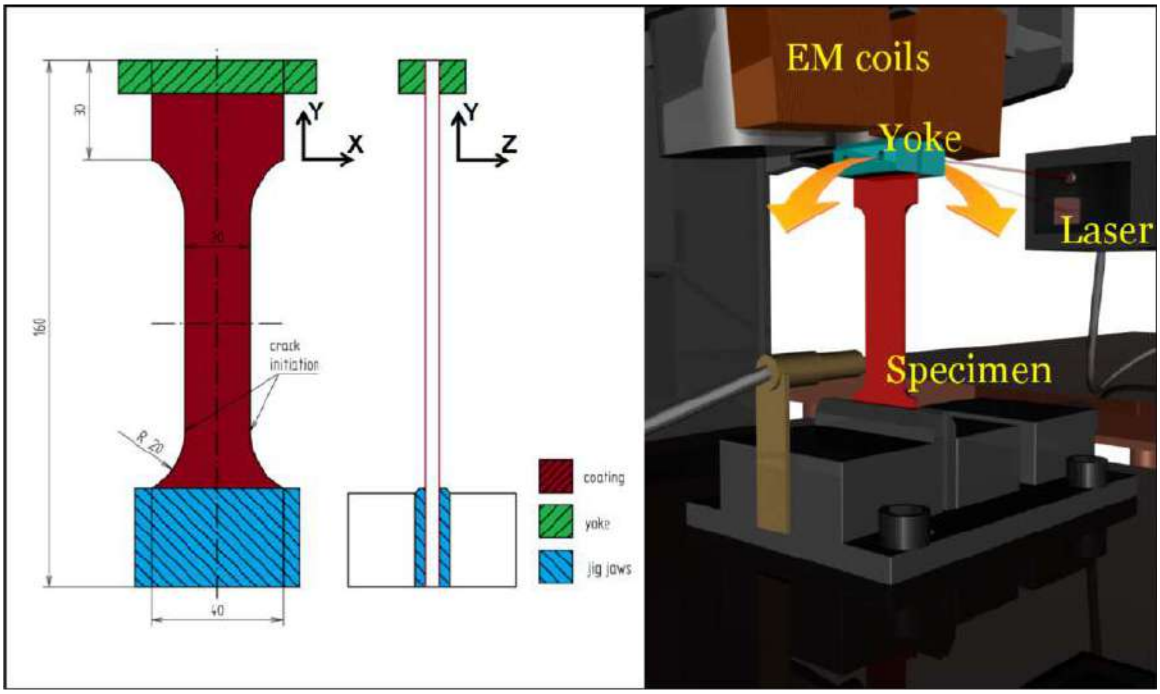

Figure 3. Specimen geometry (left) and loading in the developed fatigue device (right).

DOI: 10.1021/acsbiomaterials.8b01545
ACS Biomater. Sci. Eng. 2019, 5, 1703−1714

Table 1. Plasma System Settings for Fabrication of Coatings under Different In-Flight Properties

set	net power [kW]	main gas flow [L min^{-1}]	auxiliary gas flow [L min^{-1}]	carrier gas flow [L min^{-1}]	feeder revolutions [RPM]	stand-off distance [mm]
01	15	50	40	7	8	120
02	12	40	30	7	8	140
03	10	30	20	7	8	160

with previous studies (e.g., refs 7, 29, 36, and 37), the substrates were not preheated prior to coating deposition.

A noncoated grit-blasted set was used as a performance benchmark. The grit-blasting procedure of this reference set was carried out to separate the effect of the subsequent coating deposition from the peening effect of the blasting medium.

Using the cross-section observations, the microstructure of the coatings was evaluated using SEM (Jeol JSM-5610) in back-scattered mode. For the sample preparation, standard metallographic procedures were employed, involving mounting the samples into a two-component epoxy resin, grinding using emery papers up to #4000, and polishing using 1 μm paste. The samples were not etched after the final polishing step. A constant magnification of 500× was used to collect five additional images per each set. Image analysis method was then used to calculate the porosity of the coatings (ImageJ software, NIH, USA).

2.3. In-Flight Properties. The in-flight temperature of the particles during the deposition process influences a number of final coating properties (e.g., chemical and phase changes, adhesion, magnitude of thermal stresses, cracking), while the particle velocity affects, for example, the porosity or elastic modulus.[7,36,38,39] Via these factors, the two quantities could also have a direct influence on the implant fatigue failure resistance.

In order to monitor the respective values in situ, a fast shutter camera system (SprayWatch 2i, Oseir, Finland) was employed. The camera was positioned orthogonally to the plasma jet (see ref 29) and was further equipped with a Hi-Watch laser stroboscope for illumination. Two-color pyrometry and time-of-flight methods were utilized in the software to detect the temperature and velocity of individual particles, respectively.

For the measurements, the SG-100 gun was moved to a specified location in front of the camera, and the in-flight data were collected for at least 2 min at given spray distances. While still running, the gun was then moved to the substrate location, and the coatings were produced.

2.4. Fatigue Testing. An electromagnetic computer-controlled in-house built testing device was used to perform the fatigue experiments. One end of the flat specimens was clamped while the other end was equipped with a ferromagnetic yoke and deflected by alternating electromagnetic field (Figure 3). The symmetric cyclical bending ($R = -1$) setup maintained a constant 4 mm deflection of the free end via a phase locked loop technique.

The excitation frequency was kept close to the first natural resonance frequency of the samples (generally, from 70 to 100 Hz). Propagation of a crack through the samples evoked a drop in the natural resonance frequency. Based on the previous results, a stop condition of 4 Hz drop was used to terminate the experiment, corresponding to approximately 40−60% specimen cross-section area damage. The number of cycles upon reaching the stop condition was taken as an indicator of each specimen's performance. The values of each set were confronted with the performance of a noncoated, grit-blasted set ("relative fatigue life", R_f). Weibull statistical processing was implemented to further analyze the obtained results. More information on the testing device and experimental details can be found in refs 22 and 40.

2.5. Fractographic Analyses. In order to understand the basic features of the crack propagation mechanisms, a fractographic analysis of the specimens was carried out. As described earlier, the specimens were not ruptured completely after the fatigue testing; in order to prepare the crack faces for observation, the samples were cooled down using liquid nitrogen and ruptured using a dynamic impact. SEM was then used (Zeiss Ultra Plus) to observe the characteristic fractography features in both coatings and substrates.

2.6. FEM Modeling. In order to better understand the internal stress development, the effect of the coating deposition was further investigated by FE method. Using Abaqus software, the two main goals of the simulations were (1) to analyze the changes in stress state due to the cooling to room temperature and (2) to predict the prospective crack propagation critical area in the specimen subjected to the external bending.

The computations involved the following two steps that contribute to the loading of the specimen materials: development of residual stresses introduced into the structure during cooling to RT after the spraying process and the external bend loading of the tested specimen. The residual stresses originate mainly due to the mismatch of the thermal expansion coefficients of the substrate and the HA and TiO_2 coatings. For the model, the initial temperature at the end of the spray process was taken as 573 K, i.e., the temperature corresponding to the experiments (mind that no substrate cooling was used in the setup). Importantly, at 573 K (or even above), the substrate material softens and can readily relax the induced stresses by plastic deformation. Therefore, cooling down from the used temperature is a sufficient approximation for the estimate of the residual stresses. The second computational step represented the mechanical loading, whereby the top end of the specimen is cyclically displaced by 4 mm in the z-direction. In total, 4 full displacements were modeled (2 in each direction) to comprehend some basic development of stresses and (plastic) deformation in the critical area. The number of simulated cycles is very small as compared to the real experimental data. However, it is sufficient regarding the applied model. The only irreversible behavior included in the model is the plasticity of the substrate. This plastic behavior saturates after two full displacements, during which the substrate plastically hardens and then behaves elastically.

Due to its symmetry, half of the test specimen was modeled only. The geometry was meshed using 3D quadratic elements with 20 nodes. Corresponding to the experimental setup, the x, y, and z computational directions are indicated in Figure 3 with the used boundary conditions given as $U_y = 0$ and $U_z = 0$ at the clamped specimen base and $U_z = U_z(t)$ at its free end. Two different geometries were compared: 4 mm substrates only and 4 mm substrates with 400 μm thick coatings on both sides. The substrate material was modeled as elastoplastic with temperature dependent parameters. The elastic parameters and yield stress summarized in Table 2 were taken from the literature.[41,42] The used substrate steel material exhibits rather low strain hardening; therefore, the plastic curve beyond $R_p0.2$ is approximated by two linear segments: the first represents a linear hardening with modulus K equal to 10% of the elastic modulus E. This is valid until the stress level equals 2 times the

Table 2. Material Properties of the 1.0038 Substrate Material Used in FE Simulations

temp [K]	E [GPa]	$R_p0.2$ [MPa]	K [GPa]	coefficient of thermal expansion [10^{-6}/K]
293 (RT)	200	205	20	11.6
373	198	187	19.8	12.5
473	193	161	19.3	13.7
573	184	122	18.4	14.8
673	167	100	16.7	15.9
873	127	50	12.7	18.1

yield stress. After this point, the material was considered as ideally plastic.

The HA and TiO_2 coatings were supposed to have purely elastic properties with a decrease in Young's modulus by 10% from 0 to 873 K. As both coating materials are of ceramic nature with negligible plasticity, the purely elastic behavior is a valid approximation. The material parameters were transferred from several literature sources and are shown in Table 3.[43−49]

Table 3. Material Properties of the HA and TiO_2 Coating Materials Used in FE Simulations

coating	temp [K]	E [GPa]	coefficient of thermal expansion $[10^{-6}/K]$
HA	293 (RT)	147	10.5
	873	132	
TiO_2	293 (RT)	237	9.7
	873	213	

It is important to note that, due to its complexity, it was not possible to comprehend the entire deposition process in the model. For one, the quenching stresses were not incorporated in the calculations. As shown in the study of Matejicek and co-workers,[50] such quenching stresses could even exceed the magnitude of the secondary (CTE mismatch) stresses under some conditions in the plasma sprayed coatings. As such, the stress level results provided by the FEM must be taken as qualitative only. Nevertheless, given the globally constant distribution of the quenching stresses, the prediction of the fracture area from the used FEM should remain valid. Further to this, the simulation results can be also used for a quantitative comparison of the stress levels induced in the different coating types. This can help to understand the importance of the particular coating qualities (such as splat connectivity, intersplat voids, quenching cracks) on the fatigue endurance.

3. RESULTS AND DISCUSSION

3.1. In-Flight Properties. The three settings of the plasma system parameters led to significant differences in the in-flight temperatures and velocities acquired by the HA and TiO_2 particles (Table 4). The maximum variation in the particle temperatures of the three individual sets reached 32% (HA) and 10% (TiO_2), while the attained velocities differed by as much as 51% (HA) and 54% (TiO_2). The melting temperature of TiO_2 is given as 2143 K in the literature (at 0.1 MPa[51]) and the incongruent decomposition temperature of HA into TTCP and β-TCP as 1843 K (with the corresponding eutectic melting at 1863 K).[7] It could be seen that all the sets were deposited at in-flight temperatures exceeding the theoretical melting/decomposing values, except for HA-3 set. Considering the agglomerated structure of the powder particles and the breadth of the particle size ranges, it could be assumed that during the deposition of this set, a partial melting of the particles also occurred.

3.2. Coatings Properties. The microstructure of the deposits corresponds to typical plasma sprayed coatings: individual splats could be readily distinguished in the heterogeneous structure, along with varying levels of internal porosity (Figure 4). The pore content linearly corresponds with the in-flight temperature and velocity and reaches values from approximately 2% to 8% (Table 4). As the velocity differences are almost the same for both materials, the somewhat higher difference of porosity among the HA coatings may be caused by the higher difference in the in-flight temperatures as the secondary factor. While all HA and the TiO_2-1 splats appear well connected (apart from the presence of microcracks), the TiO_2 sets 2 and 3 exhibited some intersplat disconnections. These are illustrated in Figure 5 and are most likely located at the interfaces corresponding to the individual gun passes. The presence of partially unmolten particles embedded in the microstructure of HA-3 coating (Figure 4e) indicates that a partial material melting occurred only, in accordance with the measured in-flight temperature nearing the theoretical decomposition level.

A dense network of microcracks was observed in the coatings. Their formation is probably a consequence of alleviation of quenching and thermal contraction stresses upon cooling to room temperature. The cracks in both coatings may indicate (total) tensile stresses, which would be compensated by compressive stresses in the substrate, thereby potentially increasing the fatigue resistance. The cracking followed a slightly different pattern for HA and TiO_2 coatings: while for HA cracks spanning several splats were observed in the structure in both horizontal and vertical directions, the generally smaller cracks in the TiO_2 deposit (finer network) mostly followed vertical direction and ranged within single splats only (through-splat orientation along the spray distance), as illustrated in Figure 6. In the latter, the cracks in the horizontal direction are very limited as compared to HA, suggesting that the fine network of cracks in TiO_2 originated due to alleviation of the quenching stresses upon solidification of the individual molten droplets. Pronounced cracking resulting from the thermal contraction stresses, usually manifested by cracks spanning several splats, was therefore not necessary upon cooling to room temperature. The observed difference may be caused by different (thermal) properties of both materials and the absolute differences in the in-flight properties during the spraying. The surface roughness of the two coating types was very similar and reached R_a = 5.372 μm for HA and R_a = 5.645 μm for TiO_2 coatings.

As opposed to the relatively even TiO_2 coatings, the produced HA coatings exhibited varying thickness, different from the target of 400 μm. This could be a consequence of different deposition efficiency of HA powder heated and

Table 4. In-Flight Temperature and Velocity of the Powder Particles, Corresponding Coatings Properties, and Fatigue Life Results

set	coating thickness [μm]	coating porosity [%]	in-flight temp [K]	in-flight velocity [m s^{-1}]	number of cycles	relative life, R_f
reference					269 016	1.00
HA-1	515	2.0	2352	199	380 342	1.41
HA-2	449	4.9	2160	150	367 377	1.37
HA-3	387	7.9	1778	132	328 444	1.22
TiO_2-1	398	2.9	2385	197	391 490	1.46
TiO_2-2	398	3.5	2267	167	271 030	1.01
TiO_2-3	389	4.7	2168	128	277 027	1.03

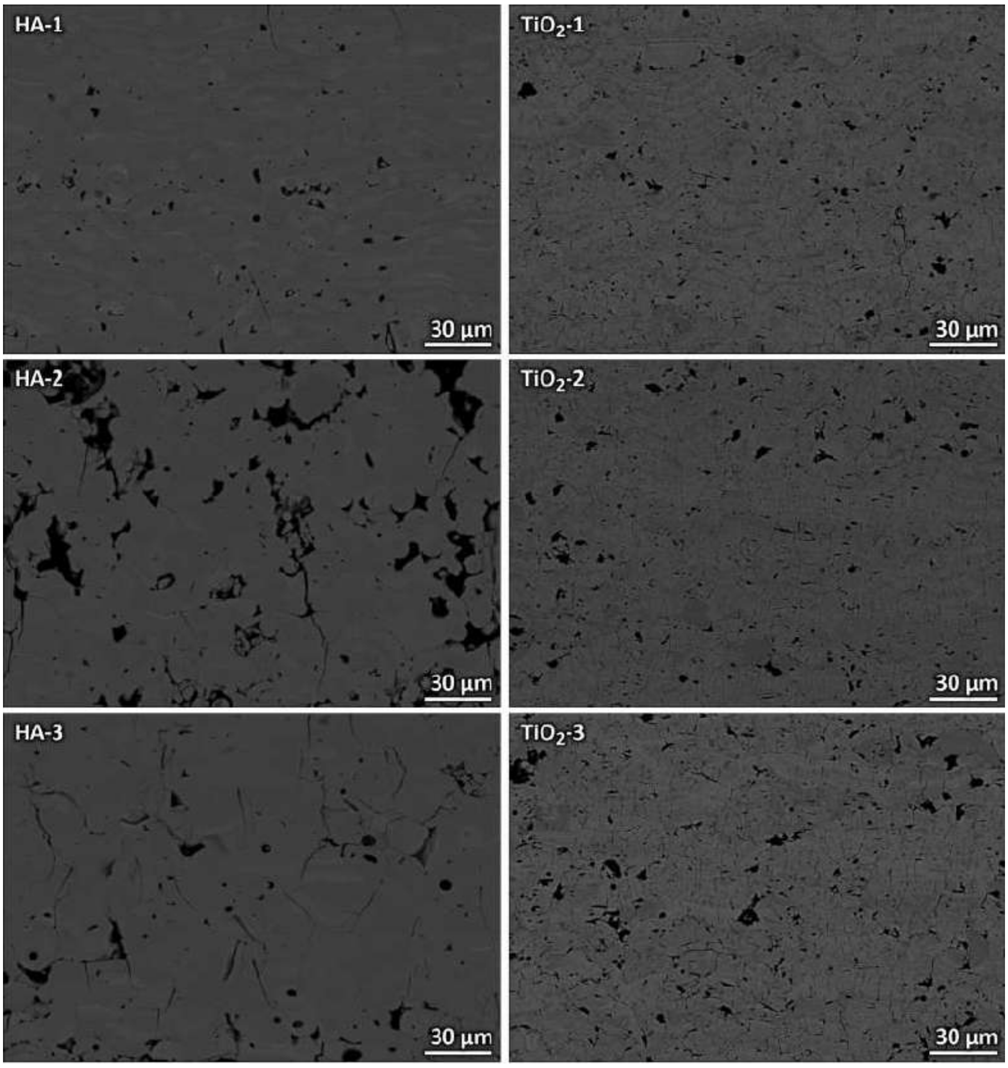

Figure 4. Microstructure of plasma sprayed hydroxyapatite and TiO_2 coating sets 1−3.

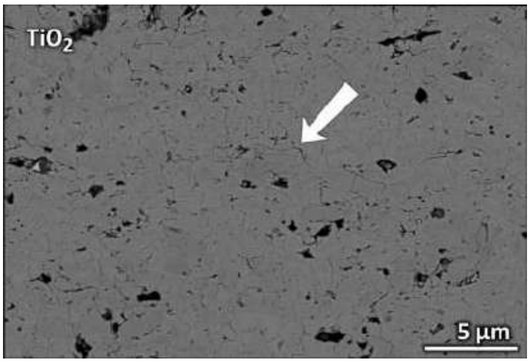

Figure 5. Illustration of debonding of a chain of splats observed in TiO_2-2 and TiO_2-3 coatings. These may be located at the regions corresponding to individual gun passes (TiO_2-3 shown).

accelerated to different in-flight temperatures and velocities while using identical robot spray parameters (across the three sets HA-1 to HA-3). The higher sensitivity of HA toward the deposition efficiency as compared to its TiO_2 counterpart could consist in its low relative density (spray dried feedstock $\rho_{powder} \approx 2.90$ g cm^{-3}, theoretical HA value $\rho_{bulk} = 3.16$ g cm^{-3}). The measured variation is probably the factor influencing the data scatter observed in Weibull plot of the HA fatigue lives. For both coating types, a linear correlation between the deposition efficiency (manifested via coating thickness in this case) and internal coating porosity was recorded. The connection between the deposition efficiency and porosity is linked to the respective in-flight properties.

The performed XRD (Figure 2, Table 5) and EDX analyses detected a chemically heterogeneous structure and Ca/P ratio higher than 1.67 in the HA coatings. Recrystallization of HA phase presumably occurred in all three samples as the calculated preferred orientations of the crystallographic planes of HA within the samples were indicated as (0 2 1) and (0 0 4) as compared to the initial (0 1 0) and (0 0 2) of the powder. The SEM images presented in Figure 4 were recorded in BSE mode, that is, sensitive toward chemical composition. The lighter contrast corresponds to CaO and TTCP phases and is responsible for the increased Ca/P ratio. Interestingly, the overall amount of detrimental CaO phase was about 4% in all three coatings, that is, irrespective of the used plasma parameters. In contrast, a slight trend in the content of

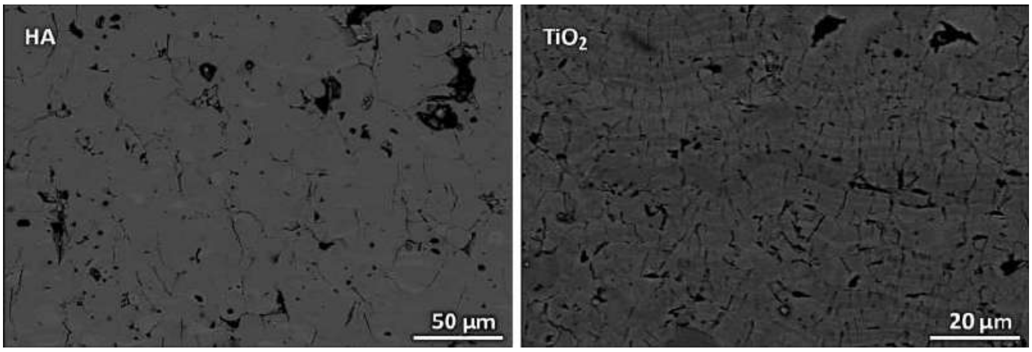

Figure 6. Observed differences in the cracking modes of the two coating types: HA coatings containing cracks in both horizontal and vertical directions (HA-3 shown) and TiO_2 coatings cracking mostly in vertical direction, that is, along the spray direction (TiO_2-2 shown).

Table 5. Nominal Phase Composition [wt %] of the Feedstock Powders and the Fabricated Coatings

set	HA	$CaCO_3$	TTCP	CaO	α-TCP	β-TCP	rutile	anatase
HA powder	95.0	5.0						
HA-1	55.4		22.3	3.8	5.4	13.1		
HA-2	61.1		26.8	4.2	1.1	6.8		
HA-3	63.4		30.7	2.9	2.1	0.9		
TiO_2 powder							100.0	
TiO_2-1							88.4	11.6
TiO_2-2							86.9	13.1
TiO_2-3							94.4	5.6

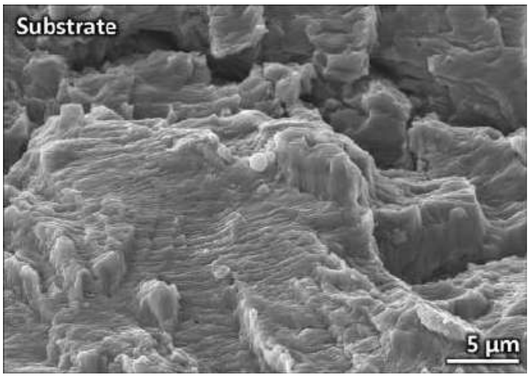

Figure 7. Typical crack surface morphology in the substrate. The crack propagation in the substrates was identical in all tested sets, that is, the coating deposition did not influence the tearing mode.

TTPC and (α- and β-)TCP phases was detected, with higher in-flight velocity giving rise to a slightly higher content of these two phases. The original 5% content of $CaCO_3$ phase was not retained in the coating; presumably, it decomposed into other phases, such as the CaO (not experimentally confirmed by this study). Negligible differences only were recorded during chemical analyses of the TiO_2 coatings. The mutual ratio of Ti/O was retained at its original value for all three coatings. The rutile feedstock underwent a partial phase change as anatase content up to 13% formed in the coatings (the small peak at 25.281°; note that the doublet of small peaks at 69.008° and 69.788° observed in all three coating spectra belongs to rutile phase). As well as CaO in HA, the amount of anatase in the fabricated coatings did not change significantly with the used spray parameters. Recrystallization analysis for the TiO_2 sprayed samples indicated (0 1 1) and (0 0 2) as the preferred orientations of the crystallographic planes of the rutile phase. No brookite phase was detected during our study.

3.3. Fatigue Lifetime Improvement.

The measured average fatigue lives of the reference and the coated sets are presented in Table 4. It could be seen that the coating procedure increased the fatigue lives of the specimens for both powders, which is most likely caused by the presence of favorable residual stresses in the substrates, in accordance with the previous experimental works with coatings of a ceramic nature (e.g., ref 52). It is important to note that the results were obtained for given materials and a specific mode of fatigue testing: in similar studies, either negative or no effect of HA layer plasma deposition was reported.[53,54] However, in these studies, different substrates were used and also the testing modes were different: stress-controlled bend fatigue tests (cf. displacement control in our study) and uniaxial testing, respectively. The difference in the coating deposition impact refers to the fact that the findings are material- and method-bound.

The obtained results indicate that the magnitude of the beneficial effect (increase of the lifetime) is different under different in-flight conditions and that the most desirable effect is reached by the coatings sprayed under the condition corresponding to the highest attained in-flight temperatures and velocities (HA-1, TiO_2-1). These resulted in an increase in fatigue life of 41% and 46%, respectively. Such difference could probably be attributed to the observed superior coatings structure (better splat interconnection, lower porosity), connected to the higher degree of melting and increased in-flight velocities of the individual particles. Toward lower temperatures and velocities, the positive coating deposition influence decreased (HA-2, HA-3). This finding is well in accordance with the theory presented, for example, in the pioneer works by Kroupa[55,56] or the more recent study:[50] quenching deformations arise in the coatings upon cooling to

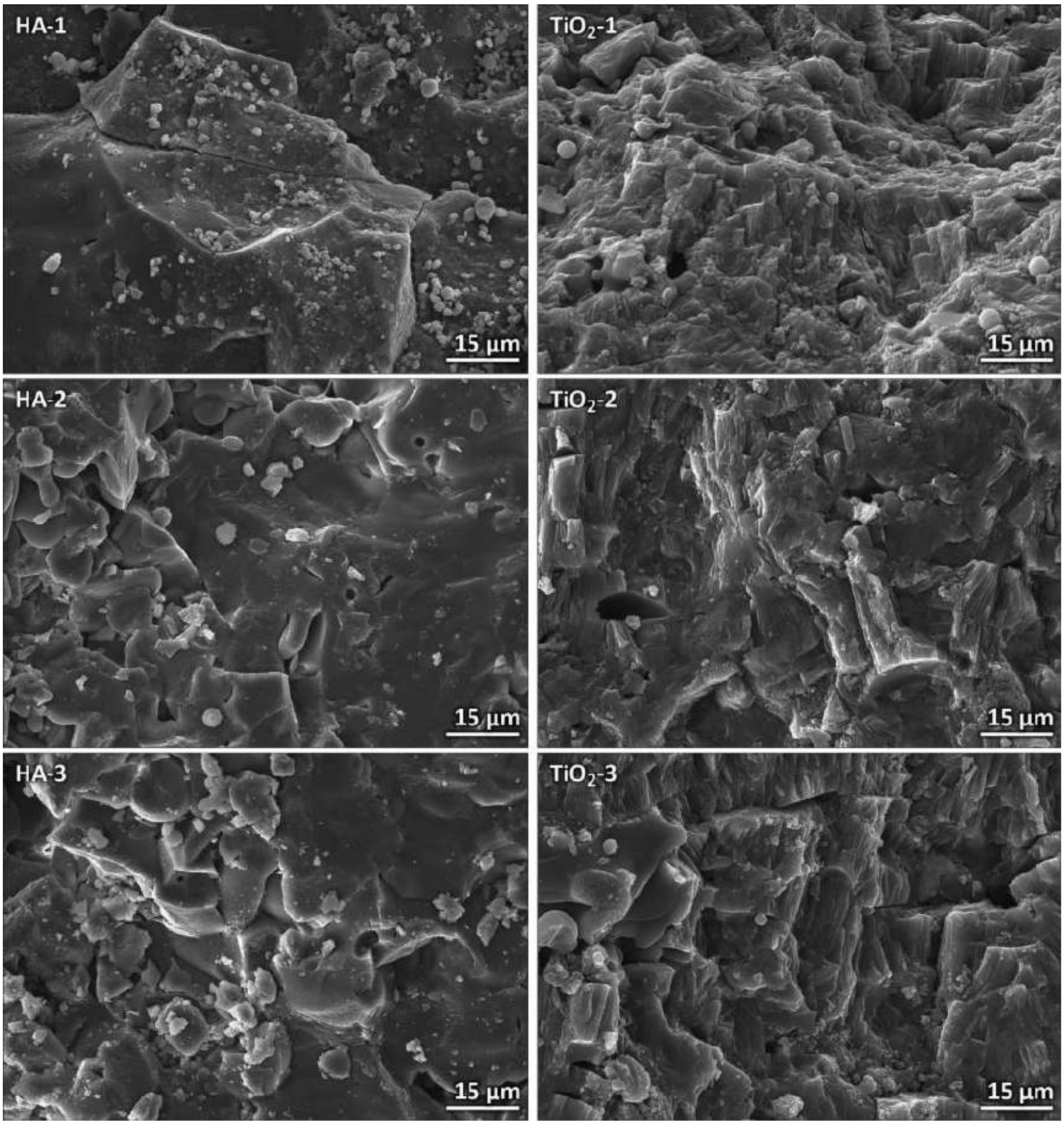

Figure 8. Typical crack surfaces of the coatings. Note the difference for coatings HA-1 and TiO_2-1.

the substrate temperature. These are relatively independent among the sprayed samples, regardless of the particle overheating over their respective T_m values. However, the different microstructures of the coatings possess, among other qualities, different moduli, E, giving rise to different levels of tensile quenching stresses within the coatings. Naturally, the response of the substrate is development of compressive stresses of higher magnitude for the superior-modulus coatings. Interestingly, such mechanism was more pronounced for the TiO_2 coatings, where the sets 2 and 3 exhibited inferior splat interconnection within the coatings, yielding induction of inferior stresses in the coatings and thereby ultimately reducing the beneficial compressive stresses in the substrates.

The fractographic analysis of the crack surface revealed that the mechanism of crack propagation in the substrate was of ductile nature. The mechanism was identical for all individual coated series and also corresponded to the crack behavior in the noncoated set. Typically, the crack propagated in a transgranular manner, with a characteristic striation pattern easily observable (Figure 7). In the region close to the end of the total crack length (i.e., in the region where the crack propagation rate could be considered the highest), the spacing of the individual striations varied around ~600 nm.

The fractographic features of the crack surfaces in the individual deposited coatings are shown in Figure 8. No clear signs of fatigue were identified in the fracture surfaces. This complicates the identification of the real crack formation process of the coatings: the crack may have propagated during the fatigue process already but could also have been formed in the final static rupture. In general, the coatings failed in a trans-particular manner with almost nonexistent share of ductile propagation. One can notice the marked difference for the sets HA-1 and TiO_2-1. In the case of the HA-1 coating, the crack propagated in a trans-splat manner, with infrequent changes in the crack plane (one such plane change is illustrated in Figure 8). Interestingly, such plane changes occurred at what seemed

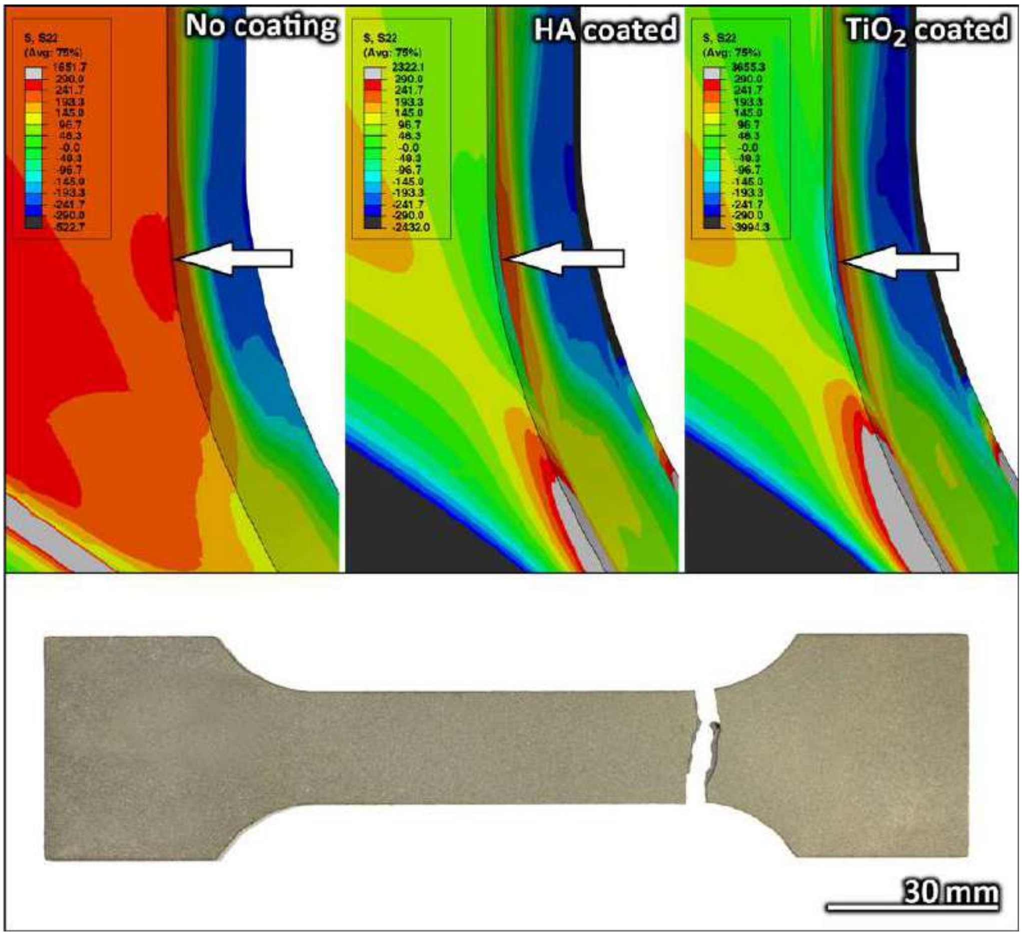

Figure 9. Distribution of the σ_{yy} total stress component in simulated specimens for different types of coating (noncoated, HA, TiO_2) during the maximal (4 mm) free sample end amplitude. The arrows show the location of maximal total (i.e., residual + applied) tensile stress value in the substrate. It corresponds to the location of crack initiation in real specimens, as shown in the image below.

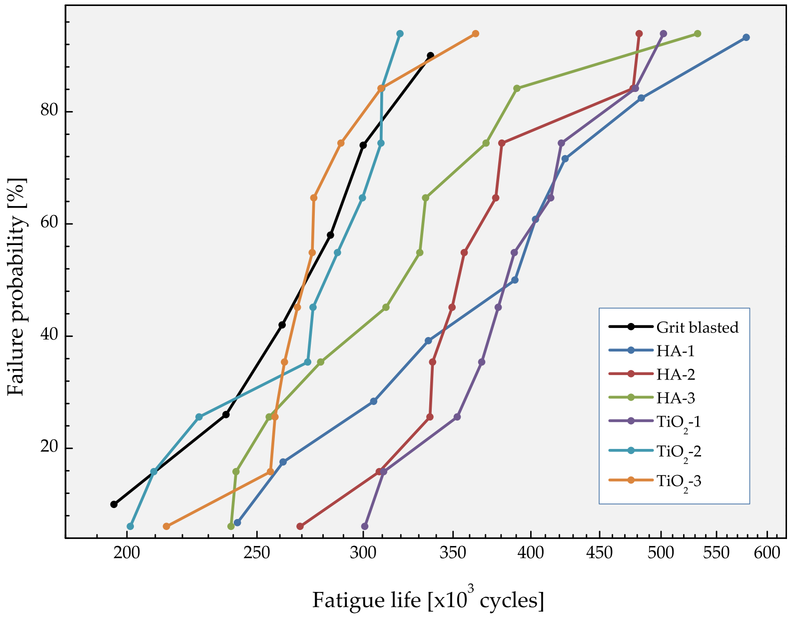

Figure 10. Weibull plot of specimen fatigue lives.

like inside of the splats, not at splat boundaries. Well in accordance with the SEM cross-section observations described earlier, such finding suggested that the HA-1 coating was highly dense and, as opposed to the HA-2 and HA-3 coatings, behaved similarly to bulk materials. The crack propagation in the other two HA coatings, in contrast, took advantage of the imperfect structure: as seen from the images, the crack often propagated using the present intersplat voids or quenching cracks. In case of titania coatings, the crack propagation mode in TiO_2-1 differed from that of the TiO_2-2 and TiO_2-3 coatings. Analogous to its HA counterpart, the crack propagation plane changed in the TiO_2-1 coating, while no marked plane changes were recorded for the other two titania coatings (also illustrated in Figure 8). Importantly, the typical fractographic features in the latter two coatings were almost an order of magnitude bigger, spanning the size of several splats frequently.

The original idea of subjecting the spalled material debris to analysis of particle sizes and to a follow-up biological response study could not be realized due to the inferior amount of the particles collected. On the other hand, this only confirmed the good quality of the deposited coatings, minimizing the risk of inflammation or exothermic reaction in contact with tissues.

The performed FEM modeling showed that the stress component in the longitudinal direction (y-direction) of the specimen is the primary factor responsible for the initiation and propagation of the fatigue cracks. Figure 9 shows the distribution of the total calculated stress, a superposition of the σ_{yy} stress and the residual CTE mismatch stress. According to the calculations, the magnitude of the latter reached approximately −300 MPa (TiO_2) to −150 MPa (HA) in the coatings. Based on the analysis, the location of the maximum stress at the 4 mm specimen deflection (denoted by an arrow) was identified. The location is identical for all three sample types (that is, noncoated as well as HA- and TiO_2-coated substrates) and corresponds well with experimental observations of crack initiation sites (see the real ruptured specimen in Figure 9). As an ideal bonding (i.e., infinite cohesive strength) was used in the FE model, such agreement also suggests that there is a good solid bonding between the coating and the substrate. Importantly, the maximum stress point is not located at the surface of the coatings, but rather at the surface of the substrate, suggesting that the crack may originate within the metallic substrates underneath the coatings. It is important to note that, due to the simplifying assumptions of the used model, the obtained stress levels are only informative, and the calculated predictions have a limited validity in terms of absolute values. Nevertheless, the model shows compressive stresses in the TiO_2 coatings two times higher than those in the HA coatings. This is clearly a result of the lower thermal expansion coefficient of titanium dioxide. Such comparison suggests that the TiO_2 coatings should result in a better fatigue endurance, as the higher compressive stress will retard crack initiation and propagation. However, this fact was not directly confirmed by the realized fatigue experiments (for instance, the two series TiO_2-2 and TiO_2-3 led to a little fatigue endurance increase of 1% and 3% only, respectively). This discrepancy could reside in the FE model representing a solid flawless coating. In reality, the plasma sprayed deposit is composed of a network of interconnected splats, containing numerous voids and cracks (as illustrated in Figure 4), which cause degradation of the fatigue endurance. In other words, improving the compactness of the two coating types could further significantly increase the fatigue properties. For the next stage, comprehending the essential influence of the quenching stress contribution or modeling of the coatings as solid nonmonolithic layer is planned.

Lastly, further statistical processing (Weibull probability plot in Figure 10) indicated that the dispersion of the coated specimens data is bigger than the dispersion of the data corresponding to the reference grit-blasted set. Partially, this is consistent with the general trends observed in fatigue, where the data variance increases with decreased loads (that is, for increased lifetimes). On the other hand, the amount of observed dispersion in this study is still relatively high. Such increased data dispersion may be further triggered by local inhomogeneity of the coatings' mechanical properties (including e.g. localized variations in bonding to the substrate) or the discussed variation in its thickness. Significant differences were also found in the shape of the respective curves. The reference set follows a linear trend, that is, the specimens follow the Weibull distribution well; they are homogeneous from the point of view of their fatigue behavior. To describe the distribution of fatigue lives of the coated specimens, different fatigue models such as Birnbaum−Saunders or log-normal may provide better fits. For comparison purposes, the Weibull distribution is shown in Figure 10 for all sample sets.

4. CONCLUSIONS

The influence of biocoating deposition on fatigue behavior of metallic substrates was studied with respect to different in-flight properties. Three different sets of HA- and TiO_2-coated specimens were prepared, and the flat specimens were subjected to symmetrical cyclical bend loading with a constant deflection of the free end. The obtained results were compared with results of a noncoated grit-blasted set. The main results of the study could be summarized as follows:

- The deposition efficiency of the process is linearly connected to the in-flight temperature and velocity of the powder particles within the plasma jet.
- The density of the coatings (represented by the internal porosity levels) is linearly dependent on the in-flight properties as well.
- The deposition of both ceramic coatings types enhances the fatigue lives of the specimens. This is most probably caused by the induction of favorable compressive stresses into the outermost layers of the substrates via the coatings deposition.
- The intensity of the favorable increase in the fatigue properties is connected to the in-flight properties of the particles.
- For both coating types (HA, TiO_2), the most positive increase in fatigue properties (lifetime) was obtained at the highest in-flight temperatures and velocities, probably due to the improved microstructure of the coatings. Importantly, such increase could be achieved without corrupting either the microstructure or phase composition of the coatings.

■ AUTHOR INFORMATION

Corresponding Author

*E-mail address: cizek@ipp.cas.cz (J. Cizek).

ORCID

J. Cizek: 0000-0001-5092-5640

Notes

The authors declare no competing financial interest.

ACKNOWLEDGMENTS

The experimental study was supported through Czech Science Foundation Grant GB14-36566G “Multidisciplinary research centre for advanced materials.” Financial support by the European Regional Development Fund in the frame of the project Centre of Advanced Applied Sciences (No. CZ.02.1.01/0.0/0.0/16_019/0000778) is gratefully acknowledged.

REFERENCES

(1) Heimann, R. B. Plasma-sprayed hydroxylapatite-based coatings: Chemical, mechanical, microstructural, and biomedical properties. *J. Therm. Spray Technol.* **2016**, *25* (5), 827–850.

(2) Dong, Y.; Svoboda, P.; Vrbka, M.; Kostal, D.; Urban, F.; Cizek, J.; Roupcova, P.; Dong, H.; Krupka, I.; Hartl, M. Towards near-permanent CoCrMo prosthesis surface by combining micro-texturing and low temperature plasma carburising. *J. Mech. Behav. Biomed. Mater.* **2016**, *55*, 215–227.

(3) Hench, L. L. Bioceramics - from concept to clinic. *J. Am. Ceram. Soc.* **1991**, *74* (7), 1487–1510.

(4) Fauchais, P. Understanding plasma spraying. *J. Phys. D: Appl. Phys.* **2004**, *37* (9), R86–R108.

(5) Tucker, R. C., Ed. *ASM Handbook: Thermal spray technology*. ASM International, 2013.

(6) Morks, M.F. Fabrication and characterization of plasma-sprayed HA/SiO2 coatings for biomedical application. *J. Mech. Behav. Biomed. Mater.* **2008**, *1* (1), 105–111.

(7) Cizek, J.; Khor, K. A. Role of in-flight temperature and velocity of powder particles on plasma sprayed hydroxyapatite coating characteristics. *Surf. Coat. Technol.* **2012**, *206* (8–9), 2181–2191.

(8) Xu, J. L.; Joguet, D.; Cizek, J.; Khor, K. A.; Liao, H. L.; Coddet, C.; Chen, W. N. Synthesis and characterization on atomphospheric plasma sprayed amorphous silica doped hydrxoyapatite coatings. *Surf. Coat. Technol.* **2012**, *206* (22), 4659–4665.

(9) Levingstone, T. J.; Barron, N.; Ardhaoui, M.; Benyounis, K.; Looney, L.; Stokes, J. Application of response surface methodology in the design of functionally graded plasma sprayed hydroxyapatite coatings. *Surf. Coat. Technol.* **2017**, *313*, 307–318.

(10) Levingstone, T.J.; Ardhaoui, M.; Benyounis, K.; Looney, L.; Stokes, J. Plasma sprayed hydroxyapatite coatings: Understanding process relationships using design of experiment analysis. *Surf. Coat. Technol.* **2015**, *283* (29–36), 29.

(11) Lima, R. S.; Li, H.; Khor, K. A.; Marple, B. R. Biocompatible nanostructured high-velocity oxyfuel sprayed titania coating: deposition, characterization, and mechanical properties. *J. Therm. Spray Technol.* **2006**, *15* (4), 623–627.

(12) Lima, R. S.; Marple, B. R.; Li, H.; Khor, K. A. Titania thermal spray coatings made from a nanostructured feedstock: an alternative as a biomedical coating. In *Proceedings ASM materials and processes for medical devices*; ASM International, 2005.

(13) Gardon, M.; Guilemany, J. M. Milestones in functional titanium dioxide thermal spray coatings: A review. *J. Therm. Spray Technol.* **2014**, *23* (4), 577–595.

(14) Marple, B. R.; Lima, R. S.; Li, H.; Khor, K. A. Biomimetic ceramic surfaces produced by thermal spraying nanostructured titania: A coating alternative to hydroxyapatite on orthopedic implants? *Key Eng. Mater.* **2006**, *309–311*, 739–742.

(15) Chouirfa, H.; Bouloussa, H.; Migonney, V.; Falentin-Daudre, C. Review of titanium surface modification techniques and coatings for antibacterial applications. *Acta Biomater.* **2019**, *83*, 37–54.

(16) Fei Yin, Z.; Wu, L.; Gui Yang, H.; Hua Su, Y. Recent progress in biomedical applications of titanium dioxide. *Phys. Chem. Chem. Phys.* **2013**, *15* (14), 4844.

(17) Larsson, C.; Thomsen, P.; Lausmaa, J.; Rodahl, M.; Kasemo, B.; Ericson, L. E. Bone response to surface modified titanium implants: studies on electropolished implants with different oxide thicknesses and morphology. *Biomaterials* **1994**, *15* (13), 1062–1074.

(18) Huang, N.; Chen, Y. R.; Luo, J. M.; Yi, J.; Lu, R.; Xiao, J.; Xue, Z. N.; Liu, X. H. vitro investigation of blood compatibility of Ti with oxide layers of rutile structure. *J. Biomater. Appl.* **1994**, *8* (4), 404–412.

(19) Tsyganov, I.; Maitz, M. F.; Wieser, E.; Prokert, F.; Richter, E.; Rogozin, A. Structure and properties of titanium oxide layers prepared by metal plasma immersion ion implantation and deposition. *Surf. Coat. Technol.* **2003**, *174–175*, 591–596.

(20) Lima, R. S.; Marple, B. R. High Weibull Modulus HVOF Titania Coatings. *J. Therm. Spray Technol.* **2003**, *12* (2), 240–249.

(21) Lima, R. S.; Marple, B. R. Optimized HVOF Titania Coatings. *J. Therm. Spray Technol.* **2003**, *12* (3), 360–369.

(22) Cizek, J.; Kovarik, O.; Siegl, J.; Khor, K. A.; Dlouhy, I. Influence of plasma and cold spray deposited ti layers on high-cycle fatigue properties of Ti6Al4V substrates. *Surf. Coat. Technol.* **2013**, *217*, 23–33.

(23) Ahmed, R.; Faisal, N. H.; Knupfer, S. M.; Paradowska, A. M.; Fitzpatrick, M. E.; Khor, K. A.; Cizek, J. Neutron diffraction residual strain measurements in plasma sprayed nanostructured hydroxyapatite coatings for orthopaedic implants. *Mater. Sci. Forum* **2010**, *652*, 309–314.

(24) Musalek, R.; Kovarik, O.; Medricky, J.; Curry, N.; Bjorklund, S.; Nylen, P. Fatigue testing of TBC on structural steel by cyclic bending. *J. Therm. Spray Technol.* **2014**, *24* (1–2), 168–174.

(25) Cizek, J.; Matejkova, M.; Dlouhy, I.; Siska, F.; Kay, C. M.; Karthikeyan, J.; Kuroda, S.; Kovarik, O.; Siegl, J.; Loke, K.; Khor, K. A. Influence of cold sprayed, warm sprayed and plasma sprayed layers deposition on fatigue properties of steel specimens. *J. Therm. Spray Technol.* **2015**, *24* (5), 758–768.

(26) Musalek, R.; Kovarik, O.; Skiba, T.; Hausild, P.; Karlik, M.; Colmenares-Angulo, J. Fatigue properties of Fe-Al intermetallic coatings prepared by plasma spraying. *Intermetallics* **2010**, *18* (7), 1415–1418.

(27) Rakngarm, A.; Mutoh, Y. Characterization and fatigue damage of plasma sprayed HAp top coat with Ti and HAp/Ti bond coat layers on commercially pure titanium substrate. *J. Mech Behav Biomed Mater.* **2009**, *2* (5), 444–453.

(28) Laonapakul, T.; Rakngarm Nimkerdphol, A.; Otsuka, Y.; Mutoh, Y. Failure behavior of plasma-sprayed HAp coating on commercially pure titanium substrate in simulated body fluid (SBF) under bending load. *J. Mech Behav Biomed Mater.* **2012**, *15*, 153–166.

(29) Cizek, J.; Khor, K. A.; Prochazka, Z. Influence of spraying conditions on thermal and velocity properties of plasma sprayed hydroxyapatite. *Mater. Sci. Eng., C* **2007**, *27* (2), 340–344.

(30) Rietveld, H. M. Line profiles of neutron powder-diffraction peaks for structure refinement. *Acta Crystallogr.* **1967**, *22*, 151–152.

(31) Legeros, R. Z.; Legeros, J. P. Dense hydroxyapatite. *An Introduction to Bioceramics*; World Scientific, 1993, pp 139–180.

(32) Sollazzo, V.; Pezzetti, F.; Scarano, A.; Piattelli, A.; Massari, L.; Brunelli, G.; Carinci, F. Anatase coating improves implant osseointegration in vivo. *J. Craniofac Surg* **2007**, *18* (4), 806–810.

(33) Tsou, H. K.; Hsieh, P. Y.; Chi, M. H.; Chung, C. J.; He, J. L. Improved osteoblast compatibility of medical-grade polyetheretherketone using arc ionplated rutile/anatase titanium dioxide films for spinal implants. *J. Biomed. Mater. Res., Part A* **2012**, *100A* (10), 2787–2792.

(34) Forberg, S. Ceramic containers for spent nuclear fuel: on the corrosion resistance of rutile. *Adv. Ceramics* **1986**, *20*, 321–327.

(35) Tsyganov, I.; Maitz, M. F.; Wieser, E. Blood compatibility of titanium-based coatings prepared by metal plasma immersion ion implantation and deposition. *Appl. Surf. Sci.* **2004**, *235* (1–2), 156–163.

(36) Cizek, J.; Khor, K. A.; Dlouhy, I. In-flight temperature and velocity of powder particles of plasma-sprayed TiO2. *J. Therm. Spray Technol.* **2013**, *22* (8), 1320–1327.

(37) Cizek, J.; Dlouhy, I.; Siska, F.; Khor, K. A. Modification of plasma-sprayed TiO2 coatings characteristics via controlling the in-

flight temperature and velocity of the powder particles. *J. Therm. Spray Technol.* **2014**, *23* (8), 1339−1349.

(38) Dyshlovenko, S.; Pateyron, B.; Pawlowski, L.; Murano, D. Numerical simulation of hydroxyapatite powder behaviour in plasma jet. *Surf. Coat. Technol.* **2004**, *179* (1), 110−117.

(39) Dyshlovenko, S.; Pawlowski, L.; Roussel, P.; Murano, D.; le Maguer, A. Relationship between plasma spray operational parameters and microstructure of hydroxyapatite coatings and powder particles sprayed into water. *Surf. Coat. Technol.* **2006**, *200* (12−13), 3845−3855.

(40) Kovarik, O.; Hausild, P.; Capek, J.; Medricky, J.; Siegl, J.; Musalek, R.; Pala, Z.; Curry, N.; Bjorklund, S. Resonance bending fatigue testing with simultaneous damping measurement and its application on layered coatings. *Int. J. Fatigue* **2016**, *82*, 300.

(41) Rothman, M. F., Ed. High-temperature property data: ferrous alloys. ASM International, 1989.

(42) Franssen, J. M.; Real, P. V.. *Fire design of steel nanostructures*; Wiley, 2016.

(43) Zamiri, A.; De, S. Mechanical properties of hydroxyapatite single crystals from nanoindentation data. *J. Mech Behav Biomed Mater.* **2011**, *4* (2), 146−152.

(44) Ching, W. Y.; Rulis, P.; Misra, A. Ab initio elastic properties and tensile strength of crystalline hydroxyapatite. *Acta Biomater.* **2009**, *5*, 3067−3075.

(45) Miyazaki, H.; Ushiroda, I.; Itomura, D.; Hirashita, T.; Adachi, N.; Ota, T. Thermal expansion of hydroxyapatite between −100c and 50c. *Mater. Sci. Eng., C* **2009**, *29* (4), 1463−1466.

(46) Ciftci, Y.; Unlu, Y.; Colakoglu, K.; Deligoz, E. The structural, thermodynamical and elastic properties of TiO. *Phys. Scr.* **2009**, *80* (2), 025601.

(47) Caravaca, M. A.; Mino, J. C.; Casali, R. A.; Ponce, C. A.; Perez, V. J. Ab initio study of the elastic properties of single and polycrystals TiO(2), ZrO(2) and HfO(2) in the cotunnite structure. *J. Phys.: Condens. Matter* **2009**, *21* (1), 015501.

(48) Meagher, E. P.; Lager, G. A. Polyhedral thermal expansion in the TiO2 polymorphs: refinement of the crystal structures of rutile and brookite at high temperature. *Can. Mineral* **1979**, *17*, 77−85.

(49) Kirby, R. K. Thermal expansion of rutile from 100 to 700k. *J. Res. Natl. Bur. Stand., Sect. A* **1967**, *71A* (5), 363−369.

(50) Matejicek, J.; Sampath, S.; Gilmore, D.; Neiser, R. In situ measurement of residual stresses and elastic moduli in thermal sprayed coatings. *Acta Mater.* **2003**, *51* (3), 873−885.

(51) Li, Y.; Ishigaki, T. Thermodynamic analysis of nucleation of anatase and rutile from TiO2 melt. *J. Cryst. Growth* **2002**, *242* (3−4), 511−516.

(52) Kovarik, O.; Siegl, J.; Nohava, J.; Chraska, P. Young's modulus and fatigue behavior of plasma-sprayed alumina coatings. *J. Therm. Spray Technol.* **2005**, *14* (2), 231−238.

(53) Evans, S. L.; Gregson, P. J. The effect of a plasma-sprayed hydroxyapatite coating on the fatigue properties of Ti-6Al-4V. *Mater. Lett.* **1993**, *16* (5), 270−274.

(54) Lynn, A. K.; DuQuesnay, D. L. Hydroxyapatite-coated Ti-6Al-4V: Part 1: the effect of coating thickness on mechanical fatigue behaviour. *Biomaterials* **2002**, *23* (9), 1937−1946.

(55) Kroupa, F. Residual stresses in thick, nonhomogeneous coatings. *J. Therm. Spray Technol.* **1997**, *6* (3), 309−319.

(56) Vysohlid, M.; Kroupa, F. Quenching stresses in thermal sprayed cylindrical coatings and free-standing tubes. *Mater. Sci. Eng., A* **2000**, *283* (1−2), 111−121.

DOI: 10.1021/acsbiomaterials.8b01545
ACS Biomater. Sci. Eng. 2019, 5, 1703−1714

Surface & Coatings Technology 291 (2016) 342–347

Contents lists available at ScienceDirect

Surface & Coatings Technology

journal homepage: www.elsevier.com/locate/surfcoat

Elastic moduli and elastic anisotropy of cold sprayed metallic coatings

Hanuš Seiner [a], Jan Cizek [b,*], Petr Sedlák [a], Renzhong Huang [c], Jan Cupera [b], Ivo Dlouhy [b], Michal Landa [a]

[a] Institute of Thermomechanics, Academy of Sciences of the Czech Republic, Dolejškova 5, 18200 Prague, Czech Republic
[b] Netme Centre, Institute of Materials Science and Engineering, Brno University of Technology, Technicka 2896/2, 616 69 Brno, Czech Republic
[c] Plasma Giken, 4-1 Imaichi, Yoriimachi, Osato-gun, Saitama 369-1214, Japan

ARTICLE INFO

Article history:
Received 28 December 2015
Revised 19 February 2016
Accepted in revised form 24 February 2016
Available online 3 March 2016

Keywords:
Kinetic spray
CGDS
Elastic properties
Metals and alloys
Deposition
Resonant ultrasound spectroscopy

ABSTRACT

Resonant ultrasound spectroscopy is applied to analyze the elastic anisotropy of thick copper, aluminum, titanium, and nickel coatings prepared by cold spraying and to determine the respective elastic moduli. The results show that the coatings exhibit only weak deviations from perfect isotropy, and the obtained elastic moduli are comparable with those of the corresponding polycrystalline bulks. The increased internal friction observed in some of the studied coatings may indicate grain refinement and consequent grain boundary sliding.

© 2016 Elsevier B.V. All rights reserved.

1. Introduction

Cold spraying (CS, [1–7]) is a versatile and efficient method for deposition of relatively thick metallic coatings. Unlike the conventional thermal spraying methods such as plasma spraying [8–10], the CS process does not involve substantial heating or melting of the sprayed powders. Instead, the formation of the coating arises from a severe plastic deformation of the accelerated powder particles upon their impingement at the substrate [11,12]. Thereby, the oxidation or phase changes in the feedstock material are effectively reduced, as well as e.g. the magnitude of the secondary residual stresses arising from the thermal expansion mismatch [13]. As such, CS has recently received a lot of attention as a novel method applicable for sensitive metals and alloys that readily undergo chemical or structural changes at elevated temperatures. Among the sprayed metallic coatings, those prepared by CS frequently exhibit superior mechanical and physical properties [1,7], such as Young's modulus [14], hardness [15], or electrical conductivity [16], often comparable to those of the respective bulks. Further to that, the coatings deposited via high-temperature processes generally exhibit high levels of anisotropy [4], a property arising due to their heterogeneous lamellar or splat-like microstructure [4,17–19] and commonly regarded as undesired. In this paper, we show that the CS coatings do not exhibit any significant elastic anisotropy, as opposed to its high-temperature counterparts.

Resonant ultrasound spectroscopy (RUS, [20–22]) has been recently used to investigate elastic anisotropy of nickel coatings prepared by the high-velocity oxygen fuel (HVOF) and atmospheric plasma spraying (APS) methods [19] and of steel coatings [23] prepared by water-stabilized plasma (WSP) spraying. In all reported cases, the difference between the in-plane and out-of plane properties of the coatings were significant, with the values of the ratio $\alpha = E_{OOP}/E_{IP}$ between the out-of-plane Young's modulus (E_{OOP}) and the in-plane Young's modulus (E_{IP}) ranging from 0.36 (for APS [19]) to 0.87 (for WSP [23]). Here we apply this method to determine the elastic constants and the strength of anisotropy for pure copper, aluminum, titanium and nickel coatings prepared by CS. The main advantage of the RUS method is that it enables the determination of all independent elastic constants of an anisotropic solid from measurements of one small sample. In addition, the RUS enables also a direct assessment of the internal friction parameter of the examined material Q^{-1} [21], which may bring an additional information on the integrity of the sprayed material or on density and activity of defects in it [24].

2. Experimental setup

2.1. Examined materials

Four commercially available powders were selected for the experiment: Al, Cu, Ni, and Ti. Considering the aim of the study, i.e. evaluation of (an)isotropy of the cold spray technology as a method, the selection of the powders was made with the aim of having feedstock material of dissimilar properties. The powder particles (Fig. 1) differed in their

---

[*] Corresponding author.
E-mail address: cizek@fme.vutbr.cz (J. Cizek).

http://dx.doi.org/10.1016/j.surfcoat.2016.02.057
0257-8972/© 2016 Elsevier B.V. All rights reserved.

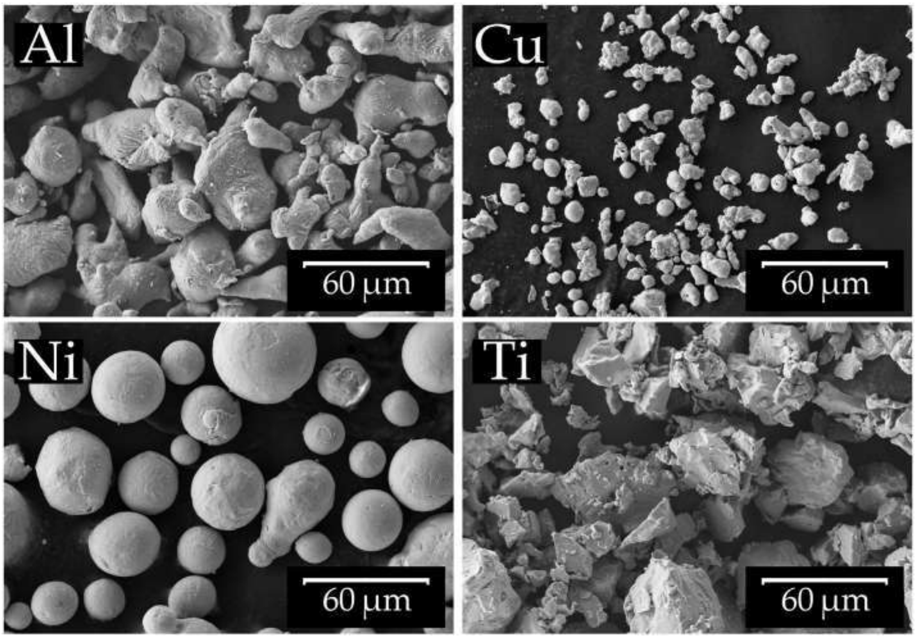

Fig. 1. Morphology of the Al, Cu, Ni, and Ti powders used for CS coatings fabrication.

apparent density (varying from 2.67–8.96 $g\cdot cm^{-3}$), morphologies (oval, fully spherical, angular; a consequence of different fabrication technologies), and average particle diameters (21–40 μm).

2.2. Coatings deposition

The analyzed materials were then deposited via high-pressure cold spray system (PCS-1000, Plasma Giken, Ltd., Japan) onto polycrystalline 6061 aluminum alloy substrates of commercial purity. The surface of the substrates was not grit-blasted prior to coatings deposition. However, chemical degreasing was used to remove any oil or contaminant films. The lateral dimensions of the coated areas were 150 × 50 mm and the robot arm movement and number of passes were set to reach a total coating thickness of at least 10 mm; the excessive thickness allowed subsequent cutting of the required samples. Further to that, the successive gun passes resulted in a further compaction of the underlying deposited layers, thereby lowering the inherent coating porosity. The spray parameters used in the deposition are proprietary to Plasma Giken and are not to be disclosed in the paper.

The properties of the fabricated coatings were studied using FE-SEM equipped with EDX mapping and EBSD detectors (Zeiss Ultra Plus) and XRD (X'Pert Pro X-ray diffractometer, Co-K $_\alpha$ source, K $_\beta$ absorption filter, X'Celerator detector; PANalytical B.V.). To determine oxygen content in the materials, Leco TC 600 thermoevolution analyzer was employed. Image analysis and the Archimedes methods were used to calculate the internal coatings porosity and Vickers microhardness was measured at 1 kgf load.

2.3. Resonant ultrasound spectroscopy

From each of the sprayed materials, a small sample of a rectangular parallelepiped-shape (approximately $3.5 \times 2.5 \times 1.5$ mm^3) was cut from the region close to the center of the sprayed area. Taking advantage of the layers compaction via impingement of particles from successive gun passes, the samples were cut from areas close to the substrate-coating interface. All samples were oriented so that longest and the shortest edge of the sample were always perpendicular to the spraying direction and aligned with the directions of motion of the nozzle during spraying. However, it was assumed (as usual for the sprayed materials [19,23,25,26]) that all samples exhibit transversal isotropy, i.e. that all directions perpendicular to the spraying direction are equivalent, and the elasticity of the material can be fully described by five independent elastic coefficients. In the shorten Voigt's notation, these elastic constants are c_{11}, c_{12}, c_{13}, c_{33} and c_{44}, assuming that the spraying direction is aligned with x_3. The engineering constants E_{IP} and E_{OOP} introduced in the Introduction can be then recalculated from c_{ij} by simple algebraic relations (see e.g. [27]).

For each sample, a resonant spectrum of free elastic vibrations was obtained in the frequency range 0.1–2 MHz, using a contact-less, laser-based RUS setup [22]. The vibrations were excited by short (8 ns) infrared pulses from a Nd:YAG laser with nominal wavelength 1.064 μm and pulse energy 25 mJ (Quantel ULTRA, USA) and recorded by a scanning laser vibrometer (24 MHz frequency bandwidth) incorporated in a Polytec Micro-System Analyzer MSA-500, which enabled an identification of the modal shapes corresponding to individual resonant peaks. The experiments were performed at ambient temperature (295 K, temperature control ± 0.05 K) under a low pressure (10 mbar) nitrogen atmosphere.

The resonant spectra were complemented by pulse-echo measurements of phase velocity of longitudinal waves in directions perpendicular to the individual faces of the samples [27], i.e. in the in-plane (v_{IP}) and out-of-plane (v_{OOP}) directions. The schematics of the RUS method used within this study is shown in Fig. 2.

3. Results and discussion

3.1. Coating properties

The fabricated coatings exhibited well-sintered and relatively homogeneous structure (Fig. 3) with only negligible oxidation levels (<0.24 wt.% in all coatings). As the oxide content was found at particle rims only (via extended duration EDX mapping), it could be safely assumed that it was present in the original feedstock already and was incorporated into the coating during the spraying. As shown in Table 1, minimal porosity content only was detected in the coatings (ranging from 0.3–1.1%, decreasing towards interface) and the microhardness differed from 50 HV1 (Al) to 222 HV1 (Ti). The mass densities of the coatings as determined by the Archimedes method are further shown in Table 1.

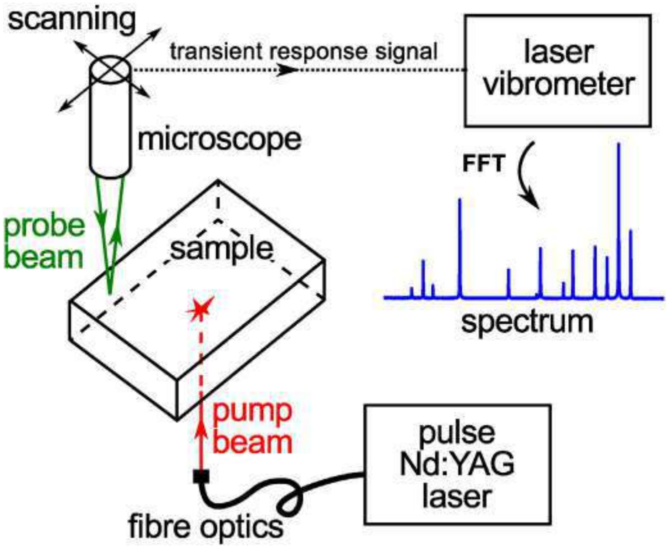

Fig. 2. Schematics of the RUS setup.

Table 1
Elastic constants c_{ij} and the Young's moduli (E_{IP}, E_{OOP}) of the analyzed CS materials; the anisotropy ratio α characterizes the difference between IP and OOP properties. For comparison, the values of the Young's moduli for bulk materials are given [40]. The constant c_{66} was calculated as $(c_{11} - c_{12}) / 2$. Further included is density, porosity, and microhardness of the coatings.

	Al	Cu	Ni	Ti
c_{11} [GPa]	86.2 ± 0.4	183.3 ± 1.4	188.8 ± 1.6	116.1 ± 0.9
c_{12} [GPa]	40.1 ± 0.4	95.5 ± 1.5	76.7 ± 2.4	48.9 ± 1.1
c_{13} [GPa]	38.6 ± 0.4	94.6 ± 1.1	75.1 ± 2.5	43.6 ± 1.3
c_{33} [GPa]	83.3 ± 0.5	179.7 ± 1.3	185.1 ± 1.6	114.7 ± 0.8
c_{44} [GPa]	23.3 ± 0.1	42.5 ± 0.1	54.6 ± 1.0	34.4 ± 0.3
c_{66} [GPa]	23.0 ± 0.1	43.9 ± 0.2	56.1 ± 2.0	33.6 ± 0.2
E_{IP} [GPa]	61.1 ± 0.6	117.9 ± 2.0	144.9 ± 2.3	89.1 ± 1.2
E_{OOP} [GPa]	59.7 ± 0.7	115.5 ± 2.1	142.7 ± 3.0	91.4 ± 1.5
$\alpha = E_{OOP}/E_{IP}$	0.98 ± 0.01	0.98 ± 0.02	0.98 ± 0.02	1.03 ± 0.02
E_{bulk} [GPa]	70	130	201	121
E_{OOP}/E_{bulk}	0.85	0.89	0.72	0.76
Density [$g \cdot cm^{-3}$]	2.59	8.75	8.36	4.28
Porosity [%]	0.8	1.1	0.4	0.3
Microhardness [HV1]	50	190	220	222

In Fig. 4, SEM micrographs of the sprayed materials in the angle selective backscatter (AsB) mode are shown. These micrographs were recorded in channeling contrast mode and reveal a finer structure of misoriented subgrains inside of the individual sprayed particles, resulting probably from the impact-induced plastic deformation. This effect was most apparent for the Ni coating, where also the bimodal character of this feature was clearly seen: while along the particle boundaries the dimensions of the subgrains were of the order of tens of nanometers, in the middle of the particles these subgrains were of the order of micrometers. Similar effect was also observed in the Al and Cu coatings. In the Ti coating, instead, fine subgrain structure was seen all over the particles, forming some kind of anisotropic pattern, probably resulting from the plastic anisotropy of the hcp titanium.

To detect any prospective texture orientation in the materials, the measurements were further supported by EBSD investigations of the coatings polished cross-section [28]. In accordance with the results obtained via RUS (Section 3.2), the EBSD polar-orientation maps suggested that the studied cold sprayed coatings did not exhibit any significant crystallographic texture and the orientation of the grains and subgrains within the structure is distributed randomly. A typical example of the pole and inversed pole maps is provided in Fig. 5 for Ni coating.

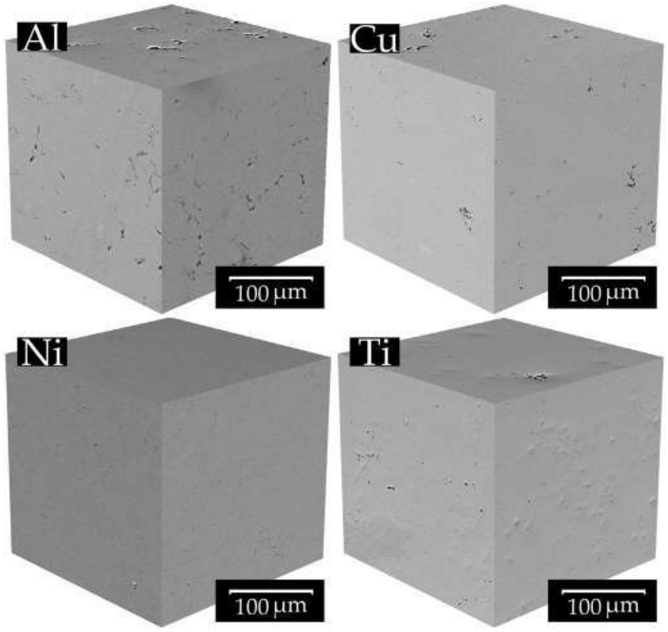

Fig. 3. Compact structure of the Al, Cu, Ni, and Ti coatings fabricated via high-pressure cold spray.

3.2. RUS results

More than 20 resonant modes were detected and identified in the measured frequency range for each sample. However, the resonant spectra for the individual samples differed significantly in the widths of the resonant peaks, i.e. in the vibration damping by internal friction. In Fig. 6, these differences are shown on selected parts of the spectrum and quantified by the internal friction parameters Q^{-1} (see e.g. [24]), which were calculated from ten most dominant peaks in each spectrum by fitting of these peaks by Lorenzian masks. The Q^{-1} values for the Cu and the Ni samples differ by nearly two orders of magnitude; the internal friction parameters for the Al and Ti samples lie between these two extremes.

Nevertheless, for all materials the internal friction was sufficiently low and the number of identifiable peaks sufficiently high for the determination of the elastic constants. For the calculation of these constants, the combined iterative inverse procedure described in detail in Ref. [22] was used; this procedure uses the RUS spectra and the pulse-echo results as the input data and finds such set of elastic constants that the resonant frequencies and the v_{IP} and v_{OOP} velocities calculated for this set fit the input data in the least squares sense. The results of this procedure are listed in Table 1, whereto the respective experimental errors were calculated via the sensitivity analysis procedure described also in Ref. [22].

As shown in Table 1, the Young's moduli of all materials in the OOP direction (which are, in general, considered as softer than those in the IP direction) were higher than 70% of the moduli of the respective bulk materials. Especially for the Cu sample, the CS material was by only approximately 10% elastically softer than bulk polycrystalline copper. This indicated very high compactness of the CS coating and good interlocking between the individual grains. The ability of the CS coatings to exhibit as high elastic moduli as 90% of the bulk value were reported already by Sundararajan et al. [29]. However, in their study such values were only reported after additional heat treatment of the coatings. In the as-sprayed state, the coatings in Ref. [29] exhibited a significant deterioration of the elastic moduli due to inter-splat boundary cracking. No evidence of such cracking was present in the presented coatings; the difference of the two studies could be attributed to the use of low-pressure system in Ref. [29] (10–20 MPa, see e.g. [30] for the discussion of the effect of the gas pressure on the CS coatings) and the use of different powder feedstock.

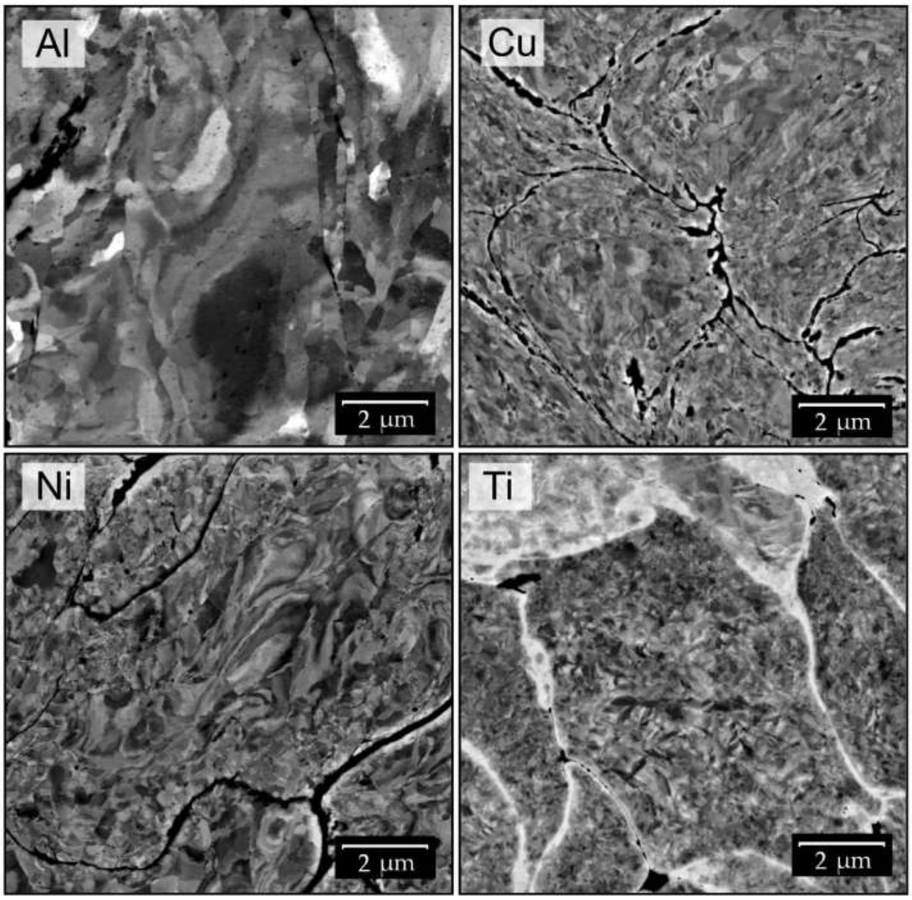

Fig. 4. Morphology of the cold spray deposited Al, Cu, Ni, and Ti coatings (Zeiss FE-SEM, AsB mode, channeling contrast, 10 kV, WD = 3.5 mm). Individual particles could be partially distinguished in the structure. Within the particles, the gray-scale contrast corresponds to misorientation of subgrains formed upon impact. In all micrographs, the vertical direction corresponds to the spraying direction.

Furthermore, all CS coatings listed in Table 1 exhibited nearly perfect elastic isotropy. The ratios between the OOP and IP Young's moduli α ranged between 0.98 and 1.03, i.e. the differences from $\alpha = 1$ were fully comparable to the experimental errors. Although a similarly perfect elastic isotropy was reported for amorphous alumina coatings [31], for crystalline metallic coatings such results are very rare.

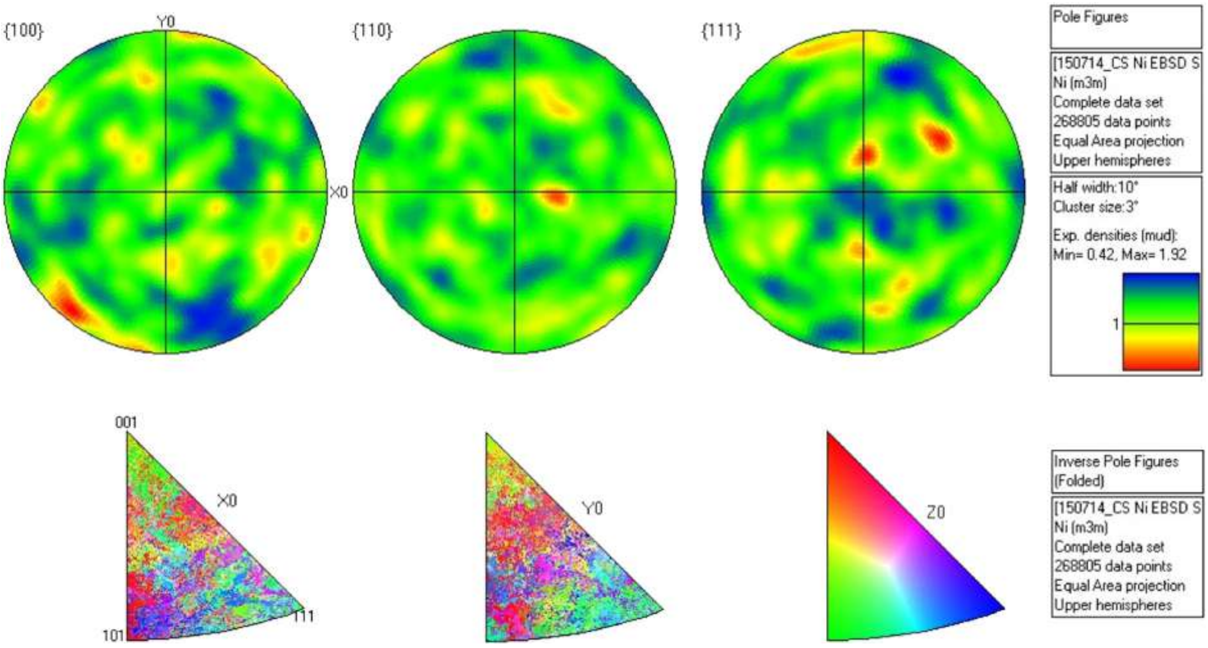

Fig. 5. EBSD pole and inverse pole figures of Ni cold spray coating. No preferred orientation texture was detected in the coatings.

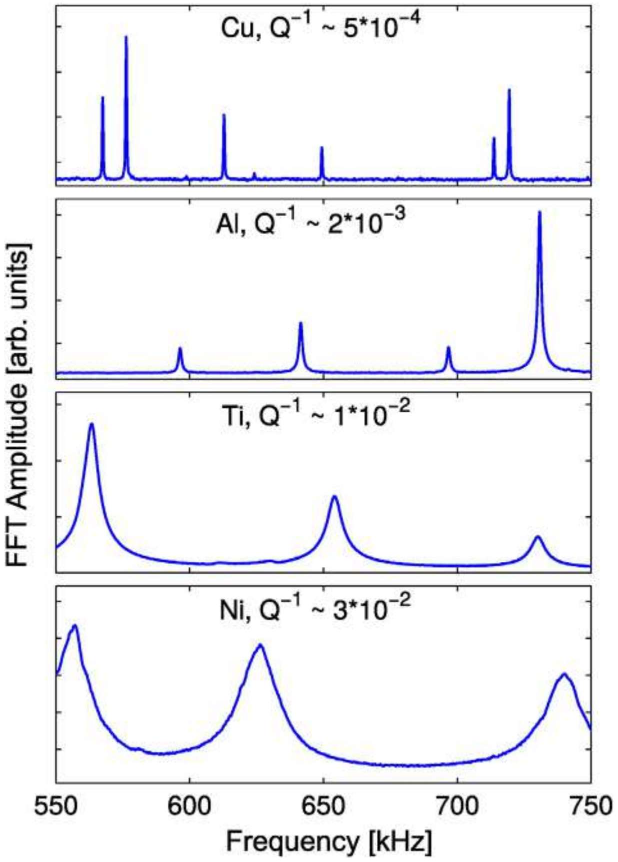

Fig. 6. Selected parts of the RUS spectra for the Cu, Al, Ti and Ni CS samples illustrating the differences in the internal friction parameters Q^{-1}.

Importantly, the isotropy was reached for all CS materials, although these materials belong to different crystallographic classes and the corresponding bulk materials differ significantly in a number of mechanical properties. For the copper coating, in particular, the observed anisotropy was even weaker than anisotropy of bulk polycrystalline copper with significant crystallographic texture and strongly anisotropic spatial arrangement of grain boundaries reported in Ref. [27].

In Fig. 7, the results obtained for the CS materials are compared with metals and metallic compounds sprayed by several other methods, in particular by high-velocity oxygen fueling (HVOF), water-stabilized plasma spraying (WSP), atmospheric spraying (APS), wire-arc spraying (WAS), flame spraying (FS), and vacuum plasma spraying (VPS). As the sprayed materials typically exhibit strongly nonlinear character (i.e. the amplitude dependence of the elastic moduli [32]), the map in Fig. 7 comprises only the results obtained by ultrasonic methods, in particular by pulse-echo [25], RUS [19,26] or by their combination [23]; therefore, all these results refer to very small straining amplitudes and high straining rates typical for ultrasound. The CS materials obviously possess a unique combination of high E_{OOP}/E_{bulk} ratio and very weak anisotropy. Comparable properties were achieved only for the APS CoNiCrAlY coating by Waki et al. [26] after an extensive heat treatment of the coating; in the as-sprayed condition, however, all reported materials exhibited both lower E_{OOP}/E_{bulk} ratios and stronger anisotropy.

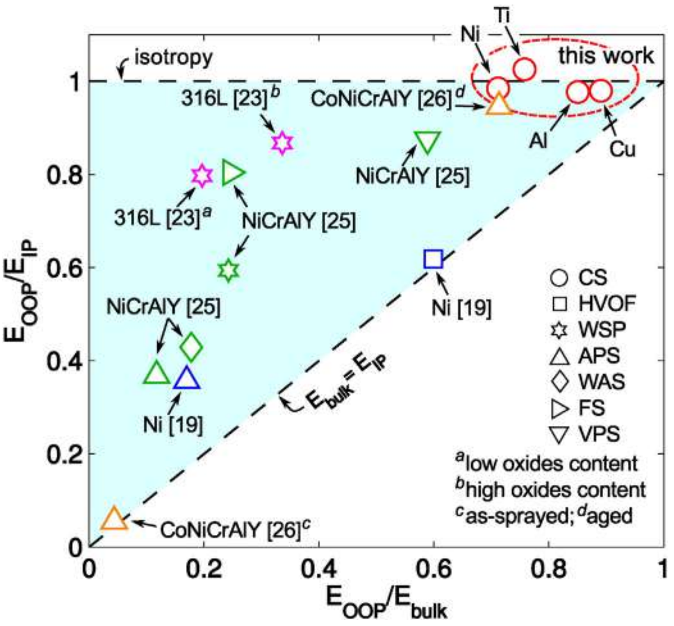

Fig. 7. A comparison of the elastic properties of the CS materials with other sprayed metals and metallic compounds; the horizontal axis of the map represents the relative elastic weakening of the sprayed material with respect to the bulk material E_{OOP}/E_{bulk}, the vertical axis gives the anisotropy of the coating E_{OOP}/E_{IP}. The shaded triangle is the area of validity of the $E_{OOP} \leq E_{IP} \leq E_{bulk}$ relation followed approximately by all plotted materials; the different markers refer to different spraying methods (see the text for the acronyms), the numbers in square brackets refer to the list of references.

The E_{OOP}/E_{bulk} ratios given Table 1 indicate that there was some correlation between this ratio and the observed differences in the internal friction shown in Fig. 6. While the Cu sample exhibited the highest relative Young's modulus and the lowest internal friction parameter Q^{-1}, the Ni sample, which is elastically the most softened with respect to the bulk material, had the highest value of Q^{-1}. As shown in Fig. 8, the same trend was also followed by the Al and Ti samples. The increase of internal friction and the simultaneous decrease of the relative Young's modulus cannot be obviously explained by the porosity, although the relative density ρ/ρ_{bulk} exhibited the same trend; the differences in ρ/ρ_{bulk} between the individual materials are by approximately one order of magnitude smaller than those in the relative Young's moduli. The discrepancy could be partially explained by the fact that the effect of porosity onto the elastic constants of the sprayed coatings may follow not only from the total volume fraction, but also from shapes and spatial arrangement of the pores (cf. [33]). However, it is plausible that there is an additional source of this simultaneous softening and internal friction increase originating directly from the microstructure of the coatings. As reported by Zou [34] and Zou et al. [35], the aluminum and nickel CS coatings contain some amount of highly misoriented, equiaxed nano-sized grains, probably formed by sub-grain rotation under impacts during the spraying, while no such grains can be found in the CS copper coatings. Consequently, it is plausible that these grains contribute to softening and internal friction of the analyzed coatings by grain boundary sliding (GBS), as GBS at room temperature in nano-

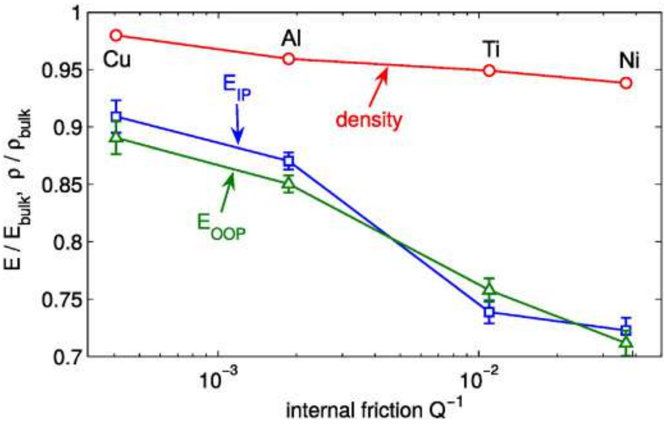

Fig. 8. Correlation between the internal friction parameter Q^{-1} and the relative density (ρ/ρ_{bulk}) and Young's moduli (E_{IP}/E_{bulk} and E_{OOP}/E_{bulk}).

grained aluminum, nickel and titanium was reported several times [36–39].

From another point of view, both the lowest value of the internal friction and the highest value of the relative Young's modulus E_{OOP}/E_{bulk} indicate that the copper coating exhibited the best integrity and compactness among the examined materials. This is in a good agreement with the fact that the sprayability of copper is the best among the examined materials. Nevertheless, even for the materials with initially worse sprayability (especially titanium with the hcp structure), the results reported in this paper show that the CS coatings exhibit, among other sprayed materials, superior elastic properties, both in the E_{OOP}/E_{bulk} ratio and as far as the resulting elastic anisotropy is concerned. As seen in the map in Fig. 7, all examined CS materials were comparable in this respect, and thus, it can be concluded that such unique properties are not particular to the individual sprayed metals, but follow from the CS technology itself.

4. Conclusions

Four cold sprayed materials (Al, Cu, Ni, Ti) were studied by contactless laser-based RUS. It was shown that, in the elastic deformation range, the fabricated metallic coatings exhibited nearly perfectly isotropic behavior, making cold spray unique among all other thermal spraying methods. Further to that, the obtained values of Young's moduli of the studied coatings were well comparable to those of the corresponding bulk materials, an additional indication of the outstanding compactness achieved by the CS process.

On the other hand, especially the Ni and Ti CS coatings exhibited an increased level of internal friction. Simultaneously, these coatings were elastically slightly softer than what could be ascribed to the effect of porosity. It is therefore assumed that this behavior can be interpreted as a result of intense plastic deformation of the sprayed material during the CS process, leading to grain refinement and, consequently, to enhanced grain boundary sliding. From this point of view, the elasticity of CS coatings may exhibit features similar to bulk materials processed by severe plastic deformation methods, for which the slight softening of elastic constants and simultaneous increase of internal friction due to grain refinement is also well detectable by RUS measurements [27,41].

Acknowledgment

The work of H.S., P.S. and M.L. has been financially supported by the Czech Science Foundation (project No. GA13-13616S). The work of J.C., J.C. and I.D. has been also financially supported by the Czech Science Foundation (project No. GA13-35890S) and has been carried out within NETME Centre Plus (LO1202) project co-funded within the support program National Sustainability Programme I.

References

[1] A. Papyrin, V. Kosarev, S. Klinkov, A. Alkhimov, V. Fomin, Cold Spray Technology, Elsevier, Amsterdam, 2007.
[2] J. Cizek, O. Kovarik, J. Siegl, K.A. Khor, I. Dlouhy, Surf. Coat. Technol. 217 (2013) 23.
[3] T. Schmidt, H. Assadi, F. Gartner, H. Richter, T. Stoltenhoff, H. Kreye, T. Klassen, J. Therm. Spray Technol. 18 (2009) 794.
[4] R. Tucker (Ed.), ASM Handbook: Thermal Spray Technology, ASM International, Materials Park, 2013.
[5] J. Cizek, O. Man, P. Roupcova, K. Loke, I. Dlouhy, Surf. Coat. Technol. 268 (2015) 85.
[6] J. Cizek, M. Matejkova, I. Dlouhy, F. Siska, C.M. Kay, J. Karthikeyan, S. Kuroda, O. Kovarik, J. Siegl, K. Loke, K.A. Khor, J. Therm. Spray Technol. 24 (2015) 758.
[7] P. Fauchais, J.V.R. Heberlein, M.I. Boulos, Thermal Spray Fundamentals: From Powder to Part, Springer US, New York, 2014.
[8] R. Musalek, O. Kovarik, J. Matejicek, Surf. Coat. Technol. 205 (2010) 1807.
[9] J. Nohava, R. Musalek, J. Matejicek, M. Vilemova, Surf. Coat. Technol. 240 (2014) 243.
[10] J. Cizek, I. Dlouhy, F. Siska, K.A. Khor, J. Therm. Spray Technol. 23 (2014) 1339.
[11] R. Morgan, P. Fox, J. Pattison, C. Sutcliffe, W. O'Neill, Mater. Lett. 58 (2004) 1317.
[12] H. Assadi, F. Gartner, T. Stoltenhoff, H. Kreye, Acta Mater. 51 (2003) 4379.
[13] R. Ahmed, N. Faisal, S. Knupfer, A. Paradowska, M. Fitzpatrick, K.A. Khor, J. Cizek, Mater. Sci. Forum 652 (2010) 309.
[14] R.C. McCune, W.T. Donlon, O.O. Popoola, E.L. Cartwright, J. Therm. Spray Technol. 9 (2000) 73.
[15] V.K. Champagne, The Cold Spray Materials Deposition Process: Fundamentals and Applications, Woodhead publishing, Abington, 2007.
[16] T. Stoltenhoff, C. Borchers, F. Gartner, H. Kreye, Surf. Coat. Technol. 200 (2006) 4947.
[17] P. Fauchais, J. Phys. D. Appl. Phys. 37 (2004) R86.
[18] V.V. Sobolev, Mater. Lett. 36 (1998) 123.
[19] Y. Tan, A. Shyam, W.B. Choi, E. Lara-Curzio, S. Sampath, Acta Mater. 58 (2010) 5305.
[20] A. Migliori, J.L. Sarrao, W.M. Visscher, T.M. Bell, L. Ming, Z. Fisk, R.G. Leisure, J. Phys. Rev. B Condens. Matter 183 (1993) 1.
[21] R.G. Leisure, F.A. Willis, J. Phys. Condens. Matter 28 (1997) 6001.
[22] P. Sedlak, H. Seiner, J. Zidek, M. Janovska, M. Landa, Exp. Mech. 54 (2014) 1073.
[23] P. Sedmak, H. Seiner, P. Sedlak, M. Landa, R. Musalek, J. Matejicek, Surf. Coat. Technol. 232 (2013) 747.
[24] A.S. Nowick, B.S. Berry, Anelastic Relaxation in Crystalline Solids, Academic Press, New York, 1972.
[25] N. Margadant, J. Neuenschwander, S. Stauss, H. Kaps, A. Kulkarni, J. Matejicek, G. Rossler, Surf. Coat. Technol. 200 (2006) 2805.
[26] H. Waki, S. Kubo, H. Ogi, A. Kobayashi, Trans. Jpn. Soc. Mech. Eng. A 762 (2010) 151.
[27] H. Seiner, L. Bodnarova, P. Sedlak, M. Janecek, O. Srba, R. Kral, M. Landa, Acta Mater. 58 (2010) 235.
[28] J. Cizek, H. Seiner, R. Huang, M. Landa, I. Dlouhy, Proceedings of the ITSC, 353ASM International, Long Beach, USA, 2015.
[29] G. Sundararajan, N.M. Chavan, S. Kumar, J. Therm. Spray Technol. 22 (2013) 1349.
[30] H. Lee, H. Shin, S. Lee, K. Ko, Mater. Lett. 62 (2008) 1579.
[31] H.J. Kim, Y.G. Kweon, Thin Solid Films 342 (1999) 201.
[32] F. Kroupa, J. Therm. Spray Technol. 16 (2007) 84.
[33] D. Schneider, T. Schwarz, Thin Solid Films 224 (1993) 177.
[34] Y. Zou, (Ph.D. thesis), McGill University, Montreal, 2010.
[35] Y. Zou, W. Qin, E. Irissou, J.G. Legoux, S. Yue, J.A. Szpunar, Scr. Mater. 61 (2009) 899.
[36] S.X. McFadden, R.S. Mishra, R.Z. Valiev, A.P. Zhilyaev, A.K. Mukherjee, Nature 396 (1998) 684.
[37] M.A. Meyers, A. Mishra, D.J. Benson, Prog. Mater. Sci. 51 (2006) 427.
[38] N.Q. Chinh, P. Szommer, Z. Horita, T.G. Langdon, Adv. Mater. 18 (2006) 34.
[39] R.Z. Valiev, A.V. Sergueeva, A.K. Mukherjee, Scr. Mater. 49 (2003) 66.
[40] A. Briggs, Acoustic Microscopy, Claredon Press, Oxford, 1992.
[41] M. Koller, P. Sedlak, H. Seiner, M. Sevcik, M. Landa, J. Straska, M. Janecek, J. Mater. Sci. 50 (2015) 808.

Composites Part B 113 (2017) 44–54

Contents lists available at ScienceDirect

Composites Part B

journal homepage: www.elsevier.com/locate/compositesb

Advanced diamond-reinforced metal matrix composites via cold spray: Properties and deposition mechanism

Shuo Yin [a, *], Yingchun Xie [b], Jan Cizek [c], Emmanuel J. Ekoi [d], Tanvir Hussain [e], Denis P. Dowling [d], Rocco Lupoi [a, **]

[a] Trinity College Dublin, The University of Dublin, Department of Mechanical and Manufacturing Engineering, Parsons Building, Dublin 2, Ireland
[b] Université Bourgogne Franche-Comté, Université de technologie Belfort-Montbéliard, LERMPS, 90010, Belfort, France
[c] Netme Centre, Institute of Materials Science and Engineering, Brno University of Technology, Technicka 2896/2, 616 69, Brno, Czechia
[d] University College Dublin, School of Mechanical and Materials Engineering, Belfield, Dublin 4, Ireland
[e] University of Nottingham, Division of Materials, Mechanics and Structure, Nottingham NG7 2RD, UK

ARTICLE INFO

Article history:
Received 7 November 2016
Received in revised form
16 December 2016
Accepted 8 January 2017
Available online 9 January 2017

Keywords:
Kinetic spray
Microstructure
Tribology
Finite element analysis
Modeling

ABSTRACT

Diamond-reinforced metal matrix composites (DMMC) have great potential for wear-resistance applications due to the superior hardness of the diamond component. Cold spray as an emerging coating technique is able to fabricate coatings or bulk materials without exceeding the material melting point, thereby significantly lowering the risk of oxidation, phase transformation, and excessive thermal residual stress. In this paper, thick DMMC coatings were deposited onto aluminum alloy substrate via cold spray of three feedstock powders: copper-clad diamond and pure copper, and their mixtures. It was found that, due to its low processing temperature, cold spray is able to prevent graphitization of the diamond in the DMMC coatings. Further to that, the original diamond phase was almost completely retained in the DMMC coatings. In case of the coatings fabricated from copper-clad diamond powders only, its mass fraction reached 43 wt%, i.e. value higher than in any previous studies using conventional pre-mixed powders. Furthermore, it was found that the added copper content powders acted as a buffer, effectively preventing the fracture of the diamond particles in the coating. Finally, the wear test on the coatings showed that the cold sprayed DMMC coatings had excellent wear-resistance properties due to the diamond reinforcement.

© 2017 Elsevier Ltd. All rights reserved.

1. Introduction

Diamond is known to possess extremely high hardness, allowing it to be used as an excellent wear-resistance material. However, for the same reason, it is difficult to be machined, which in turn limits its direct applications. To overcome the limitations, diamond is normally applied in a form of thin, wear-resistant coatings. Chemical vapor deposition (CVD) technique can be used to produce such films. However, CVD films are restricted in terms of thickness, frequently suffer from low toughness, and tend to crack or peel off completely from the substrate due to the large thermal and residual stress generated during their solidification [1,2].

Diamond-reinforced metal matrix composites (DMMC) are novel materials in which the metallic phase acts as a binder (yielding the DMMC deformable and machinable), while the reinforcement diamond phase helps to improve the material properties. Currently, the common ways to fabricate bulk DMMC are powder metallurgy [3–7] and pressure infiltration techniques [8–12]. These methods mostly require extremely high processing temperatures to melt the metal binder, thereby significantly increasing the risk of the metal phase transformation and diamond graphitization, which, in turn, may potentially yield inferior material performance [5]. In terms of DMMC thin films for wear-resistance applications, various thermal spray techniques such as oxy-acetylene thermal spray [13–15], HVOF [15], supersonic laser deposition [16,17], and laser cladding [17] were applied. Analogous to the powder metallurgy and pressure infiltration techniques for producing bulk DMMC, these thermal spray techniques also require high working temperatures and the films/coatings therefore potentially face identical problems (in particular, graphitization of the diamond content [17]). Higher diamond contents in the

---

* Corresponding author.
** Corresponding author.
E-mail addresses: yins@tcd.ie (S. Yin), lupoir@tcd.ie (R. Lupoi).

http://dx.doi.org/10.1016/j.compositesb.2017.01.009
1359-8368/© 2017 Elsevier Ltd. All rights reserved.

coatings is known to improve the coating wear-resistance by reducing the wear rate [13]. However, in the thermally sprayed coatings, the diamond content is usually much lower than the binder phase content. Combined, these disadvantages significantly lower the wear-resistance properties of the thermally sprayed DMMC coatings. Therefore, it is rather meaningful to develop a novel fabricating method of DMMC coatings that would avoid the risk of diamond phase graphitization and simultaneously retain high diamond contents.

Cold spray as an emerging coating technique is capable to deposit metals, MMC [18–20] and even ceramics [21,22], thereby attracting great interests over the last decades [23]. In this process, feedstock materials in the form of micron-sized powders are accelerated by a supersonic gas passing through Laval nozzle, and subsequently impact onto a substrate to form the coating [24–28]. During the deposition process, the feedstock remains solid state without any melting; the coating is formed through a metallurgical or mechanical bonding at the interface of adjacent particles and coating/substrate. Thereby, difficulties and defects such as oxidation, detrimental thermal residual stress development, and phase transformations which commonly appear in powder metallurgy, pressure infiltration, or thermal spray processes can be considerably avoided [29]. Furthermore, the coatings in cold spray can be deposited onto various substrates (such as metals, polymers, ceramics) and the respective thickness growth is almost unlimited for most metals and MMC, allowing cold spray to act as an additive manufacturing technique for producing bulk materials [30,31].

To date, very few attempts of cold spray of DMMC coatings for improving the hardness and Young's modulus have been carried out [32,33]. The state of the art suggests that the limitation for fabricating DMMC (also applicable for other MMC) via cold spray is the feedstock powders. Typically, either mechanically pre-mixed or ball milled feedstock is used. However, using the pre-mixed powders frequently leads to a reduction of the diamond phase content in the coating as compared to the original feedstock due to its low deposition efficiency, while the ball-milling procedure in turn results in a serious fracture of the diamond phase or its graphitization [32,33]. Aside from reducing the cost efficiency of the process through the loss of diamond powder in such case, the coating performance is significantly lowered, too [16,17,34].

In this paper, DMMC coatings were fabricated via cold spray technique. In order to avoid the disadvantages and problems associated with using the conventional pre-mixed or ball-milled feedstock, a novel copper-clad diamond powder (and its mixture with copper powder) was used as the feedstock to fabricate the coatings instead. In the previous work, this copper-clad diamond powder has been proven to significantly increase the diamond contents in the coating [35]. As the base material, copper was selected due to its ease of deposition and high deposition efficiency, allowing it to be an excellent binder in the MMC coatings. Wear test of the fabricated DMMC coatings was further carried out to investigate the coating wear-resistance capability. With copper not being a typical wear-resistance metal, the results better reflect the role of the diamond reinforcement. In the future work, using typical wear-resistance metals such as cobalt and nickel is planned.

2. Experimental methodology

2.1. Coating fabrication

Pure copper (−38 + 15 μm, > 99.9%, Safina, Czech Republic) and copper-clad diamond (−53 + 45 μm, PDA C50, Element-Six, Ireland) powders and their respective mixtures were used as the feedstock. Fig. 1a–b shows the morphology of both powders observed by SEM (Carl Zeiss ULTRA, Germany). The copper-clad

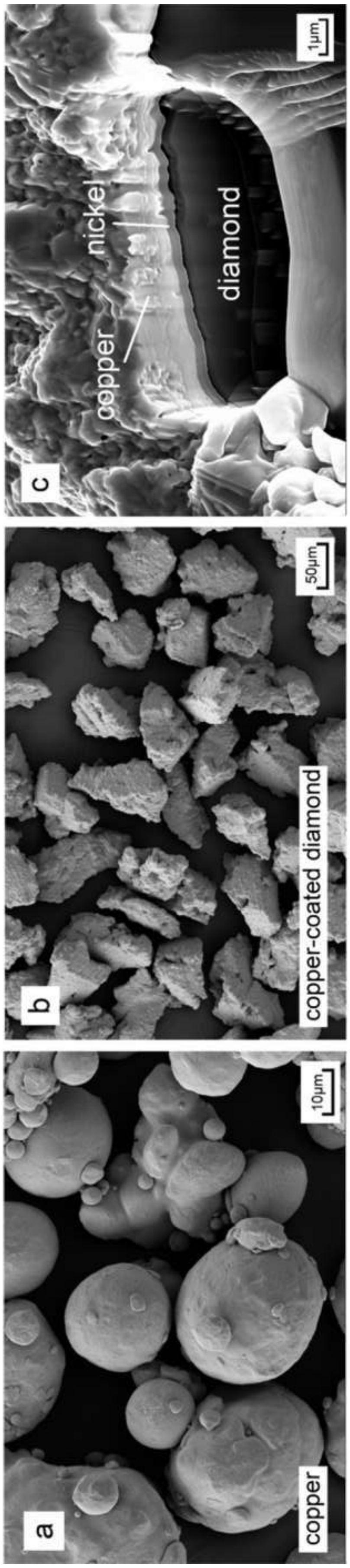

Fig. 1. Morphology of the (a) copper and (b) copper-clad diamond powders used in this study. (c) cross-section of typical copper-clad diamond particle.

diamond powder particles typically consist of three different layers: a diamond core enclosed in a thin nickel inter-layer and an outside electroless copper cladding, as can be seen from the powder cross-section shown in Fig. 1c (FIB, DB235, FEI Strata, USA). The nickel inter-layer is used due to its superior bonding with diamond as compared to copper. According to the supplier, the weight ratio of the diamond phase to both metals in a single particle is approximately 1:1, and thus the diamond core diameter was calculated as roughly between 40 and 47 μm.

The annotation of the produced coatings as well as the respective feedstock information and cold spray deposition conditions are provided in Table 1. The benchmark coating denoted as 'P0' was fabricated from pure copper powder only, i.e., no copper-clad diamond phase was present. The coatings were deposited onto common aluminum alloy substrates using an in-house cold spray system (Trinity College Dublin, Ireland). The system consists of high pressure nitrogen/helium gas from cylinders, gas heater, powder feeder, CNC working platform for controlling the substrate movement, Laval nozzle and a computer control system. In this work, nitrogen was used to produce P0 coating under previously optimized parameters, while helium was applied to produce the DMMC coatings. Each coating was fabricated with two gun passes at a

Table 1
Annotation of the produced coatings, the respective feedstock composition and cold spray deposition conditions.

Coating	Feedstock powders	Gas	Pressure [MPa]	Temperature [°C]	Gun speed [mm/s]	Standoff distance [mm]
P0	Copper	N_2	3.0	350	15	45
P1	Copper + copper-clad diamond (8:1 by weight)	He	2.0	25	15	45
P2	Copper + Copper-clad diamond (1:1 by weight)	He	2.0	25	15	45
P3	Copper clad diamond	He	2.0	25	15	45

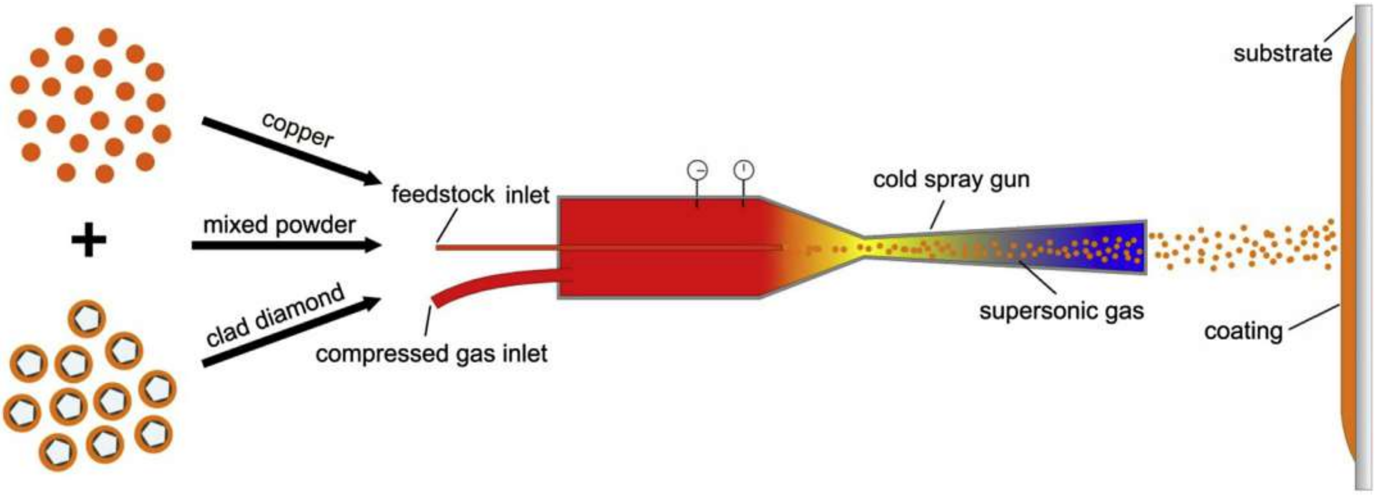

Fig. 2. Schematic of the DMMC coating fabrication via cold spray.

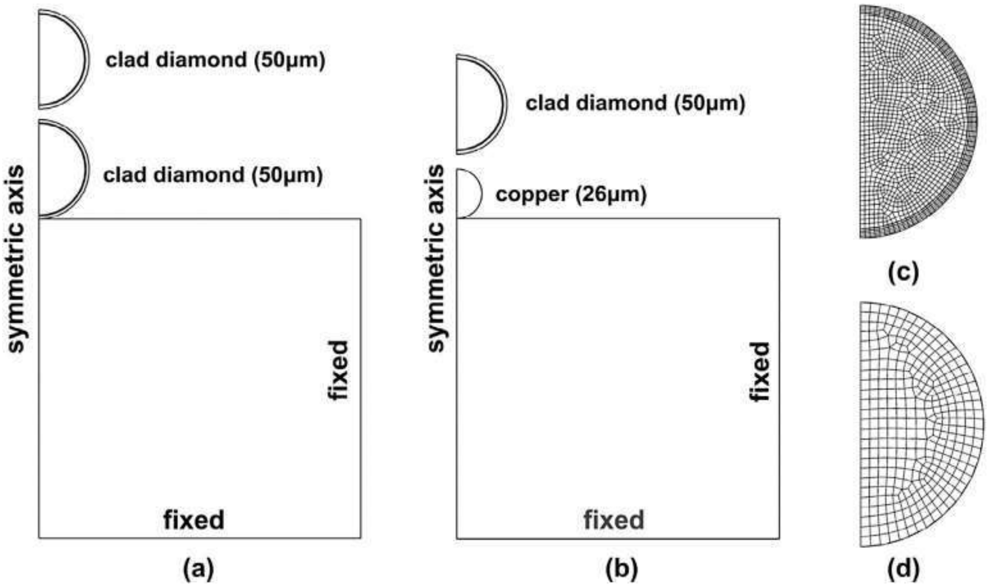

Fig. 3. Computational domain, meshing and boundary conditions of the FEA two-particle subsequent impact model. (a) two copper-clad diamond particles, (b) copper and copper-clad diamond particles, (c) mesh for copper-clad diamond powder and (d) mesh for copper powder.

robot arm traversal speed of 15 mm/s. A schematic of the cold spray coating fabrication process is shown in Fig. 2.

2.2. Materials characterization

To examine the phase content and the prospective graphitization of the diamond during the coating fabrication process, the as-sprayed coatings were examined by an X-Ray diffractometer (Siemens D500, Germany) with the Co ($\lambda = 1.789$ Å) source at a current of 40 mA, voltage of 35 kV and scan step of 0.02°. To assess the coating microstructure via SEM, the as-sprayed coating samples were prepared using standard metallographic procedures with the final polishing applied by 0.05 μm Al_2O_3 solution. Fracture surface was also obtained by breaking the as-sprayed samples and then observed by SEM. The element analysis (primarily, the mass fractions of Cu and Ni) on the coating surfaces and polished cross-sections was performed with an EDS unit (Oxford Instruments INCA system, UK) equipping on the SEM system. Given its inaccuracy in measuring low molecular weight elements, the mass fraction of diamond was then calculated based on the results of copper and nickel. For each sample, five locations were randomly selected from the coating surface or polished cross-section and the measured data was then averaged.

2.3. Wear test

The wear properties were measured using POD-2 pin-on-disc system (Teer Coatings Ltd., UK) at room temperature. For accurate measurement of the wear rates, the sample surfaces were polished using Al_2O_3 solution to 1 μm roughness prior to the test and the samples were then mounted on a carrier disc. A tungsten carbide ball with a diameter of 5 mm was used as a counterpart under a constant load of 4 N. The disk rotated at a linear speed of 10 mm/s for 15000 revolutions. To determine the coating and pin ball wear rates, the material volume loss was calculated according to ASTM G 99 standard [26]. The amount of wear was determined by weighing the specimens before and after the test. The respective wear rate was then calculated as the volume loss per unit load and per traverse distance.

It was reported that the mean free path between reinforcement particles is an important parameter affecting the coating wear-resistance property [25,36,37]. The mean free path was calculated by drawing a total of 10 random lines on multiple coating cross-sectional images and counting the number of intersects with diamond particles. Then, the mean free path could be calculated according to the following equation:

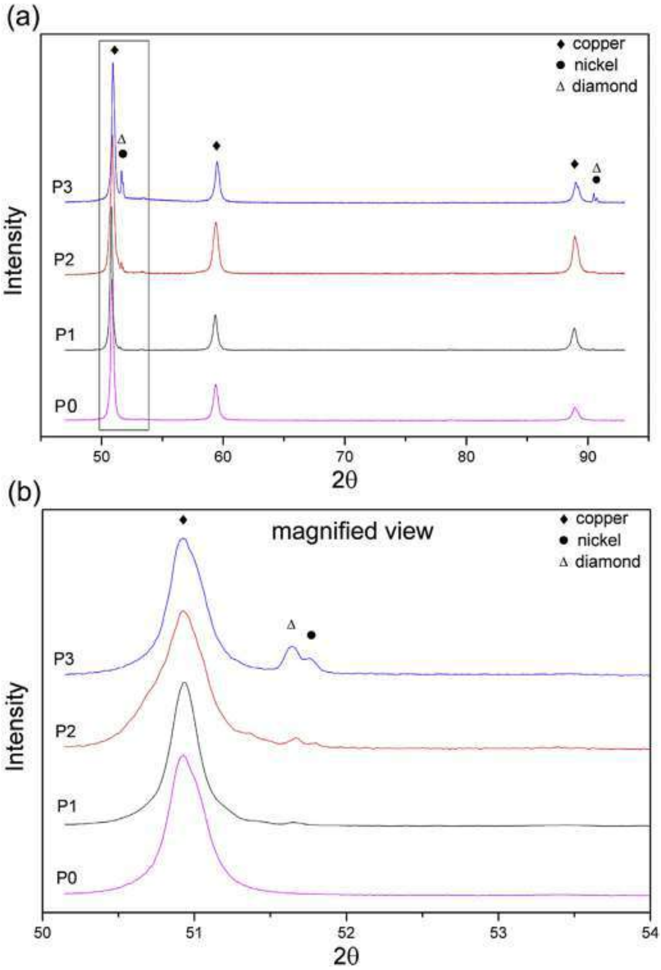

Fig. 5. Comparison of the XRD spectra of the produced P0-P3 coatings (a) and local magnified view marked by black square in Fig. 5a (b). Note the increasing content of Ni and diamond phases toward P3.

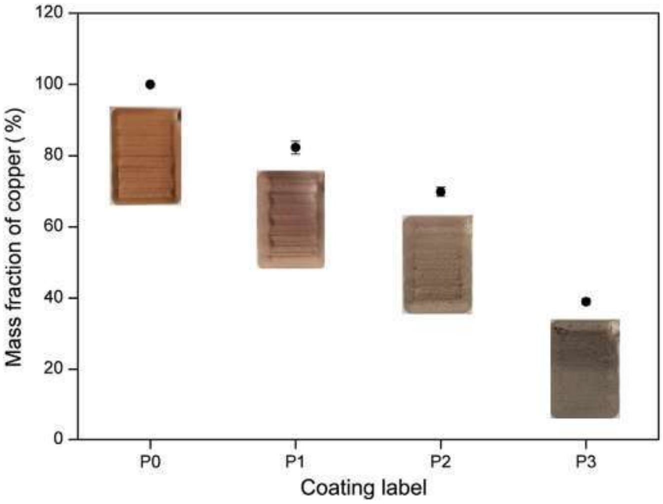

Fig. 4. Copper content (wt%) on the P0-P3 coating surfaces as determined by EDS.

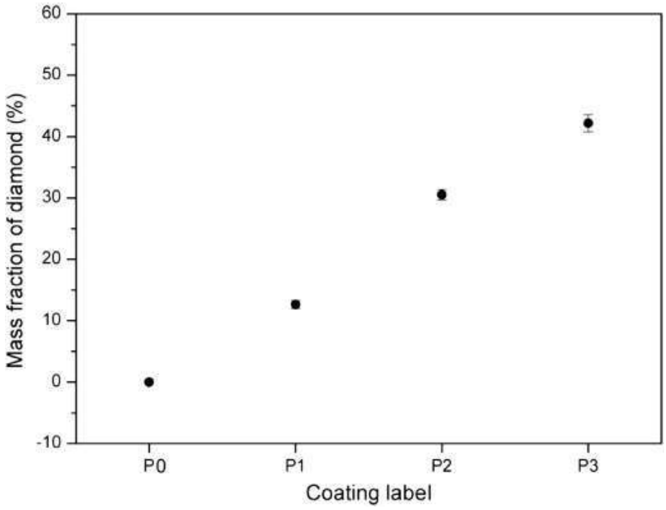

Fig. 6. Mass fraction of diamond on the coating cross-section.

$$\lambda = \frac{1 - V_p}{N_L} \tag{1}$$

where N_L is the number of diamond particle intercepts per unit length of test line and V_p is the volume fraction of the reinforcing particles.

3. Numerical methodology

In order to study the powder particles deposition behavior during the coating formation process, finite element analysis (FEA) of the inter-particle impact was carried out using ABAQUS. The impact process was simplified as two particles successively depositing on the substrate in the same line. The contact pressure between the two particles was then calculated and compared with the diamond fracture stress to evaluate the diamond fracture behavior in the coating. Lagrangian algorithm with the dynamic explicit procedure was applied to build the computational model. The aluminum alloy substrate was defined as a cylinder, having a diameter and height of 320 and 160 μm, respectively. Based on the average size of the powders used in the experiment, the copper particle was defined as a sphere with a diameter of 26 μm. For the preliminary evaluation, the irregular copper-clad diamond powder was simplified as a sphere of an equivalent diameter of 50 μm. Of that, the diameter of the diamond core and the thickness of the

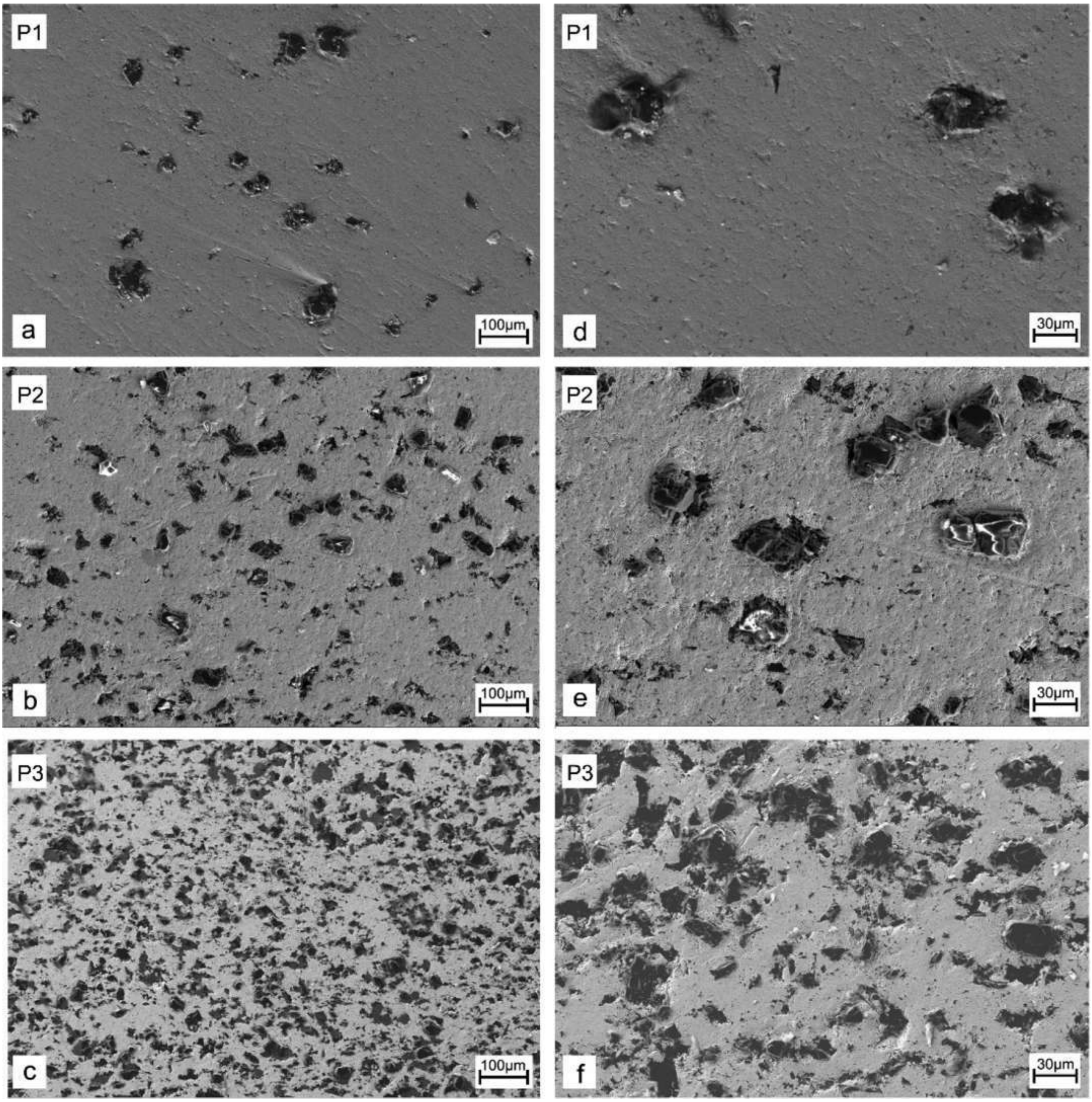

Fig. 7. Microstructure of the produced P1 (a,d), P2 (b,e), and P3 (c,f) cold sprayed coatings.

nickel inter-layer and copper cladding were defined as 44.5, 0.4 and 2.4 μm, respectively, in accordance with the composition information of the real powder. The metal materials including nickel, copper and aluminum alloy were modeled using Johnson and Cook plasticity model [38]. The diamond was considered as a linear elastic model with high elastic modulus [39]. The model inherently does not allow considering the fracture of the diamond, but the maximum contact pressure between the particles can be obtained. Detailed materials parameters applied to both models can be found elsewhere [39,40]. Fig. 3 shows the computational domain, meshing and boundary conditions of the used FEA model. Due to its symmetric character, the model was simplified as axisymmetric in order to reduce the computational time. The geometry was partitioned by four-node bilinear axisymmetric quadrilateral elements with reduced integration and hourglass control (CAX4R). The axisymmetric condition was applied to the axis and the fixed boundary condition was enforced to the bottom and lateral. The contact process was implemented by using the surface-to-surface penalty contact algorithm with balanced contact pair formulation. The particle impact velocities for copper and copper-clad diamond at the applied spray conditions (Table 1) and nozzle geometries were calculated as 600 m/s and 480 m/s in a separate study (ANSYS-FLUENT 14.1 [41]).

The used FEA model inherently does not comprehend all experimental details and differs from reality in several aspects, such as in-line impact, spherical particles or not taking into account the potential out-of-equilibrium conditions of the particle materials arising from their fabrication routes (such as e.g. cold working, internal stresses, etc). As such, the model could not work (and was not used) to properly explain e.g. the deformation mechanisms or materials flow. However, the model's features suffice to achieve the main aim, i.e. to calculate the level of stresses achieved at the contact and compare those with the diamond fracture stress values.

4. Results and discussion

4.1. Chemical and phase transformations of DMMC coatings

The cold sprayed coatings thickness exceeded 5 mm in all cases, i.e. order of magnitude higher than what is possible to obtain using vapor deposition processes. As the mass fraction of the copper-clad diamond feedstock increased (i.e., the copper content decreased, from P0 to P3), the coating color changed from copper red to gray. Fig. 4 shows the copper content on the P0-P3 coating surfaces as determined by EDS as well as the corresponding sample appearance.

Graphitization of the diamond frequently occurs when fabricating the DMMC via sintering, infiltration or thermal spray techniques due to the high processing temperatures [4,5,16,17]. The obtained XRD spectra in Fig. 5 showed no graphite peaks, indicating that no graphitization occurred during the fabrication of the cold sprayed DMMC. This fact clearly shows the advantage of cold spray over the other fabrication techniques in preventing diamond graphitization. Moreover, the spectra presented in Fig. 5 further suggested an increasing content of nickel and diamond phases from P1 to P3. This was supported by EDS cross-section analysis of the diamond content (Fig. 6). The coating P3 that was fabricated from copper-clad diamond powder only (50 wt% of diamond phase) contained 43 wt% diamond, suggesting its fairly high deposition efficiency in the process. In our previous work, even higher value of 56 wt% was obtained by the EDS measurements. However, it is rather safe not to attribute the difference to a change in deposition efficiency as the higher value was obtained from coating fracture (i.e., not polished) surfaces [35]. In the previous cold spray works where mechanically pre-mixed metal and diamond powders were used as the feedstock [34,42,43], most of the diamond could not successfully deposit and thus the diamond mass fraction in the coatings was generally low. The diamond fraction obtained in our works is higher than in any previous studies using conventional pre-mixed powders. The excellent performance of the copper-clad diamond powder clearly indicates that it is a promising feedstock for fabrication of cold sprayed DMMC coatings.

4.2. DMMC coating microstructure

Fig. 7 shows the cross-sectional features of the DMMC coatings fabricated using different powders. It is known that a uniform distribution of the reinforcement phase in the MMC is of great

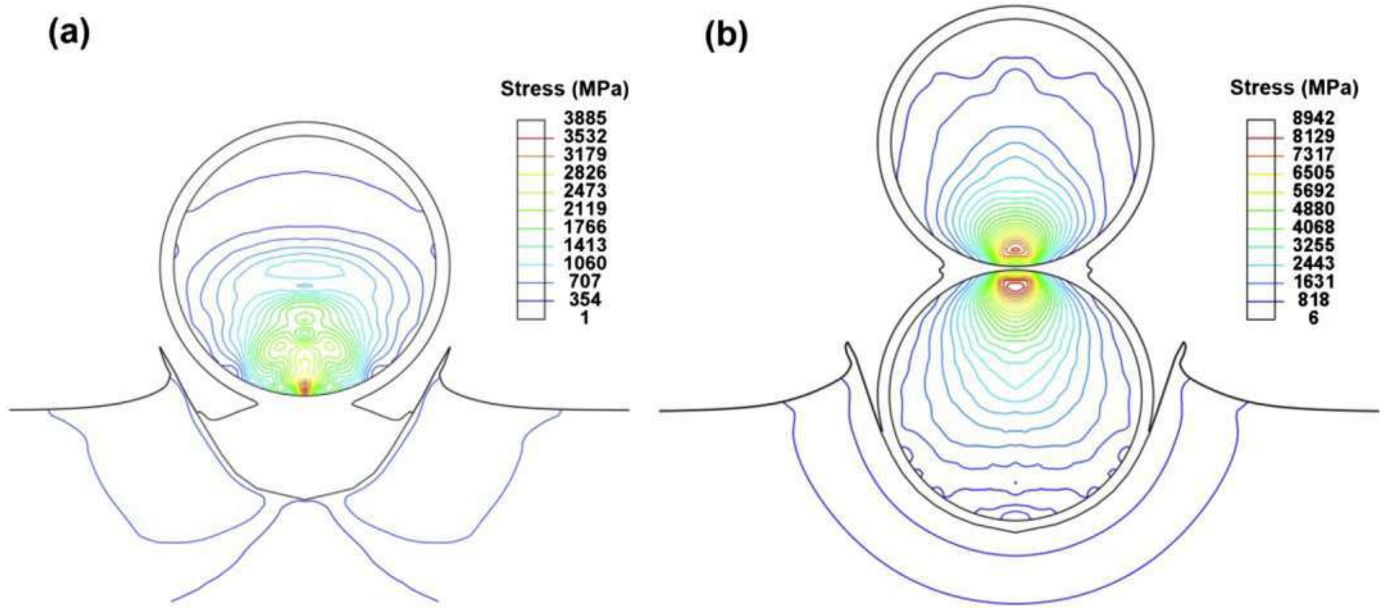

Fig. 8. FEA modeling results of the stress distribution at the moment of particle-particle impact with the inlet pressure of 2.0 MPa and helium as the propulsive gas. (a) copper-clad diamond onto copper, (b) copper-clad diamond onto copper-clad diamond.

importance to the final materials properties [44–46]. In this work, the cold sprayed DMMC coatings fabricated with the copper-clad diamond powders exhibited excellent uniformity, providing an essential condition for the high-quality materials properties. Besides, an obvious difference in the diamond mass fraction between each sample can be seen. The observed diamond contents in the coatings (P3 > P2 > P1) were well consistent with the EDS element analysis shown in Fig. 6.

The magnified images of the cross-section provided in Fig. 7d–f illustrate the diamond particles sizes in the produced coatings. Most of the diamond in the coating fabricated with the P1 and P2 powders had a diameter of approximately 40 μm. This value was quite comparable to the diamond core diameter of original feedstock (−47 + 40 μm), which indicated that diamond did not exhibit substantial fracturing during deposition. In fact, the diamond phase in P1 exhibited almost no damage, while few cracks and several small diamond shards only could be found in P2. Assumedly, the matrix consisting of the free copper powder particles provided ductile component absorbing the impact energy and thereby effectively preventing the diamond phase fragmentation. However, in the case of P3 coating, which was fabricated entirely using copper-clad diamond powder only, the diamond phase was considerably smaller, containing a large number of diamond shards with a diameter of less than 10 μm, suggesting the occurrence of fracturing. Despite the fracture, previous works reported that tiny shards or fine particles may improve the toughness of cold sprayed composite coating [19,20].

For well explaining the reason for inducing diamond fracture behavior in the pure copper-clad diamond coating, Fig. 8 shows the predicted stress distribution at the moment of (i.e., at the precise moment when the nominal stress reaches its maximum during the entire process) a copper-clad diamond powder impact (onto either copper or copper-clad diamond particles), with room-temperature helium under 2.0 MPa pressure as the propellant gas (i.e., identical to spraying conditions). For P1 and P2 coatings, the soft copper particles could act as a ductile matrix to the copper-clad diamond particles, dissipating most of the impact kinetic energy through the plastic deformation of copper. The predicted maximum impact stress in such case (Fig. 8a) reached almost 3900 MPa, i.e. significantly lower than the diamond fracture stress calculated elsewhere (5900 MPa, [39]). Therefore, the impacting stress was unlikely to damage the diamond in case of impact into the copper matrix. The minor fragmentation of the diamond phase observed in P2 coatings (considerably lower than in P3 coatings, nevertheless; cf. Fig. 7e–f) could be caused by a prospective diamond-diamond contact given its higher content as compared to P1 coating. For P3, the outside metal cladding was very thin and most of the energy was directly imposed on the inner diamond cores due to the absence of softer buffer materials. The impact stress reached 8900 MPa (Fig. 8b). In this case, most of the diamond was certainly fractured during the deposition, in accordance with the observed microstructure (Fig. 7c,f).

To further observe the coating microstructure and clarify the diamond phase behavior, coating fracture surfaces were observed using SEM (Fig. 9). The diamond particles in P1 coating were complete without any visible signs of damage, while the P2 coatings contained both undamaged and slightly damaged diamonds. However, for the P3 coating shown in Fig. 9c, the diamond phase observed a frequent cracking, producing small diamond shards surrounding the parent particles. In such cases, bonding occurred between the thin copper claddings only and the coating was formed through the fractured diamond sub-particles uniformly dispersing into the metal phase [35].

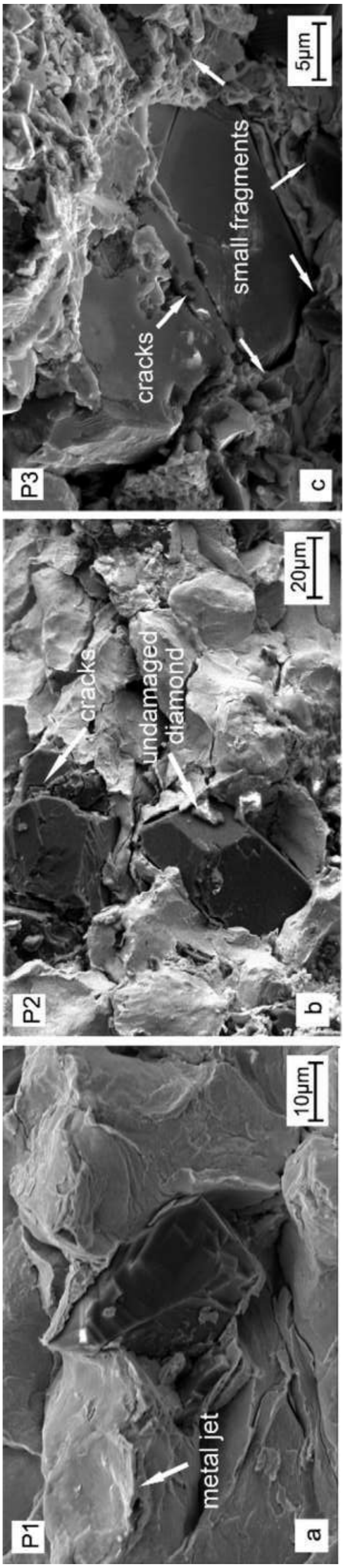

Fig. 9. Fracture surfaces of the produced P1-P3 coatings and the respective diamond phase fragmentation behavior.

4.3. *Coatings deposition mechanisms*

Following the coating microstructure analysis, the following deposition mechanisms are suggested herein. Fig. 10 shows the schematic of the deposition mechanisms for different coating types. For the coatings produced using a mixture of copper and copper-clad diamond particles (Fig. 10a), the copper-clad diamond particles have a limited chance to impact with each other only. Instead, they mostly impact onto copper and, as a result, the metallic bonding in the coating mainly occurs between the copper particles only or between the copper claddings of the diamond cores and copper particles. In addition, as the energy caused by the high-velocity impact is mostly transformed into the plastic deformation of copper, the impact stress imposed on the diamond phase does not reach its fracture stress threshold and the entire diamond content therefore uniformly embeds and distributes in the copper phase.

For the copper-clad diamond coatings (Fig. 10b), pure copper particles are absent in the deposition process, leading to impacts of the copper-clad diamond particles with each other directly. Then, the metallic bonding in the coatings only takes place between copper claddings. Although the copper cladding dissipates part of the kinetic energy through plastic deformation, it is too thin (2–5 μm) to act as a buffer. Most of the kinetic energy is dissipated via the interaction between the diamond cores rather than the plastic deformation of the copper part. As a consequence, the impact stress imposed onto the diamond is large, exceeding the diamond fracture stress, as discussed in the last section. Diamonds hence fracture into shards during the deposition and disperse into the copper phase to form the DMMC.

4.4. *Coatings wear test*

The DMMC coatings experienced almost no wear during the test. Instead, the tungsten carbide pin ball counterpart exhibited signs of damage. Also, a large amount of black debris worn from the tungsten carbide pin ball was left on the worn track after the testing. As the debris surely affected the sample weight, the coating wear rate measurement could not be taken as valid from this test. Fig. 11 provides the measured wear rate of the tungsten carbide pin ball as a function of the calculated mean free path. It is clearly seen that the mean free path decreased from P1 to P3, while the wear rate of the pin ball increased gradually. This fact indicated that the coating wear-resistance performance steadily improved as the mean free path decreased, in good agreement with the previous work [37]. The wear rate of the pure copper coating was also measured for comparison reason. The copper coating was found to exhibit significant wear after the test with the wear rate of 0.0077 mm^3/N.mm while the pin ball did not experience any significant signs of damage. The comparison clearly indicates the importance of the diamond reinforcements in improving the coating wear-resistance properties. Moreover, in the previous works related to cold sprayed wear-resistance coatings (e.g., Al5056/SiC [47], CuSn8/AlCuFeB [48]), materials loss normally occurred on the coating surface, while the wear of WC-Co pin ball was not reported. This fact further suggests the excellent wear-resistance properties of the cold sprayed DMMC coatings obtained in this work.

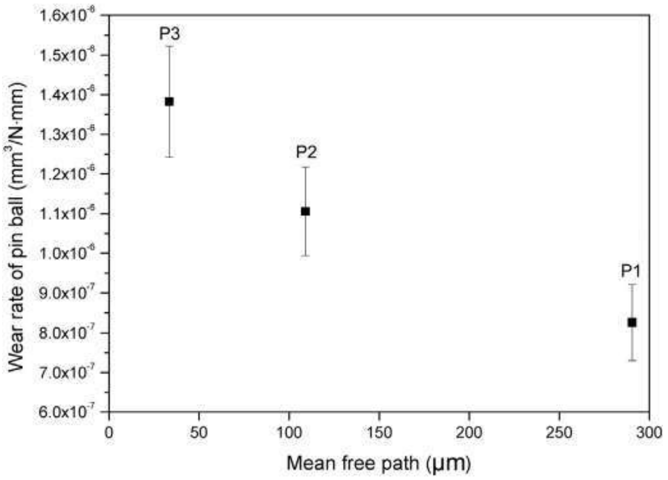

Fig. 11. Experimentally measured wear rate of the tungsten carbide pin ball against mean free path between diamond particles in the respective produced DMMC coatings.

To further investigate the coating wear mechanism, the worn surfaces are provided in Fig. 12. For the pure copper coating (P0), the worn surface was characterized by smooth profile with slight signs of delamination only. For P1 (having the lowest content of the diamond phase among P1-P3), tungsten carbide film worn off from the pin ball was detected on the worn surface. Also, the diamonds

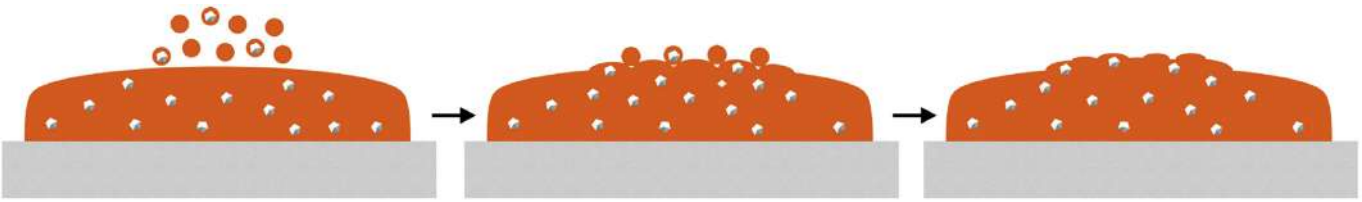

(a) Copper-clad diamond+copper

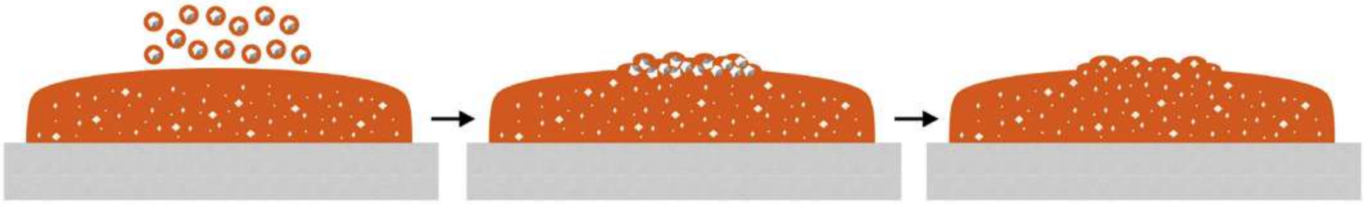

(b) Copper-clad diamond

Fig. 10. Schematic of the deposition mechanisms for (a) copper-clad diamond + copper coating and (b) copper-clad coating.

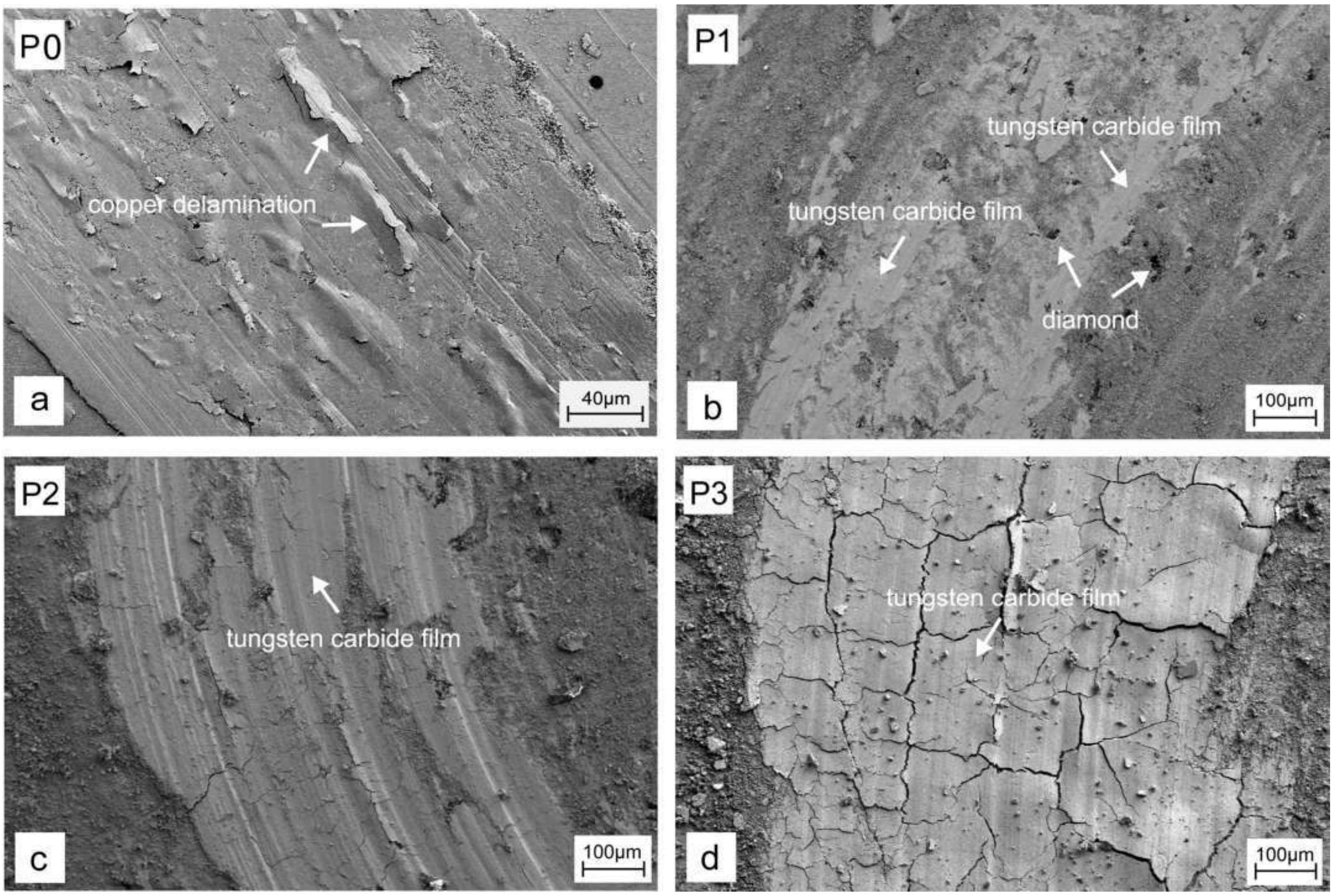

Fig. 12. SEM images of the worn surface of the cold sprayed P0-P3 coatings.

were not removed from but rather remained embedded in the P1 coating. They prevented the pin ball from wearing the metal phase of the coating, but led to the serious abrasion of pin ball. With the pin ball continuously sliding on the coating surface, the tungsten carbide debris formed a thin film on the worn surface. As the diamond contents increased (P2), the area of the tungsten carbide film became larger (i.e., increased pin ball abrasion), lowering the area of the exposed coating materials. Therefore, the wear rate of the pin ball was higher than that of P1. In the case of P3 fabricated with copper-clad diamond powder only, a large amount of diamond resulted in the entire worn surface covered by the black and thick tungsten carbide film without any exposure of the underlying coating material whatsoever. The wear rate of the pin ball was therefore the highest in all tests. It is known that copper is not a typical material for wear-resistance coating due to its relatively low hardness [27]. Therefore, it is plausible to suggest that the wear-resistance capability of the produced DMMC is attributed to the diamond reinforcements. The performed wear test results clearly indicate the great potential of cold spray technique for producing wear-resistance DMMC coatings.

5. Conclusions

In this paper, a range of diamond-reinforced metal matrix composites (DMMC) were fabricated via cold spray using copper-clad diamond powder or its mixture with pure copper powder. Copper-clad diamond is a novel powder consisting of an inside diamond powder, a thin interbedded nickel layer and an outside electroless copper cladding. The sprayed DMMC coatings fabricated using different powders had thickness exceeding 5 mm, i.e. order of magnitude thicker than those typically produced by chemical vapor deposition (CVD) processes. Due to the low working temperature, the coatings exhibited no phase transformations. In the coatings fabricated from the mixed feedstock of copper and copper-clad diamond, the additional copper powders acted as a buffer, dissipating most of the kinetic energy through the plastic deformation of copper, thereby effectively preventing the fracture of the diamond phase in the coatings. When using pure copper-clad diamond powder as the feedstock only, the impact stress imposed on the diamonds exceeded the diamond fracture stress, leading to a frequent diamond phase fragmentation during the deposition. The pure copper-clad diamond coating was then formed through the bonding between the copper claddings only and the fractured diamond uniformly dispersed into the metal phase. In all coatings, the diamond in the feedstock was fully transferred from the feedstock, with negligible losses only (e.g., reduction from 50 wt% to 43 wt% in the copper-clad diamond coating) – a results never achieved in the previous cold spray works with conventional premixed powders.

Finally, the wear test on the DMMC coating clearly showed that the cold sprayed DMMC coating had superior wear-resistance properties. With copper not being a typical wear-resistance metal, the results clearly reflect the role of the diamond reinforcement in improving the wear-resistance capability. In the future works, copper may be replaced by other wear-resistance metals, such as e.g. cobalt and nickel.

Acknowledgments

The authors would like to thank the CRANN Advanced Microscopy Laboratory (AML) of Trinity College for the support in the analysis; and the European Space Agency and Enterprise Ireland for the contribution, and Dr. Barry Aldwell from Trinity College for the support in the experiment. The work was also supported by the Czech Science Foundation project GACR 13-35890S.

References

[1] Wan BQ, Sun XY, Ma HT, Feng RF, Li YS, Yang Q. Plasma enhanced chemical vapor deposition of diamond coatings on Cu—W and Cu—WC composites. Surf Coat. Technol 2015;284:133—8. http://dx.doi.org/10.1016/j.surfcoat.2015.06.079.

[2] Qin F, Chou YK, Nolen D, Thompson RG. Coating thickness effects on diamond coated cutting tools. Surf Coat. Technol 2009;204:1056—60. http://dx.doi.org/10.1016/j.surfcoat.2009.06.011.

[3] Che QL, Zhang JJ, Chen XK, Ji YQ, Li YW, Wang LX, et al. Spark plasma sintering of titanium-coated diamond and copper—titanium powder to enhance thermal conductivity of diamond/copper composites. Mater Sci Semicond Process 2015;33:67—75. http://dx.doi.org/10.1016/j.mssp.2015.01.041.

[4] Abyzov AM, Kruszewski MJ, Ciupiński Ł, Mazurkiewicz M, Michalski A, Kurzydłowski KJ. Diamond—tungsten based coating—copper composites with high thermal conductivity produced by Pulse Plasma Sintering. Mater Des 2015;76:97—109. http://dx.doi.org/10.1016/j.matdes.2015.03.056.

[5] Shao WZ, Ivanov VV, Zhen L, Cui YS, Wang Y. A study on graphitization of diamond in copper-diamond composite materials. Mater Lett 2004;58:146—9. http://dx.doi.org/10.1016/S0167-577X(03)00433-6.

[6] Chu K, Liu Z, Jia C, Chen H, Liang X, Gao W, et al. Thermal conductivity of SPS consolidated Cu/diamond composites with Cr-coated diamond particles. J Alloys Compd 2010;490:453—8. http://dx.doi.org/10.1016/j.jallcom.2009.10.040.

[7] Schubert T, Ciupiński Ł, Zieliński W, Michalski A, Weißgärber T, Kieback B. Interfacial characterization of Cu/diamond composites prepared by powder metallurgy for heat sink applications. Scr Mater 2008;58:263—6. http://dx.doi.org/10.1016/j.scriptamat.2007.10.011.

[8] Abyzov AM, Kidalov SV, Shakhov FM. High thermal conductivity composite of diamond particles with tungsten coating in a copper matrix for heat sink application. Appl Therm Eng 2012;48:72—80. http://dx.doi.org/10.1016/j.applthermaleng.2012.04.063.

[9] Feng H, Yu JK, Tan W. Microstructure and thermal properties of diamond/aluminum composites with TiC coating on diamond particles. Mater Chem Phys 2010;124:851—5. http://dx.doi.org/10.1016/j.matchemphys.2010.08.003.

[10] Kang Q, He X, Ren S, Zhang L, Wu M, Guo C, et al. Preparation of copper-diamond composites with chromium carbide coatings on diamond particles for heat sink applications. Appl Therm Eng 2013;60:423—9. http://dx.doi.org/10.1016/j.applthermaleng.2013.05.038.

[11] Li J, Zhang H, Zhang Y, Che Z, Wang X. Microstructure and thermal conductivity of Cu/diamond composites with Ti-coated diamond particles produced by gas pressure infiltration. J Alloys Compd 2015;647:941—6. http://dx.doi.org/10.1016/j.jallcom.2015.06.062.

[12] Dong Y, Zhang R, He X, Ye Z, Qu X. Fabrication and infiltration kinetics analysis of Ti-coated diamond/copper composites with near-net-shape by pressureless infiltration. Mater Sci Eng B 2012;177:1524—30. http://dx.doi.org/10.1016/j.mseb.2012.08.009.

[13] Venkateswarlu K, Ray AK, Gunjan MK, Mondal DP, Pathak LC. Tribological wear behavior of diamond reinforced composite coating. Mater Sci Eng A 2006;418:357—63. http://dx.doi.org/10.1016/j.msea.2005.12.004.

[14] Richardson AF, Neville A, Wilson JIB. Developing diamond MMCs to improve durability in aggressive abrasive conditions. Wear 2003;255:593—605. http://dx.doi.org/10.1016/S0043-1648(03)00049-8.

[15] Venkateswarlu K, Rajinikanth V, Naveen T, Sinha DP, Atiquzzaman Ray AK. Abrasive wear behavior of thermally sprayed diamond reinforced composite coating deposited with both oxy-acetylene and HVOF techniques. Wear 2009;266:995—1002. http://dx.doi.org/10.1016/j.wear.2009.02.001.

[16] Yang L, Li B, Yao J, Li Z. Effects of diamond size on the deposition characteristic and tribological behavior of diamond/Ni60 composite coating prepared by supersonic laser deposition. Diam Relat Mater 2015;58:139—48. http://dx.doi.org/10.1016/j.diamond.2015.06.014.

[17] Yao J, Yang L, Li B, Li Z. Beneficial effects of laser irradiation on the deposition process of diamond/Ni60 composite coating with cold spray. Appl Surf Sci 2015;330:300—8. http://dx.doi.org/10.1016/j.apsusc.2015.01.029.

[18] Cavaliere P, Perrone A, Silvello A. Mechanical and microstructural behavior of nanocomposites produced via cold spray. Compos Part B Eng 2014;67:326—31. http://dx.doi.org/10.1016/j.compositesb.2014.07.023.

[19] Yang GJ, Gao PH, Li CJCX, Li CJCX. Simultaneous strengthening and toughening effects in WC-(nanoWC-Co). Scr Mater 2012;66:777—80. http://dx.doi.org/10.1016/j.scriptamat.2012.02.005.

[20] Yang G-J, Gao P-H, Li C-X, Li C-J. Mechanical property and wear performance dependence on processing condition for cold-sprayed WC-(nanoWC-Co). Appl Surf Sci 2015;332:80—8. http://dx.doi.org/10.1016/j.apsusc.2015.01.138.

[21] Yang GJ, Li CJ, Han F, Li WY, Ohmori A. Low temperature deposition and characterization of TiO2 photocatalytic film through cold spray. Appl Surf Sci 2008;254:3979—82. http://dx.doi.org/10.1016/j.apsusc.2007.12.016.

[22] Lee HY, Yu YH, Lee YC, Hong YP, Ko KH. Interfacial studies between cold-sprayed WO3, Y2O3 films and Si substrate. Appl Surf Sci 2004;227:244—9. http://dx.doi.org/10.1016/j.apsusc.2003.11.073.

[23] Papyrin A. Cold spray technology. Adv Mater Process 2001;159:49—51.

[24] King PC, Zahiri SH, Jahedi M. Focused ion beam micro-dissection of cold-sprayed particles. Acta Mater 2008;56:5617—26. http://dx.doi.org/10.1016/j.actamat.2008.07.034.

[25] Melendez NM, Narulkar VV, Fisher GA, McDonald AG. Effect of reinforcing particles on the wear rate of low-pressure cold-sprayed WC-based MMC coatings. Wear 2013;306:185—95. http://dx.doi.org/10.1016/j.wear.2013.08.006.

[26] Dosta S, Couto M, Guilemany JM. Cold spray deposition of a WC-25Co cermet onto Al7075-T6 and carbon steel substrates. Acta Mater 2013;61:643—52. http://dx.doi.org/10.1016/j.actamat.2012.10.011.

[27] Yin S, Wang X, Suo X, Liao H, Guo Z, Li W, et al. Deposition behavior of thermally softened copper particles in cold spraying. Acta Mater 2013;61:5105—18. http://dx.doi.org/10.1016/j.actamat.2013.04.041.

[28] Yin S, Meyer M, Li W, Liao H, Lupoi R. Gas flow, particle acceleration, and heat transfer in cold spray: a review. J Therm Spray Technol 2016;25:1—23. http://dx.doi.org/10.1007/s11666-016-0406-8.

[29] Grujicic M, Zhao CLC, DeRosset WSW, Helfritch D. Adiabatic shear instability based mechanism for particles/substrate bonding in the cold-gas dynamic-spray process. Mater Des 2004;25:681—8. http://dx.doi.org/10.1016/j.matdes.2004.03.008.

[30] Choi HJ, Lee M, Lee JY. Application of a cold spray technique to the fabrication of a copper canister for the geological disposal of CANDU spent fuels. Nucl Eng Des 2010;240:2714—20. http://dx.doi.org/10.1016/j.nucengdes.2010.06.038.

[31] Champagne VK. The repair of magnesium rotorcraft components by cold spray. J Fail Anal Prev 2008;8:164—75. http://dx.doi.org/10.1007/s11668-008-9116-y.

[32] Woo DJ, Heer FC, Brewer LN, Hooper JP, Osswald S. Synthesis of nanodiamond-reinforced aluminum metal matrix composites using cold-spray deposition. Carbon N. Y 2015;86:15—25. http://dx.doi.org/10.1016/j.carbon.2015.01.010.

[33] Woo DJ, Sneed B, Peerally F, Heer FC, Brewer LN, Hooper JP, et al. Synthesis of nanodiamond-reinforced aluminum metal composite powders and coatings using high-energy ball milling and cold spray. Carbon N. Y 2013;63:404—15. http://dx.doi.org/10.1016/j.carbon.2013.07.001.

[34] Kim HJ, Jung DH, Jang JH, Lee CH. Study on metal/diamond binary composite coatings by cold spray. Mater Sci Forum 2007;534—536:441—4. doi:10.4028, www.scientific.net/MSF.534-536.441.

[35] Aldwell B, Yin S, Mcdonnell KA, Trimble D, Hussain T, Lupoi R. A novel method for metal — diamond composite coating deposition with cold spray and formation mechanism. Scr Mater 2016;115:10—3. http://dx.doi.org/10.1016/j.scriptamat.2015.12.028.

[36] Melendez NM, McDonald AG. Development of WC-based metal matrix composite coatings using low-pressure cold gas dynamic spraying. Surf Coat. Technol 2013;214:101—9. http://dx.doi.org/10.1016/j.surfcoat.2012.11.010.

[37] Kumari K, Anand K, Bellacci M, Giannozzi M. Effect of microstructure on abrasive wear behavior of thermally sprayed WC-10Co-4Cr coatings. Wear 2010;268:1309—19. http://dx.doi.org/10.1016/j.wear.2010.02.001.

[38] Li WY, Yin S, Wang XF. Numerical investigations of the effect of oblique impact on particle deformation in cold spraying by the SPH method. Appl Surf Sci 2010;256:3725—34. http://dx.doi.org/10.1016/j.apsusc.2010.01.014.

[39] Na H, Bae G, Shin S, Kumar S, Kim H, Lee C. Advanced deposition characteristics of kinetic sprayed bronze/diamond composite by tailoring feedstock properties. Compos Sci Technol 2009;69:463—8. http://dx.doi.org/10.1016/j.compscitech.2008.11.015.

[40] Yin S, Wang XF, Li WY, Jie HE. Effect of substrate hardness on the deformation behavior of subsequently incident particles in cold spraying. Appl Surf Sci 2011;257:7560—5. http://dx.doi.org/10.1016/j.apsusc.2011.03.126.

[41] Yin S, Zhang M, Guo Z, Liao H, Wang X. Numerical investigations on the effect of total pressure and nozzle divergent length on the flow character and particle impact velocity in cold spraying. Surf Coat. Technol 2013;232:290—7. http://dx.doi.org/10.1016/j.surfcoat.2013.05.017.

[42] Kwon H, Cho S, Kawasaki A. Diamond-Reinforced Metal Matrix Bulk Mater Fabr by a Low-Pressure Cold-Spray Process 2015;56:108—12.

[43] Shin S, Xiong Y, Ji Y, Kim HJ, Lee C. The influence of process parameters on deposition characteristics of a soft/hard composite coating in kinetic spray process. Appl Surf Sci 2008;254:2269—75. http://dx.doi.org/10.1016/j.apsusc.2007.09.017.

[44] Chen LY, Konishi H, Fehrenbacher A, Ma C, Xu JQ, Choi H, et al. Novel nanoprocessing route for bulk graphene nanoplatelets reinforced metal matrix nanocomposites. Scr Mater 2012;67:29—32. http://dx.doi.org/10.1016/j.scriptamat.2012.03.013.

[45] Yang N, Boselli J, Sinclair I. Simulation and quantitative assessment of homogeneous and inhomogeneous particle distributions in particulate metal matrix composites. J Microsc 2001;201:189—200. http://dx.doi.org/10.1046/j.1365-2818.2001.00766.x.

[46] Iacob G, Ghica VG, Buzatu M, Buzatu T, Petrescu MI. Studies on wear rate and

micro-hardness of the Al/Al2O3/Gr hybrid composites produced via powder metallurgy. Compos Part B Eng 2014;69:603–11. http://dx.doi.org/10.1016/j.compositesb.2014.07.008.

[47] Yu M, Suo XK, Li WY, Wang YY, Liao HL. Microstructure, mechanical property and wear performance of cold sprayed Al5056/SiCp composite coatings: effect of reinforcement content. Appl Surf Sci 2014;289:188–96. http://dx.doi.org/10.1016/j.apsusc.2013.10.132.

[48] Guo X, Chen J, Yu H, Liao H, Coddet C. A study on the microstructure and tribological behavior of cold-sprayed metal matrix composites reinforced by particulate quasicrystal. Surf Coat. Technol 2015;268:94–8. http://dx.doi.org/10.1016/j.surfcoat.2014.05.062.

Surface & Coatings Technology 337 (2018) 447–452

Contents lists available at ScienceDirect

Surface & Coatings Technology

journal homepage: www.elsevier.com/locate/surfcoat

Formation mechanism and microstructure characterization of nickel-aluminum intertwining interface in cold spray

Yingchun Xie[a], Shuo Yin[b,*], Jan Cizek[c], Jan Cupera[d], Enyu Guo[e], Rocco Lupoi[b,*]

[a] National Engineering Laboratory for Modern Materials Surface Engineering Technology, The Key Lab of Guangdong for Modern Surface Engineering Technology, Guangdong Institute of New Materials, Guangzhou 510651, PR China
[b] Trinity College Dublin, The University of Dublin, Department of Mechanical and Manufacturing Engineering, Parsons Building, Dublin 2, Ireland
[c] Institute of Plasma Physics, Czech Academy of Sciences, Za Slovankou 1782/3, 182 00 Prague, Czech Republic
[d] Netme Centre, Institute of Materials Science and Engineering, Brno University of Technology, Technicka 2896/2, 616 69 Brno, Czech Republic
[e] School of Materials, The University of Manchester, Manchester M13 9PL, UK.

ARTICLE INFO

Keywords:
Kinetic spray
Materials mixing
Grain refinement
Dynamic recrystallization
Nanostructure

ABSTRACT

Experimental investigation was carried out to explore the formation mechanism of nickel-aluminum intertwining interface in cold spray, and to characterize the microstructure of deposited nickel particles at the intertwining interface. Shear stress was found to induce the intertwining interface through elongating and breaking of the nickel particles at the coating-substrate interface. The in-situ temperature measurement indicated that the temperature at the intertwining interface did not exceed the recrystallization temperature of nickel during the entire deposition process, suggesting that the nickel particles at the intertwining interface were in solid state rather than thermally softened viscous state. Electron channeling contrast (ECC) and electron backscatter diffraction (EBSD) imaging revealed a development of elongated subgrain ($200\,\text{nm} < D < 1\,\mu\text{m}$) and localized equiaxed ultrafine grain ($D < 200\,\text{nm}$) microstructure within the highly deformed and fractured nickel particles at the intertwining interface. Such microstructures were induced by the dislocation accumulation due to the high strain/strain-rate plastic deformation and grain refinement caused by adiabatic temperature rise, respectively. Moreover, equiaxed ultrafine grains were also found to localize within a shear band near the center of the nickel particles, which experimentally confirms the existence of shear stress at the intertwining interface.

1. Introduction

Cold spray is an emerging coating and additive manufacturing technology, which was developed in the 1980s. In this process, micro-scale powders are accelerated by a supersonic gas passing through a de-Laval nozzle and subsequently impact onto a substrate to form a coating or bulk deposit [1]. Metals [2], metal matrix composites [3] and even ceramics [4] can be deposited onto various substrates via cold spray without exceeding their melting points. Thereby, defects encountered in the related high-temperature deposition processes such as oxidation, thermal residual stress and phase transformation, can be effectively avoided [5–10].

Microstructure evolution of cold sprayed metal coatings has been intensively studied during the past decades. It is well known that a significant grain refinement down to elongated subgrains ($200\,\text{nm} < D < 1\,\mu\text{m}$) and ultrafine grains ($D < 200\,\text{nm}$) occurs near the inter-particle interface during the deposition process due to the impact-induced high strain/strain-rate plastic deformation [11–19]. The formation mechanism of the elongated subgrains is attributed to the dislocations pile-up that produces an array of dislocation walls, further transforming into subgrain boundaries [11]. At the highly deformed inter-particle interfacial regions where adiabatic shear instability phenomenon occurs, the elongated subgrains are further broken into smaller pieces and rotated by additional shear force due to dynamic recrystallization, ultimately leading to the formation of equiaxed ultrafine grains [11]. Such grain refinement phenomenon was observed in cold sprayed Ni [11], Cu [12,13], Ti [14,15] and Al coatings [16–19].

Bonding mechanism of the materials in contact has also been a major research focal point due to its crucial importance in the cold spray field. It has been well recognized that a successful inter-particle and coating-substrate bonding only takes place when the particle impact velocity exceeds a so-called "critical velocity" [20,21]. The well-documented metallurgical bonding resulting from a nano-scale chemical reaction at the interface is known to be the dominant mechanism for both inter-particle and coating-substrate bonding [5,7,8,22,23]. In

---

* Corresponding authors.
E-mail addresses: yins@tcd.ie (S. Yin), lupoir@tcd.ie (R. Lupoi).

https://doi.org/10.1016/j.surfcoat.2018.01.049
Received 1 November 2017; Received in revised form 12 January 2018; Accepted 15 January 2018
0257-8972/ © 2018 Elsevier B.V. All rights reserved.

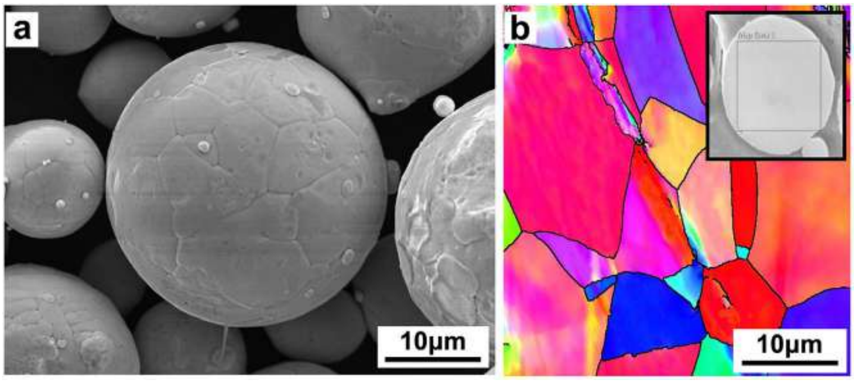

Fig. 1. Nickel feedstock characterization: (a) surface morphology observed by SEM, and (b) grain structure observed by EBSD.

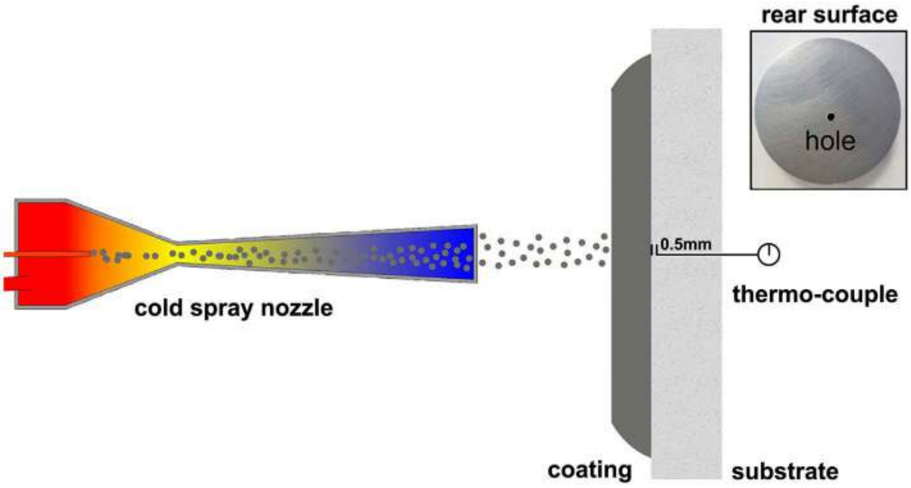

Fig. 2. Schematic of the interfacial temperature measurement setup and a digital photo of the 25 mm cylindrical substrate rear surface with the drilled thermocouple inlet. The front surface of the substrate was polished.

Fig. 3. General view of the intertwining nickel-aluminum alloy interface observed by SEM.

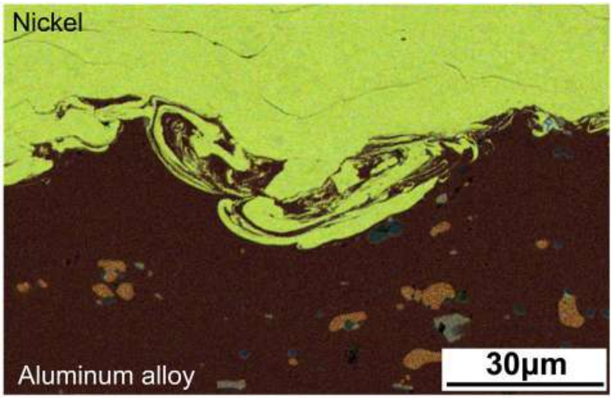

Fig. 4. Magnified view of the intertwining nickel-aluminum alloy interface colored by EDX mapping.

this respect, adiabatic shear instability and an intimate metal-to-metal contact arising from the impact-induced oxides removal are the prerequisites for the occurrence of such chemical reaction [20,24]. Another important mechanism contributing to the overall coating-substrate adherence is commonly present in cases when the substrate material is softer than the particle material: mechanical interlocking. Non-chemical bonding in its nature, the interlocking is represented by hard particle material being embedded into and trapped by the soft substrate material [5,8].

Apart from the two major bonding mechanisms, another bonding phenomenon in the form of particle elongation, fracture and mutual intertwining at the coating-substrate interface was observed in very limited cases when hard coatings were deposited onto soft substrates [25–29]. Although it has been years since the first report of such structure [25], only few studies addressed this interesting bonding phenomenon in more detail till now [27,29]. These studies mainly ascribed the formation of such intertwining interface to the so-called 'Kelvin-Helmholtz instability (KHI)' phenomenon in which two viscous materials move in parallel at different velocities to generate interfacial perturbation. This hypothesis seems to explain the formation mechanism of the vortex structure at the intertwining interface. However, some essential conditions for inducing the KHI may not be satisfied at cold spray coating-substrate interfaces. For one, KHI requires both materials to be in a viscous state. In cold spray, however, the low deposition temperature disallows the large-scale transformation of materials from a solid state to the viscous state. Note that the adiabatic shear

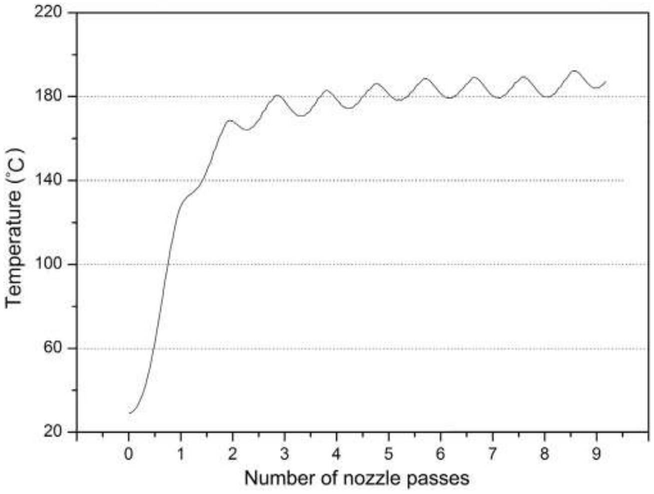

Fig. 5. Measured temporal evolution of the intertwining interface temperature during the coating deposition.

instability occurring at particle-substrate and inter-particle interfaces could lead to a localized temperature rise (beyond dynamic recrystallization temperature) and hence material thermal softening phenomenon, but such thermal softening is only confined at the micro-scale 'jetting region', [5,30,31], i.e. the large-scale viscous flow condition of KHI is not met. Considering this discrepancy, it is plausible to assume other mechanisms inducing the formation of intertwining interfaces in cold spray. Furthermore, the KHI hypothesis does not specify the origin of the force triggering the relative movement between the two materials. Therefore, the major objective of this paper is to explore the possible reasons for inducing the intertwining interface through experimental observation and characterization using a nickel-aluminum intertwining interface.

2. Experimental methodology

2.1. Fabrication of cold sprayed Ni coating

The cold sprayed nickel coating was fabricated under 10 nozzle passes using CGT K3000 system. Compressed air was used as the propellant gas with the inlet pressure and temperature of 2.4 MPa and 360 °C, respectively. The standoff distance from the nozzle exit to the substrate surface and the nozzle traverse speed were set as 30 mm and 100 mm/s, respectively. Spherical nickel powder (ECKA Granules Metal Powders Ltd, Germany) with the average diameter of 32 μm was selected as the feedstock. To aid in understanding the conditions of the two materials in contact, an auxiliary computational study was realized using CFD calculation in Ansys-Fluent software. The results indicate that, for a nickel particle of the 32 μm in diameter, the in-flight velocity and temperature upon impact reach 400 m/s and 46 °C, respectively. Detailed description of the computational model can be found in our previous paper [32]. Fig. 1a shows the surface morphology of the nickel powders observed by scanning electron microscope (SEM, Carl Zeiss Ultra Plus, Germany), suggesting an internal grain structure of the individual nickel particles. Fig. 1b provides the electron backscatter diffraction (EBSD) imaging of a typical nickel particle at its cross-section. The statistical results indicated that, in the as-received state, the average internal grain size within the particles reached micro-scale levels (average of 8.14 μm; 141 grains from 8 different particles counted, grains smaller than 4 μm were omitted from the statistics as these were residues formed in the cross-section preparation) and the grains were mostly of equiaxed character (average aspect ratio of 1.76). Flat cylinder-shaped 2024 aluminum alloy (4% Cu, 1% Mg, 0.5% Mn) with a diameter of 25 mm was used as the substrate (Fig. 2). In order to allow for a detailed study of the interface microstructure evolution, the substrate was polished prior to cold spray deposition using standard metallographic procedures with the final polishing applied by 0.05 μm SiC solution. The microstructure of the coating and substrate materials at the intertwining interface was studied by SEM in a secondary electrons mode and energy-dispersive X-ray spectroscopy (EDX, Oxford Instruments AZtec, UK). Determination of the grain and sub-grain deformation behavior were carried out using electron channeling contrast (ECC, working distance 3 mm, accelerating voltage 10 kV, aperture 120 μm) and EBSD imaging.

2.2. In-situ temperature measurement at the intertwining interface

To aid in understanding the microstructure evolution mechanism, the coating-substrate intertwining interface temperature was measured by a thermo-couple inserted into the substrate through a small hole drilled from its rear surface [33]. The intertwining interface temperature is defined as the temperature at the near coating-substrate interface region (± 100 μm from the interface; i.e., the whole intertwining region falls within this area as will be shown in the results and discussion section). Fig. 2 shows the schematic of the temperature measurement setup and a digital photo of the substrate rear surface. Note that the thermocouple was actually placed 0.5 mm away from the substrate upper surface, yielding the measured values somewhat lower than the real intertwining interface temperature.

3. Results and discussion

3.1. General characterization of the intertwining interface

Fig. 3 shows a general view of the nickel-aluminum intertwining interface observed by SEM. As can be seen, the intertwining structures were present along the entire interface length in the form of prominent nickel elongation and fracture, and mixture of the nickel and 2024 aluminum alloy materials. This fact indicates that the intertwining is not an incidental phenomenon occurring at discrete interface areas only, but rather a regular, deformation-induced coating-substrate bonding pattern. Fig. 4 shows an EDX element mapping of the vortex-like structure under higher magnification, providing a clearer view of the intertwining structure. Obviously, the deposited nickel particles were seriously fractured and showed strip-like shape, indicating the occurrence of elongation before their fracture at the intertwining interface.

In order to identify the temperature at which the intertwining structure was formed, Fig. 5 shows the temporal evolution of the measured coating-substrate intertwining interface temperature during the coating deposition process. As can be seen, the temperature rapidly increased to nearly 130 °C after the first nozzle pass. The heating rate then decelerated, eventually steadying the substrate temperature at 190 °C for the rest of the deposition process. Generally, the recrystallization temperature of any metallic element is roughly 40–50% of its melting temperature (T_m = 1455 °C for nickel) [34]. In this study, the measured temperature of 190 °C was far substantially lower than the recrystallization temperature of nickel (est. 420–590 °C), which suggested that the deformation of the nickel particles and evolution of their microstructure during the intertwining formation occurred at "cold working" rather than "hot working" conditions. In other words, the nickel particles were in solid state rather than thermally softened viscous state at all time during the formation process of intertwining interface.

Fig. 6 shows the cross-sectional SEM and ECC imaging of typical nickel particles at two different locations: the bottom (Fig. 6b and d) and center (Fig. 6c and e) of the intertwining interface, respectively. The nickel particles at the intertwining zone were elongated and seriously fractured in the form of disconnected fragments further disrupted by present ribbon-like deep slits (indicated by white arrows in Fig. 6b

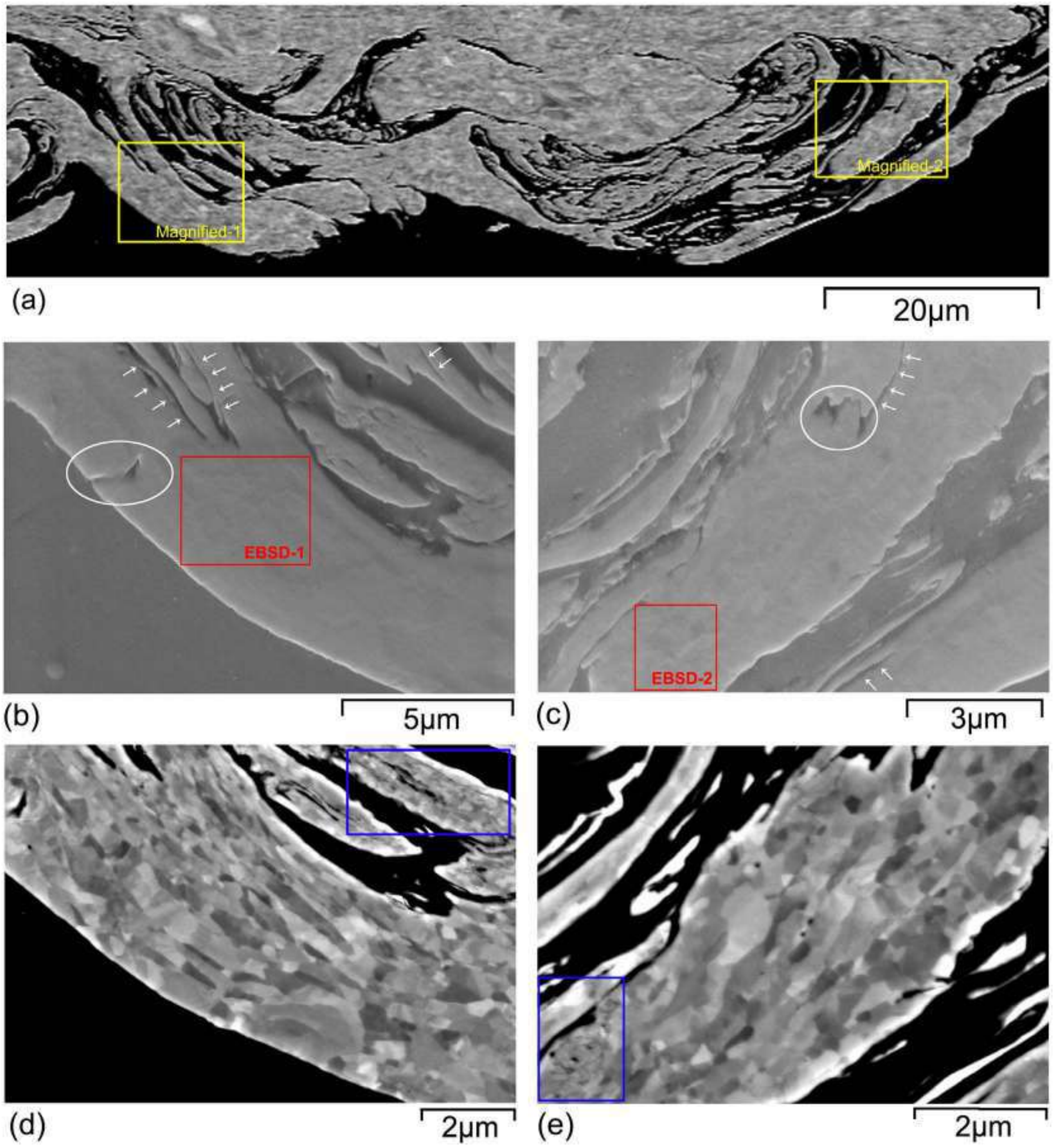

Fig. 6. Cross-sectional SEM and ECC imaging of typical fractured nickel particles fragments: (a) low magnification overview of the intertwining interface, (b, d) high magnification view of the structure at the bottom and (c, e) center of the intertwining zone. White arrows indicate open slits (sliding-mode fracture), white ellipses indicate tear-mode fracture. Yellow rectangles in (a) are areas selected for high magnification (b, d, c, e), red rectangles in (b, c) are areas selected for EBSD imaging (Fig. 7), blue rectangles indicate areas with extremely fine grains. (For interpretation of the references to color in this figure legend, the reader is referred to the web version of this article.)

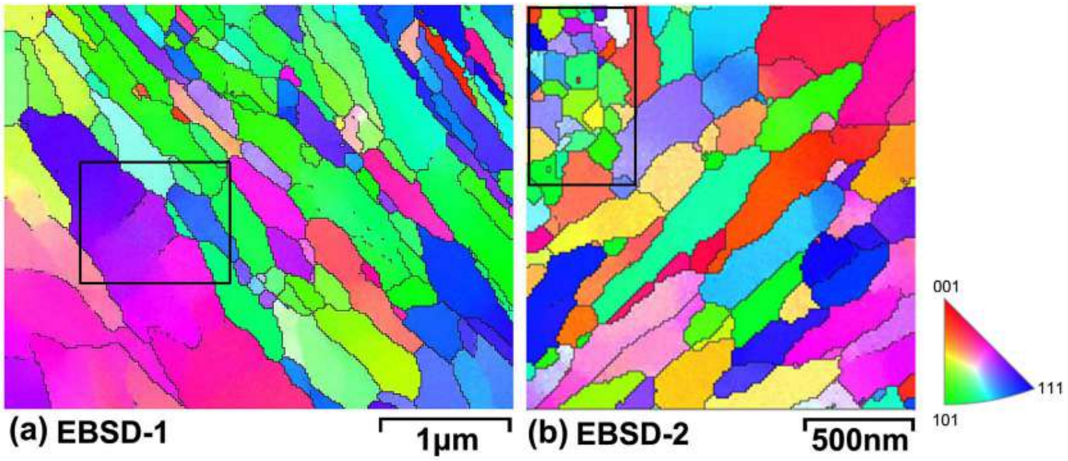

Fig. 7. EBSD imaging of fragmented nickel particles: (a) area selected from Fig. 6b, and (b) area selected from Fig. 6c. Black rectangle in EBSD-1 indicates dislocation pile-up phenomenon leading towards the formation of subgrain boundaries; black rectangle in EBSD-2 indicates a region of equiaxed ultrafine grains smaller than 200 nm.

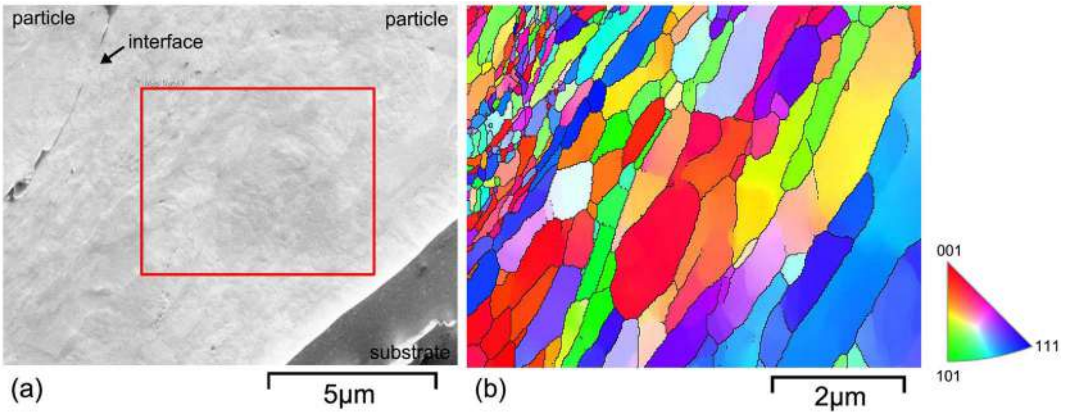

Fig. 8. EBSD imaging of a non-twinned nickel particle interacting directly with the substrate. Equiaxed ultrafine grains were formed within a shear band further from particle rims, as opposed to studies where no intertwinning phenomenon was recorded.

and c). The fragments and slits had a roughly parallel orientation, exhibiting a sliding-mode fracture. Apart from the frequently observed sliding fracture, tearing-mode fracture represented by serration-like deep cracks could also be distinguished as indicated by white ellipses in Fig. 6b and c. Moreover, it was observed that the two identified modes of fracture (i.e., sliding and tearing) combined occasionally to form a hybrid fracture (one such is illustrated in Fig. 6c). It is suggested herein that such hybrid mechanism induced the formation of the observed coatings fragments, i.e. the formation of the relatively harder deposited material fragments (nickel) requires concurrent incidence of both modes. Importantly, such elongation and fracture phenomena clearly demonstrate the existence of shear stress at the intertwining interface. In fact, the intertwining structure and particle fracture phenomenon in cold spray is quite similar to the friction stir welding process of dissimilar materials where a rotational shoulder provides high shear stress to induce the materials intertwining structure and fracture [35]. Such analogy, in turn, further supports the rationality of the shear-induced elongation and fracture mechanism. Furthermore, in Fig. 6d and e, it is clearly observed that the grains in the fractured nickel particles are mostly flattened and their grain sizes are much lower (average of 0.27 μm, aspect ratio of 2.51; 120 grains counted, grains smaller than 0.1 μm were omitted from the statistics due to uncertainty in the detection threshold limit) than in the original nickel particles (cf. the equiaxed relatively coarse ~8 μm grain structure of the feedstock particles in Fig. 1, having initial aspect ratio of 1.76). Detailed grain structure analysis will be provided in the following section.

3.2. *Grain structure characterization of the nickel particles at the intertwining interface*

For quantitative analysis of the grain structure of the nickel particles at the intertwining interface, EBSD imaging at selected areas located at two different depths within the substrate was realized (Fig. 7). Obviously, directionally elongated subgrains with low-angle boundaries were formed through a dislocation pile-up mechanism within the feedstock grains due to the extensive, impact-induced high strain/strain-rate plastic deformation. Such dislocation pile-up leading to the formation of new subgrain boundaries in a coarse grain can be clearly observed (illustrated by black rectangle in Fig. 7a). Infrequently, small areas of equiaxed ultrafine grains ($D < 200$ nm) with high-angle boundaries were observed (denoted by blue-bordered rectangles in Fig. 6d and e, and black-bordered rectangle in the EBSD pattern in Fig. 7b). Formation of such grains is known to be a consequence of dynamic recrystallization due to the adiabatic shear-induced temperature rise [11,12,15]. The grain structure evolution in the fractured nickel particles observed herein is quite similar with that in cold sprayed coatings reported in [11,13]. Also, the grain structure further confirms that there was no large-scale recrystallization and no significant thermal input leading to a transformation from solid state to viscous state of the nickel particles during the deposition, which is in agreement with the above in-situ intertwining interface temperature analysis.

Fig. 8 shows the EBSD imaging at the cross-section of non-fractured nickel particle contacting directly to the substrate. In the particle, equiaxed ultrafine grains formed and localized in a band-shape region could be observed. As discussed earlier, in almost all previous works where no intertwining structure was generated, such equiaxed ultrafine grains were formed at the inter-particle interfacial regions only. However, in this case, the ultrafine grains were observed deep inside a deposited particle, suggesting that a local high-strain-rate shear band can also be generated inside a deformed particle [36]. Such shear band was certainly not induced by the localized deformation of the particle itself during its deposition, but was likely to be triggered through the impact of the following deposited particles which enabled further deformation. This fact, for the first time, experimentally confirms the existence of shear stress in the fractured particles at the intertwining interface, which is in agreement with the proposed particle fracture modes as discussed in Fig. 6. Such nanostructured shear band is more brittle than other areas, which may become a potential source of fracture [37,38].

4. Conclusions

In summary, the formation mechanism and microstructure evolution of the nickel-aluminum intertwining interface were discussed in the current work. The experimental result indicates that shear stress may be the reason for inducing such intertwining interface. Under the shear stress, nickel particles were elongated and fractured. The fracture behavior of the nickel particles at such interface was dominated by sliding mode, tearing mode, and hybrid mode (i.e., their combination). The in-situ temperature measurement indicated that the temperature at the intertwining interface did not exceed the recrystallization temperature of nickel during the entire deposition process. That said, the intertwining interface developed at “cold working” rather than “hot working” conditions, which suggested that the nickel particles at the intertwining interface were in solid state rather than thermally softened viscous state at all time.

ECC and EBSD imaging analysis revealed that the nickel particles at the intertwining interface were mostly nanostructured, consisting of a large volume of elongated subgrains and localized equiaxed ultrafine grains. Such microstructures were induced by the dislocation accumulation due to the high strain/strain-rate plastic deformation and localized dynamic recrystallization caused by adiabatic temperature rise respectively. In addition, for the first time, equiaxed ultrafine grains were found near the center of the cold sprayed particle rather than at its periphery. They were localized within a shear band, which was believed to arise from the impact of the following particles. This finding experimentally confirms the existence of shear stress in the particles at the intertwining interface.

Acknowledgments

The authors would like to thank the financial support from Irish Research Council project (GOIPD-2017-912), Enterprise Ireland project (CF20144626), Czech Science Foundation project (GACR 17-13573S) and Guangdong Special Project of Science and Technology Development (2018GDASCX-0945).

References

[1] A.P. Alkhimov, V.F. Kosareve, A.N. Papyrin, A method of cold gas-dynamic spray deposition, Dokl. Akad. Nauk SSSR 315 (1990) 1062–1065.

[2] S. Yin, X. Suo, Y. Xie, W. Li, R. Lupoi, H. Liao, Effect of substrate temperature on interfacial bonding for cold spray of Ni onto Cu, J. Mater. Sci. 50 (2015) 7448–7457, http://dx.doi.org/10.1007/s10853-015-9304-6.

[3] S. Yin, Y. Xie, J. Cizek, E. Ekoi, T. Hussain, D. Dowling, R. Lupoi, Advanced diamond-reinforced metal matrix composites via cold spray: properties and deposition mechanism, Compos. Part B Eng. 113 (2017) 44–54, http://dx.doi.org/10.1016/j.compositesb.2017.01.009.

[4] L.-S. Wang, H.-F. Zhou, K.-J. Zhang, Y.-Y. Wang, C.-X. Li, X.-T. Luo, G.-J. Yang, C.-J. Li, Effect of the powder particle structure and substrate hardness during vacuum cold spraying of Al2O3, Ceram. Int. 43 (2017) 4390–4398, http://dx.doi.org/10.1016/j.ceramint.2016.12.085.

[5] C. Lee, J. Kim, Microstructure of kinetic spray coatings: a review, J. Therm. Spray Technol. 24 (2015) 592–610, http://dx.doi.org/10.1007/s11666-015-0223-5.

[6] X.-T. Luo, C.-X. Li, F.-L. Shang, G.-J. Yang, Y.-Y. Wang, C.-J. Li, High velocity impact induced microstructure evolution during deposition of cold spray coatings: a review, Surf. Coat. Technol. 254 (2014) 11–20, http://dx.doi.org/10.1016/j.surfcoat.2014.06.006.

[7] M.R. Rokni, S.R. Nutt, C.A. Widener, V.K. Champagne, R.H. Hrabe, Review of relationship between particle deformation, coating microstructure, and properties in high-pressure cold spray, J. Therm. Spray Technol. (2017) 1–48, http://dx.doi.org/10.1007/s11666-017-0575-0.

[8] T. Klassen, H. Assadi, H. Kreye, F. G, Cold spraying – a materials perspective, Acta Mater. 116 (2016) 382–407, http://dx.doi.org/10.1016/j.actamat.2016.06.034.

[9] A.M. Vilardell, N. Cinca, A. Concustell, S. Dosta, I.G. Cano, J.M. Guilemany, Cold spray as an emerging technology for biocompatible and antibacterial coatings: state of art, J. Mater. Sci. (2015) 4441–4462, http://dx.doi.org/10.1007/s10853-015-9013-1.

[10] S. Yin, E.J. Ekoi, T.L. Lupton, D.P. Dowling, R. Lupoi, Cold spraying of WC-Co-Ni coatings using porous WC-17Co powders: formation mechanism, microstructure characterization and tribological performance, Mater. Des. 126 (2017) 305–313, http://dx.doi.org/10.1016/j.matdes.2017.04.040.

[11] Y. Zou, W. Qin, E. Irissou, J.G. Legoux, S. Yue, J.a. Szpunar, Dynamic recrystallization in the particle/particle interfacial region of cold-sprayed nickel coating: electron backscatter diffraction characterization, Scr. Mater. 61 (2009) 899–902, http://dx.doi.org/10.1016/j.scriptamat.2009.07.020.

[12] Y. Xiong, K. Kang, G. Bae, S. Yoon, C. Lee, Dynamic amorphization and recrystallization of metals in kinetic spray process, Appl. Phys. Lett. 92 (2008) 144–147, http://dx.doi.org/10.1063/1.2928218.

[13] P.C. King, S.H. Zahiri, M. Jahedi, Microstructural refinement within a cold-sprayed copper particle, Metall. Mater. Trans. A Phys. Metall. Mater. Sci. 40 (2009) 2115–2123, http://dx.doi.org/10.1007/s11661-009-9882-5.

[14] K. Kim, M. Watanabe, J. Kawakita, S. Kuroda, Grain refinement in a single titanium powder particle impacted at high velocity, Scr. Mater. 59 (2008) 768–771, http://dx.doi.org/10.1016/j.scriptamat.2008.06.020.

[15] K. Kim, M. Watanabe, S. Kuroda, Thermal softening effect on the deposition efficiency and microstructure of warm sprayed metallic powder, Scr. Mater. 60 (2009) 710–713, http://dx.doi.org/10.1016/j.scriptamat.2008.12.050.

[16] Q. Wang, D. Qiu, Y. Xiong, N. Birbilis, M.X. Zhang, High resolution microstructure characterization of the interface between cold sprayed Al coating and Mg alloy substrate, Appl. Surf. Sci. 289 (2014) 366–369, http://dx.doi.org/10.1016/j.apsusc.2013.10.168.

[17] M.R. Rokni, C.A. Widener, G.A. Crawford, Microstructural evolution of 7075 Al gas atomized powder and high-pressure cold sprayed deposition, Surf. Coat. Technol. 251 (2014) 254–263, http://dx.doi.org/10.1016/j.surfcoat.2014.04.035.

[18] K. Kang, J. Won, G. Bae, S. Ha, C. Lee, Interfacial bonding and microstructural evolution of Al in kinetic spraying, J. Mater. Sci. 47 (2012) 4649–4659, http://dx.doi.org/10.1007/s10853-012-6332-3.

[19] K. Kang, H. Park, G. Bae, C. Lee, Microstructure and texture of Al coating during kinetic spraying and heat treatment, J. Mater. Sci. 47 (2012) 4053–4061, http://dx.doi.org/10.1007/s10853-012-6259-8.

[20] M. Grujicic, C.L.C. Zhao, W.S.W. DeRosset, D. Helfritch, Adiabatic shear instability based mechanism for particles/substrate bonding in the cold-gas dynamic-spray process, Mater. Des. 25 (2004) 681–688, http://dx.doi.org/10.1016/j.matdes.2004.03.008.

[21] T. Schmidt, F. Gärtner, H. Assadi, H. Kreye, Development of a generalized parameter window for cold spray deposition, Acta Mater. 54 (2006) 729–742, http://dx.doi.org/10.1016/j.actamat.2005.10.005.

[22] S. Yin, X. Wang, X. Suo, H. Liao, Z. Guo, W. Li, C. Coddet, Deposition behavior of thermally softened copper particles in cold spraying, Acta Mater. 61 (2013) 5105–5118, http://dx.doi.org/10.1016/j.actamat.2013.04.041.

[23] Y. Xie, S. Yin, C. Chen, M. Planche, H. Liao, R. Lupoi, New insights into the coating/substrate interfacial bonding mechanism in cold spray, Scr. Mater. 125 (2016) 1–4, http://dx.doi.org/10.1016/j.scriptamat.2016.07.024.

[24] G. Bae, Y. Xiong, S. Kumar, K. Kang, C. Lee, General aspects of interface bonding in kinetic sprayed coatings, Acta Mater. 56 (2008) 4858–4868, http://dx.doi.org/10.1016/j.actamat.2008.06.003.

[25] V.K. Champagne, D. Helfritch, P. Leyman, S. Grendahl, B. Klotz, Interface material mixing formed by the deposition of copper on aluminum by means of the cold spray process, J. Therm. Spray Technol. 14 (2005) 330–334, http://dx.doi.org/10.1361/105996305X59332.

[26] X.L. Zhou, a.F. Chen, J.C. Liu, X.K. Wu, J.S. Zhang, Preparation of metallic coatings on polymer matrix composites by cold spray, Surf. Coat. Technol. 206 (2011) 132–136, http://dx.doi.org/10.1016/j.surfcoat.2011.07.005.

[27] L. Ajdelsztajn, B. Jodoin, G.E. Kim, J.M. Schoenung, Cold spray deposition of nanocrystalline aluminum alloys, Metall. Mater. Trans. A Phys. Metall. Mater. Sci. 36 (2005) 657–666, http://dx.doi.org/10.1007/s11661-005-0099-y.

[28] X.L. Zhou, X.K. Wu, H.H. Guo, J.G. Wang, J.S. Zhang, Deposition behavior of multi-particle impact in cold spraying process, Int. J. Miner. Metall. Mater. 17 (2010) 635–640, http://dx.doi.org/10.1007/s12613-010-0367-8.

[29] M. Grujicic, J.R. Saylor, D.E. Beasley, W.S. DeRosset, D. Helfritch, Computational analysis of the interfacial bonding between feed-powder particles and the substrate in the cold-gas dynamic-spray process, Appl. Surf. Sci. 219 (2003) 211–227, http://dx.doi.org/10.1016/S0169-4332(03)00643-3.

[30] H. Assadi, F. Gärtner, T. Stoltenhoff, H. Kreye, Bonding mechanism in cold gas spraying, Acta Mater. 51 (2003) 4379–4394, http://dx.doi.org/10.1016/S1359-6454(03)00274-X.

[31] P.C. King, G. Bae, S.H. Zahiri, M. Jahedi, C. Lee, An experimental and finite element study of cold spray copper impact onto two aluminum substrates, J. Therm. Spray Technol. 19 (2010) 620–634, http://dx.doi.org/10.1007/s11666-009-9454-7.

[32] S. Yin, Q. Liu, H. Liao, X. Wang, Effect of injection pressure on particle acceleration, dispersion and deposition in cold spray, Comput. Mater. Sci. 90 (2014) 7–15, http://dx.doi.org/10.1016/j.commatsci.2014.03.055.

[33] S. Yin, X.F. Wang, W.Y. Li, X.P. Guo, Examination on substrate preheating process in cold gas dynamic spraying, J. Therm. Spray Technol. 20 (2011) 852–859, http://dx.doi.org/10.1007/s11666-011-9623-3.

[34] A. Russell, K.L. Lee, Structure-property relations in nonferrous metals, Struct. Relations Nonferrous Met, Wiley, 2005, pp. 28–37.

[35] S. Ji, X. Meng, Z. Liu, R. Huang, Z. Li, Dissimilar friction stir welding of 6061 aluminum alloy and AZ31 magnesium alloy assisted with ultrasonic, Mater. Lett. 201 (2017) 173–176, http://dx.doi.org/10.1016/j.matlet.2017.05.011.

[36] J. Peirs, W. Tirry, B. Amin-Ahmadi, F. Coghe, P. Verleysen, L. Rabet, D. Schryvers, J. Degrieck, Microstructure of adiabatic shear bands in Ti6Al4V, Mater. Charact. 75 (2013) 79–92, http://dx.doi.org/10.1016/j.matchar.2012.10.009.

[37] H. Li, F. Ebrahimi, Tensile behavior of a nanocrystalline Ni-Fe alloy, Acta Mater. 54 (2006) 2877–2886, http://dx.doi.org/10.1016/j.actamat.2006.02.033.

[38] H. Yu, A.K. Tieu, C. Lu, X. Liu, M. Liu, A. Godbole, C. Kong, Q. Qin, A new insight into ductile fracture of ultrafine-grained Al-Mg alloys, Sci. Rep. 5 (2015) 9568, , http://dx.doi.org/10.1038/srep09568.

coatings

Article

Cold Sprayed Tungsten Armor for Tokamak First Wall

Jan Cizek [1,2,*], Monika Vilemova [1], Frantisek Lukac [1], Martin Koller [3], Jan Kondas [4,5] and Reeti Singh [4]

[1] Institute of Plasma Physics, The Czech Academy of Sciences, 182 00 Prague, Czech Republic; vilemova@ipp.cas.cz (M.V.); lukac@ipp.cas.cz (F.L.)
[2] Institute of Materials Science and Engineering, Brno University of Technology, 616 69 Brno, Czech Republic
[3] Institute of Thermomechanics, The Czech Academy of Sciences, 182 00 Prague, Czech Republic; koller@it.cas.cz
[4] Impact Innovations GmbH, 84431 Rattenkirchen, Germany; jk@impact-innovations.com (J.K.); rs@impact-innovations.com (R.S.)
[5] Department of Mechanical Engineering, Politecnico di Milano, 20156 Milan, Italy
* Correspondence: cizek@ipp.cas.cz; Tel.: +420-266-052-096

Received: 9 September 2019; Accepted: 2 December 2019; Published: 7 December 2019

Abstract: Harnessing nuclear fusion is a challenging task, in particular because of the demands put on the used materials. In tokamaks, future energy sources, the inner-most chambers are to be coated with dense coatings of W, or W-Cr-based alloys. So far, the attempts for such coatings formation by other methods failed due to oxidation, high porosity, insufficient adhesion, high specific surface, or even insufficient thickness below 10 µm. Cold spraying seems a promising technology for the task. In our study, we demonstrate the first successful fabrication of thick pure W coatings. W-Cr and W-Cr-Ti coatings were further prepared without oxidation of the metals. All coatings exhibited high hardness levels, good interface quality with three tested substrates and, importantly, a promising potential for formation of stable Cr_2WO_x phases.

Keywords: cold gas kinetic spray; W-Cr; W alloys; oxidation shield; nuclear fusion; thick coatings; self-passivation; PFC; plasma facing components

1. Introduction

Nuclear fusion is a process in which two or more light atomic nuclei combine to form a different, heavier nucleus and subatomic particles, neutrons or protons. Due to the difference in the binding energy of the nuclei, a significant amount of energy is released in the reaction (an amount surpassing even that of nuclear fission). The reaction that is currently considered the most promising for future power production is fusion of two hydrogen isotopes, deuterium (D) and tritium (T):

$$D + T \longrightarrow {}^{4}_{2}He + {}^{1}_{0}n. \tag{1}$$

Combining these leads to formation of helium atoms carrying 3.5 MeV energy used to further heat the fuel, and free neutrons having energies of 14.1 MeV. This energy is used for breeding of tritium as well as the energy production. In order to achieve positive energy balance, it is necessary to ensure a sufficient frequency of these reactions (collisions of D and T). This translates into the requirement to keep the fuel at sufficiently high temperatures and concentrations for sufficiently long times [1–3]. Meeting these criteria, tokamaks are torus-shaped fusion facilities where the plasma is confined using magnetic fields. They represent an inherently safe and relatively cheap energy technology (considering the abundance of fuel) that produces radioactive waste with relatively short half-life. An illustration of a tokamak vessel is provided in Figure 1.

Coatings **2019**, *9*, 836; doi:10.3390/coatings9120836

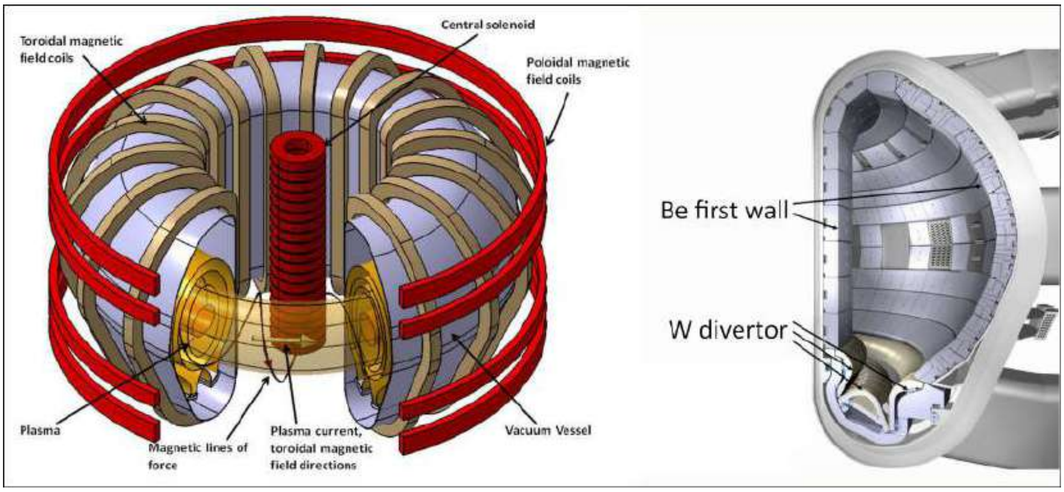

Figure 1. (**Left**) Schematic of a tokamak fusion reactor [4]. (**Right**) Cross section of ITER vacuum vessel and the plasma facing components (courtesy of ITER).

In these reactors, the materials will be subjected to extreme thermo-mechanical or radiation conditions and required to sustain functionality for prolonged periods of time. To get a basic insight, the plasma housed in the tokamaks could reach temperatures up to 10^8 °C due to its density and amount of stored energy. Despite the plasma being confined by the strong magnetic fields preventing a direct contact, the selection of refractory materials for the so called plasma-facing components (PFCs, [1,2]) presents one of the major challenges in the surface engineering of the components used for construction of the tokamak vessel. In the recent years, the studied materials for the PFC armor included variations of graphite (mostly in a form of carbon-reinforced carbon) or beryllium (later rejected due to its toxicity), while low-activation steels such as EUROFER were used for the PFC structural frame.

Tungsten and its alloys have many favorable properties, such as high melting point ($T_m = 3422$ °C for pure W), thermal conductivity superior to the structural steels, low erosion (i.e., high energy threshold to suffer from sputtering) as well as low tritium retention. Understandably, pure tungsten is therefore intended to be applied in the lower part of the reactor vessel, so called divertor region (Figure 1 shows such solution for the tokamak ITER), while tungsten alloys are planned for the remaining surfaces of the so called first wall. Unfortunately, the processing of PFCs is complicated by tungsten's inherent brittleness (high ductile-to-brittle transition temperature), poor weldability and machinability, thermal expansion coefficient mismatch with the structural steels, or susceptibility to grain growth and to oxidation above 500 °C.

At normal vessel operation, the latter factor should not present an issue as the entire system is vacuum tight. However, bearing in mind the safety aspects, an extensive oxidation triggering formation of volatile oxides would present a major threat in case of an accident such as loss of coolant and simultaneous air ingress into the reactor vessel. Interaction of oxygen with tungsten at high temperatures leads to formation of WO_3 that is highly volatile. During reactor operation, the tungsten will be activated by the high energy neutrons and thus, without any risk mitigation, large amounts of radioactive WO_3 might be dispersed into the surrounding. Such safety concerns led to development of self-passivation tungsten alloys via addition of various oxide-forming elements, triggering a formation of protective oxide scale upon exposure to air. For instance, significant improvement of oxidation behavior have been achieved with W-Cr-Y and W-Cr-Ti systems [5,6].

Ideally, the chromium content should be evenly distributed throughout the tungsten matrix in a form of a solid solution. This is, however, complicated due to the miscibility gap limiting the maximum chromium concentration in the solid solution (Figure 2). Another complication is the fact that fabrication of pure W and W-Cr bulk alloys via traditional metallurgy routes is very difficult.

Aside from the economic aspects (mind the very high melting temperatures), the reactivity of both metals with oxygen presents a major problem, as well as the fact the the melting point of W is above the boiling point of Cr (2672 °C). Given that, the research focus is shifting toward the potential of surface engineering methods/manufacturing techniques. This field is largely unexplored and a lot of effort will be needed to provide perfect armor coatings for the W-based components. At the moment, there is a critical need for a robust, simple and cost-effective technology that would ideally sidetrack the need for welding. Cold spray is one such technology. It is a commercially available, high-throughput, large-scale and versatile process capable of fabricating protective coatings directly onto structural parts. This presents yet another potential advantage as the armor coatings could be produced directly onto the first wall surface, without a need for second technological step such as joining or welding. Importantly, cold spray is a single-step technology that does not require (except for final surface machining) any subsequent technological procedures such as heat treatment. As noted by Pintsuk [2], the tungsten compacts furnace-sintered from powders at 2500 °C still possess 80% of the bulk density. Again, this is resolved by cold spraying as the method allows pore-free coating formation (a significant improvement over e.g., plasma spraying).

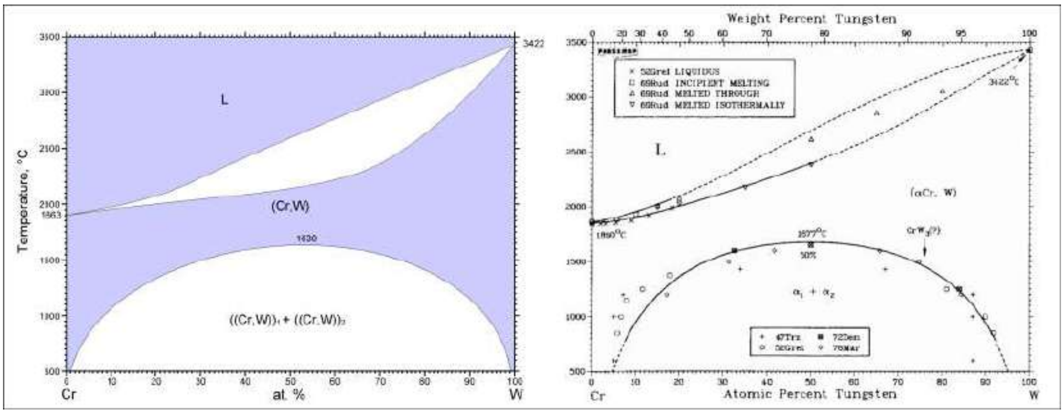

Figure 2. Binary phase diagram of W-Cr showing miscibility gap and limited chromium concentration in the W-based solid solution at room temperature. (**Left**) Calculated diagram reproduced from ASM International binary phase diagram collection database 2017. (**Right**) measured diagram from Naidu et al. [7].

Using kinetic energy in lieu of thermal input, the method is particularly suitable for deposition of metals [8,9]. As opposed to thermal spray processes such as plasma spray or HVOF, the temperatures involved in this process remain relatively low, thereby effectively eliminating oxidation of the materials. In cold spray, the metallic particles are accelerated to high velocities and adhere to the underlying material by means of extensive plastic deformation upon impact. By subsequent movement of the torch over the prepared surface, a coating is formed.

Cold spraying of tungsten is a challenging task. Up to date, no pure W thick coating was successfully fabricated, with some of the results showing a one-layer structure formed owing to the relative substrate softness (embedded particles). As a workaround, mixing of the tungsten phase with other, more malleable and ductile elements can be used. This is frequently combined with enhancing the coating properties by a targeted selection of the ductile matrix that contributes to the desired application properties. Even then, the studies employing such concept are limited in the literature and involve successful depositions of W-Cu by Kang and Kang [10] and Deng et al. [11], W-Ni-Fe by Xia et al. [12], and low tungsten content in W-90Ta coatings by Barnett et al. [13] only. Considering their excellent wear properties, a significantly broader series of studies involved the research of cemented carbides in a form of WC-Co [14–31], WC-Ni [32–41], WC-Co-Ni [42], WC-Co-Cr [31,43–45], or WC-Cu-MoS_2 [46,47]. Unfortunately, the carbides could not be used for PFCs and so we could not built on these results.

Considering the limited outputs on W-based materials processed by cold spray and the fact that cold spray technology is apparently rather unfamiliar to the nuclear fusion sector, the focal point of the presented study is to prove that pure W and W-based coatings can be produced by the technology, with high quality ensuring a potential application in nuclear fusion industry.

2. Experimental Setup

2.1. Materials

In order to aid in our understanding of the process, three different commercially available tungsten powders were used in the study. Their respective particle size ranges were classified into 20–28 µm, 10–15 µm, +20 µm. The chemical purity of the powders was indicated as 99.95%. The used −30 µm flaky chromium powder was fabricated via pulverization method (US Research Nanomaterials, Houston, USA) with purity indicated as 99.5%. Lastly, plasma atomized titanium powder of the sieve range 15–45 µm and 99.5% purity was used in some combinations (Advanced Powders & Coatings Inc., Boisbriand, Canada).

Taking advantage of powder metallurgy routes, six different series of feedstock were prepared from the primary powders, as listed in Table 1. Pure W (for coating A), to manifest that thick W coatings can be deposited by cold spray technology at its current state-of-the-art. Further, a blend of W and 10% Cr (coatings B, C; weight percentages are used throughout this paper) was prepared, a combination that could be of interest to fusion science owing to its oxidation behavior. Thirdly, blends of W and 5% Ti (coating D) and W and 10% Cr and 5% Ti (coating E) were produced to observe the improvement in the coating build-up and density by exploiting the ductile binder phase phenomenon in cold spray. The last coating (F) was produced by mechanically alloying of W and 12% Cr powders (Pulverisette 5 premium line, Fritsch, Idar-Oberstein, Germany), after which 5% Ti was blended into the mixture. In the milling, a WC-based milling jar and balls were used with the ball-to-powder ratio of 3.5:1. Protective argon atmosphere was used. The milling parameters were set as 100 rpm and 15 h. The milling process was then interrupted and resumed for another 25 h at 120 rpm. The final feedstock morphologies are shown in Figure 3, along with a cross-section microstructure of the milled powder used for coating F. In this powder, the W and Cr content formed layered alternating lamellae, i.e., the powder offered an extended mutual contact interface between the two metals. Due to the dissimilar densities of the constituents, the blending process of each blend B–F was carried out for at least four hours using a horizontal jar mill. The powders were not heated prior to deposition.

Table 1. Six different W-based feedstock materials cold sprayed in this study. Note that three different substrates were used in order to assess the influence of the materials' relative hardness.

Coating Annotation	**Content (wt.%)**			**Substrate**	**Feedstock Preparation**
	W	**Cr**	**Ti**		
A	100			Al 6060	
B	90	10		Al 6060	mechanically blended
C	90	10		Steel 1.1191	mechanically blended
D	95		5	AISI 304	mechanically blended
E	85	10	5	AISI 304	mechanically blended
F	83	12	5	AISI 304	W+Cr milled, Ti blended

To tackle the phenomenon of difficulty of thick W coatings formation (discussed in studies [10–12]), three different substrate materials were used. These included a relatively soft Al 6060 alloy (62 HV1), medium-hardness stainless steel AISI 304 (232 HV1), and relatively hard steel 1.1191 (ferrite-pearlite steel with 0.42–0.5% C, 278 HV1). Considering the hardness differences, the interface observations will aid in our understanding of the W-based coating formation process.

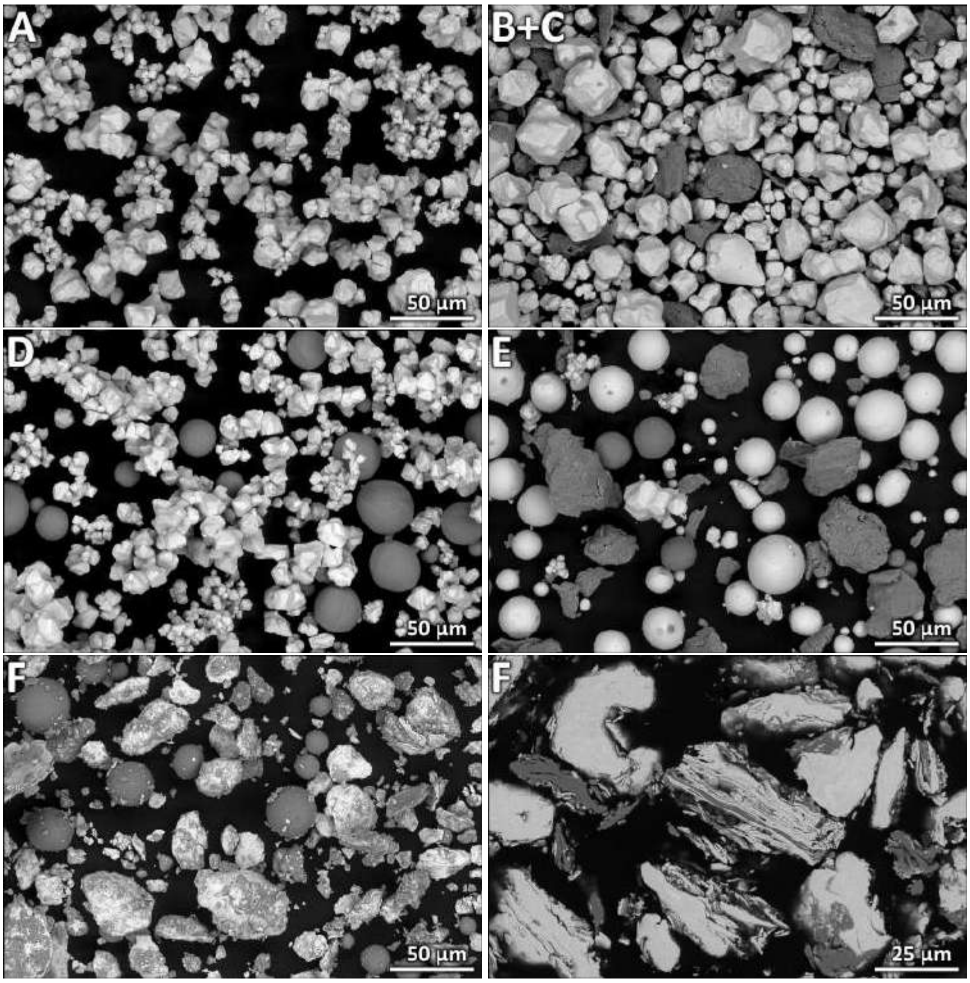

Figure 3. Morphologies of the powder blends used in this study. The annotation corresponds to the coating annotation presented in Table 1 and Figure 4. The last image shows internal (cross-section) microstructure of the milled powder used for coating F, illustrating the layered character of the particles.

2.2. Cold Spray Deposition

Prior to deposition, KSS software (version 1.4.0, Kinetic spray solutions, Buchholz in der Nordheide, Germany) was used to simulate the spray conditions and obtain the parameters required to deposit the W coatings. Given the average particles sizes of the used W powders and the geometry of the used torch nozzle, average particle velocities of $v_p = 601~\mathrm{m \cdot s^{-1}}$ were achievable. In turn, this triggered the need to use very high spray parameters.

The deposition was therefore realized using a high-pressure system 5/11 from Impact Innovations GmbH (Rattenkirchen, Germany). The torch is capable of achieving the pressures of 5.0 MPa and temperatures of 1100 °C of the nitrogen main process gas. Fine-tuning of the spray parameters for the pure W, or blended or mechanically alloyed (metallurgically bonded) feedstock was realized. Aside from the W-based combinations (B–F), the high torch parameters showed to be crucial in the deposition of pure W (coating A). The in-flight particle velocity of pure W reached 780 $\mathrm{m \cdot s^{-1}}$ (an average measured from 1000 particles).

The AISI 304 steel substrates were grit-blasted prior to deposition. An area of 30 × 20 mm^2 was sprayed on the 1.1191 steel, an area of 40 × 30 mm^2 on the AISI 304 and an extended area of 80 × 300 mm^2 on the Al 6060 substrates. No secondary treatment of the samples (e.g., heat-treatment or HIP consolidation) was carried out after the deposition.

2.3. Coatings Characterization

Given the rather dissimilar properties of the used materials, a specific methodology was used for the preparation of metallographic samples. After the grinding and polishing using 1 µm diamond paste, the samples were further processed in OPS (colloidal silica) for extended times of 24 h in vibratory polisher (Vibromet 2, Buehler, Lake Bluff, USA).

The cross-section specimens were then used for SEM imaging (Evo MA 15, Zeiss, Oberkochen, Germany) realized in back-scattered electron (i.e., atomic number sensitive) mode at short work distances 6–8 mm. EDX analyses and mapping were realized using Quantax SDD XFlash 5010 detector (Bruker, Billerica, USA). Phase composition was determined by Rietveld refinement of the acquired XRD spectra (D8 Discover, Bruker) equipped with 1D LynxEye detector. Hardness of the materials was measured at 100 gf and 300 gf (coatings) and 1000 gf (substrates) load and dwell times of 10 s using Q10A+ universal hardness tester (Qness, Golling an der Salzach, Austria). At least 12 valid measurements were included in calculation of the average.

Elastic properties of the coatings were further determined by measuring ultrasonic waves velocities by through-transmission method [48]. For each coating, a ∼300 µm thick sample was cut so that the thickness of the sample was parallel to the spraying axis. Individually, the samples were then inserted between two longitudinal wave ultrasonic transducers (Ultran DCB25-10 with 10 MHz nominal frequency) and the velocities of quasi-longitudinal waves v_{qL} were obtained by measuring times of flight of the ultrasonic waves propagating through the samples. Similarly, transverse waves transducers (Ultran SRD25-2 with 2 MHz nominal frequency) were used to measure the velocities of quasi-transverse waves v_{qT}. The elastic coefficients of c_{11} and c_{44} were determined as

$$\begin{aligned} c_{11} &= \rho v_{qL}^2 \\ c_{44} &= \rho v_{qT}^2, \end{aligned} \tag{2}$$

where ρ is the density of the coatings [49]. Moreover, Young's moduli E and Poisson's ratios ν were calculated from these values, utilizing the standard conversion formulae for elastic moduli [50].

The propensity of the coatings to oxidation was evaluated by exposing the coatings to air atmosphere at 1000 °C. For these, samples with the base of 5 × 5 mm^2 were cut. To study the development at the interface, the substrates were not removed from these. No surface polishing was applied. The experiments were performed in a high temperature furnace using synthetic air (20.9% O_2, 78.8% N_2, 3 ppm H_2O). The heating rate to the final oxidation temperature was 5 °C·min^{-1} and the hold time at the oxidation temperature was 10 h. A subsequent cooling to 700 °C was then conducted at a controlled rate of 5 °C·min^{-1}, followed by free cooling to room temperature. Such conditions are somewhat more severe as compared to those the materials will be subjected to during steady state operation conditions (500–600 °C). However, their selection was made to simulate the case of LOCA (loss of coolant accident) where the temperatures could increase to 1000–1200 °C due to radioactive decay. As the most important information for any future coating optimization is the prospective formation of non-volatile oxides stable above 1000 °C, XRD was selected as the evaluation tool, with the obtained spectra processed by Rietveld analysis [51] for quantification of the oxidation products. In these test, the latter coatings D–F containing 5% Ti were used only. The selection is based on the fact that these coatings exhibited a significantly higher deposition efficiency, a rather critical condition considering the intended application of the technology for the large-scale first wall in tokamaks.

3. Results and Discussion

The microstructure of the fabricated cold sprayed coatings can be seen from Figure 4. The pure W coating reached average thickness 78 µm and appeared dense along its entire length. The tungsten particles embedded into the relatively soft Al 6060 substrate were less deformed as compared to the particles deposited by the subsequent torch passes. Demonstration of such tamping effect [52–54] is a consequence of decreasing deposition efficiency, as shown by Xie et al. [55]. The W-10Cr coatings B and C exhibited similar tamping phenomenon towards the free surface, with the coating C experiencing higher overall level of particles spreading. This could have been triggered by two factors: deposition onto harder steel substrate and repeated delamination of portions of the coatings upon the spraying (evidenced by surface view SEM examination), exposing the previously deposited material to further particle impingement. The thickness of coatings B and C exceeded 200 μm and, importantly, the chromium content in both coatings was distributed evenly. In both cases, however, the overall deposition efficiency was rather low (this could be improved in the near future as first studies on a successful deposition of Cr were presented recently [56]) and the mutual cohesion of the particles was not flawless as cracks spanning several particles were observed in the microstructures. This led to the idea of adding a binder material to the blends. Considering the half-lives and ease of sprayability, and taking into account the fact that it had been used in self-passivation alloys previously [57–59], titanium was selected as the prime candidate over Al, Ni, or Cu.

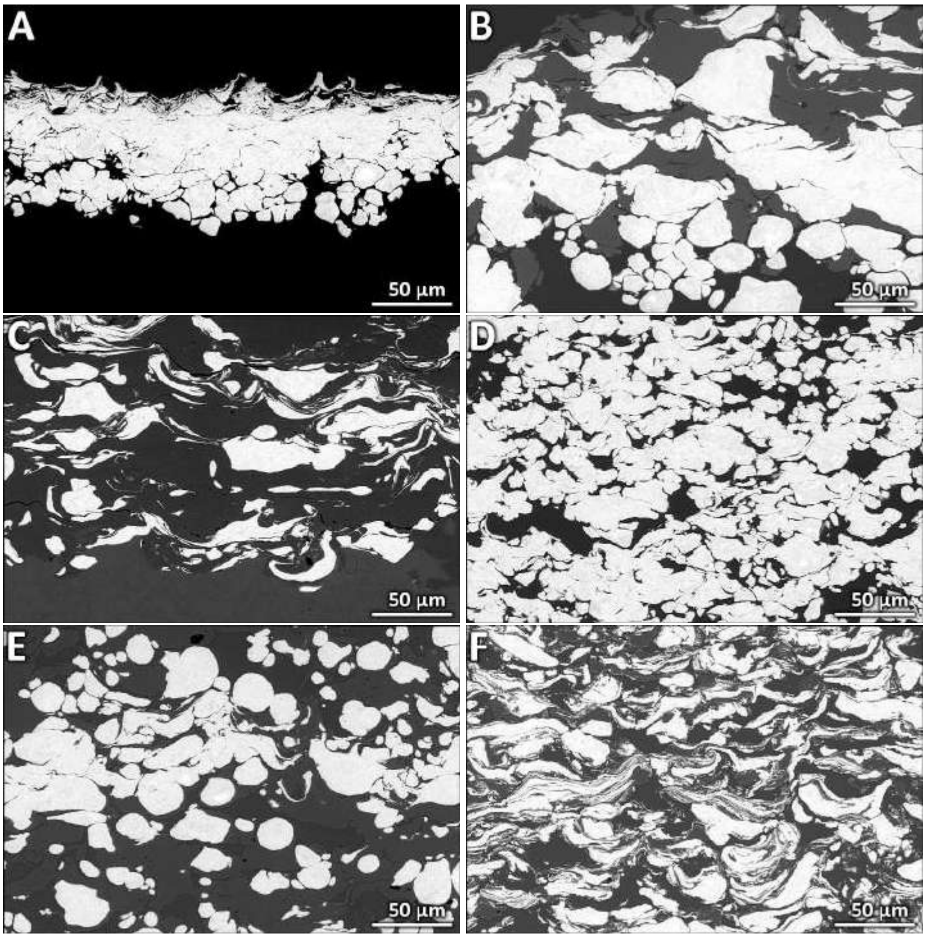

Figure 4. Microstructure of the produced cold spray coatings A–F The bright phase is tungsten. In coatings B, C, the dark phase is chromium, in coating D titanium. In coatings E, F, titanium is darker than chromium; see the EDX mapping of the two coatings in Figure 5 for more magnified view.

The coatings containing 5% titanium exhibited significantly improved, crack-free microstructure. The principle exploited here is the ductile binder aiding in the adherence of incoming tungsten (and chromium) particles, as in the studies [10–13]. The coatings easily reached thicknesses from 450–1100 μm and experienced no troubles with deposition efficiency. The tamping effect observed for coatings A–C was not manifested. Again, the chromium and titanium contents were distributed evenly throughout the entire thickness and, in the case of coatings D and E, prevented excessive deformation of the W particles. The effect of mechanical alloying of the W and Cr powders in coating F can be nicely seen in comparison with the mixed-only blend of coating E (Figure 5). The individual W particles were in fact layered alternating lamellae of W and Cr, a microstructure inherited from the feedstock powder. Such finer microstructure of the particles could contribute to oxidation resistance of the coatings by shortening the diffusion path of oxide scale forming elements. The microstructure of coatings E and F seems very promising towards formation of chromium-based oxides.

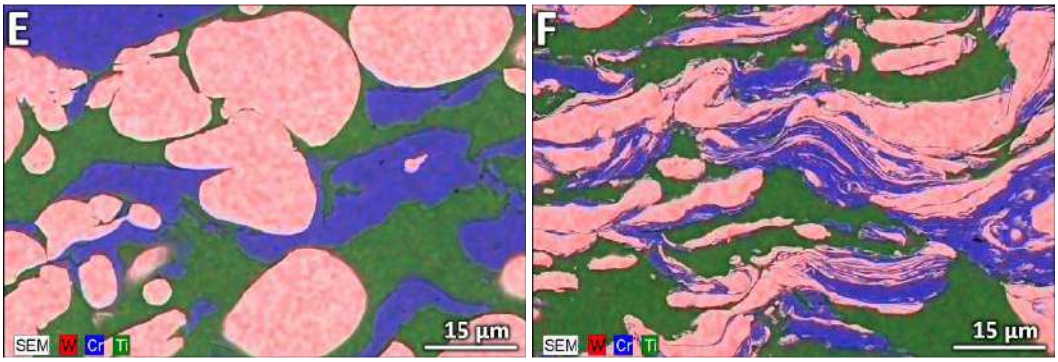

Figure 5. Enhanced elemental maps of the produced cold spray coatings E and F. Note the difference between blended-only W and Cr particles in coating E and the lamellar structure of the co-milled W and Cr particles in coating F.

The interface quality of the six produced coatings is shown in Figure 6. Non-deformed (slightly deformed) particles could be clearly seen at the interface of coatings A and B and the Al 6060 alloy substrate. Preservation of the original morphology of the particles is due to the embedding phenomenon commonly encountered in cold spraying onto soft substrates. Contrary to this, the coating C deposited onto relatively hard steel 1.1191 exhibits a significant ratio of particle flattening directly at the interface already. Somewhat in between these in terms of plastic deformation of the first layer of particles are coatings D–F deposited onto medium hardness AISI 304 steel (note that the deformation of particles in coating F stems from the powder milling process). Overall, the interface quality of all coatings is very good, with only minor imperfections observed infrequently. This result is very promising and suggests a potential of the cold spray method for the fusion applications.

Owing to the particle impingement principle, the surface of all coatings was relatively rough as compared to e.g., PVD or CVD processes. Their high specific surface area (in the as-sprayed condition) could potentially lead to unfavorable susceptibility to plasma particle erosion, triggering contamination of the plasma by the eroded tungsten content, yielding the coatings unsuitable for PFCs. However, this does not present a major problem as metallic cold sprayed coatings are easily machinable [60] by e.g., turning or milling. Thereby, the surfaces could be smoothed to a specified roughness without jeopardizing other coating properties.

In the literature, four sources pertaining to tungsten-based cold sprayed coatings can be found. In 2003, Kang and Kang [10] presented cold spraying of agglomerated (milled) W-25Cu composite powder. The starting feedstock W particle sizes were very small, ≤ 1 µm, while the copper was ≤ 45 µm. The final powder was classified into ≤ 75 µm range and preheated to 470 °C prior to spraying using nitrogen at 37.27 MPa (this reported datum actually may be too high, a value of 3.727 MPa would seem more probable at this state of CS technology development). The final coating thickness reached 600 µm and the retained W content dropped to 37%. This is significantly higher W phase loss than in our study, probably due to lower spray parameters used. Also, a formation of porosity was observed in their study, but the values remained fairly low, from 0.5–1.0%. Understandably, the pores were mostly found around the W-rich regions in the coatings. Sixteen years later, the same materials combination was sprayed and its wear resistance was studied by Deng and co-workers [11]. In their study, three different

W contents were used: 30, 50, and 70%. Again, these were formed using a very small W feedstock ($\leq$3 μm) and relatively big copper particles (15–53 μm) blended together for 15 h. Upon spraying with air at 500 °C at feedrates of 2.3–3.1 $\text{kg}\cdot\text{h}^{-1}$, the coatings exhibited declining thickness with increasing W content, reaching a total of 710 μm, 220 μm, and 35 μm. Importantly, the thickness reduction was triggered even though the final W phase content in the coatings was dramatically reduced, yielding 12% and 19% of W only for the original 30% and 50%W powders. The W content for the coating from 70%W powder was not provided. Interestingly, there was a major disagreement between their study and the study of Kang and Kang [10]: while the former study suggested a decreasing 2–5% porosity content with increasing W content (explained by the tamping effect of non-bonded brittle W particles), Kang and Kang observed a completely inverse trend (explained by insufficient energy of incoming W particles). We speculate here that the difference could be caused by the different feedstock preparation routes (blend vs. agglomerated composite). Still, considering that the used spray parameters of the latter study are actually stronger, this interesting discrepancy well illustrates the somewhat uncomprehended nature of deposition of difficult-to-spray materials.

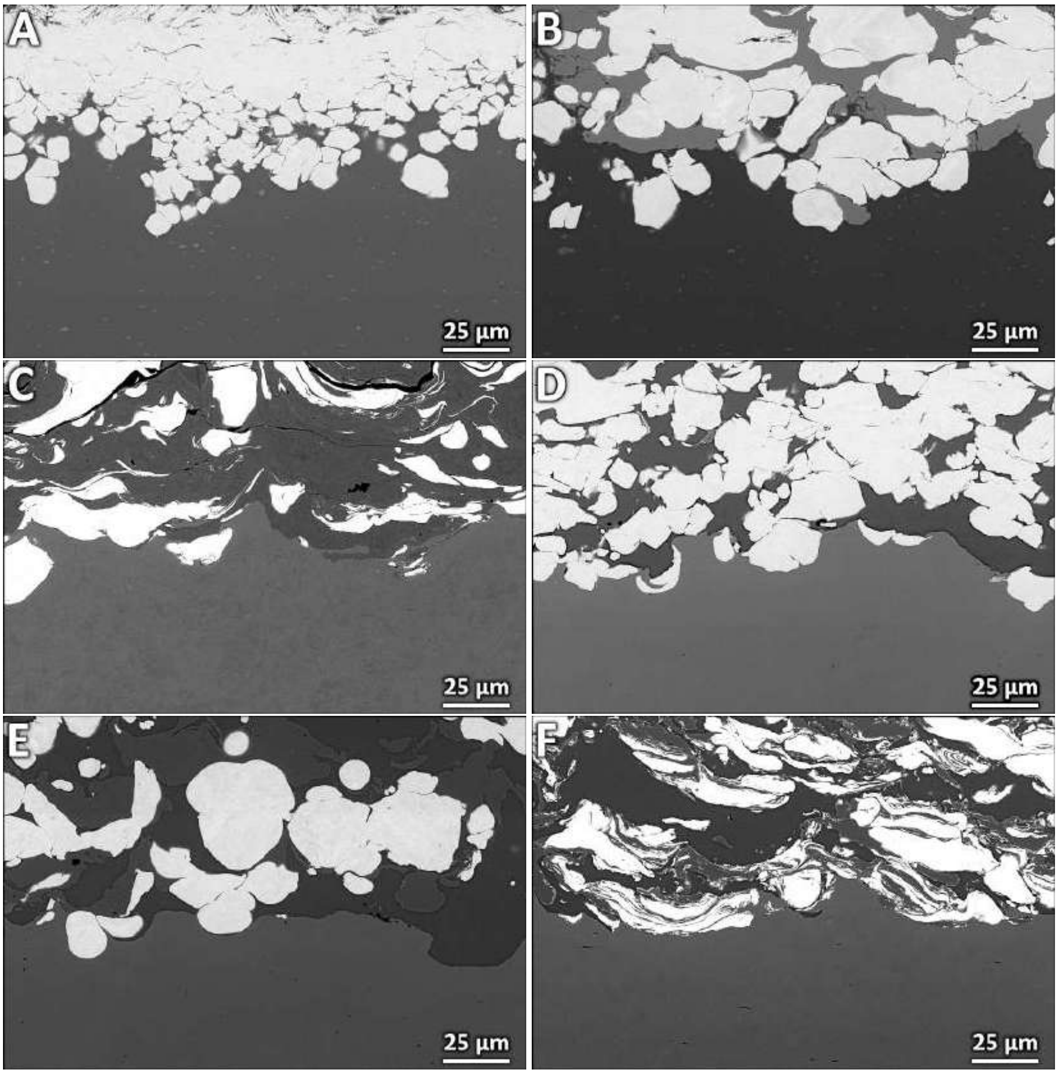

Figure 6. Interface of the produced cold spray coatings and underlying substrates. Al 6060 alloy was used for coatings A and B, relatively hard steel 1.1191 for coating C and medium hardness AISI 304 steel for coatings D–F.

Another study performed by Barnett and colleagues [13] presented spraying of refractory mixtures to form donor tubes for explosive cladding. In their study, they used tantalum as the binder phase and a fairly low content of W (10%). Again, the tungsten powder was rather small (5 µm, cf. the 10–15 µm and ≥20 µm sizes of the W powders in our study), suggesting its better suitability for cold spraying at lower parameters. Using (expensive) helium at 400 °C and 2.5 MPa, they successfully managed to deposit coatings with thickness exceeding 1.5 mm (and subsequently remove the substrates by machining, thereby forming free-standing parts). Given the rather high content of the binder matrix, they reached deposition efficiencies as high as 85%.

The study closest to ours in terms of W content was made by Xia and co-workers [12] in 2016. In their study, the binder matrix was a combination of nickel and iron at two different ratios: 17.5Ni + 7.5Fe and 4.9Ni + 2.1Fe (yielding 75% and 93% of W in the feedstock, respectively). This time, the feedstock powders were all very small (3–10 µm W, 2–5 µm Ni, 2 µm Fe) and were co-milled for 12 h. Prior to spraying, the powder was heated to 630 °C to soften and then sprayed using air at 2.5 MPa. The W content in the final coatings (30% and 64%) was comparable to the mixed feedstock results in our study and the porosities were rather low (0.2–0.7%). The coating thickness reached up to 1.9 mm and the exhibited good adhesion (≥32 MPa according to ASTM C-633 standard).

The elemental analysis and EDX mapping of our samples showed significant difference in the chemical composition of the coatings as compared to the starting feedstock. The difference in the W/Cr/Ti ratios is caused by a selective deposition of the individual constituents. This is, in turn, triggered by different densities of the three metals, their different particle sizes and morphologies, and also their individual crystallographic lattices (manifested in their deformability). The chromium levels in coatings B and C were 26% and 52%, respectively. In combination with more deformed particles, the somewhat higher Cr content in the latter coating suggests more difficult W deposition from the process beginning that may be attributed to the harder steel substrate. In coating D, the initial W/Ti ratio of 95/5 changed to 76/24. This is, again, given by the selective deposition of the two constituents. Even though the higher Ti content does not present any major complication for the PFCs per se, a future experimental work is planned to reach a lower ∼10% Ti content in the final coatings. The composition of coatings E and F was very similar, with both retaining 45 and 51% of tungsten upon spraying, respectively. However, they differed slightly in the Cr/Ti ratio (28/27 vs. 18/31). This could be a consequence of the chromium content either inserted in its original pulverized form (i.e., relatively free of deformation) or in the form of a mechanically alloyed particles (i.e., with very high dislocation density and partially depleted of ductility).

Importantly, the coatings were not oxidized and retained metallic coloration. Upon a long-term EDX mapping, a slight oxygen content was observed to follow the Cr particles in the coating (absent for W and Ti particles). This is related to the same oxygen indication in the feedstock Cr powder, i.e., it is not attributed to the spray process. The absence of oxides is in accordance with the previous studies on CS deposition of W [10–13] and was further confirmed by the XRD process where the detected elements were confirmed as pure. The non-oxidized state is a prime advantage of the cold spray method over the other processes such as plasma spraying or HVOF, meeting the stringent criteria imposed by the fusion community on the armor coatings for the first wall in tokamaks.

The measured hardness of the coatings corresponded to their chemical composition (Table 1). The lowest hardness was recorded for the samples with the lowest W content (C, E). Similarly low content was recorded in the coating F. However, in this case, the pre-spray milling operation led to a significant increase in the hardness. The increase was caused by the increased dislocation density triggered by the cold working endured within the milling process. This suggests that the coating hardness can be increased by the feedstock milling; importantly, this can be achieved without compromising the tungsten component content (given the rather similar W levels in coatings E and F). Naturally, the coatings with the high W content (A, D, B) exhibited highest hardness values (504 HV0.1, 444 HV0.3 and 410 HV0.3, respectively). Comparing the obtained results with the two studies that measured hardness of W-based cold sprayed coatings [11,12], one can see a trend of increasing hardness with increasing W content (Figure 7). Interestingly, this is somewhat irrespective of the binder matrix material (Cu [11], Ni + Fe [12], Cr + Ti in our study), suggesting a dominant role of W in this property. In accordance with our results, the coatings fabricated from milled feedstock in [11] reached higher hardness values.

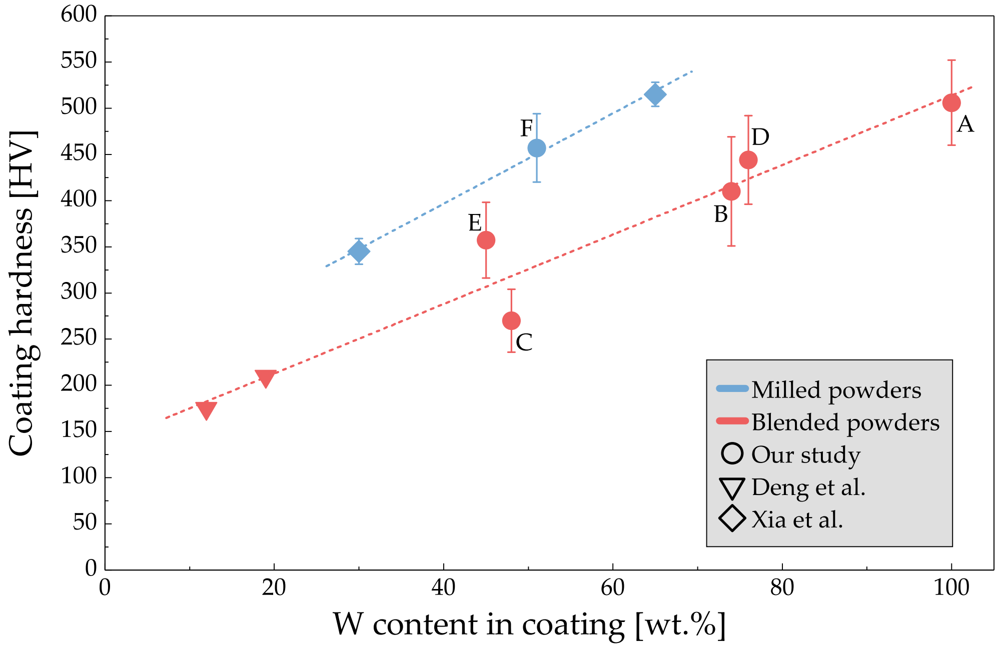

Figure 7. Hardness of the coatings from our study and two studies by Deng et al. [11] and Xia et al. [12]. There is a clear trend of increasing hardness with increasing W content (disregarding the different binder phases). The milled feedstock clearly reaches higher coating hardness values as opposed to the blended-only powders. The hardness in the graph is HV0.3 with the exception of the study [11] (HV0.05) and the coating with 100% W from our study (HV0.1).

The measured values of longitudinal (~4300 m·s^{-1}) and transversal (~2200 m·s^{-1}) waves propagation in the three Ti-containing coatings D–F (Table 2) are approximately 20% lower than those in pure polycrystalline bulk tungsten (indicated as 5220 m·s^{-1} and 2890 m·s^{-1} [61]). The waves propagation measurement allowed to determine the elastic constants of the three coatings. The density of the coating D was found to be higher, mostly because of the high W content (Table 2). The two coatings E, F differed only slightly as their chemical content was similar. Considering the theoretical moduli of the bulk W, Cr, and Ti (406 GPa, 248 GPa and 120 GPa, respectively [61,62]) and the average composition of the coatings D–F, their theoretical average values should reach 392 GPa, 303 GPa, and 289 GPa. However, the measured moduli of the coatings are in general lower than these values, reaching 50–55% only (Table 2). Such reduced stiffness would suggest an imperfect bonding of the individual particles, potentially leading to elastic anisotropy in mechanical properties [63]. The determined waves propagation velocities of the three coatings are similar and do not exhibit any significant differences in either direction. That said, the differences in the elastic moduli of the three coatings are given by their different average densities rather than different mechanisms.

Table 2. Elastic constants of the coatings D–F measured by through-transmission waves propagation method. Uncertainty levels resulting from the methodology are marked as "StDev". The relative moduli were calculated as the ratio of measured values to the theoretical prediction based on average elemental composition of the coatings.

Property	**Unit**	**StDev**	**Coating**		
			D	**E**	**F**
Density	$g\cdot cm^{-3}$	0.30	15.44	11.99	11.94
Longitudinal waves velocity	$m\cdot s^{-1}$	80	4284	4377	4361
Transversal waves velocity	$m\cdot s^{-1}$	80	2195	2297	2192
Young's modulus	GPa	10	197	166	153
Relative modulus	%	–	50	55	53
Poisson number	–	0.020	0.322	0.310	0.331

A preliminary oxidation test was carried out to evaluate the potential of the coatings to mitigate formation of WO_3, yielding them suitable as the armor coatings for the fusion application. Upon exposure to air at 1000 °C for 10 h, the coatings D–F were completely oxidized. As expected, the coating D without chromium content prompted a severe oxidation of the tungsten, giving rise to formation of 78% of WO_3 oxide and 22% of TiO_2 (rutile). Given the expansion of W upon oxidation, such results would not be suitable for the application and could potentially jeopardize the integrity of the reactor. The two combinations with Cr content (E, F) showed an interesting (desired) potential to significantly suppress the WO_3 formation, all the way to 38% and 34% content only, respectively. That said, the finer microstructure of the W and Cr particles in coating F brought only a slight improvement (a difference of 4% of WO_3 as compared to the coating E from mixed-only feedstock). In both cases, the decrease was triggered by a formation of Cr_2WO_6 and Cr_2WO_3 chromium-tungstate oxides (9% and 8%, respectively). Such complex oxides could be formed by a reaction of WO_3 and Cr_2O_3. The latter actually forms a volatile CrO_3 in the 1000–1200 °C region. As such, more detailed oxidation experiments are planned to understand the formation mechanisms, kinetics, and evaporation rates.

4. Conclusions

In our study, we presented a cold spray deposition of thick W and W-based coatings to be potentially used as a first wall armor in nuclear fusion. As opposed to other considered processes, the method presents a simple, one-step, commercially available technology capable of rapid covering of large-scale surfaces with coatings spanning hundreds of microns in thickness.

Owing to the observed good interface quality with the substrates, it should be trouble-free to securely and easily machine the coatings by turning or milling, without the requirement for any post-process technological steps. As we have shown, the materials are relatively hard, oxide-free and contain levels of tungsten that were never reached before (in fact, 100% pure 80 μm tungsten coating was deposited for the first time). The coatings possess elastic moduli lower than bulks, and their densities (and chemical composition) can be fine-tuned by the feedstock selection. Importantly, their oxidation behavior improved by the addition of Cr content.

Combined, the cold spray technology holds a great potential for application in the nuclear fusion sector. Given the promising results, our ongoing research efforts are, at the moment, aimed at further improvement of the microstructure and properties of coatings with lower Cr contents as well as advanced oxidation tests of smooth, machined surfaces.

Author Contributions: conceptualization, J.C. and M.V.; methodology, J.C., M.V. and J.K.; software, J.K.; validation, J.C. and M.V.; investigation, J.C., M.V., F.L., M.K., J.K. and R.S.; resources, M.V., F.L., J.K. and R.S.; data curation, J.C., M.V. and F.L.; writing-original draft preparation, J.C. and M.V.; writing-review and editing, J.C., M.V., M.K. and R.S.; visualization, J.C.; project administration, J.C.; funding acquisition, M.V., F.L. and M.K.

Funding: This research was funded by Czech Science Foundation grants 17-23154S (M. Vilemova, F. Lukac) and 17-13573S (M. Koller).

Conflicts of Interest: The authors declare no conflict of interest.

References

1. Matejicek, J. Materials for fusion Applications. *Acta Polytech.* **2013**, *53*, 197–212.
2. Pintsuk, G. Tungsten as a Plasma-Facing Material. In *Comprehensive Nuclear Materials*; Elsevier: Amsterdam, The Netherlands, 2012; Chapter 4.17, pp. 551–581.
3. Cizek, J.; Klecka, J. Harnessing fusion power: W and W-Cr armor coatings for plasma-facing components in tokamaks. *Adv. Mater. Process.* **2019**, *177*, 46–49.
4. Kikuchi, M.; Lackner, K.; Tran, M.Q. (Eds.) *Fusion Physics*; International Atomic Energy Agency: Vienna, Austria, 2012.
5. Litnovsky, A.; Wegener, T.; Klein, F.; Linsmeier, C.; Rasinski, M.; Kreter, A.; Unterberg, B.; Coenen, J.; Du, H.; Mayer, J.; et al. Smart tungsten alloys as a material for the first wall of a future fusion power plant. *Nucl. Fusion* **2017**, *57*, 066020. [CrossRef]
6. Lopez-Ruiz, P.; Ordas, N.; Iturriza, I.; Walter, M.; Gaganidze, E.; Lindig, S.; Koch, F.; Garcia-Rosales, C. Powder metallurgical processing of self-passivating tungsten alloys for fusion first wall application. *J. Nucl. Mater.* **2013**, *442*, S219–S224. [CrossRef]
7. Naidu, S.; Sriramamurthy, A.; Rao, P. The Cr-W (chromium-tungsten) system. *Bull. Alloy Phase Diagrams* **1984**, *5*, 289–292. [CrossRef]
8. Cizek, J.; Man, O.; Roupcova, P.; Loke, K.; Dlouhy, I. Oxidation performance of cold spray Ti-Al barrier coated gamma-TiAl intermetallic substrates. *Surf. Coat. Technol.* **2015**, *268*, 85–89. [CrossRef]
9. Cizek, J.; Matejkova, M.; Dlouhy, I.; Siska, F.; Kay, C.; Karthikeyan, J.; Kuroda, S.; Kovarik, O.; Siegl, J.; Loke, K.; et al. Influence of Cold Sprayed, Warm Sprayed and Plasma Sprayed Layers Deposition on Fatigue Properties of Steel Specimens. *J. Therm. Spray Technol.* **2015**, *24*, 758–768. [CrossRef]
10. Kang, H.; Kang, S. Tungsten/copper composite deposits produced by a cold spray. *Scr. Mater.* **2003**, *49*, 1169–1174. [CrossRef]
11. Deng, N.; Tang, J.; Xiong, T.; Li, J.; Zhou, Z. Fabrication and characterization of W-Cu composite coatings with different W contents by cold spraying. *Surf. Coat. Technol.* **2019**, *368*, 8–14. [CrossRef]
12. Xia, M.; Huang, P.; Cu, R.; Ge, C. Cold sprayed W/Ni/Fe alloy coating: Microstructure and mechanical properties. *Surf. Coat. Technol.* **2016**, *291*, 376–381. [CrossRef]
13. Barnett, B.; Trexler, M.; Champagne, V. Cold sprayed refractory metals for chrome reduction in gun barrel liners. *Int. J. Refract. Met. Hard Mater.* **2015**, *53*, 139–143. [CrossRef]
14. Ji, G.; Wang, H.; Chen, X.; Bai, X.; Dong, Z.; Yang, F. Characterization of cold-sprayed multimodal WC-12Co coating. *Surf. Coat. Technol.* **2013**, *235*, 536–543. [CrossRef]
15. Ji, G.; Chen, X.; Wang, H.; Bai, X.; Dong, Z. Deformation Behaviors of Cold-Sprayed WC-Co Particles. *J. Therm. Spray. Technol.* **2015**, *24*, 1100–1110. [CrossRef]
16. da Silva, F.; Cinca, N.; Dosta, S.; Cano, I.; Couto, M.; Guilemany, J.; Benedetti, A. Corrosion behavior of WC-Co coatings deposited by cold gas spray onto AA 7075-T6. *Corros. Sci.* **2018**, *136*, 231–243. [CrossRef]
17. Kim, H.; Lee, C.; Hwang, S. Fabrication of WC-Co coatings by cold spray deposition. *Surf. Coat. Technol.* **2005**, *191*, 335–340. [CrossRef]
18. Kim, H.; Lee, C.; Hwang, S. Superhard nano WC-12%Co coating by cold spray deposition. *Mater. Sci. Eng. A* **2005**, *391*, 243–248. [CrossRef]
19. Gao, P.; Li, C.; Yang, G.; Li, Y.; Li, C. Influence of substrate hardness on deposition behavior of single porous WC-12Co particle in cold spraying. *Surf. Coat. Technol.* **2008**, *203*, 384–390. [CrossRef]
20. Gao, P.; Li, Y.; Li, C.; Yang, G.; Li, C. Influence of Powder Porous Structure on the Deposition Behavior of Cold-Sprayed WC-12Co Coatings. *J. Therm. Spray Technol.* **2008**, *17*, 742–749. [CrossRef]
21. Gao, P.; Li, C.; Yang, G.; Li, Y.; Li, C. Influence of substrate hardness transition on built-up of nanostructured WC-12Co by cold spraying. *Appl. Surf. Sci.* **2010**, *256*, 2263–2268. [CrossRef]
22. Wang, H.; Chen, X.; Bai, X.; Ji, G.; Dong, Z.; Yi, D. Microstructure and properties of cold sprayed multimodal WC-17Co deposits. *Int. J. Refract. Met. Hard Mater.* **2014**, *45*, 196–203. [CrossRef]
23. Lima, R.; Karthikeyan, J.; Kay, C.; Lindemann, J.; Berndt, C. Microstructural characteristics of cold-sprayed nanostructured WC-Co coatings. *Thin Solid Films* **2002**, *416*, 129–135. [CrossRef]

24. Couto, M.; Dosta, S.; Torrell, M.; Fernandez, J.; Guilemany, J. Cold spray deposition of WC-17 and 12Co cermets onto aluminum. *Surf. Coat. Technol.* **2013**, *235*, 54–61. [CrossRef]
25. Couto, M.; Dosta, S.; Fernandez, J.; Guilemany, J.M. Comparison of the Mechanical and Electrochemical Properties of WC-25Co Coatings Obtained by High Velocity Oxy-Fuel and Cold Gas Spraying. *J. Therm. Spray Technol.* **2014**, *23*, 1251–1258. [CrossRef]
26. Couto, M.; Dosta, S.; Guilemany, J. Comparison of the mechanical and electrochemical properties of WC-17 and 12Co coatings onto Al7075-T6 obtained by high velocity oxy-fuel and cold gas spraying. *Surf. Coat. Technol.* **2015**, *268*, 180–189. [CrossRef]
27. Dosta, S.; Couto, M.; Guilemany, J. Cold spray deposition of a WC-25Co cermet onto Al7075-T6 and carbon steel substrates. *Acta Mater.* **2013**, *61*, 643–652. [CrossRef]
28. Dosta, S.; Bolelli, G.; Candeli, A.; Lusvarghi, L.; Cano, I.; Guilemany, J. Plastic deformation phenomena during cold spray impact of WC-Co particles onto metal substrates. *Acta Mater.* **2017**, *124*, 173–181. [CrossRef]
29. Ang, S.; Berndt, C.; Cheang, P. Deposition effects of WC particle size on cold sprayed WC-Co coatings. *Surf. Coat. Technol.* **2011**, *205*, 3260–3267. [CrossRef]
30. Li, C.; Yang, G.; Gao, P.; Ma, J.; Wang, Y.; Li, C. Characterization of Nanostructured WC-Co Deposited by Cold Spraying. *J. Therm. Spray Technol.* **2007**, *16*, 1011–1020. [CrossRef]
31. Yandouzi, M.; Sansoucy, E.; Ajdelsztajn, L.; Jodoin, B. WC-based cermet coatings produced by cold gas dynamic and pulsed gas dynamic spraying processes. *Surf. Coat. Technol.* **2007**, *202*, 382–390. [CrossRef]
32. Lioma, D.; Sacks, N.; Botef, I. Cold gas dynamic spraying of WC-Ni cemented carbide coatings. *Int. J. Refract. Met. Hard Mater.* **2015**, *49*, 365–373. [CrossRef]
33. Alidokht, S.; Manimunda, P.; Vo, P.; Yue, S.; Chromik, R. Cold spray deposition of a Ni-WC composite coating and its dry sliding wear behavior. *Surf. Coat. Technol.* **2016**, *308*, 424–434. [CrossRef]
34. Alidokht, S.; Vo, P.; Yue, S.; Chromik, R. Erosive wear behavior of Cold-Sprayed Ni-WC composite coating. *Wear* **2017**, *376-377*, 566–577. [CrossRef]
35. Alidokht, S.; Yue, S.; Chromik, R. Effect of WC morphology on dry sliding wear behavior of cold-sprayed Ni-WC composite coatings. *Surf. Coat. Technol.* **2019**, *357*, 849–863. [CrossRef]
36. Torgerson, T.; Harris, M.; Alidokht, S.; Scharf, T.; Aouadi, S.; Chromik, R.; Zabinski, J.; Voevodin, A. Room and elevated temperature sliding wear behavior of cold sprayed Ni-WC composite coatings. *Surf. Coat. Technol.* **2018**, *350*, 136–145. [CrossRef]
37. Nunthavarawong, P.; Sacks, N.; Botef, I. Effect of powder feed rate on the mechanical properties of WC-5 wt%Ni coatings deposited using low pressure cold spray. *Int. J. Refract. Met. Hard Mater.* **2016**, *61*, 230–237. [CrossRef]
38. Sacks, N. Low pressure cold gas dynamic spraying of tungsten carbide-nickel coatings. *Met. Powder Rep.* **2016**, *71*, 356–358. [CrossRef]
39. Melendez, N.; Narulkar, V.; Fisher, G.; McDonald, A. Effect of reinforcing particles on the wear rate of low-pressure cold-sprayed WC-based MMC coatings. *Wear* **2013**, *306*, 185–195. [CrossRef]
40. Melendez, N.; McDonald, A. Development of WC-based metal matrix composite coatings using low-pressure cold gas dynamic spraying. *Surf. Coat. Technol.* **2013**, *214*, 101–109. [CrossRef]
41. Lee, Y.; Ashrafizadeh, H.; Fisher, G.; McDonald, A. Effect of type of reinforcing particles on the deposition efficiency and wear resistance of low-pressure cold-sprayed metal matrix composite coatings. *Surf. Coat. Technol.* **2017**, *324*, 190–200. [CrossRef]
42. Yin, S.; Ekoi, E.; Lupton, T.; Dowling, D.; Lupoi, R. Cold spraying of WC-Co-Ni coatings using porous WC-17Co powders: Formation mechanism, microstructure characterization and tribological performance. *Mater. Des.* **2017**, *126*, 305–313. [CrossRef]
43. Peat, T.; Galloway, A.; Toumpis, A.; Steel, R.; Zhu, W.; Iqbal, N. Enhanced erosion performance of cold spray co-deposited AISI316 MMCs modified by friction stir processing. *Mater. Des.* **2017**, *120*, 22–35. [CrossRef]
44. Peat, T.; Galloway, A.; Toumpis, A.; McNutt, P.; Iqbal, N. The erosion performance of cold spray deposited metal matrix composite coatings with subsequent friction stir processing. *Appl. Surf. Sci.* **2017**, *396*, 1635–1648. [CrossRef]
45. Peat, T.; Galloway, A.; Toumpis, A.; McNutt, P.; Iqbal, N. The erosion performance of particle reinforced metal matrix composite coatings produced by co-deposition cold gas dynamic spraying. *Appl. Surf. Sci.* **2017**, *396*, 1623–1634. [CrossRef]

46. Zhang, Y.; Epshteyn, Y.; Chromik, R. Dry sliding wear behaviour of cold-sprayed Cu-MoS2 and Cu-MoS2-WC composite coatings: The influence of WC. *Tribol. Int.* **2018**, *123*, 296–306. [CrossRef]
47. Zhang, Y.; Descartes, S.; Chromik, R. Influence of WC on third body behaviour during fretting of cold-sprayed Cu-MoS2-WC composites. *Tribol. Int.* **2019**, *134*, 15–25. [CrossRef]
48. Koller, M.; Seiner, H.; Landa, M.; Nieto, A.; Agarwal, A. Anisotropic elastic and acoustic properties of bulk graphene nanoplatelets consolidated by spark plasma Sintering. *Acta Phys. Pol. A* **2015**, *128*, 670–674. [CrossRef]
49. Sedlak, P.; Seiner, H.; Landa, M.; Novak, V.; Sittner, P.; Manosa, L. Elastic constants of bcc austenite and 2H orthorhombic martensite in CuAlNi shape memory alloy. *Acta Mater.* **2005**, *53*, 3643–3661. [CrossRef]
50. Hartsuijker, C.; Welleman, J. *Engineering Mechanics: Stresses, Strains, Displacements*; Springer: Berlin, Germany, 2007; Volume 2. [CrossRef]
51. Rietveld, H. Line profiles of neutron powder-diffraction peaks for structure refinement. *Acta Cryst.* **1967**, *22*, 151–152. [CrossRef]
52. Koivuluoto, H.; Vuoristo, P. Effect of powder type and composition on structure and mechanical properties of Cu+Al_2O_3 coatings prepared by using low-pressure cold spray process. *J. Therm. Spray Technol.* **2010**, *19*, 1081–1092. [CrossRef]
53. Koivuluoto, H.; Bolelli, G.; Milanti, A.; Lusvarghi, L.; Vuoristo, P. Microstructural analysis of high-pressure cold-sprayed Ni, NiCu and NiCu+Al_2O_3 coatings. *Surf. Coat. Technol.* **2015**, *268*, 224–229. [CrossRef]
54. Lee, H.; Jung, S.; Lee, S.; You, Y.; Ko, K. Correlation between Al_2O_3 particles and interface of Al-Al_2O_3 coatings by cold spray. *Appl. Surf. Sci.* **2005**, *252*, 1891–1898. [CrossRef]
55. Xie, Y.; Yin, S.; Cizek, J.; Cupera, J.; Guo, E.; Lupoi, R. Formation mechanism and microstructure characterization of nickel-aluminum intertwining interface in cold spray. *Surf. Coat. Technol.* **2018**, *337*, 447–452. [CrossRef]
56. Walters, J.; Romero, J.; Mueller, A.; Stiteler, R.; Shah, H.; Oelrich, R. Thin cold sprayed coatings for nuclear fuel with enhanced accident tolerance. In Proceedings of the International Thermal Spray Conference, Yokohama, Japan, 26–29 May 2019; pp. 420–426.
57. Calvo, A.; Garcia-Rosales, C.; Koch, F.; Ordas, N.; Iturriza, I.; Greuner, H.; Pintsuk, G.; Sarbu, C. Manufacturing and testing of self-passivating tungsten alloys of different composition. *Nucl. Mater. Energy* **2016**, *9*, 422–429. [CrossRef]
58. Lessmann, M.; Sudic, I.; Fazinic, S.; Tadic, T.; Calvo, A.; Hardie, C.; Porton, M.; Garcia-Rosales, C.; Mummery, P. The effects of ion irradiation on the micromechanical fracture strength and hardness of a self-passivating tungsten alloy. *J. Nucl. Mater.* **2017**, *486*, 34–43. [CrossRef]
59. Vilemova, M.; Illkova, K.; Lukac, F.; Matejicek, J.; Klecka, J.; Leitner, J. Microstructure and phase stability of W-Cr alloy prepared by spark plasma sintering. *Fusion Eng. Des.* **2018**, *127*, 173–178. [CrossRef]
60. Yin, S.; Cizek, J.; Yan, X.; Lupoi, R. Annealing strategies for enhancing mechanical properties of additively manufactured 316L stainless steel deposited by cold spray. *Surf. Coat. Technol.* **2019**, *370*, 353–361. [CrossRef]
61. Lee, H.; Ando, S.; Coenen, J.; Mao, Y.; Riesch, J.; Gietl, H.; Kasada, R.; Hamaji, Y.; Ibano, K.; Ueda, Y. Longitudinal and shear wave velocities in pure tungsten and tungsten fiber-reinforced tungsten composites. *Phys. Scr.* **2017**, *T170*, 014024. [CrossRef]
62. Mason, W. Acoustic properties of solids. In *American Institute of Physics Handbook*; McGraw-Hill: New York, NY, USA, 1972; Chapter 3f, pp. 98–117.
63. Seiner, H.; Cizek, J.; Sedlak, P.; Huang, R.; Cupera, J.; Dlouhy, I.; Landa, M. Elastic moduli and elastic anisotropy of cold sprayed metallic coatings. *Surf. Coat. Technol.* **2016**, *291*, 342–347. [CrossRef]

© 2019 by the authors. Licensee MDPI, Basel, Switzerland. This article is an open access article distributed under the terms and conditions of the Creative Commons Attribution (CC BY) license (http://creativecommons.org/licenses/by/4.0/).